

AFOSR-TR-79-1263

⑤ LEVEL

AD A 0 78952

DDC FILE COPY

DISTRIBUTION STATEMENT A  
Approved for public release;  
Distribution Unlimited

DDC  
RECEIVED  
JAN 7 1980  
RECEIVED  
B

REPORT DOCUMENTATION PAGE READ INSTRUCTIONS BEFORE COMPLETING FORM

1. REPORT NUMBER **AFOSR/TR-79-12631** 2. GOVT ACCESSION NO. 3. RECIPIENT'S CATALOG NUMBER

4. TITLE (and Subtitle) **ON THE FEEDBACK PHENOMENON OF AN IMPINGING JET** 5. TYPE OF REPORT & PERIOD COVERED **INTERIM**  
**Apr 1977 - Sep 79** 6. PERFORMING ORG. REPORT NUMBER

7. AUTHOR(s) **NAGY SABET M. NOSSEIR**  
**CHIH-MING** 8. CONTRACT OR GRANT NUMBER(s) **F49620-78-C-0060/4**

9. PERFORMING ORGANIZATION NAME AND ADDRESS **UNIVERSITY OF SOUTHERN CALIFORNIA**  
**AEROSPACE ENGINEERING DEPARTMENT**  
**LOS ANGELES, CA 90007** 10. PROGRAM ELEMENT, PROJECT, TASK AREA & WORK UNIT NUMBERS **2307A2**  
**61102F**

11. CONTROLLING OFFICE NAME AND ADDRESS **AIR FORCE OFFICE OF SCIENTIFIC RESEARCH/NA**  
**BLDG 410**  
**BOLLING AIR FORCE BASE, D C 20332** 12. REPORT DATE **September 1979**  
13. NUMBER OF PAGES **254**

14. MONITORING AGENCY NAME & ADDRESS (if different from Controlling Office) **1-2511** 15. SECURITY CLASS. (of this report) **UNCLASSIFIED**  
15a. DECLASSIFICATION DOWNGRADING SCHEDULE

16. DISTRIBUTION STATEMENT (of this Report)  
**Approved for public release; distribution unlimited.**

17. DISTRIBUTION STATEMENT (of the abstract entered in Block 20, if different from Report)

18. SUPPLEMENTARY NOTES

**DDC**  
**RECEIVED**  
**JAN 7 1980**  
**B**

19. KEY WORDS (Continue on reverse side if necessary and identify by block number)  
**TURBULENT JET**  
**JET IMPINGEMENT**  
**RESONANCE**  
**FEEDBACK**  
**PRESSURE FLUCTUATIONS**

20. ABSTRACT (Continue on reverse side if necessary and identify by block number)  
The resonance phenomenon which occurs when a high speed turbulent jet impinges on a large flat plate, is experimentally studied. The far field noise is also investigated for a wide range of impinging jet speeds. The study involves far field, near field, and surface pressure measurements. A feedback of pressure waves between the nozzle and the plate is found to be the mechanism responsible for the resonance. The feedback loop is formed by downstream traveling large coherent structures, and upstream acoustic waves propagating in the nearby stagnant region around the jet. The upstream acoustic waves are generated by the impingement of

*462 11*

~~UNCLASSIFIED~~

large scale structures on the plate. Near the nozzle exit these waves are locked in-phase with the oscillations of the thin shear layer, which is forced to roll into large eddies at the resonance frequency  $f_r$ . Furthermore, the experimental data revealed the following interesting results: (i) The total period of the feedback loop is an integer  $N$  times the resonance period,  $N$  being constant over a resonance frequency stage. A jump from one frequency stage to another (occurring at certain nozzle-to-plate separation distances), takes place through a quantum unit change in  $N$ , so as to preserve the phase lock between the two oscillations at the nozzle. (ii) As the wavy shear layer evolves into large vortices, a strong interaction develops among the initial instability vortices. This phenomenon is referred to as "collective interaction", and is believed to be the mechanism responsible for the sharp drop in the passage frequency of the vortices near the nozzle exit. The frequency drops from the high instability frequency  $f_{(n)}$  to that of the resonance frequency  $f_r$ . Visual observations in a forced two-dimensional free shear layer by Ho and Huang (1978) further support the collective interaction concept. The mechanism of noise generation is also investigated using far field measurements at 90° to the jet axis. The measured far field power spectra exhibit both high and low frequency peaks. These peaks are the signature of a well organized flow field between the nozzle and the plate. The high frequency noise sources are confined to a short distance from the nozzle exit (due to the effect of the collective interaction), and radiate sound directly to the far field. The enhanced large scale structures (due to the feedback and vortex stretching) radiate low frequency noise when they impinge on the plate.

79

RE: AFOSR-TR-1263  
 Page 99 in this document is not missing but is misnumbered per Ms. Christiani, AFOSR/XOPD

ACCESSION for		
NTIS	White Section	<input checked="" type="checkbox"/>
DDC	Buff Section	<input type="checkbox"/>
UNANNOUNCED		<input type="checkbox"/>
JUSTIFICATION _____		
BY _____		
DISTRIBUTION/AVAILABILITY CODES		
Dist.	Avail	nd/or SPECIAL
A		

**FOSR-TR. 79 - 1263**

**ON THE FEEDBACK PHENOMENON OF AN  
IMPINGING JET**

by

**Nagy Sabet M. Nousseir, and**

**Ho, Chih-Ming**

**Department of Aerospace Engineering  
University of Southern California  
Los Angeles, California 90007**

September 1979

Prepared under Contract No. F 49620-78-C-0060  
US Air Force Office of Scientific Research

The views and conclusions contained in this document are those of the authors and should not be interpreted as necessarily representing the official policies or endorsements, either expressed or implied, of the Air Force Office of Scientific Research of the U.S.

1

Approved for public release;  
distribution unlimited.

79 12 10 027

## ACKNOWLEDGMENTS

The Authors would like to express their thanks to Dr. J. Laufer for many valuable discussions concerning this work. Generous help from Mr. D. Plocher during the course of the research was highly appreciated. Thanks is also due to Drs. P. Weidman and P. Huerre for their comments on this research. Finally, we would like to thank Ms. Celestine Holguin for typing the text.

One of the authors (Nagy S. M. Nasseir) based his Ph.D. Thesis on this work.

The support by the Air Force Office of Scientific Research under Contract No. F 49620-78-C-0060 is gratefully acknowledged.

AIR FORCE OFFICE OF SCIENTIFIC RESEARCH  
NO. 1  
1  
1  
1  
A. P. 1988  
Technical Information Officer

## ABSTRACT

The resonance phenomenon which occurs when a high speed turbulent jet impinges on a large flat plate, is experimentally studied. The far field noise is also investigated for a wide range of impinging jet speeds. The study involves far field, near field, and surface pressure measurements.

A feedback of pressure waves between the nozzle and the plate is found to be the mechanism responsible for the resonance. The feedback loop is formed by downstream travelling large coherent structures, and upstream acoustic waves propagating in the nearby stagnant region around the jet. The upstream acoustic waves are generated by the impingement of large scale structures on the plate. Near the nozzle exit these waves are locked in-phase with the oscillations of the thin shear layer, which is forced to roll into large eddies at the resonance frequency  $f_r$ . Furthermore, the experimental data revealed the following interesting results:

(i) The total period of the feedback loop is an integer  $N$  times the resonance period,  $N$  being constant over a resonance frequency stage. A jump from one frequency stage to another (occurring at certain nozzle-to-plate separation distances), takes place

through a quantum unit change in  $N$ , so as to preserve the phase lock between the two oscillations at the nozzle .

(ii) As the wavy shear layer evolves into large vortices, a strong interaction develops among the initial instability vortices. This phenomenon is referred to as "collective interaction", and is believed to be the mechanism responsible for the sharp drop in the passage frequency of the vortices near the nozzle exit. The frequency drops from the high instability frequency  $f_{in}$  to that of the resonance frequency  $f_r$ . Visual observations in a forced two-dimensional free shear layer by Ho and Huang (1978), further support the collective interaction concept.

The mechanism of noise generation is also investigated using far field measurements at  $90^\circ$  to the jet axis. The measured far field power spectra exhibit both high and low frequency peaks. These peaks are the signature of a well organized flow field between the nozzle and the plate. The high frequency noise sources are confined to a short distance from the nozzle exit (due to the effect of the collective interaction), and radiate sound directly to the far field. The enhanced large scale structures (due to the feedback and vortex stretching) radiate low frequency noise when they impinge on the plate.

## TABLE OF CONTENTS

Chapter		Page
	ACKNOWLEDGMENTS .....	ii
	ABSTRACT .....	iii
	LIST OF ILLUSTRATIONS .....	vii
	LIST OF SYMBOLS .....	xiv
1	INTRODUCTION .....	1
	1.1 REVIEW OF PREVIOUS INVESTIGATIONS .....	2
	1.2 MOTIVATION AND SCOPE OF THE PRESENT STUDY ..	11
2	EXPERIMENTAL FACILITIES .....	14
	2.1 WATER JET .....	14
	2.2 AIR JET .....	17
	2.2.1 Anechoic Chamber .....	17
	2.2.2 Jet Facilities .....	18
	2.2.3 The Flat Plate and the Supporting Mechanism .....	20
	2.3 DATA PROCESSING .....	23
	2.3.1 Measuring and Recording Equipments ...	23
	2.3.2 Digital Data Processing .....	26
3	GENERAL CHARACTERISTICS OF THE IMPINGING JET ....	34
	3.1 VISUALIZATION OF JET IMPINGEMENT - WATER JET	34
	3.2 PRESSURE MEASUREMENTS - AIR JET .....	41
	3.2.1 Surface Pressure Loading .....	42
	3.2.2 Eddy-Convection Velocity on the Plate: Comparison of Different Techniques ...	45
	3.2.3 Stability Modes of the High Speed Jet	54
4	THE TWO BRANCHES OF THE FEEDBACK LOOP .....	57
	4.1 CORRELATIONS OF NEAR FIELD PRESSURE MEASUREMENTS .....	58
	4.1.1 Characteristics of the Upstream Wave .	60
	4.2 A SIMPLE MATHEMATICAL MODEL .....	65
	4.2.1 The correlation Function .....	68

TABLE OF CONTENTS  
(Continued)

Chapter		Page
4.3	MEASURED CORRELATIONS: COMPARISON WITH THE MODEL .....	73
4.4	TWO WAVES: THE DOWNSTREAM AND THE UPSTREAM TRAVELLING WAVES .....	76
5	THE PHASE LOCK AND THE COLLECTIVE INTERACTION ...	81
5.1	PHASE LOCK BETWEEN THE TWO WAVES AT THE NOZZLE EXIT PLANE .....	81
5.2	RESONANCE FREQUENCY STAGES .....	86
5.2.1	Prediction of Plate Locations at the Frequency Jumps .....	90
5.2.2	Jet Behaviour at a Frequency Jump ....	92
5.2.3	The Disappearance of Resonance .....	93
5.2.4	Comparison with Cavity Resonance .....	93
5.3	THE COLLECTIVE INTERACTION .....	95
5.4	THE RESPONSE OF THE SHEAR LAYER TO ACOUSTIC EXCITATIONS FROM OUTSIDE OR INSIDE THE JET .	103
6	FAR FIELD NOISE OF THE IMPINGING JET .....	107
6.1	THE ROLE OF LARGE SCALE STRUCTURES IN NOISE GENERATION .....	109
6.1.1	Major Noise - Production Region on the Plate .....	115
6.1.2	A Model for the Noise Generation by Large Coherent Impinging Structures ..	117
6.2	HIGH-FREQUENCY FAR FIELD NOISE RADIATION ...	119
7	CONCLUDING REMARKS .....	125
7.1	THE FEEDBACK MECHANISM .....	125
7.2	THE MECHANISM OF NOISE GENERATION .....	127
	REFERENCES .....	231
Apendix		
A	STANDING WAVE PATTERN .....	235

## LIST OF ILLUSTRATIONS

### Figure

- (1-1) (a) Coordinate System, (b) Schematic Diagram of Pressure Transducers
- (2-1a) Photograph of the Impinging Water Jet Facility
- (2-1b) Schematic of the Impinging Water Jet Facility
- (2-2) Jet Noise Research Facilities at USC
- (2-3) Photograph of the Flat Plate Inside the Anechoic Chamber
- (2-4) Dynamic and Static Pressure Holes in the Flat Plate
- (2-5) Flat Plate Transverse Mechanism
- (2-6) Kulite Pressure Transducer Assembly
- (2-7) Kulite Transducer Amplifier Circuit
- (2-8) Block Diagram of Digital Data Processing
- (3-1) Axisymmetric Vortical Rings in the Impinging Water Jet, Pattern 1: Small Spacing Between Rings, ( $Re=5000$ ,  $x_0=4$ )
- (3-2) Pattern 2: Large Spacing Between Rings, same conditions as in Fig. (3-1)
- (3-3)  $x-t$  Diagram of Ring Vortices ( $x_0=2 \frac{2}{3}$ )
- (3-4) Vortex Pairing, same conditions as in Fig. (3-1)
- (3-5) Hydrogen Bubble Visualization, ( $Re=5000$ ,  $x_0=4$  in.,  $d=1.5$  in.)
- (3-6) Stretching of Ring Vortices on the Plate, ( $Re=5000$ ,  $x_0/d=2$ )
- (3-7) Curvature of Bubble Lines Indicating Velocity Profiles During Impingement, ( $Re=5000$ ,  $x_0=2$ )
- (3-8) Multiple Exposure of Hydrogen Bubbles Showing Shear Layer Growth and Turbulent Entrainment, same conditions as in Fig. (3-5)

LIST OF ILLUSTRATIONS  
(Continued)

Figure

- (3-9) Azimuthal Instability of Vortex Ring,  
( $Re=7000$ ,  $x_0=4$ )
- (3-10) Higher Instability Mode: A Spiral Mode,  
( $Re=8000$ ,  $x_0=3$ )
- (3-11) Raw Signals of Surface Pressure Fluctuations,  
( $x_0/d=4$ ,  $r_0/d=0$ .)
- (3-12) Normalized Power Spectra of Surface Pressure  
Fluctuations, ( $x_0/d=4$ ,  $r_0/d=1.5$ )
- (3-13a) Radial Variation of rms Surface Pressure  
Fluctuations, ( $M=.5$ ,  $x_0/d=2, 3, 7$ )
- (3-13b) Radial Variations of rms Surface Pressure  
Fluctuations, ( $M=.9$ ;  $x_0/d=2, 4, 7.5$ )
- (3-14) Radial Variation of rms Surface Pressure  
Fluctuations, ( $M=.3, .5, .8$  and  $.9$ ;  $x_0/d=2$ )
- (3-15) Variation of rms Surface Pressure Fluctuations  
with Plate Locations
- (3-16) Variation of rms Surface Pressure Fluctuations  
with Plate Locations
- (3-17) Two-Point Measurements, indices refer to the  
sketch in Fig.(3-19), ( $M=.8$ ,  $x_0/d=6$ )  
(a) Cross-Spectrum and Phase Angle  
(b) Coherence and Phase Angle  
(c) Coherence and Phase Velocity
- (3-18) Cross-Spectrum and Phase Angle Functions,  
indices refer to the sketch in Fig. (3-19),  
( $M=.5$ ,  $x_0/d=4.5$ )
- (3-19) Space-Time Surface Pressure Correlations
- (3-20) Surface Pressure Correlations-Constant  
Separation Distance  $\xi/d=.5$ , ( $M=.5$ ,  $x_0/d=4.5$ )
- (3-21) Surface Pressure Raw Signals  $p(t)$ -arbitrary  
units, ( $M=.9$ ,  $x_0/d=4.5$ ,  $d=1.0$  in.)
- (3-22) Normalized Surface Pressure Power Spectra,  
( $M=.9$ ,  $x_0/d=4.5$ )

LIST OF ILLUSTRATIONS  
(Continued)

Figure

- (3-23a) Cross-Spectrum and Phase Angle, indices refer to the sketch in Fig. (3-19), ( $M=.9$ ,  $x_0/d=4.5$ )
- (3-23b) Prewhitened Cross-Spectrum and Phase Angle, same conditions as in Fig. (3-23a)
- (3-24) Surface Pressure Cross-correlation, same conditions as in Fig. (3-23a)
- (3-25a) Space-Time Prewhitened Correlations at the Stagnation Region, indices refer to the sketch in Fig. (3-19), ( $M=.9$ ,  $x_0/d=4.5$ )
- (3-25b) Space-Time Prewhitened correlations, same conditions as in Fig. (3-25a)
- (3-26) Eddy-Convection Velocity on the Plate
- (3-27) Correlations between Surface Transducers at Different Azimuthal Angles,  $\phi_{01}=0^\circ$  and  $\phi_{02}=270^\circ$ , ( $M=.8$ ,  $x_0/d=4$ ,  $r_{01}=r_{02}=1.5d$ )
- (3-28) Prewhitened Azimuthal Correlations, same conditions as in Fig. (3-27)
- (3-29) Azimuthal Cross-Spectrum (Smooth Estimate) and Phase Angle, same conditions as in Fig. (3-27)
- (3-30) Azimuthal Correlations at the Nozzle Exit Plane (a) before and (b) after Prewhitening,  $\Delta\phi=135^\circ$ ,  $r_I=r_{II}=1.5d$ , ( $M=.8$ ,  $x_0/d=4$ )
- (4-1) Near Field Normalized Power Spectra, indices refer to the sketch in Fig. (4-2), ( $M=.8$ ,  $x_0/d=7$ )
- (4-2) Correlations of Near Field Pressure Signals
- (4-3) Near Field Cross-Spectra and Phase Angle Functions, ( $M=.9$ ,  $x_0/d=5$ )
- (4-4) Cross-correlation of Near Field Pressure Signals (a) before and (b) after Prewhitening, same conditions as in Fig. (4-3)
- (4-5) Cross-correlation of Near Field Pressure Signals (a) before and (b) after Prewhitening, same conditions as in Fig. (4-3)

LIST OF ILLUSTRATIONS  
(Continued)

Figure

- (4-6) Radial Variation of rms Pressure Fluctuations in Decibels, at the Nozzle Exit Plane
- (4-7) Variation of the Phase Angle at the Resonance Frequency at the Nozzle Exit Plane, ( $M=.9$ ,  $x_0/d=5$ )
- (4-8) Raw Pressure Signals at the Nozzle Exit Plane, same conditions as in Fig. (4-7)
- (4-9) Phase Angle Functions of Near Field Signals near the Nozzle, same conditions as in Fig. (4-7)
- (4-10) Prewhitened Optimum Cross-Correlation Coefficients, same conditions as in Fig. (4-7)
- (4-11) Comparison between Measured Upstream Wave Velocity in  $\hat{\theta}$ -Direction ( $C_p$ ), and Plane Acoustic Waves, from Eqn. (4-2), ( $M=.9$ ,  $x_0/d=5$ ,  $\theta_a=35^\circ$ )
- (4-12) Angle of Upstream Acoustic Propagation to the Jet Axis, for Different Plate Locations
- (4-13) Coordinate System for the Mathematical Model
- (4-14) Autocorrelations of Near Field Pressure Signals, indices refer to the sketch in Fig.(4-2), ( $M=.8$ ,  $x_0/d=7$ )
- (4-15) Correlations of Near Field Pressure Signals, same conditions as in Fig. (4-14)
- (4-16) Correlations of Near Field Pressure Signals, indices refer to the sketch in Fig. (4-2), ( $M=.8$ ,  $x_0/d=5.5$ )
- (4-17) Prewhitened Correlations of a Resonance Case, indices refer to the sketch in Fig. (4-2), ( $M=.9$ ,  $x_0/d=4$ )
- (4-18) Comparison between Measured Cross-Correlations  $\tau^{(3)}$  and the Model
- (4-19) Comparison between Measured Cross-Correlations  $\tau^{(4)}$  and the Model, ( $x_0/d=5.5$  and 7)

LIST OF ILLUSTRATIONS  
(Continue)

Figure

- (4-20) Comparison between Time Delay of the Second Peak in the Measured Autocorrelations and the Model
- (4-21) Downstream and Upstream Wave Propagation Velocities, Broadband Velocity ( $C_1, C_2$ ) and Phase Velocity at the Resonance Frequency  $C_1(f_r)$ ,  $C_2(f_r)$
- (5-1) Phase Angle Variations of the Two Waves at the Resonance Frequency ( $M=.8$ ,  $x_0/d=4$ )
- (5-2) Phase Angle Variations for Different Plate Locations
- (5-3) Variation of Resonance Strouhal Number ( $St_r = f_r d/U$ ) with Plate Location
- (5-4) Variation of Resonance Strouhal Number  $St_r = f_r d/U$  with Plate Location
- (5-5) Resonance Frequency Stages,  $N = x_0/\lambda_1 + x_0/\lambda_2$  ( $M=.9$ )
- (5-6) Frequency Jump Phenomenon, ( $M=.9$ ,  $x_0/d=2.35$ )
- (5-7) Variation of rms Near Field Pressure Fluctuations at the Nozzle Exit Plane with Plate Location, ( $M=.9$ ,  $r_I/d=.51$ ,  $r_{II}/d=2.7$ )
- (5-8) Comparison between Measured Cavity Tones and Eqn. (5-4b)
- (5-9) Comparison between Cavity Tones for Different Cavity Dimensions as Measured by Many Investigators [taken from Tam and Block (1978)], and Eqn. (5-4b)
- (5-10a) Raw Near Field Pressure Signals of a Non-Resonance Case, ( $M=.4$ ,  $x_0/d=4.5$ )
- (5-10b) Raw Near Field Pressure Signals of a Resonance Case, ( $M=.9$ ,  $x_0/d=4.5$ )
- (5-11a) Near Field Power Spectra, same conditions as in Fig. (5-10a)

LIST OF ILLUSTRATIONS  
(Continue)

**Figure**

- (5-11b) Near Field Power Spectra, same conditions as in Fig. (5-10b)
- (5-12) Instability and Resonance Strouhal Numbers for Free and Impinging Jets
- (5-13) Collective Interaction in a Two-Dimensional Free Shear Layer, Flow from Left to Right, Forcing Frequency  $\ll$  Natural Initial Instability Frequency, Courtesy of Ho and Huang (1978)
- (5-14) Collective Interaction
- (5-16) Ratio of Cross-Flow Velocity at the Shear Layer for Case-A and Case-B, versus Upstream Acoustic Incidence Angle
- (6-1) Coordinate System for Far Field Noise Analysis
- (6-2) Overall Sound Pressure Level Variation with Plate Locations, ( $M=.9$ ,  $\theta=89^\circ$ )
- (6-3) Variations of Sound Pressure Level with Mach Number,  $\theta=89^\circ$
- (6-4) Cross-Correlations with Far Field Microphone, point 2 is at  $r_0/d=1$ , indices refer to the sketch in Fig. (4-2), ( $M=.8$ ,  $x_0/d=5.5$ ,  $\theta_n/d=90$ )
- (6-5) Cross-Correlations between Surface and Far Field Signals, indices refer to the sketch in Fig. (3-19) same conditions as in Fig. (6-4)
- (6-6) Schematic of a Model for Far Field Noise Radiation due to the Impinging Large Scale Structures
- (6-7) Comparison between the Optimum Time Delays of the Correlation with the Far Field and the Model
- (6-8) Far Field Power Spectra,  $x_0/d=4.5$ ,  
(a)  $M=.4$ , (b)  $M=.9$
- (6-9) Cross-Correlation between Far Field and Near Field (Close to the Nozzle Exit) Signals, indices refer to locations shown in Fig. (6-10), ( $M=.4$ ,  $x_0/d=4.5$ )

LIST OF ILLUSTRATIONS  
(Continued)

Figure

- (6-10) High Frequency Far Field Noise Radiation Path  
from  $r^{(iii)}$  [e.g. Peak(iii) in Fig.(6-9)],  $x_0/d=4.5$
- (6-11) Summary of Noise Generation Mechanisms in an  
Impinging Jet

## LIST OF SYMBOLS

$\hat{a}(\xi) , \hat{b}(\xi)$	Amplitudes of the two waves in the model of Sec.4.2, Eqn. (4-4)
$a_0$	Ambient speed of sound
B	Frequency resolution of digital data. Also, effective low frequency cutoff during digital processing
C	Eddy convection velocity on the plate
$C(f)$	Phase velocity of convected eddies on the plate
$C_g(f)$	Group velocity
$\vec{c}_1$	Velocity vector of downstream travelling waves ( $\vec{c}_1 = c_1$ )
$\vec{c}_2$	Velocity of upstream travelling waves in a direction $\ominus_a$ , ( $\vec{c}_2 = c_2$ )
$c_1(f) , c_2(f)$	Magnitude of phase velocity of downstream and upstream waves
$\bar{c}_1 , \bar{c}_2$	Magnitude of broadband velocity of downstream and upstream waves
d	Nozzle diameter
f	Frequency (Hz)
$G_i(f)$	Normalized power spectrum of $i(t)$
$G_{i,j}(f)$	Normalized cross-spectrum between $i(t)$ and $j(t)$

LIST OF SYMBOLS

( Continued )

$\bar{G}_i(f)$ , $\bar{G}_{i,j}(f)$	Smooth estimates of $G_i(f)$ and $G_{i,j}(f)$ (Sec. 2.3.2)
$\tilde{G}_i(f)$ , $\tilde{G}_{i,j}(f)$	Prewhitened $G_i(f)$ and $G_{i,j}(f)$
$h$	Sampling rate of digitization
$i(t)$ , $j(t)$	Pressure signals from pickups at positions $i$ and $j$
$\hat{k}_1$ , $\hat{k}_2$	Wave numbers of downstream and upstream waves ( $\hat{k}_1 = k_1$ and $\hat{k}_2 = k_2$ )
$k_{2_x}$ , $k_{2_r}$	Axial and radial components of $\hat{k}_2$
$K_v$	The ratio $C_1/U$
$M$	Jet exit Mach number = $U/a_0$
$N$	Integer representing resonance frequency stages ( $N=1,2,\dots$ ), and is given by Eqn. (5-3)
$p(t)$	Fluctuating pressure
$p'$	rms value of pressure fluctuations
$q$	Dynamic pressure head = $1/2 \rho U^2$
$r$	Radial coordinate
$r_0$	Radial distance on the plate
$R_{i,i}(\tau)$ , $R_{i,j}(\tau)$	Cross-correlation between $i(t)$ and $j(t)$ , $i(t)$ delayed
$Re$	Reynolds number = $\frac{\rho U r}{\mu}$

LIST OF SYMBOLS

( Continued )

SLF	Slow factor (ratio of analog tape speed during recording to playback speed during digitization)
(St)	Strouhal number = $fd/U$
t	Time
$T_r$	Resonance period
U	Jet exit speed
$V_t$	Cross-flow velocity at $y=0$ of transmitted acoustic waves, Eqn. (5-5)
x	Axial Coordinate
$x_0$	Nozzle-to-plate distance
$\gamma_{i,j}(f)$	Coherence function of $i(t)$ and $j(t)$
$\zeta$	Distance to the far field microphone
$\Theta$	Inclination angle to the jet axis
$\Theta_a$	Angle between the propagation direction of the upstream acoustic waves and the jet axis
$\hat{\Theta}_a$	Unit vector making an angle $\Theta_a$ to the upstream of the jet axis
$\lambda_1, \lambda_2$	Wavelength of downstream and upstream waves
$\mu$	Dynamic viscosity

LIST OF SYMBOLS

( Continued )

$\psi_{i,j}(f)$	Phase angle between $i(t)$ and $j(t)$ , $i(t)$ delayed
$\psi_0$	Constant phase shift between the two waves in the model of Sec. 4.2 , Eqn. (4-10)
$\xi$	Separation distance in the correlations. Also, composite coordinate, Fig. (6-1), defined by Eqn. (6-1)
$\vec{r}$	Position vector, e.g. $\vec{r}_{III}$ , $\vec{r}_{II}$ are position vectors of $III$ and $II$ . Therefore, $\vec{r}_{III,II} = \vec{r}_{III} - \vec{r}_{II}$ is the separation vector between $III$ and $II$ ( $\vec{r}_{III,II} =  \vec{r}_{III} - \vec{r}_{II} $ )
$\rho$	Ambient density
$\tau$	Time delay of correlations
$\phi$	Azimuthal angle
$\phi_0$	Azimuthal angle on the plate
subscript	
$I, II, III ; IV$	Near field microphone positions
$0, 1, 2, \dots$	Surface pressure transducers' positions
FF	Far field microphone position
$i ; j$	Variable indices = $I, II, \dots, 0, 1, \dots, FF$
In	Instability
r	Resonance

LIST OF SYMBOLS

( Continued )

s Apparent sound source on the plate

superscript

(1),(2),(3);(4) Near field correlation peaks

(i),(ii),(iii) Peaks in the correlations with far field microphone

---

CHAPTER 1  
INTRODUCTION

The impinging of a turbulent jet on a surface is an interesting fluid mechanics research subject. The problem has a diverse flow field that includes a free turbulent jet before impingement, augmented vortices interacting with the surface, and a developed wall jet. Furthermore, at high subsonic impinging jet speeds, the flow develops self-sustained oscillations accompanied by an intense screech tone. The main motivation of the present study is to arrive at a better understanding of the feedback mechanism responsible for the resonance phenomenon at high jet speeds.

The jet impingement process is also important in many applications. For example, short take-off and landing (STOL) aircraft utilizes an externally blown flap technique. Hot gasses that exhaust from the engine at high speeds are deflected by direct impingement on the flaps to

create extra lift during take-off. Problems encountered in this design include heat transfer and fatigue due to excessive loading on the flaps, and high levels of noise radiation.

### 1.1 REVIEW OF PREVIOUS INVESTIGATIONS

According to Refs. 1 to 4, the flow field of an impinging jet is divided into three regions. A free jet region, where the mean jet characteristics remain unchanged despite the presence of the plate, an impinging region, and a developed wall jet region.

Donalson, et al. (1971) scaled the heat transfer and pressure gradient at the impinging region with the mean properties of the free jet at the impinging plane, as if the plate was removed. Giralt, et al. (1977) preferred to use the free jet properties in a plane upstream of the plate to scale the impinging region properties. The plane was chosen such that the centerline velocity is 98% of its free value. In this way, they accounted for the change in entrainment at the region of strong interaction near the plate, as compared to the scaling of Donalson, et al. (1971). Preisser and Block (1976) noted that the surface pressure fluctuations normalized with the dynamic head in the wall jet region are independent of the Mach number and

the distance from the nozzle to the plate. Gutmark, et al. (1976) measured velocity fluctuations in a plane jet near its impingement on a flat plate. Spectral measurements showed that the plate plays the role of a low-pass filter for the turbulent energy. A neutral scale was detected at which turbulent energy is neither augmented nor attenuated. At higher frequencies the turbulence is attenuated due to viscous dissipation, while at lower frequencies the turbulence is augmented due to vortex stretching as the plate is approached. The convection velocity of turbulent vortical eddies on the plate was measured by Strong, et al. (1967) via two-point cross-correlation. The velocity of convected eddies was found to vary along the plate.

For high subsonic impinging jets, an audible screech tone was reported in Refs. 7, 8, and 9. Westley, et al. (1972) observed the screech tone and speculated a similar mechanism to that of an under-expanded supersonic jet. Wagner (1971), and later Neuworth (1973), reported that the screech tone occurs at jet Mach numbers greater than .6 when the plate is less than six diameters from the nozzle.

Supported by visualizations, Wagner (1971) and Neuworth (1973) adopted the following model to explain the

feedback mechanism responsible for this resonance phenomenon. The observed standing wave in the jet core was assumed to result from the superposition of a downstream convected wave due to the large turbulent eddies, and an upstream propagating wave emanating from the stagnation region of the plate. The jet core simulated an acoustic wave-guide, with the shear layer as its boundaries. The upstream acoustic wave was assumed to propagate in a direction inclined to the jet axis, and to reflect from the shear layer with phase reversal. The upstream waves reached the nozzle and forced the shear layer there to form a new series of eddies that convected downstream. A minimum jet Mach number for the resonance to occur was found, at which the shear layer acted as a sound hard boundary, which means the forcing of the shear layer near the nozzle was not possible. Also, a minimum limit for the resonance frequency was derived below which, the acoustic waves were so inclined to the jet axis, that no upstream propagation towards the nozzle took place. Irrespective of the Mach number or the frequency, resonance disappeared when the plate was one to two diameters beyond the potential core of the jet. The reason for this, was the disintegration of ring vortices at these downstream locations.

Wagner (1971) and Neuworth (1973) showed that the resonance frequency decreases as the plate is moved down-

stream until it reaches a minimum and jumps to a higher value. Wagner predicted that the decrease in frequency is due to an increase in the spacing between the vortices, and the frequency jump occurs due to the addition of a new vortex in the flow field between the nozzle and the plate. In a similar fashion, Neuworth speculated that the sum of the individual periods of the vortices and the upstream waves is a number that remains unchanged between consecutive jumps. The jump takes place as a result of an increase by one of the total number of periods in the loop.

The resonance frequency jumps and the observed enhancement of large coherent eddies furnish a striking resemblance to similar shear layer-induced self-sustained oscillations in the flow over cavities and edge tones. A close look to theoretical and experimental work in these areas would be helpful.

Most of the models for flow over cavities and edge tones seem to have the following general features [Rockwell and Naudascher (1979)]: the shear layer interacts with the solid boundary (a corner or a wedge) downstream; acoustic or hydrodynamic disturbances are generated and trigger the instability of the shear layer upstream. Powell (1961a) modeled the acoustic source at the downstream boundary as a distribution of dipoles. Later

(1961b) he showed that the radiated field of dipoles and vorticity are equivalent. The flow field was presented as a control system with a complex transfer function. For self-sustained oscillations, the magnitude of the transfer function is unity, and the phase angle is  $2N\pi$ . Rossiter's (1964) empirical model suggested that the vortices interact with the downstream wall of the cavity and the generated acoustic waves propagate upstream inside the cavity, causing the shedding of new vortices near the upstream edge. The sound source in the mathematical model of Tam and Block (1978) was chosen proportional to the fluctuations of the shear layer at the downstream corner. Consequently, the acoustic waves are generated due to the interaction of the inviscid flow with the downstream corner. The model accounted for finite shear layer thickness effects, and acoustic reflections from the bottom and upstream cavity walls in calculating the cavity pressure oscillations. Sarohia (1976) adopted a different model for the low speed flow over cavities. Here cavity oscillations result from propagating disturbances which get amplified along the cavity shear layer, rather than from acoustic feedback. Hot wire measurements and visualizations showed that the shear layer deflects in and out of the cavity near the downstream corner. This lateral motion of the shear layer resulted in a periodic shedding of vortices from the downstream corner at the resonance fre-

quency. The shedding of vortices at the downstream corner was rather shown as "clipping" and "nonclipping" of vortices in the pictures of Rockwell and Knisely (1978).

Flow visualizations [Rockwell and Naudascher (1979)] showed that the presence of a downstream solid boundary tends to organize and enhance large scale structures in the turbulent flow. This enhancement takes place mostly through a feedback, or sometimes just through stretching of vortices due to the diverging streamlines. A study of large coherent structures in turbulent shear flows is, therefore, essential.

The visualizations of Brown and Roshko (1971) showed for the first time that large scale two-dimensional vortices make up the fully turbulent two-dimensional mixing layer. Laufer (1975) suggested that these quasi-ordered structures are deterministic, in the sense that they have a characteristic shape, size and convection motion that can be determined within a relatively small standard deviation. A somewhat different picture of turbulence, therefore, emerges that reflects the double-structured nature of turbulent flows: time dependent quasi-ordered large scale structures, and fine-scale random structures. Numerous experiments have been conducted to document the characteristics of these deterministic orderly structures.

Lau, et al. (1972) reported results from different experimental investigations that consistently yield a value of  $0.6U$  for the convection velocity of large scale structures. They modeled the shear layer as an axial array of discrete vortices spaced at about  $1.25d$  (where  $d$  is the nozzle diameter). Measurements were made in the potential core, shear layer and entrainment region of the jet. Their model helped to explain the phase relationships between measured fluctuating pressure and components of fluctuating velocity. Petersen (1978) measured the convection velocity of large scale structures from cross-correlation of near field pressure signals. The convection velocity was found to be constant and equal to  $.6U$  over the first five diameters. It then decreased continuously further downstream. The spatial stability theory of Michalke (1972) showed that the wavelength of the initial instability is determined by the initial shear layer thickness, which depends on the exit Reynolds number. The most unstable wave has a frequency which corresponds to  $f\delta_1/U = .017$  (where  $\delta_1$  is the momentum thickness) and a phase velocity equal to  $.6U$  (same as the value measured for the convection velocity of the large scale structures downstream). Crow and Champagne (1971) observed visually the instability waves of the thin laminar boundary layer leaving the nozzle lip, and orderly large scale

puffs further downstream. The instability waves scaled with the thickness of the boundary layer [Michalke(1971)]. In contrast, the large puffs scaled with the nozzle diameter, and were forming at a constant average Strouhal number  $fd/U=0.3$ . They observed that the jet was most unstable when the forcing frequency corresponded to a Strouhal number of 0.3.

The growth of the shear layer is attributed mainly to "pairing" between consecutive large vortical structures as was first pointed out by Winant and Browand (1974). Laufer (1974) hinted that turbulent energy production which is the energy transfer from large structures to small scale turbulence, is phase related to the pairing between large eddies. Indeed, that was observed later in the disintegration of large vortical rings and the production of small scale turbulence during the pairing, especially near the end of the potential core of a round jet [Browand and Laufer (1975)].

This review is now completed by a discussion of the far field noise of impinging jets. The far field noise, as described by Curl's equation [see Ref. 25], is the sum of a volume integral of Lighthill's stress tensor over the flow field, and a surface integral of pressure fluctuations over the plate. Powell (1960) applied Curl's equa-

tion to both the real flow system and an image system. The result is that the volume integral over the image provides the same contribution to the far field noise as does the surface integral over the actual surface. Since the image system is a pure reflection of the real flow, Powell's model indicates that the role of the plate is passive, i.e., merely reflecting the sound generated by the flow.

Preisser and Block (1976) reported levels of measured far field noise higher than those pertaining to the free jet. The increase in the noise level is a function of the angle and the nozzle-plate distance. Cross-spectra between the surface and the far field showed that the outer portion of the impinging region (between  $d$  and  $3d$  from the stagnation point) is the major contributor of noise. It is worth mentioning here that the present study will show that large coherent structures impinge on the plate surface in a region between one to two nozzle diameters from the stagnation point. Preisser (1979) showed later that far field spectra peaks at  $St_r = .3$ . These peaks have higher levels than those in the spectra of a free jet. He suggested that the presence of the plate enhanced the noise generated by large coherent structures.

The experimental studies of Preisser and Block (1976)

and Preisser (1979) could only localize the impinging region as a major apparent noise-producing region. The question of whether the noise is originating in a flow region near the surface and is being reflected by the surface, or if it is being generated by the surface itself, could not be answered. The exact role of the plate in the noise production can only be determined by evaluating the volume integral over the flow in Curl's equation. Such a calculation requires near field as well as surface measurements [Pan (1975)].

## 1.2 MOTIVATION AND SCOPE OF THE PRESENT STUDY

The first objective of the present investigation was to study the resonance phenomenon that occurs in a high subsonic impinging jet. The goal was to explore a possible feedback mechanism between the nozzle and the plate, and to determine the role of large coherent structures in that mechanism. The second objective was to study the far field noise of the impinging jet in general, i.e., for both resonant and nonresonant jets (covering a range of  $.3 < M < .9$ , and  $3 < x_0/d < 7.5$ ). Our goal was to locate major noise-producing regions, and to study the noise-generation mechanisms.

The present work is based on pressure measurements

taken in the far field, near field, and on the surface of the plate. Fig. (1-1) shows the coordinate system used for the jet-plate configuration along with a schematic diagram of the pressure transducers. Visualizations in water were used to study the general behaviour of coherent vortical structures during impingement, and are presented in the first section of Chapter 3. The rest of the investigation deals with measurements in air. Data pertaining to pressure loading and eddy convection velocity on the plate are included in Chapter 3. Conclusive experimental evidence for the existence of convected large scale structures, and upstream acoustic waves generated from the impingement of these structures on the plate is presented in Chapter 4. Also, a simple mathematical model purporting to explain the particular behaviour of measured near field correlations is included in Chapter 4. A phase lock near the nozzle exit between the two waves necessary for self-sustained flow oscillations is established in Chapter 5. A new phenomenon named "collective interaction" is also described in connection with the forcing of the shear layer near the nozzle by the upstream acoustic waves. The chapter is concluded by a mathematical analysis of the respective efficiencies of acoustic forcing, when the shear layer is excited from the ambient region and from the jet core region.

---

The role of coherent flow including both the high-frequency shear layer instability waves near the nozzle and the downstream impinging large scale structures, in the noise generation is discussed in Chapter 6.

---

## CHAPTER 2

### EXPERIMENTAL FACILITIES

The experimental facilities and data processing methods used in the present investigation are discussed in this chapter. A description of the low speed impinging water jet and associated visualization techniques are presented first. Then the high speed air jet facility where most of the measurements were taken will be described. The analog and digital data processing will be discussed in the last section.

#### 2.1 WATER JET

The water jet set up is shown in Fig. (2-1a) and schematically in Fig. (2-1b). The nozzle assembly consisted of a stilling chamber and a detachable nozzle. The flow enters the stilling chamber through a conical diffuser with three screens, then passes through a honeycomb straightner to the nozzle. The axisymmetric nozzle has a contraction ratio of 1.5 and an exit diameter of

1.5 in. The jet exit velocities ranged from 5 in/sec. to 15 in/sec. with the corresponding Reynolds numbers,  $Re = \frac{\rho U d}{\mu}$ , of 5000 to 15000. The turbulence level was measured on the jet centerline just upstream of the nozzle exit and is reported in Ref. 24. The rms longitudinal fluctuation level is about .5% at a jet speed of 5 in/sec., and is lower at higher jet speeds.

In operation, the jet is immersed vertically in a 32 x 32 x 48 in. plexiglas tank. A centrifugal pump capable of providing 0.55 gal/sec. against a head of 30 feet of water is used to circulate the water in this closed system. The jet impinges on a 23 x 23 x 1/2 in. plexiglas plate. The ratio of the surface area of the plate to the tank's cross-sectional area is approximately 1:2. The uniform diffusion of the dye over the whole tank, above and under the plate, indicated no significant plate blockage effect on the jet flow. The plate is supported from its corners by four 1.0 in. PVC rods, which are connected to a wooden frame on top of the tank. The wooden frame is also used to support the nozzle assembly. The nozzle to plate distance is changed by lowering the plate through 1/2 in. steps. After impingement, the flow is collected in an exhaust diffuser at the bottom of the tank. The flow rate is monitored by a Fisher-Porter flow meter with a gate valve providing the required throttling.

---

The flow was visualized in two ways:

1. Colored shear layer

Dye was introduced into the nozzle wall boundary layer through a series of fine slots. The dye used was common red food coloring. This is a convenient coloring agent since it can be cleared by ordinary laundry bleach. Still photographs and films were taken. Back-lighting through a translucent screen was used, and was found to give the best lighting conditions.

2. Hydrogen bubble technique

Hydrogen bubbles were generated from a thin platinum wire that was stretched across the exit plane of the nozzle. The wire was a cathode in an electric circuit, and was connected to a pulse generator and a power amplifier. The anode was a long rod immersed in the water near the wire. An electrolyte, table salt, was added to the water in a quantity selected to maximize the production of hydrogen bubbles. A .002 in. diameter platinum wire and voltage pulses of approximately 40 volts in amplitude were used to produce a sequence of hydrogen bubble lines. The wire was small enough to produce the desired bubble size

and yet strong enough to withstand drag forces due to the jet flow. The axial slice of the jet was illuminated using either a commercial spot lamp with a vertical slit or a stroboscope lamp and a system of lenses with a vertical slit. The stroboscope was triggered by the pulse generator, and this setup was used for multi-exposure still pictures. The room was completely darkened to provide good contrast between the bubbles and the background. The level of illumination was minimal for photography. The negatives of both the still pictures and movie films had to be pushed to as high as ASA 3000 in the developing process.

## 2.2 AIR JET

### 2.2.1 Anechoic Chamber

The anechoic chamber at the University of Southern California was constructed by Eckel Industries. The interior walls are faced with fiberglas wedges which have a depth of 16 1/2 in., resulting in a lower cut-off frequency of 150 Hz. The interior measures 15' 8" wide by 20' 4" long and by 11' 11" high. Eight inches above the floor wedges a tensioned cable is suspended from the walls to permit easy access to the chamber. The jet flow is vented

to the outside by a 4' x 4' opening with a baffled cut. At various convenient locations in the chamber threaded couplings for standard 1 1/2 in. I.P.S. pipes are mounted to provide a base for mounting the flat plate and its traverse mechanism. The chamber is mounted on large coil springs to assure a complete isolation from any vibrations. A schematic of the chamber and jet facilities is shown in Fig. (2-2).

#### 2.2.2 Jet Facilities

The air supply system consists of a 2500 psi, 142 ft.<sup>3</sup> /min., Chicago pneumatic air compressor which supplies air to five storage pressure vessels. The compressor has two mechanical filters and a chemical dehydration system which provides dry air with a dew point of -48 F. The compressor is used to fill the storage tanks and is not operated during test runs.

The air flow from the pressure vessels is controlled by a low-noise, self-drag valve built by Control Components Inc. of Irvine, California. The valve is opened by a Moore 3-15 psi positioner which receives a pneumatic pressure signal from a Honeywell Batch-0-Line Controller. The controller was operated manually, while the settling chamber pressure time history was recorded on a strip

chart. A Gould Brush Model 220 dual channel chart recorder was used, which was connected to a Validyne Model DP 15TL pressure transducer. The variation of the stagnation pressure during the measurements was maintained to within 2% of the mean gauge pressure. The above setup provided excellent monitoring of the mean flow pressure and this proved to be critical for the present investigation: we observed, even audibly, that relatively small fluctuations in the stagnation pressure in the order of 6 to 9% can significantly alter the resonance at high subsonic jet speeds.

After discharging from the control valve, the air flows through a 500 KW Hynes Radi-Fin electric heater. The heater was not used in the present investigation. Immediately after the heater the flow passes to the settling chamber through a diffuser that is fitted with screens to prevent flow separation. To reduce turbulence five screens and a 4 in. layer of steel wool are installed inside the 16 15/16" diameter settling chamber. The turbulence level downstream of the last screen has been measured to be 0.4%. This is, of course, further reduced by the contraction downstream of the settling chamber.

For the present study a subsonic axisymmetric nozzle

of 1" diameter was used, yielding a contraction ratio of approximately 17:1. During this investigation the jet Mach number was restricted to the range 0.3 to 0.9. More details about the jet facilities, the contraction section downstream of the settling chamber, and the nozzle are reported in Ref. 29.

### 2.2.3 The Flat Plate and the Supporting Mechanism

A flat steel plate (30"x30"x.25") provided a large surface for the impinging jet. Fig.(2-3) shows a picture of the nozzle and the plate inside the anechoic chamber. First holes were drilled in the plate at dynamic and static pressure measurement sites. The details of these holes and their approximate locations are shown in Fig.(2-4). The exact locations of these holes are shown in Table-1. The plate surface facing the jet was then ground to a commercial mirror finish (16 microinch surface finish). Finally the surface was treated with black chrome for corrosion resistance. The unused dynamic pressure holes in the plate were filled by dummy transducers.

The holes of the pressure taps had clean sharp edges at the surface. With both pressure and dummy transducers flush mounted on the plate, it was believed that the resulting smooth surface would not interfere with the flow

No.	$r_0$ in.	$\phi_0^\circ$	No.	$r_0$ in.	$\phi_0^\circ$
1	0	0	24	2	135
2	1	0	25	2.5	135
3	1.5	0	26	3	135
4	2	0	27	.5	180
5	2.5	0	28	2	180
6	3	0	29	5	180
7	5	0	30	7	180
8	7	0	31	1	225
9	9	0	32	1.5	225
10	.5	45	33	2	225
11	1	45	34	2.5	225
12	2	45	35	3	225
13	3	45	36	.5	270
14	1	90	37	1	270
15	1.5	90	38	1.5	270
16	2	90	39	2	270
17	2.5	90	40	2.5	270
18	3	90	41	3	270
19	5	90	42	5	270
20	7	90	43	.5	315
21	9	90	44	1	315
22	1	135	46	3	315
23	1.5	135	46	3	315

Table (2-1) Locations of dynamic pressure holes on the plate (looking at the plate from the nozzle side)

near the plate.

The plate was mounted on a traverse mechanism as shown in Fig.(2-5). The vertical motion was provided by a motor that slides the plate over a Thomson Linear Ball Bearing (Type SPB-12-OPN) with shaft assemblies Type SA12-30. The plate could rotate in a pitching mode, and be fixed at any angle to the jet axis between  $90^\circ$  to  $180^\circ$ . In the present study, normal jet impingement only was used. The plate was connected by a simple truss to a base. The base was connected to eight 1.5 in. I.P.S. pipes that were screwed tightly into the floor of the chamber. The base allowed manual horizontal transverse motion and motorized axial motion. The axial motion was used to vary the nozzle-to-plate distance  $x_0$ . The plate can move from  $x_0=0$  to  $x_0=25$  in. The vertical and axial motions were remotely controlled.

The plate and its supporting mechanism were examined for structural vibrations during jet operation. The amplitude of the vibrations of the plate was measured by an accelerometer (Bruel&Kjaer 4324). With the highest speed jet,  $M=.9$ , the amplitude of vibrations was only  $1.12 \times 10^{-5}$  in.

## 2.3 DATA PROCESSING

### 2.3.1 Measuring and Recording Equipment

#### Dynamic pressure pickups

The surface pressure fluctuations were measured by 1/8 in. Kulite XTE-1-190-25 piezoresistive pressure transducers with type B screens. From previous experience difficulties were anticipated during installation and removal of the transducers. The screen was glued to the transducer's tip and frequently would be pried during removal because it has the same diameter as the transducer tip and precise alignment was difficult. A pressure port for the transducer was designed. The transducer and its port [Fig. (2-6)] were always used as a single piece during the mounting and removal from the plate. In this way the transducers were protected from possible damage.

The natural frequency of the Kulite transducer is in excess of 100 KHz. A preamplifier circuit was built for each Kulite and is shown in Fig. (2-7). The first stage of the circuit is a voltage follower to reduce the output impedance of the transducer. The second stage is an amplifier which provides a gain of 200, 500 or 1000.

### Near field microphones

Four 1/8" B & K Type 4138 condenser microphones were used. They had a frequency response from 7 Hz to 140 KHz and a range of 76-185 dB.

### Far field microphones

A 1/4" B & K Type 4135 condenser microphone was used. It had a frequency response from 4 Hz to 100 KHz and a range of 59-164 dB.

### Microphone preamplifiers

Five B & K Type 2618 preamplifiers were used with the near field and far field microphones. The frequency response of these preamplifiers were 2 Hz - 200 KHz and could provide a gain of -20, 0, or +20 dB.

### Microphone power supply

A 7- channel B & K Model 222 power supply was used. A gain of up to +40 dB can be provided by the power supply for each channel.

---

### Microphone calibrator

B & K Type 4220 pistonphone calibrator was used to calibrate the B & K microphones.

### Magnetic tape recorder

During each run, the data were recorded on a 14-channel Hewlett-Packard Model 3955A type recorder. Measurements of surface pressure fluctuations were recorded in FM mode with frequency bandwidth from DC to 20 KHz at a tape speed of 60 ips. The near-field and far-field data were recorded in direct mode with response from 300 Hz to 300 KHz at the same tape speed.

### On-line equipment

During and after the run the signals were displayed on the screen of a two channel Hewlett Packard Type 1217A oscilloscope. The rms of the pressure signals were measured from a Hewlett-Packard 400E AC Voltmeter. A Hewlett-Packard 3721A correlator was used to give on-line autocorrelation and cross-correlation of the recorded signals. The delay offset provided in the correlator was helpful for observing long optimum time delays in the cross-correlation between near-field and far-field signals.

### 2.3.2 Digital Data Processing

#### Digitization

Most of the analysis in the present study was done digitally. The analog data were digitized and processed on a Digital Equipment Corporation PDP-11/55 minicomputer. The subsystem used for digitization consists of 16 sample and hold circuits and an analog to digital converter interfaced with the minicomputer. The maximum sampling rate attained in this study was

$$h = 13 \times (\text{number of channels}) + 20 \text{ microseconds}$$

The maximum sampling rate was found to depend on many parameters including how busy the computer was during digitization, the block size of digitized data written to magnetic tape, and the quality of the digital tape. However, an effective faster sampling rate could be obtained by slowing down the analog tape during the digitization process. A slow factor (SLF) as much as 32 was used for some cases, by using an analog playback tape speed of  $1 \frac{7}{8}$  ips during digitization. As mentioned before recordings were performed at 60 ips speed.

The high frequency cutoff from digitization [Ref. 30] is

$$f_c = (\text{SLF}) \frac{1}{2h} ,$$

where  $f_c$  is the Nyquist folding frequency. The frequency resolution is

$$B = (\text{SLF}) \frac{1}{N_T \cdot h} , \quad (2-1)$$

where  $N_T$  is the number of points per channel in the record being processed. The equations above show a trade off between the frequency range and the frequency resolution. (SLF) = 32 was used to look at the high frequency components of a signal, such as in measuring the shear layer initial instability frequency in Ch. 5 and the high-frequency far field noise in Ch. 6. Otherwise, slow factors of 1 and 8 were used.

#### Data analysis procedures

Figure (2-8) shows a block diagram depicting most of the digital data analysis procedures used in the present study. The limitations on the available computer storage required that the Fast Fourier Transform (FFT) and the evaluation of the power spectrum components be carried out over one block of digital data and then be summed and averaged over the total number of blocks digitized. This

is, in effect a high frequency filter with a low frequency cutoff equal to the frequency resolution  $B$  given by Eqn. (2-1).

The spectra and correlation functions

Most of the following analysis is based on definitions and notations given in Ref. 30. The cross spectrum function for two time-signals  $i(t)$  and  $j(t)$  is by definition

$$\hat{G}_{ij} = C_{ij}(f) - i Q_{ij}(f) \quad , \quad (2.2a)$$

where

$$C_{ij}(f) = \frac{1}{TB_e} \int_0^T i(t, f, B_e) j(t, f, B_e) dt \quad , \quad (2.2b)$$

which is called the coincident-spectral density function and

$$Q_{ij}(f) = \frac{1}{TB_e} \int_0^T i(t, f, B_e) j^\circ(t, f, B_e) dt \quad , \quad (2.2c)$$

which is called the quadrature-spectral density function. In Eqn. (2-2)  $i(t, f, B_e)$  and  $j(t, f, B_e)$  are the signals passed through a narrow band-pass filter with bandwidth  $B_e$  and center frequency  $f$ ;  $j^\circ(t, f, B_e)$  is 90-degree phase shifted from  $j(t, f, B_e)$ .  $T$  is the record time of both  $i(t)$  and  $j(t)$  and is equal to  $1/B$ .

A more useful form of Eqn. (2-2) is

$$G_{i,j}(f) = \frac{1}{\sqrt{i^2(f)} \sqrt{j^2(f)}} [C_{ij}^2(f) + Q_{ij}^2(f)]^{1/2}$$

$$\varphi_{i,j}(f) = \tan^{-1} \left[ \frac{Q_{ij}(f)}{C_{ij}(f)} \right],$$

} (2-3)

where  $G_{i,j}(f)$  is a normalized spectrum satisfying

$$\int_0^{\infty} G_{i,j}(f) df = 1$$

and  $\varphi_{i,j}(f)$  is the phase angle function.

The cross-correlation function is given in normalized form by

$$R_{i,j}(\tau) = \frac{\overline{i(t) j(t+\tau)}}{\sqrt{\overline{i^2(t)}} \sqrt{\overline{j^2(t+\tau)}}}, \quad (2-4)$$

where

$$\overline{i(t) j(t+\tau)} = \frac{1}{T} \int_0^T i(t) j(t+\tau) dt$$

Eqn. (2-4) is evaluated, as shown in Fig. (2-8), by an Inverse Fourier Transform of the cross-spectrum  $G_{i,j}(f)$ , i.e.

$$R_{i,j}(\tau) = \mathcal{F}^{-1} \{ \hat{G}_{ij}(f) \}$$

$$= \frac{1}{\sqrt{i^2(t)} \sqrt{j^2(t)}} \int_0^{\infty} [C_{ij}(f) \cos 2\pi f \tau + Q_{ij}(f) \sin 2\pi f \tau] d\tau.$$

If the input signals in Fig. (2-8) are the same, say both are  $i(t)$ , Eqn. (2-2) gives the power spectrum  $G_i(f)$ , and Eqn. (2-4) the autocorrelation function  $R_{i,i}(\tau)$

$$G_i(f) = \frac{1}{i^2(t)} \frac{1}{TB_e} \int_0^T i^2(t, f, B_e) dt \quad (2-5)$$

$$R_{i,i}(\tau) = \frac{1}{i^2(t)} \frac{1}{T} \int_0^T i(t) i(t+\tau) dt. \quad (2-6)$$

A rough estimate of the spectrum can be evaluated from Eqns. (2-2) and (2-3) for  $B_e = B$  and is referred to in the text as  $G(f)$ . If the signals were of a limited band-width white noise, the standard normalized error of the spectral estimates would be  $\epsilon_r = 1.0$ , which means that the error is of the same order as the estimate itself. However, most of the signals measured in the present study are of a narrow-band random noise type and  $\epsilon_r$  is expected to be less than unity. This proved to be true when  $G(f)$  was compared with the smooth spectrum estimates in the form of the coherence function  $\gamma_{i,j}(f)$ , which is defined

as

$$\gamma_{i,j}(f) = \frac{|\overline{G_{i,j}}(f)|^2}{\overline{G_i}(f) \overline{G_j}(f)} .$$

The barred quantities are the smooth spectral estimates averaged over frequency band of width  $B_e = nB$ . The changes in spectral estimates for different values of  $n$  were studied for different samples of signals and were found to be negligibly small for  $n \geq 8$ . The value for  $n = 8$  was, therefore, chosen in calculating  $\gamma_{i,j}(f)$  in the present study.

#### The prewhitening technique

As we shall see later, at high subsonic jet speeds the pressure signals take the form of distorted sine waves. The spectra then are dominated by a peak at the resonance frequency, while the cross-correlation function would show a sinusoidal behavior with no distinguishable optimum peak. The cross-correlation functions in these cases do not provide much information. A data processing method called prewhitening is quite useful for analyzing small random signals superimposed on a high amplitude pure tone. A conventional prewhitening technique [Williams and Purdy (1970)] separates the random signals from the pure tone by subtracting an in-phase sine wave from the origi-

nal signal by analog methods. A prewhitening technique was developed here using digital methods, and was found to be much simpler. A cross-correlation function of two prewhitened signals was obtained by the following sequence of operations:

1. Compute the individual power spectra  $G_i(f)$  and  $G_j(f)$  and also the cross-spectrum  $G_{i,j}(f)$ .

2. Remove the pure tone from the above three spectra by replacing the high spectral peak with the averaged value of the two neighboring frequency components. This results in a prewhitened  $\tilde{G}_i(f)$ ,  $\tilde{G}_j(f)$  and  $\tilde{G}_{i,j}(f)$ .

3. Inverse Fourier Transform  $\tilde{G}_i(f)$  and  $\tilde{G}_j(f)$  to get the autocorrelations  $\tilde{R}_{i,i}(\tau)$  and  $\tilde{R}_{j,j}(\tau)$ . Note that  $\tilde{R}_{i,i}(\tau)$  and  $\tilde{R}_{j,j}(\tau)$  are the mean square values of the random signals remaining from  $i(t)$  and  $j(t)$ .

4. Inverse Fourier Transform  $\tilde{G}_{i,j}(f)$  and normalize to obtain

$$\tilde{R}_{i,j}(\tau) = \frac{\mathcal{F}^{-1}\{\tilde{G}_{i,j}(f)\}}{\sqrt{\tilde{R}_{i,i}(0)} \sqrt{\tilde{R}_{j,j}(0)}} \quad (2-7)$$

Results derived from the prewhitening method are shown in

Figs. (3-24) and (4-4).

## CHAPTER 3

### GENERAL CHARACTERISTICS OF THE IMPINGING JET

A general idea about the common properties of an impinging jet is presented here before discussing specific details of the feedback mechanism and the noise radiation. In the first part, visualizations in water are used to describe the general behavior of large vortical rings during their impingement on a flat plate. The water jet is limited to a low Reynolds number range,  $Re = 5000$  to  $15000$ . In the second part, surface pressure loading, eddy convection velocity on the plate, and the stability modes of the impinging jet are discussed for air jets with a Reynolds number range of  $1.8 \times 10^5$  to  $5.3 \times 10^5$ .

#### 3.1 VISUALIZATION OF JET IMPINGEMENT-WATER JET

As mentioned in Chapter 1, the flow field of the impinging jet is divided into three regions: the free jet region, the impinging region, and the wall jet region. From the dye and hydrogen bubble techniques, coherent

structures in the free jet region and the impinging region were clearly visible. Both the dye and the hydrogen bubble lines lost their coherent features due to the developing turbulence in the wall jet region.

The flow field between the nozzle and the plate is shown in the dye picture of Fig. (3-1). The flow is initially laminar for approximately one diameter downstream of the nozzle exit. The shear layer rolls into axisymmetric vortical rings. These rings are convected downstream until they impinge on the plate. For the same flow parameters, a similar pattern is shown in Fig. (3-2) except that both the initial laminar column near the nozzle exit and the spacing between the vortical rings are larger. The larger spacing between rings takes place through "pairing" between two consecutive rings. Observation of the movies showed the flow intermittently jumping between the two patterns of Fig. (3-1) and (3-2).

The two patterns described above are further shown by the coherent flow motion presented by the x-t diagram of Fig.(3-3). The diagram is constructed from a frame by frame analysis of a movie. Each curve in the figure starts when a "bulge" in the initial laminar column is detected. These "bulges" evolve into vortical rings downstream. Both the bulge and its corresponding toroidal

vortex is referred to here as a vortical ring. Hence, each curve in the figure represents an individual ring path originating just downstream of the nozzle exit and terminating near the plate before impinging. The of the time axis is arbitrary and is not indicative of the first ring observed in the run. For  $t > 2$  sec. pairing does not occur in this  $x-t$  diagram. A vertical line at  $t = 2.4$  sec., for example, intersects ring paths at points corresponding to the instantaneous locations of the rings. A snap shot at  $t = 2.4$  sec. would give a flow pattern similar to that of Fig.(3-1). During the period  $.5 \text{ sec.} < t < 2 \text{ sec.}$  pairing takes place. Here intersections between ring paths and the vertical line at  $t = 1.6$  sec. give instantaneous ring locations which correspond to the pattern displayed in Fig. (3-2). Based on the intersections between vertical lines and ring paths, the following remarks can be made:

1. The rings are approximately evenly spaced between the nozzle and the plate.

2. Through pairing, the flow reorganizes itself into a different pattern, where the spacing between consecutive rings is almost doubled.

Browand and Laufer(1975) and later Petersen(1978) have shown that vortical rings were quasiperiodically

spaced in a free jet. A comparison between their  $x-t$  diagrams and Fig.(3-3) showed that the rings seem to be more regularly spaced for the impinging jet. Furthermore, vortices are shed at a rather constant frequency as one would deduce from intersections between ring paths and a horizontal line at  $x/d < 1.0$  in Fig.(3-3). This indicates that the presence of the plate, especially near the nozzle, tends to organize the flow field between the nozzle and the plate. A possible "hydrodynamic" feedback could exist at such low subsonic speeds [Ho and Nasseir(1977)]. However, further investigations are needed before one could make a definite conclusion in that matter.

Winant and Browand(1974) were the first to observe pairing between vortices in the two-dimensional shear layer. They pointed out that the shear layer growth is due to pairing between these vortical structures. Petersen(1978) argued that rings coalesce when the local mixing layer attains a critical thickness which scales with the wave length of the vortex pair. Pairing between consecutive rings is shown in Fig.(3-4) and is described as follows: the downstream ring slows down and grows slightly in diameter, while the upstream ring increases its velocity and shrinks. The upstream ring is then "swallowed" by the downstream one and they both form a larger ring.

The pairing process is also shown in the hydrogen bubble picture of Fig.(3-5). The bubble lines near the nozzle exit are equally spaced indicating a constant flow speed, and form horizontally straight lines indicating a uniform speed; these effects are characteristic of the potential core. Each line curves at the outer edge of the jet due to the retarded velocity in the shear layer. In this region the hydrogen bubbles approximately provide instantaneous u-velocity profiles. Two lines are shown curved in opposite directions near the plate. The upper curvature indicates a high convection velocity in the "curved" shear layer. In fact, this is the high velocity upstream ring as it catches up with the slow moving downstream ring as mentioned before. Browand and Laufer(1975) described an identical pairing process based on the vortices mean velocity from their x-t diagram. Fig.(3-5) further provides the shape of the velocity profiles of the vortices during pairing. In the present experiment the convected rings stretch as they impinge on the plate. The ring cores impinge at locations  $1.0 < r_0/d < 1.5$  depending on the plate distance from the nozzle. Fig. (3-6) shows the survival of vortex rings as they stretch to more than two nozzle diameters after impingement. Ho and Kovaszny (1974) described a similar process for the impingement of isolated vortical rings on a plate. They observed that the ring radius increases rapidly on the plate to a limit-

ing value. The vortex ring then disappears by dissipation. The limiting radius was found to be a function of the downstream location of the plate. The process is similar in the case of the impinging jet. The difference is that the jet rings are superimposed on a mean flow. Therefore, the vortical rings continue to stretch on the plate because of mean flow velocity, until they disintegrate by dissipation.

The slope of ring paths of Fig. (3-3) gives the convection velocity of these structures. The average convection velocity of 40 rings was found to be  $.67 U$ , which is approximately the same value measured by Browand and Laufer (1975) in the free jet. Furthermore, it was observed from the movie that the velocity of ring cores along the curved shear layer near impingement does not change significantly. At the mean time, the potential flow in the jet core decelerates as it approaches the stagnation point on the plate. This is shown in Fig. (3-7). The distance between bubble lines decreases as the flow approaches the plate, which indicates a decelerating flow near the jet axis. The convex curvature towards the plate side of the two lines nearest to the plate indicates a slower speed near the center of the jet as compared to the outer shear layer.

The shear layer growth is shown in the multiple exposure hydrogen bubble picture of Fig. (3-8). The rate of increase of the shear layer thickness is faster near the plate. Note that bubbles produced by the platinum wire outside the jet column in Fig. (3-7), display nicely the particle paths of the ambient entrainment in the multiple exposure of Fig. (3-8). These entrainment lines appear clearer in the left hand side of the jet because of its closer proximity to the light source. The lines indicate that most of the entrainment takes place near the plate, especially at the outer edge of the impinging region, i.e. at the end of the curved shear layer  $1.5 < r_0/d < 2.0$ . Pairing between vortices on the plate was observed to take place in this region. The high turbulent energy production associated with the pairing [Laufer (1975)] is the cause for this high level of entrainment.

Widnall and Sullivan (1973) and Maxworthy (1976) observed azimuthal instability of isolated vortex rings. The amplitude of the instability waves grew in a direction  $45^\circ$  to the direction of ring propagation. The number of waves was determined from the condition of zero self-induced rotation of the waves around the filament axis in the theoretical model of Widnall, et al. (1974). Maxworthy (1976) showed that the number of instability waves, which is inversely proportional to the ring core

diameter, increases monotonically with the ring Reynolds number. Browand and Laufer (1975) noticed enhanced azimuthal instability during the pairing of two rings in the free jet. They argued that this secondary instability explains the breakdown of the rings' coherence downstream of the potential core. Azimuthal instability was also observed in the impinging vortex ring and is shown in Fig. (3-9). However, the presence of the plate and the associated stretching of the vortices during impingement seems to prevent or at least delay, the breakdown of the coherent rings due to these waves.

At  $Re \geq 8000$  a higher instability mode was observed. At  $Re = 8000$ , Fig. (3-10) shows a spiral mode that was observed to occur intermittently with the axisymmetric mode. This was also observed in the free jet by Browand and Laufer (1975).

### 3.2 PRESSURE MEASUREMENTS - AIR JET

The study of the water jet presented above was predominately qualitative in nature. The remaining part of the present investigation deals with quantitative results derived from the study of an impinging air jet. Surface pressure fluctuations due to the impingement of a turbulent jet are generally random with respect to time for low

jet Mach numbers,  $M$ . As an example, the raw signal from a surface pressure transducer at  $M = .5$  is shown in Fig. (3-11). However, the pattern of the signal changes completely for  $M > .6$  and  $x_0/d < 6$ . At  $M = 0.9$  the signal can be described as a slightly distorted sine wave as shown in the figure. This behaviour was usually accompanied by a screech tone that was clearly audible, especially for  $M > .8$ . A resonating field between the nozzle and the plate is believed to be responsible for that screech tone reported in Refs. 7, 8 and 9. The resonance phenomenon is also observed in the normalized power spectra of Fig. (3-12). The energy is substantially reduced at different frequency bands, and is increased in a narrow band around the resonance frequency.

### 3.2.1 Surface Pressure Loading

The rms of surface pressure fluctuations along the plate, normalized by the dynamic pressure  $q$  is plotted for  $M = .5$  and  $.9$  in Fig. (3-13). At  $x_0/d < 5$ ,  $p'/q$  has a peak at  $r_0/d \approx 1.5$ . This is the approximate location where vortex rings impinge on the plate, as was shown earlier in the water jet [see also Ho and Kovasznay (1974)]. For  $r_0/d > 3$ ,  $p'/q$  is independent of the plate location, which is a characteristic of the developed wall jet. The normalized pressure levels are higher for  $M = .9$  than for  $M =$

.5 at locations  $r_0/d < 3.0$ . This is shown for several Mach numbers in Fig. (3-14). At resonance,  $M = .8$  and  $.9$ , the surface loading is generally higher. The reason for higher pressure levels at  $M = .8$  than at  $M = .9$  is discussed later in connection with changing the plate location  $x_0/d$ .

As mentioned before, the plate is divided into two regions, the impinging region and the wall jet region. Based on the surface pressure fluctuations, the impinging region is further divided into two regions: an inner impinging region ( $0 < r_0/d \leq .5$ ) and an outer impinging region ( $.5 < r_0/d < 2$ ). The wall jet region is at  $r_0/d > 3$ . These divisions and their boundaries are rather arbitrary and are made for convenience in the future discussion of different flow characteristics. The effect of plate location  $x_0/d$  on  $p'/q$  for these regions is presented in Figs. (3-15) and (3-16). In the inner impinging region,  $p'/q$  increases as the plate moves away from the nozzle [Fig. (3-15)]. Strong, et al. (1967), showed that  $p'/q$  reaches its maximum value of 0.12 at  $x_0/d = 7$ . Fig. (3-15) also shows that  $p'/q$  in the wall region is independent of both  $M$  and  $x_0/d$ . The flow there is so dominated by the wall through the viscous forces that it tends to "forget" its past history.

The behavior of the pressure fluctuations in the outer impinging region is different between the resonant and nonresonant jets. In the resonant case of  $M = .9$ , Fig. (3-16a) shows that the pressure fluctuations  $p'/q$  goes through jumps as it decreases with increasing  $x_0/d$ . These jumps are similar to jumps in the resonance frequency observed when  $x_0/d$  changes as reported later in Sec. 5.2 [also see Fig. (5-4)]. At  $M = .8$ , Fig. (3-16b) shows that  $p'/q$  remains at a value .115 up to  $x_0/d = 2.7$  and then decreases with no jumps as  $x_0/d$  increases. The reason is possibly due to a "weak" resonance at  $M = .8$  (see Sec. 5.2). The surface pressure loading in the outer impinging region is due to the impingement of the large scale structures and is strongly dependent on both the jet Mach number  $M$ , and the plate location  $x_0$ . The values of  $p'/q$  seem to fall between two limits in fig. (3-16c): a lower limit of a non-resonant case at  $M = .5$  and an upper limit of the resonant case at  $M = .9$ . The pressure at  $M = .9$  is shown to jump between the two limits, passing through an intermediate stage with values corresponding to the "weak" resonant case of  $M = .8$ . The jumps in  $p'/q$  at  $M = .9$  is, therefore, the reason for the lower levels of pressure observed in Fig. (3-14) at  $x_0/d = 2.0$  compared to the  $M = .8$  case.

### 3.2.2 Eddy-Convection Velocity on the Plate: Comparison of Different Techniques

The convection velocity  $C$  is usually evaluated from the correlation function  $R$  by either of two ways (Ho and Kovaszny (1976)): constant separation distance  $\xi_1$  with varying the time delay  $\tau$ , where  $C$  satisfies the condition

$$\partial R(\xi_1, \tau) / \partial \tau = 0$$

or constant time delay  $\tau_1$  with varying the separation distance  $\xi$ , where  $C$  satisfies the condition

$$\partial R(\xi, \tau_1) / \partial \xi = 0$$

The calculated values by the two methods are generally different. Wills (1964) indicated that they are only equal if the turbulent flow satisfies Taylor's hypothesis in which the "frozen" eddies are convected unchanged. To remove the ambiguity in evaluating a single convection velocity, he argued that  $C$  has to be expressed in terms of either a wave number  $k$  or frequency  $f$ . He derived the convection velocity  $C(k)$  as a function of the wave number, and defined an overall convection velocity as the propagation velocity of the peak of the turbulent energy, integrated over different wave numbers  $k$ . This method is suit-

able whenever the convection velocity of different wavelength is needed as in water-wave generation.

In the present study the frequency is chosen as a parameter in the evaluation of convection velocities. The calculation of convection velocity at any frequency  $C(f)$ , especially at the resonance frequency, is more appropriate in studying the feedback mechanism. The group velocity  $C_g(f)$  is defined as the velocity of energy propagation at frequency  $f$ , which is relevant to the condition used by Wills (1964) to evaluate  $C(k)$ . Naturally, for nondispersive waves the convection velocity  $C(f)$  of the present study and  $C(k)$  of Wills (1964) are the same.

In this section the convection velocity along the plate will be calculated by different techniques discussed earlier in Sec. 2.3. Values calculated from space-time correlation functions are compared with those using constant-separation correlation functions. The narrow-band convection velocity, which is called the phase velocity  $C(f)$ , evaluated from cross-spectra function is also presented. The prewhitening technique is used to calculate convection velocities for resonant cases.

The phase velocity, or the narrow-band convection velocity  $C(f)$  is calculated from the relation

---

$$C(f) = (2\pi f) \xi / \psi(f) , \quad (3-1)$$

where  $\psi(f)$  is the phase angle between two signals at points separated by  $\xi$ . The group velocity is proportional to the slope of the phase angle and is given by

$$C_g(f) = 2\pi \xi / \frac{d\psi(f)}{df} . \quad (3-2)$$

For a nondispersive wave the slope of the phase angle is constant and hence

$$C_g(f) = C(f) = \text{constant} .$$

An example of the cross-spectrum and phase angle functions between two points on the plate is shown in Fig. (3-17a) for  $M = .8$  and  $x_0/d = 6$ . The cross-spectrum  $G(f)$  has a broad peak at  $f=3200$  Hz. The Strouhal number of this peak,  $fd/U = .30$ , corresponds to the frequency of large scale structures at the end of the potential core in a free jet. The phase angle  $\psi(f)$  fluctuates around a straight line, indicating a nondispersive convected wave. Misleading data appear in both  $G(f)$  and  $\psi(f)$  at low frequencies ( $f < 700$  Hz) and are attributed to the low frequency cutoff in evaluating the spectrum from a finite digital

record length [Eqn. (2-1)]. Fig. (3-17b) shows the coherence function  $\gamma(f)$  for the same flow parameters of Fig. (3-17a). The coherence  $\gamma(f)$  takes a similar shape as  $G(f)$ . The phase angle function in the figure is evaluated from smoothed frequency components as mentioned earlier in Sec. 2.3 (with  $n = 8$ ). The phase angle function has a clear constant slope over the shown frequency range. Eqn. (3-1) is used to calculate the phase velocity from  $\varphi(f)$  of Fig. (3-17b) and is shown in Fig. (3-17c). As expected from the constant slope of  $\varphi(f)$ , the phase velocity is the same for different frequencies and equal to .62 of the jet exit velocity  $U$ , which is indicative of the nondispersiveness of the convected eddies on the plate.

At low jet Mach number ( $M = .5$ ), Fig. (3-18) shows a similar cross-spectrum function and a constant-slope phase angle function.

The correlation coefficients are presented in Figs. (3-19) and (3-20). The correlation coefficients are plotted as a function of separation distance and time delay  $\tau$  for the case of  $M = .8$  in Fig. (3-19). The characteristic forms of these correlation curves are in agreement with those of Refs. 3 and 6. The correlation coefficient was very small (<5%) between any point in the inner impinging region and the rest of the plate. This is possibly

due to turbulent flow circulation in the "stagnation bubble" reported by Donalson, et al. (1971). Point 2 ( $r_0/d = 1.0$ ) is chosen as a fixed reference point. This point is in the region where the vortex rings were observed to impinge on the plate in the water jet experiment. The figure shows a 50% correlation coefficient which is almost constant over the outer impinging region ( $1 < r_0/d < 2$ ). The correlation coefficient drops for larger separation distance, since convected eddies tend to lose their identities due to viscous dissipation and the development of small scale turbulence.

At low jet speed ( $M = .5$ ), the correlation coefficient was found to drop sharply for a separation distance larger than one nozzle diameter. The reason is that large scale structures are less coherent for a weak feedback at such low jet speed. The correlation function is, therefore, shown in Fig. (3-20) as a function of  $\tau$  with constant separation distance equal to  $d/2$ . The correlation coefficient between two points in the inner impinging region  $R_{0,1}(\tau)$  is again small and of the same order of magnitude as the noise. It increases as we enter the outer impinging region where the large coherent structures impinge on the plate.

At high subsonic jet speed and small nozzle to plate

distance, resonance occurred and the pressure signal was a distorted sine wave. The correlation function also took a sinusoidal pattern with no clear optimum peak to evaluate eddy convection velocity. The prewhitening technique reported in Sec. 2.3 was used.

The raw surface pressure signals at different locations on the plate for a resonant jet at  $M = .9$  and  $x_0/d = 4.5$  is shown in Fig. (3-21). The signal at  $r_0/d = 0$  is almost a pure sine wave owing to the induced field of the impinging coherent eddies. This is supported by the relatively low rms value of the pressure fluctuations at  $r_0/d = 0$  in Fig. (3-13). The signals at the outer impinging region exhibit rather distorted sine waves because of the small scale turbulence.

The power spectra of these signals are presented in Fig. (3-22). Most of the energy is concentrated in a narrow band around the resonance frequency at the location  $r_0/d = 0$ . In the outer impinging region other frequency components appear in the spectra. It is noticeable that at  $r_0/d = .5$ , the energy is more evenly distributed over a wide band of frequencies due to the random flow in the "stagnation bubble". In all the spectra, a smaller peak is observed at the first harmonic of the resonance frequency.

The cross-spectrum between two points is shown in Fig. (3-23a). Two peaks at the resonance frequency and its first harmonic is shown. A narrow-band digital filter (bandwidth = 312 Hz) was used in the prewhitening process to average out these two peaks. The result is shown in Fig. (3-23b) with the corresponding phase angle function. The real gain from prewhitening is shown in the correlation functions of Fig. (3-24). As expected, the correlation functions before prewhitening are sinusoidal with respect to the delay time, while the prewhitened correlation function shows a distinctive peak. The delay time of this peak is used to evaluate a broad-band convection velocity  $C$  for resonant cases. Fig. (3-25) shows a space-time prewhitened cross-correlation functions of a resonant case ( $M = .9$  and  $x_0/d = 4.5$ ). The cross-correlation function for the inner impinging region is plotted separately in Fig. (3-25a). The correlation between point 0 and 1 shows a negative time delay peak, indicating a reversed flow towards the stagnation point. This is consistent with flow circulation in the stagnation bubble as reported by Donalson, et al. (1971). The correlation coefficients in the outer impinging region are shown in Fig. (3-25b). Here, the correlation coefficients show a continuous decrease with increasing the separation distance and time delay, which is different from

the behaviour of those in Fig. (3-19). The reason is that the coherent part of the signals used to produce the correlation functions has been reduced substantially during the prewhitening process.

The convection velocity  $C$  along the plate is plotted in Fig. (3-26). Except for a negative value near the stagnation point, the convection velocity increases to a peak at  $r_0/d = 1.25$  and then decreases asymptotically to a value of  $.45 U$ . The higher convection velocity near the outer impinging region ( $\approx .65 U$ ) agrees with observation of pictures and movies [see Figs. (3-3) and (3-7)] of the impinging water jet. The shear layer was observed to curve as it approaches the plate. The deceleration is balanced by the acceleration due to shear layer curvature, and the vortex rings were seen to maintain their free speed (or even accelerate) during impingement.

The data points in Fig. (3-26) for  $M = .8$  are evaluated from the separation distance and the optimum time delay of two different correlation plots. The convection velocity  $C$  is plotted at the half point of the separation distance. The values of  $C$  at  $r_0/d = 1.75$  and  $2.5$  are evaluated from a constant separation distance correlation function (with  $\delta = d/2$ ) similar to those of Fig. (3-20). These points are in accord with others calculated by the

variable separation distance correlation functions of Fig. (3-19). As previously noted, this should not happen unless Taylor's hypothesis is satisfied. Lin (1952) has shown that Taylor's hypothesis is valid only if the turbulence level is low, viscous forces are negligible, and the mean shear is small. It is, therefore, unreasonable to expect the hypothesis to apply to the flow of an impinging jet on a plate. Hence, the concept of convected "frozen" eddies is excluded as a reason for the agreement in the velocity calculated by the two methods. To understand this result, the expected difference in the calculated values of  $C$  by the two correlation function plots must be discussed first. As the separation distance increases, small eddies are bound to lose their identity and become uncorrelated in comparison with larger size eddies. This is in effect a lowpass filter with a cutoff frequency decreasing with increasing  $\xi$ , added during the evaluation of correlation coefficients. With a fixed  $\xi$ , the correlation estimates are most sensitive to the convection of eddies with a size corresponding to the fixed bandwidth filter. The consistency of the calculated convection velocity irrespective of the effective filter used indicates that eddies with different sizes convect at the same speed. In other words, if one uses the method proposed by Wills (1964), the calculated convection velocity for different wave numbers  $C(k)$  would be constant. Thus, the flow over

the plate for  $r_0/d > 1.25$  satisfies the relation  $\omega/k = C(k)$   
= constant, which upon differentiation gives

$$\frac{d\omega}{dk} = C_g = \text{constant}.$$

This is another way of showing the nondispersiveness of the convected eddies on the plate as observed earlier in Fig. (3-17c).

### 3.2.3 Stability Modes of the High Speed Jet

It was shown in the pictures of Sec. 3.1 that the coherent structures have a vortex ring shape. At high Reynolds number ( $Re > 8000$ ) a higher instability mode, namely a helical mode, appeared. Browand and Laufer (1975) observed both the axisymmetric and helical modes in a free jet at  $Re = 5000$  to  $20,000$ . Fuchs and Michel (1977) used a set of near field microphones placed in a plane perpendicular to and at equal distances from the jet axis. By Fourier analyzing the real part of the cross-spectrum between these microphones, they were able to determine the azimuthal constituents of the turbulent energy at any frequency. For a range of  $10^4 < Re < 2 \times 10^7$  ( $.3 < M < .7$ ), they found that the energy was mostly contained in the axisymmetric mode, although higher modes were present. Neuworth (1973) observed that, while at  $M = .5$  pictures showed an

axisymmetric coherent structures, at  $M = .9$  a helical mode appeared in the free jet. However, when the plate was inserted his pictures and those of Wagner (1971) showed that only the axisymmetric mode remained. Neuworth predicted that waves reflecting from the plate were responsible for the axisymmetric excitation of the free shear layer near the nozzle.

In the present study the stability modes were examined by placing five pressure transducers at equal distance from the stagnation point on the plate. Gross features of the stability modes of the impinging jet were examined from the correlation function between points on the plate at different azimuthal angles. An example of the correlation function between two points separated by  $\Delta\phi_0 = 270^\circ$  is shown in Fig. (3-27). The correlation for this resonant case has a maximum at  $\tau = 0$ , which suggests that the axisymmetric mode is dominant. The prewhitened correlation function is also shown with a peak at  $\tau = 0$ , indicating that the turbulent portion of the surface pressure fluctuations are also dominated by an axisymmetric mode. Similar results are shown for different azimuthal angles in Fig. (3-28). Furthermore Fig. (3-29) shows that the phase angle is approximately equal to zero over all frequencies, which suggests that the existing turbulent scales are axisymmetric.

---

Similar analysis was carried out to ensure axisymmetry in the flow field between the nozzle and the plate. Fig. (3-30) shows the cross correlation function before and after prewhitening between two transducers at the exit plane of the nozzle. Axisymmetry is indicated by the peaks at  $\tau = 0$ .

---

CHAPTER 4  
THE TWO BRANCHES OF THE FEEDBACK LOOP

In the previous chapter, general characteristics of the impinging jet were presented. The validity of different digital data techniques was examined. The convection velocity on the plate was found to be consistent when evaluated by these techniques, and to agree well with results from Refs. 3 and 6. Finally, the flow field of the impinging jet was found to be dominantly axisymmetric.

As mentioned earlier in Chapter 1, a conjecture for the feedback mechanism causing the resonance could take the following form: coherent eddies are convected downstream and impinge on the plate; waves are generated which propagate upstream and excite the shear layer near the nozzle; the shear layer rolls into new coherent eddies and the feedback loop is closed. In this chapter, pressure measurements are used to detect waves propagating in the near field between the nozzle and the plate. The characteristics of these waves are studied and the relation between them at  $\alpha = 0$  is investigated.

#### 4.1 CORRELATIONS OF NEAR FIELD PRESSURE MEASUREMENTS

Power spectra of signals from near field microphones are shown in Fig. (4-1) for  $M = .8$  and  $x_0/d = 7$ . The spectra do not show a distinguished high peak, indicating no resonance. The correlations of these signals are plotted in Fig. (4-2) as functions of separation distance and time delay  $\tau$ . For positive  $\tau$ , the correlation coefficient peaks indicate a downstream convected wave. On the other hand, other peaks at negative time delays are also present. While the peak in  $R_{I,II}(\tau)$  at negative time delay may appear as a result of normal oscillations in the correlation function, the one in  $R_{I,III}(\tau)$  does not. These peaks, therefore, indicate upstream propagation, and the behavior of the correlations suggest the possibility of two waves propagating in the near field.

At resonance the correlation functions are sinusoidal with respect to  $\tau$  and provide no information about wave propagation. However, the presence of the two waves is observed in the cross-spectra and phase angle functions in Fig. (4-3). The cross-spectrum between two microphones near the axis of the jet  $G_{I,II}(f)$  is dominated by two strong resonance peaks. The presence of two resonance peaks instead of one is attributed to the tendency of the

jet to intermittently jump between two resonance frequency stages in this specific case ( $M = .9$  and  $x_0/d = 5$ ). These frequency jumps are discussed later in Sec. 5.2. The phase angle  $\varphi_{I,II}(f)$ , despite some discrepancies at  $5.5 \text{ KHz} < f < 6 \text{ KHz}$ , increases with frequency. These discrepancies may be due to very low levels of energy at this frequency band [ $G_{I,II}(f) < 10^{-4}$ ]. Here the noise signal is expected to be of the same order of magnitude as the measured signals. However, the positive slope of  $\varphi_{I,II}(f)$  indicates a downstream convected wave. Although  $G_{III,IV}(f)$  shows peaks at the same resonance frequencies,  $\varphi_{III,IV}(f)$  behaves differently. The negative slope of  $\varphi_{III,IV}(f)$  for these microphones located further away from the jet axis indicates the existence of an upstream wave.

The cross-correlations between microphones I & II before and after prewhitening are shown in Fig. (4-4) and the corresponding cross-correlations between III & IV are shown in Fig. (4-5). The correlation function  $R_{I,II}(\tau)$  is a sine wave as expected from two resonant signals. However, the prewhitened correlation  $\tilde{R}_{I,II}(\tau)$  shows two optimum peaks at positive and negative time delays. This is in agreement with earlier observations in the non-resonant case of Fig. (4-2). In Fig. (4-5) the correlations  $R_{III,IV}(\tau)$  and  $\tilde{R}_{III,IV}(\tau)$  measured at locations further away from the jet axis show only negative time delay peaks, in-

dicating predominant upstream propagation.

The above two-point measurements provide evidence for the presence of two waves propagating in the near field. Furthermore, the upstream propagating wave is shown to be dominant in the near field away from the jet axis. This provides an opportunity to study one of the two waves, namely the upstream wave, through measurements taken away from the jet axis.

#### 4.1.1 Characteristics of the Upstream Wave

The pressure fluctuations,  $p'^2$ , measured in decibels by a microphone moving outwards in a plane perpendicular to the jet axis at the nozzle exit is plotted in Fig. (4-6). The figure shows  $p'^2$  for a free jet at  $M = .8$  compared to an impinging jet at  $M = .8$  and  $.9$ . In a free jet,  $p'^2$  drops sharply from  $r/d = .5$  to  $r/d = 1.0$  (not shown in the figure) and then descends at a rate proportional to  $r^{-1.6}$ . This is in agreement with Chu (1975), who also showed that the near field of the present jet extends to  $r/d = 30$  at  $\theta = 90^\circ$ . For the impinging jet  $p'^2$  has higher levels, but behaves like the free jet up to  $r/d = 3$ . These high levels are mainly due to added energy from the upstream wave. At large radii,  $p'^2$  increases for  $3 < r/d < 6.5$  and then decreases at a rate proportional to

$r^{-2}$ . This indicates that the energy is dominated by the upstream wave for  $r/d > 3$ , and that the far field of this wave is reached at  $r = 6.5$ , after which  $p'^2$  follows the inverse square law.

The phase difference at the resonance frequency between two microphones in a plane perpendicular to the jet axis at the nozzle exit is shown in Fig. (4-7). One of the microphones was fixed near the nozzle lip at  $r/d = .5$ , while the other was allowed to move radially away from the jet axis. For  $r/d > 3$ , the phase angle increases almost linearly with  $r$ . In this region the upstream wave was shown to be dominant from the pressure measurements of Fig. (4-6), and also from the spectra and correlation functions of Figs. (4-3) and (4-5). Therefore, the phase angle plotted against  $r$  for  $r/d > 3.0$  represents an almost plane wave front propagating in the upstream direction. The direction of propagation is the perpendicular to the average slope  $\frac{d\varphi_{I,II}(f_r)}{dr}$

For  $r/d < 3.0$ , Fig. (4-7) shows that the two signals are in phase except for a "bulge" around  $r/d = 2$ . This bulge is believed to be an erroneous deviation from a zero phase value (a zero phase at the nozzle exit is discussed further in Sec. 5.1). The deviation is due to the fact that signals around  $r/d = 2$  contain random frequency com-

ponents [Fig. (4-8)], and that the phase angle was calculated at a single frequency  $f_r$  by averaging over a long time record. The appearance of random high frequencies in the signals at  $r/d = 2$  is possibly due to the following two reasons:

1. The acoustic waves radiated from the stagnation region of the plate to this region suffer (as will be shown later) from random scattering as they travel through a thick turbulent shear layer, and/or

2. A microphone in this vicinity is sensitive to pressure integrated over the whole flow field.

Fig. (4-8) shows that a resonant sinusoidal signal dominates close to the edge of the shear layer at  $r/d = .5$ , and away from the jet axis at  $r/d = 6.5$  where the upstream wave is strong

In order to evaluate the speed of the upstream wave, a third microphone **III** is placed downstream of the moving one. The phase angle  $\varphi_{III,II}(f)$  is plotted in Fig. (4-9) as a function of frequency  $f$ . Three samples of  $\varphi_{III,II}(f)$  at different  $r_{II}/d$  are shown in the figure. The phase angle increases linearly with  $f$ . Since **III** is delayed, the constant positive slope indicates a nondispersive upstream

propagating wave. It is also noticeable that fluctuations in  $\gamma_{\text{III,II}}(f)$  around its mean decrease as  $r_{\text{II}}/d$  increases, owing to the dominant contributions of the upstream wave over the pressure signals in the near field away from the jet axis. It is now clear that the upstream wave can be treated as a nondispersive [Fig. (4-9)], plane [Fig. (4-7)] wave. Furthermore, the angle  $\Theta_a$  between the jet axis and the direction of propagation, can be calculated from the mean slope of the wave front according to the relation

$$\Theta_a = \tan^{-1} \left[ \frac{d\overline{\gamma}(f_r)}{d(r/d)} \right]. \quad (4-1)$$

From Fig. (4-7) a value of  $\Theta_a = 35^\circ$  is calculated using Eqn. (4-1). This value is further confirmed from the prewhitened cross correlation functions between II and III. The correlation coefficients optimum peaks  $R_{\text{III,II}}(\tau_p)$  are plotted versus  $r_{\text{II}}/d$  in Fig. (4-10). A broad peak of  $R_{\text{III,II}}(\tau_p)$  shown around  $r_{\text{II}}/d = 3.3$  corresponds to a propagation direction  $\Theta_a = 33^\circ$ . This is in good agreement with the value calculated above.

The speed of the nondispersive upstream wave  $C_2$  can be calculated from the slope of the phase angle between two microphones (e.g. II & III) by the following relation

$$\bar{C}_2 = \left\{ 2\pi (\bar{\xi}_{\text{II},\text{II}} \hat{\Theta}_a) / \frac{d\varphi_{\text{II},\text{II}}(f)}{df} \right\}, \quad (4-2)$$

where  $\hat{\Theta}_a$  is the unit vector in the direction of upstream wave propagation inclined by an angle  $\Theta_a$  to the jet axis. Eqn. (4-2) is used to plot the magnitude of the upstream wave speed normalized with respect to the ambient speed of sound  $a_0$ , for different  $r_{\text{II}}/d$  in Fig. (4-11). It is shown that the upstream wave travels with a speed that is equal to the speed of sound  $a_0$ .

A constant value of  $\Theta_a = 35^\circ$  from the mean slope  $\frac{d\varphi(f_r)}{d(r/d)}$  of Fig. (4-7) was used in Fig. (4-11). However, Fig. (4-7) shows that the wave front is slightly curved and that  $d\varphi(f_r)/d(r/d)$  increases as  $r/d$  increases. This resulted in smaller values of  $C_2/a_0$  for larger  $r_{\text{II}}/d$ , which is the trend one observes in the figure.

The direction of the upstream wave propagation for different plate locations  $x_0$  is presented in Fig. (4-12). It is shown that as the plate moves closer to the nozzle, the upstream wave propagates at a larger angle relative to the jet axis.

## 4.2 A SIMPLE MATHEMATICAL MODEL

The correlation and cross-spectra functions of the measured pressure signals have shown a downstream and an upstream propagating wave. The upstream wave can be treated as a plane sound wave propagating along a path inclined at an angle  $\Theta_a$  to the jet axis. The following simple mathematical model presupposes two counterpropagating waves in the near field of the jet. This model will help to explain the feedback mechanism through analysis of measured correlation functions.

The pressure at any point in the near field between the nozzle and the plate is the superposition of two parts

$$p(t, \vec{r}) = \alpha(t, \vec{r}) + \beta(t, \vec{r}), \quad (4-3)$$

where,

$\vec{r}$  is the position vector with respect to the center of the nozzle exit plane [see Fig. (4-13)], and  $\alpha$  and  $\beta$  are the two parts of the signal due to the downstream and the upstream travelling waves, respectively. Eqn. (4-3) is also expressed as a pair of travelling waves, i.e.

$$p(t, \vec{r}) = a(\vec{r}) e^{i(\omega_1 t - \vec{k}_1 \cdot \vec{r} + \phi_1)} + b(\vec{r}) e^{i(\omega_2 t + \vec{k}_2 \cdot \vec{r})}, \quad (4-4)$$

where  $a(\vec{j})$ ,  $b(\vec{j})$  are the wave amplitudes,  
 $\vec{k}_1, \vec{k}_2$  are the downstream and the upstream wave numbers  
 respectively, and  
 $\gamma_0$  is a constant phase shift between the two waves.

The following assumptions are made in order to simplify the model:

1. The two waves are assumed to be plane waves. It is anticipated that the downstream wave, which is due to the convected large scale structures, is travelling along the jet axis. The upstream wave propagates in a direction making an angle  $\Theta_a$  with the jet axis.

2. The waves are monochromatic, i.e. only one frequency component at the resonance frequency (or the dominant frequency in a non-resonant case) is considered. The two waves are also assumed to have the same frequency since the upstream one is generated from the incidence of the downstream wave on a solid surface, i.e.

$$\omega_1(\vec{k}_1) = \omega_2(\vec{k}_2) = \omega_r .$$

Eqn. (4-4) then takes the form

$$p = a e^{i(\omega_r t - \vec{k}_1 \cdot \vec{x} + \gamma_0)} + b e^{i(\omega_r t + \vec{k}_2 \cdot \vec{x})} . \quad (4-5)$$

By definition, the phase velocity of the downstream wave in the x-direction is

$$C_1 = \frac{\omega_r}{k_1} , \quad (4-6)$$

and the phase velocity of the upstream wave is

$$\vec{C}_2 = \frac{\omega_r}{|\vec{k}_2|} \hat{\Theta}_0 . \quad (4-7)$$

The phase shift  $\varphi_0$  in Eqn. (4-5) can be evaluated by applying the boundary condition at the plate. Since the upstream wave is assumed to be generated by the downstream wave as it impinges on the plate, the phase difference between the two waves should be equal to zero there. The phase difference between the two waves at any location is

$$\varphi = -k_1 x - \vec{k}_2 \cdot \vec{\mathcal{F}} + \varphi_0 . \quad (4-8)$$

The boundary condition is

$$\varphi = 0 \quad \text{at} \quad \vec{\mathcal{F}} = \vec{\mathcal{F}}_s , \quad (4-9)$$

where  $\vec{\mathcal{F}}_s$  is the position vector of an apparent sound source on the plate [Fig. (4-13)]. Substituting (4-9) in (4-8), one obtains

$$\gamma_0 = k_1 x_0 + \vec{k}_2 \cdot \vec{J}_S \quad (4-10)$$

Hence eqn. (4-8) may be written

$$\gamma = k_1 (x_0 - x) + \vec{k}_2 \cdot (\vec{J}_S - \vec{J}) \quad (4-11)$$

which represents the phase difference between the two waves at any location in the near field between the nozzle and the plate.

#### 4.2.1 The Correlation Function

From Eqn. (4-5) the pressure at points I and II are

$$\begin{aligned} p_I &= a_1 e^{i(\omega_r t - k_1 x_I + \gamma_0)} + b_1 e^{i(\omega_r t + \vec{k}_2 \cdot \vec{J}_I)} \\ &= a_1 \alpha_1 + b_1 \beta_1 \\ p_{II} &= a_2 e^{i(\omega_r t - k_1 x_{II} + \gamma_0)} + b_2 e^{i(\omega_r t + \vec{k}_2 \cdot \vec{J}_{II})} \\ &= a_2 \alpha_2 + b_2 \beta_2 \end{aligned} \quad (4-12)$$

where  $\alpha_1, \beta_1, \alpha_2, \beta_2$  are the signal components due to the two waves.

The correlation function of two signals, each is the sum of two stationary processes is given in Ref 30. Similarly, the correlation function of the two signals of Eqn. (4-12) is

$$R_{I,II}(\tau) = a_1 a_2 R_{\alpha_1, \alpha_2}(\tau) + b_1 b_2 R_{\beta_1, \beta_2}(\tau) + a_1 b_2 R_{\alpha_1, \beta_2}(\tau) + b_1 a_2 R_{\beta_1, \alpha_2}(\tau). \quad (4-13)$$

The above equation shows the correlation function  $R_{I,II}(\tau)$  as the algebraic sum of the individual component correlation functions. The correlation functions of these components are by definition:

$$R_{\alpha_1, \alpha_2}(\tau) = \frac{1}{2} e^{i[\omega_r \tau - k_1(x_{II} - x_I)]} \quad (4-14a)$$

$$R_{\beta_1, \beta_2}(\tau) = \frac{1}{2} e^{i[\omega_r \tau + \vec{k}_2 \cdot \vec{r}_{I,II}]} \quad (4-14b)$$

$$R_{\alpha_1, \beta_2}(\tau) = \frac{1}{2} e^{i[\omega_r \tau - k_1 x_{II} - \vec{k}_2 \cdot \vec{r}_I + \gamma_0]} \quad (4-14c)$$

$$R_{\beta_2, \alpha_1}(\tau) = \frac{1}{2} e^{i[\omega_r \tau + \vec{k}_2 \cdot \vec{r}_{II} + k_1 x_I - \gamma_0]} \quad (4-14d)$$

Using Eqn. (4-6), Eqn. (4-14a) gives an optimum time delay

$$\tau^{(1)} = + \frac{x_{II} - x_I}{C_1}, \quad (4-15)$$

and using Eqn. (4-7), Eqn. (4-14b) similarly gives

$$\tau^{(2)} = - \frac{\vec{f}_{I,II} \cdot \hat{\Theta}_a}{C_2}, \quad (4-16)$$

where  $C_2$  is the speed of the upstream wave inclined at an angle  $\Theta_a$  to the jet axis. Similarly from Eqns. (4-10), (4-14c), and (4-14d)

$$\tau^{(3)} = - \left[ \frac{x_0 - x_{II}}{C_1} + \frac{\vec{f}_{I,S} \cdot \hat{\Theta}_a}{C_2} \right] \quad (4-17)$$

$$\tau^{(4)} = + \left[ \frac{x_0 - x_I}{C_1} + \frac{\vec{f}_{S,II} \cdot \hat{\Theta}_a}{C_2} \right], \quad (4-18)$$

where  $\vec{f}_{I,S}$  is the vector connecting I and S, and  $\vec{f}_{S,II}$  is the vector connecting S and II [Fig. (4-13)].

Eqns. (4-13) and (4-15) to (4-18) predict that the correlation function between two points in the near field

exhibits two peaks with positive time delays as well as two peaks with negative time delays. The physical interpretation of the four time delays of these peaks is explained as follows:  $\tau^{(1)}$  is the time it takes the downstream wave to travel from I to II;  $\tau^{(2)}$  is the time it takes the upstream wave to travel from II to I and should appear as a negative time delay in  $R_{I,II}(\tau)$ ;  $\tau^{(4)}$  is the time it takes the downstream wave to travel from I to the plate with velocity  $C_1$ , plus the time it takes for the generated wave to propagate back from the plate to II;  $\tau^{(3)}$  is the time for the downstream wave to go from II to the plate plus the time for the generated upstream wave to bounce back to I.  $\tau^{(3)}$  should, therefore, appear as a negative time delay in  $R_{I,II}(\tau)$ .

The correlation function between the near field pressure signal and a surface pressure signal in the impinging region on the plate can be derived by substituting

$x_{II} = x_0$  and  $\xi_{II} = \xi_s$  in Eqns. (4-15) to (4-18) which yields

$$\tau^{(1)} = \tau^{(4)} = \frac{x_0 - x_I}{C_1}, \quad (4-19)$$

$$\tau^{(2)} = \tau^{(3)} = - \frac{\vec{\xi}_{I,s} \cdot \hat{\theta}_\alpha}{C_2}. \quad (4-20)$$

These later results show that the four peaks degenerate into only two in the correlation between a point I in the near field and a point S on the plate. The positive time delay of one peak [Eqn. (4-19)] corresponds to the downstream convection to the plate and the negative time delay of the other peak [Eqn. (4-20)] corresponds to the upstream propagation from the plate to point I.

For the special case of  $x_I = x_{II} = x_I$ , Eqn. (4-13) gives the autocorrelation function  $R_{i,i}(\tau)$  with optimum time delays from Eqns. (4-15) to (4-18) given by

$$\left. \begin{aligned} \tau^{(1)} &= \tau^{(2)} = 0 \\ \tau^{(4)} = -\tau^{(3)} &= \frac{x_0 - x_i}{C_1} + \frac{\bar{z}_{i,S} \cdot \hat{\theta}_a}{C_2} \end{aligned} \right\} (4-21)$$

where the index  $i$  refers to positions I, II, III, or IV. Eqn. (4-21) predicts that, due to the presence of the plate, an autocorrelation function should exhibit an extra peak besides the usual one at  $\tau = 0$ . The time delay of that extra peak corresponds to the time it takes the downstream wave to travel to the plate combined with the time it takes for the generated wave to propagate back to the same point. Eqn. (4-21) also indicates that the extra peak appears in both the negative and positive time dela-

ys, which is consistent with the autocorrelation being an even function.

#### 4.3 MEASURED CORRELATIONS: COMPARISON WITH THE MODEL

The pressure in Eqn. (4-5) is expressed as the sum of two waves that have the same single frequency component  $\omega_r$ . The frequency  $\omega_r$  is the dominant resonance frequency or the peak frequency of the narrow-band signals for non-resonant cases. However, the measured pressure signals contain other frequency components due to the randomness of the turbulent flow. This randomness adds unique characteristics to each convected event in the flow field. Accordingly, the predicted optimum time delays of Eqns. (4-15) to (4-18) are expected to correspond to peaks of high correlation levels in the correlation coefficients of measured signals. The correlation functions for the non-resonant cases are shown in Figs. (4-14) to (4-16), and the prewhitened correlation functions for a strong resonant case are displayed in Fig. (4-17).

The autocorrelation functions in Fig. (4-14) for  $M = .8$  and  $x_0/d = 7$  show extra peaks [peaks (3) and (4)] besides the usual unity peak at  $\tau = 0$ , in agreement with the model. The space-time correlations for this non-resonant case are plotted in Fig. (4-15). For zero separation,

$R_{I,I}(\tau)$  shows that  $\tau^{(1)} = \tau^{(2)} = 0$ . As the separation distance increases, peak (1) moves to larger positive time delays indicating a downstream convection, while peak (2) moves in the opposite direction indicating an upstream convection. Peaks (3) and (4) are at larger time delays and they meet with (1) and (2) in the correlation function with the transducer on the plate  $R_{I,0}(\tau)$ , as predicted by Eqns. (4-19) and (4-20).

The approximate loci of these peaks form the letter "W" as indicated by the dashed lines in Fig. (4-16). In this figure, the correlation functions are separated vertically in proportion to actual physical separation distance between microphones, along the jet axis. For a constant convection velocity in the x-direction, the dashed lines forming the "W" should be straight. However, since the upstream waves propagate in a direction inclined by  $\Theta_a$  to the jet axis, these dashed lines appear with a small curvature.

Periodic oscillations are observed in the correlation plots for  $\tau^{(4)} < \tau < \tau^{(3)}$  in Figs. (4-15) and (4-16). These oscillations correspond to the passage period  $2\pi/\omega_T$ . This criterion was used in some cases to define peak (4) in the correlation functions.

The prewhitened correlation functions for the resonance case of  $M = .9$  and  $x_0/d = 4$  are shown in Fig. (4-17). The plots show a similar behavior to those in Figs. (4-14) to (4-16).

Comparison between the mathematical model and the optimum time delays from the measured correlation functions are presented in Figs. (4-18) to (4-20). Eqns. (4-17) and (4-18) can be written in the nondimensional forms

$$-\frac{a_0 T_{i,j}^{(3)}}{\Delta x} = -\frac{1}{MK_v} + \left( \frac{1}{MK_v} + \cos \Theta_a \right) \frac{x_0 - x_i}{\Delta x}, \quad (4-25)$$

$$\frac{a_0 T_{i,j}^{(4)}}{\Delta x} = -\cos \Theta_a + \left( \frac{1}{MK_v} + \cos \Theta_a \right) \frac{x_0 - x_i}{\Delta x}, \quad (4-26)$$

where  $\Delta x = x_j - x_i$  is the separation distance along the jet axis between the two correlated points  $i$  &  $j$ . The angle  $\Theta_a$  is a weak function of the plate location  $x_0$  [Fig. (4-12)], therefore an average value of  $\Theta_a = 30^\circ$  is used to simplify Eqns. (4-25) and (4-26) so that they represent straight lines. Also, as shall be seen in the following section [Fig. (4-21)], the convection velocity of the downstream wave measured from the optimum time delay  $\tau^{(u)}$  has a value which corresponds to  $C_1/U = K_v = .62$ ,

while the upstream wave speed is  $C_2 = a_0$ .

Fig. (4-18) shows very good agreement between Eqn. (4-25) and the measured time delay  $\tau^{(3)}$  for  $M = .8$  and  $.9$ . Even at low subsonic jet speed ( $M = .5$ ), two measured peaks were recognizable in the correlation functions and are in good agreement with the model in Fig. (4-18b). These points indicate the existence of the two waves even at low impinging jet speeds, except that resonance does not occur. Eqn. (4-26) is also in excellent agreement with measurements of  $\tau^{(4)}$  as shown in Fig. (4-19).

The magnitude of the time delay of the extra peak in the autocorrelation function from Eqn. (4-21) can be expressed in dimensionless form as

$$\frac{a_0 |\tau|^{(3),(4)}}{x_0} = \left( \frac{1}{M K_V} + \cos. \Theta_a \right) \left( 1 - \frac{x}{x_0} \right). \quad (4-27)$$

This equation is plotted in Fig. (4-20) and also is in good agreement with the measured data.

#### 4.4 TWO WAVES: THE DOWNSTREAM AND THE UPSTREAM TRAVELLING WAVES

In a resonant case the phase velocity at the resonance frequency can be obtained from the cross-spectrum

between two points in the near field. For points close to the jet axis (small  $r$ ), and points away from the jet axis (large  $r$ ). Eqn. (4-5), after some manipulation [see Appendix A and Neuworth (1973)], takes the following forms  $r/d \leq 1.0$ :

$$p \approx 2bk' e^{i\omega_r t} + (a-b) e^{i[\omega_r t - k_1(x-x_0)]}, \quad (4-28a)$$

$r/d > 1.0$ :

$$p \approx 2ak' e^{i\omega_r t} + (b-a) e^{i[\omega_r t + k_2 \cdot (\vec{r} - \vec{r}_0)]}, \quad (4-28b)$$

where

$$k' = \cos. \left\{ \frac{k_1 + k_2 x}{2} (x_0 - x) + \frac{k_2 r}{2} (r_0 - r) \right\}.$$

The first term on the right hand side of Eqn. (4-28) is a standing wave. The second term is a downstream travelling wave in Eqn. (4-28a) and an upstream travelling wave in Eqn. (4-28b). Therefore, at resonance, the downstream phase velocity  $C_1(f_r)$  can be calculated from the

phase difference between two microphones placed near the jet axis (small  $r$ ). Also, the upstream phase velocity  $C_2(f_r)$  can be calculated from two microphones placed in the near field further away from the jet axis [see Fig. (4-3)].

The phase velocity at the resonance frequency  $C(f_r)$  and the broad-band convection velocity  $C$  for the two waves are plotted in Fig. (4-21) as a function of the distance  $x$  along the jet axis. These velocities were calculated as follows:

1. The downstream phase velocity  $C_1(f_r)$  was calculated from Eqn. (3-1) using the phase angle  $\psi(f_r)$  between two points closest to the outer edge of the shear layer (along a line extending from the nozzle lip and making an angle of  $12^\circ$  with the  $x$ -axis).

2. The phase velocity of the upstream wave  $C_2(f_r)$  at an angle of  $\Theta_a$  to the jet axis was calculated from the relation

$$C_{2,ij}(f_r) = 2\pi f_r \frac{\vec{r}_{i,j} \cdot \hat{\Theta}_a}{\gamma_{i,j}(f_r)} \quad i,j = I, II, \dots, O, 1, \dots$$

The angle  $\theta_a$  is given by Fig. (4-12) for each plate location  $x_0/d$ .

3. The downstream and upstream convection velocities  $C_1$  and  $C_2$  were calculated from the correlations' optimum time delays  $\tau^{(1)}$  and  $\tau^{(2)}$  respectively.

The figure indicates that the upstream wave is propagating in a direction  $\hat{\theta}_a$  with the speed of sound. However, the downstream wave is travelling with a speed equal to .62 U. This is the convection velocity of the large scale structures as measured in the free jet and reported in Refs. 19 and 20. Furthermore, Neuworth (1973) estimates of the convecting speed of large eddies in a high speed impinging jet, obtained from a frame by frame analysis of movie film, is in excellent agreement with the present data as shown in the figure. One notices, also, that  $C_1(f_r)$  agrees well with the value .62 U, indicating that large coherent eddies play the main role in the resonance phenomenon.

The conclusive experimental data of this chapter exhibits two waves travelling in the near field between the nozzle and the plate. Large coherent structures are convected downstream at a speed equal to 0.62 U. Upstream waves are propagating at an angle  $\theta_a$  to the jet axis with

the speed of sound  $a_0$ . Furthermore, the simple model of Sec. 4.2 assumed a boundary condition of zero phase difference between the two waves at the plate. The agreement between the measured optimum time delays  $\tau^{(2)}$  and  $\tau^{(1)}$  and the model implies that the assumed boundary condition is indeed correct. We conclude, therefore, that the upstream wave is truly a reflection from the plate due to the impinging coherent structures.

## CHAPTER 5

### THE PHASE LOCK AND THE COLLECTIVE INTERACTION

The establishment of two waves achieved in Chapter 4 is not, by itself, sufficient to explain the resonance observed in the impinging jet. In order to have self-sustained oscillations and to close the feedback loop, the downstream travelling wave and the upstream propagating wave should be phase locked. The thin shear layer near the nozzle exit is supposed to be the most vulnerable portion of the jet column to external excitations. Therefore, the shear layer, most probably near the nozzle, should always respond to the upstream forcing waves thereby closing the feedback loop. This phase lock has never been established experimentally in the literature: it is the main feature of the first half of this chapter.

#### 5.1 PHASE LOCK BETWEEN THE TWO WAVES AT THE NOZZLE EXIT PLANE

The variations of the phase angle at the resonance

frequency  $\varphi(f_r)$  along the jet axis for both waves are presented in Fig. (5-1). The figure shows the case  $M = .8$ ,  $x_0/d = 4$  where  $f_r = 5506$  Hz, which corresponds to  $(St)_r = .51$ . The variations of  $\varphi(f_r)$  along the downstream traveling wave were determined by placing a series of microphones close to the shear layer's outer edge ( $r/d \approx 1.25$ ). The phase variations from the plate to the nozzle exit plane along the upstream wave were calculated from microphones at  $r/d > 2.5$ . At the plate the two waves have the same phase angle (taken equal to zero), according to the boundary condition (4-9).

The  $\varphi(f_r)$  variations from the nozzle lip to the plate (at  $r_0/d = 1.0$ ) is presented in the figure by the upper curve and the lower curve represents  $\varphi(f_r)$  variations from the plate back to the nozzle exit plane. The phase difference between the two waves at any location  $x$  is, therefore, equal to the vertical distance between the two curves. This is also expressed by Eqn. (4-11) of the model in Sec. 4.2. The first term represents the upper straight line with a slope equal to  $k_1 = \omega_r/C_1$ . The second term represents the lower line with a slope proportional to  $1/C_2$ . The most important result of the figure is that the phase difference between the two waves at the nozzle exit ( $x = 0$ ) is a multiple of  $2\pi$ . This indicates that the upstream propagating wave is in-phase with the

downstream travelling wave at the nozzle exit.

The consistency of the above zero phase difference between the two waves at the nozzle exit was examined for different plate locations and is shown in Fig. (5-2). The positions of the four near field microphones used are shown in Fig. (4-3). Two microphones were placed near the jet (I & II) to measure  $\psi(f_r)$  variations along the downstream travelling wave. The other two microphones (III & IV) were at  $r/d = 2.7$  to measure  $\psi(f_r)$  variations over the upstream propagating wave. For each plate location  $x_0$ , the phase reference point on the plate, which will be called the apparent sound source "S", is determined as follows:

1. The angle between upstream propagation and the jet axis is first calculated by the relation

$$\Theta_a = \cos^{-1} \left\{ a_0 \left[ \frac{d\{\psi_{III,IV}(f)\}}{df} / 2\pi \zeta_{III,IV} \right] \right\}, \quad (5-1)$$

where  $\frac{d\psi_{III,IV}(f)}{df}$  is the constant phase angle slope of the nondispersive upstream wave.

2. Using  $\Theta_a$  from Eqn. (5-1), a series of cross spectrum functions between III and different surface pres-

sure transducers on the plate were evaluated. The apparent sound source "S" is the the location of the transducer which best satisfies the relation

$$2\pi \frac{\vec{\zeta}_{M,S} \cdot \hat{\Theta}_a}{[d\{\zeta_{M,S}(f)\}/df]} = a_0 \quad (5-2)$$

other words, the criteria for choosing "S" on the plate is that acoustic propagation from S to  $\underline{m}$  in a direction making  $\Theta_a$  to the jet axis be given by Eqn. (5-1), [and plotted in Fig. (4-12)].

For the case  $M = .9$  in Fig. (5-2), the apparent sound source satisfying Eqn. (5-2) was found to be

$$r_s/d = 1.0 \quad \text{for} \quad 3.25 < x_0/d < 7.5$$

$$r_s/d = 1.5 \quad \text{for} \quad x_0/d < 3.25$$

The percentage deviation from satisfying condition (5-2) was less than 12% for transducers within one nozzle diameter of the above values. This indicates that the "source" of the upstream propagating waves emanates from a region

on the plate, rather than a point.

The phase variations in Fig. (5-2) for all  $x_0/d$  show the same characteristics as in Fig. (5-1). The phase difference between the two waves at the nozzle exit remains as an integer multiple of  $2\pi$  for all plate locations. This phase lock will prove to be important in understanding the resonance frequency stages, the topic of discussion in the following section.

The results of both figures indicate that the  $2\pi$  phase difference between the two waves, as implied by Powell's (1961) theory on edge tones, takes place at the nozzle lip. This closes the feedback loop which allows for a self-sustained system of oscillations. Furthermore, the results of the conditional sampling technique employed by Petersen (1978) showed that the pressure measured by microphones at the outer edge of the shear layer is  $90^\circ$  out of phase with the cross flow velocity component. It is well known that this phase relation is also the same between the sound wave pressure and the induced particle velocity. Therefore, Bechert and Michel's (1975) in-phase assumption for the cross flow velocity of a shear layer at the separation point of a semi-infinite plate and the velocity induced by external acoustic forcing is supported by the present pressure measurements.

## 5.2 RESONANCE FREQUENCY STAGES

Although the phase difference between the two waves at the nozzle is preserved for different plate locations, the resonance frequency  $f_r$  changes. Figs. (5-3) and (5-4) show the variation of the resonance Strouhal number  $(St)_r = f_r d/U$ , versus the plate location  $x_0/d$  for  $M = .8$  and  $.9$ . In both figures  $(St)_r$  decreases with increasing  $x_0/d$  until it reaches a minimum value [minimum  $(St)_r \approx .5$  and  $.33$  for  $M = .8$  and  $.9$  respectively]. Beyond the minimum, the Strouhal number jumps to a higher value, then decreases again with increasing  $x_0$  and the cycle repeats. The frequency jumps occur over a small, but finite, region of plate locations such as  $4.8 < x_0/d < 5$  and  $6 < x_0/d < 6.5$ .

At  $M = .9$ , a strong augmentation of energy was always observed in the power spectra at the resonance frequency [e.g. Fig. (3-22)]. Moreover, this energy augmentation takes place at a single resonance frequency most of the time, except when the plate is in a frequency jump region as indicated by Fig. (5-4). However, at  $M = .8$ , the resonance peaks in the spectra were not clearly distinguishable for  $x_0/d > 3.5$  (also screech tones were barely audible). This can be explained by the additional frequency content indicated in Fig. (5-3); clearly the energy is

distributed over more than one frequency band. It is believed that the impinging jet at relatively low Mach numbers,  $M < .8$ , is still not in a well established resonance state. This is the reason for choosing the case of  $M = .9$  to study most of the details of the resonance phenomenon in the present investigation.

The resonance frequency stages in Figs. (5-3) and (5-4) are typical of self-sustained oscillations problems, such as flow over cavities [Refs. 10, 13, and 14] and edge tones [Ref. 43]. Two common elements are used in the empirical or semi-empirical resonance frequency prediction techniques. A phase reference is assigned and an integer is used to fit the measured frequency at different frequency stages. In each method, the question of when the frequency jumps occur has not been answered. Sarohia's (1975) prediction of experimentally observed frequencies is based on a prescribed phase difference equal to  $\pi$  between separation and impingement. This is only one branch of the feedback loop which means that his prediction completely neglects upstream acoustic feedback. Rossiter's (1964) and Block's (1976) models include the effect of an acoustic feedback. However, their formulae require an empirical constant, which is in effect a phase difference between the feedback acoustic wave and the shear layer disturbances near the upstream separation, as

will be shown later.

A zero phase difference between the two waves at the nozzle exit, as established by the present data, implies that the number of wave-lengths along the feedback loop has to be an integer. The feedback loop constitutes a circuit from the nozzle to the plate, returning again back to the nozzle. The forward branch from the nozzle to the plate is due to large scale structures, while the upstream acoustic waves form the rearward branch from the plate to the nozzle. The total number of periods at any time over the loop is given by

$$N = \frac{x_0}{\lambda_1(f_r)} + \frac{x_0}{\lambda_{2_x}(f_r)}, \quad (5-3)$$

where

$$\lambda_1(f_r) = \frac{C_1(f_r)}{f_r}, \quad \text{and}$$

$$\lambda_{2_x}(f_r) = \frac{C_2(f_r)/\cos. \theta_a}{f_r},$$

are the wavelengths of the two waves along the jet axis. Eqn. (5-3) is, in fact, Eqn. (4-10) of the model, with

$\Psi_0$  substituted by  $2\pi N$ .

Fig. (5-4) can be replotted in terms of  $N$  versus the plate location  $x_0/d$ . This is shown in Fig. (5-5) along with the conventional plot of  $(St)_r$  versus  $x_0/d$ . The figure indicates that the integral number of periods over the feedback loop is constant over each frequency stage. For  $x_0/d < 3$ , near field measurements were not possible because of interference between the microphones, its mountings, and the plate. Eqn. (5-3) is used to calculate  $N$  for  $x_0/d < 3$  using the values

$$C_1(f_r) = .62 U$$

$$C_2(f_r) = a_0$$

$$\Theta_a = 35^\circ \quad \text{from Fig. (4-12)}$$

and  $f_r$  is measured from surface pressure transducers. The calculated values of  $N$  follow the same pattern of the measured data and correspond to stage  $N = 2$  in the figure.

The frequency stages observed in flows with self-sustained oscillations has constituted a puzzling problem for some time. However, with the knowledge of the convection speeds of the two waves, the angle of propagation of the upstream wave, and the phase lock, an understanding of the frequency stages emerges from the results

of Fig. (5-5). As the nozzle-to-plate separation distance increases, the wavelength of both waves increases to preserve the phase lock at the nozzle exit. This results in a decrease in frequency since the phase velocity is almost constant. A minimum frequency that corresponds to a long wave length is reached, beyond which large scale structures cannot maintain their coherence. The flow jumps to a higher frequency at which the number of waves along the loop increases by one. Then the frequency decreases with increasing separation distance and the cycle is repeated.

#### 5.2.1 Prediction of Plate Locations at the Frequency Jumps

The minimum frequency before the jumps corresponds to  $(St)_r = .33$ . In a free jet, large scale structures are observed to lose their coherence beyond the end of the potential core. The passage frequency of these structures there corresponds to the above minimum Strouhal number before the frequency jumps. This is also in the range of the Strouhal number of the preferred mode of large scale structures as pointed out by Crow and Champagne (1971).

The minimum frequency can, therefore, be used with the phase lock at the nozzle as presented by Eqn. (5-3) to predict plate locations where jumps occur. Eqn.

(5-3) can be written in the form

$$\frac{x_0}{d} = \frac{1}{(St)_r} \frac{N}{\sqrt{K_v} + M \cos. \theta_a}, \quad (5-4a)$$

where  $N = 1, 2, \dots$

Values of  $\theta_a$  are taken from Fig. (4-12),  $K_v = .62$  and  $(St)_r = (St)_r|_{\min} = .33$  at  $M = .9$ . Comparison between the plate locations at which frequency jumps occur, as predicted by Eqn. (5-4a) and as observed from the measured data of Fig. (5-4), is presented in Table (5-1). The predicted values in the second column is in excellent agreement with the measured values in the third column.

freq. stage N	$x_0/d$	
	from Eqn. (5-4a)	from Fig. (5-4)
1	1.25	
2	2.50	2.4
3	3.74	3.75
4	4.99	4.8 - 5.0
5	6.24	6.0 - 6.5
6	7.49	7.5

Table (5-1) Relative distance between nozzle exit and plate at the frequency jumps.

### 5.2.2 Jet Behaviour at a Frequency Jump

At a frequency jump more than one resonance peak appears in the power spectrum of either the near field or surface pressure signals. For example, the spectra of Fig.(4-3) shows two peaks representing the jump at  $x_0/d=5$  in Fig.(5-4).

The frequency jump phenomenon is studied in Fig.(5-6). The long time average cross-spectrum shows two peaks at the two frequencies that correspond to the jump at  $x_0/d=2.35$ . When the spectrum of the same signals was calculated over short time intervals, each peak intermittently appeared alone. This indicates that during a frequency jump the flow switches from one resonance mode to another, and this happens intermittently.

The mechanism by which the flow field switches its frequency during a frequency jump, could possibly be the same as the one observed in the low Reynolds number water jet. There the frequency at which vortex rings hit the plate intermittently changed as the flow jumped from Pattern 1 [Fig. (3-1)] to Pattern 2 [Fig, (3-2)] through "pairing".

### 5.2.3 The Disappearance of Resonance

The resonance disappeared at  $x_0/d < 2$ . According to Fig.(4-12), the upstream propagating waves at these small plate to nozzle distances diverge away from the jet axis. These locations correspond to a minimum frequency stage of  $N_{\min} = 2$  as shown in Fig.(5-5).

At large plate to nozzle distances ( $x_0/d > 6$ ), large scale structures would lose their coherence before they impinge on the plate. The resonance, consequently, becomes weaker and then disappears. Furthermore, an oncoming fully developed turbulent flow would refract a wide band acoustic wave away from the jet axis, further weakening the feedback to the nozzle exit. This is shown in the plots of pressure fluctuations at the nozzle exit plane versus  $x_0/d$  in Fig. (5-7). The pressure signals, especially at **IV**, are dominated by the upstream acoustic wave as was shown earlier in Ch. 4. The pressure levels are low for  $x_0/d > 6.5$  near the disappearance of resonance.

### 5.2.4 Comparison With Cavity Frequency

Eqn. (5-4a) can be rewritten in the form

$$\frac{f_r X_0}{U} = \frac{N}{1/k_v + M \cos. \Theta_a}, \quad (5-4b)$$

$N = 1, 2, \dots$

The above equation is similar to Rossiter's (1964) equation for cavity frequency which takes the form

$$\frac{f_r X_0}{U} = \frac{N - \gamma'}{1/k_v + M},$$

with  $\gamma'$  an empirical constant. In Eqn. (5-4b) the empirical constant is absent owing to the zero phase difference between the two waves at the upstream shear layer separation plane.

In Figs. (5-8) and (5-9) the cavity frequency measured by several investigators and reported by Tam and Block (1978) is compared with Eqn. (5-4b). In the theoretical model of Tam and Block (1978), the upstream acoustic waves reflect from both the bottom and the upstream wall of the cavity. However, they argued that waves reflecting off the upstream wall are the strongest in forcing the instability of the shear layer. Therefore,  $\Theta_a$  is taken equal to zero in Eqn. (5-4b) since the present model considers the feedback to occur through the ambient

region (the stationary region outside of the jet) corresponding to the inside of the cavity. Eqn. (5-4) shows a surprisingly good overall agreement with the measured data.

If the shear layer of the jet is approximated by a two-dimensional one, half of the impinging jet configuration would resemble flow over a cavity of infinite depth. This possibly explains why Eqn. (5-4b) appears as an upper limit to the measured data in Figs. (5-8) and (5-9).

### 5.3 THE COLLECTIVE INTERACTION

So far the present study has revealed the presence of two waves in the near field of the impinging jet. The upstream acoustic waves were found to be phase locked with the downstream travelling hydrodynamic waves induced by the convected coherent eddies. These findings close the feedback loop. However, a few questions remain to be answered concerning the coupling between the upstream acoustic waves and the shear layer near the nozzle. Do the upstream waves force the initial shear layer instability, are the developed instability waves different from those of the free jet, and how do these instability waves evolve downstream into large coherent structures with a

passage frequency equal to the resonance frequency ? It was logical then to measure the instability frequency near the nozzle for both the free and the impinging jet.

The instability frequency of the free jet was measured from the autocorrelation function of a pressure signal as given by a microphone placed at the nozzle lip. This frequency is plotted for different jet Mach numbers in Fig. (5-12) and is discussed later.

For the impinging jet, two microphones were placed near the nozzle exit. The raw pressure signals are shown in Fig. (5-10). Fig. (5-10a) shows signals for the non-resonant case of  $M = .4$  and  $x_0/d = 4.5$ . A high frequency signal appears immediately downstream of the nozzle exit at  $x/d = .13$ . Farther downstream at  $x/d = .92$ , a low frequency signal appears with the high frequency signal superimposed. The low frequency signal is due to the evolving large scale structures. At resonance Fig. (5-10b) shows that for  $M = .9$  and  $x_0/d = 4.5$ , the high frequency components are superimposed on the resonance frequency signal near the nozzle exit. At the downstream location  $x/d = 1.31$ , the amplitudes of the high frequency signal are substantially reduced.

The power spectra of these signals are shown in Fig.

(5-11) and can provide information about the nature of the high frequency components observed in the pressure signals. A small spectral peak at high frequency appears in the spectrum at  $x/d = .13$  in Fig. (5-11a). The same peak becomes clearer in the spectrum at  $x/d = .92$ . The frequency of this peak is exactly the instability frequency measured in the free jet [see Fig. (5-12)]. At resonance Fig. (5-11b) shows similar high frequency spectral peak, except it is broader. The energy contained in this high frequency peak is understandably much smaller than the resonance frequency energy. One also notices that unlike the non-resonant case of Fig. (5-11a), the energy at high frequency appears to vanish at the downstream location  $x/d = 1.31$ .

The above measurements for different jet Mach numbers are plotted in terms of the Strouhal number in Fig. (5-12). The high frequency signals for both the free jet and the impinging jet are shown to follow a straight line with a slope equal to  $1/2$ . This is in agreement with the linear instability theory of Michalke (1971). The data, thus, indicate that the initial instability frequency of the shear layer appears unchanged by the presence of the plate or the feedback.

The resonance frequency is also shown in Fig.

(5-12). The vertical bars used in the plot does not represent the accuracy of the measurements but rather the range of resonance frequencies in the different frequency stage, as it appears in Figs. (5-3) and (5-4). The figure shows that the resonance frequency is much lower than the instability frequency measured near the nozzle exit. The ratio  $(St)_{in}/(St)_r$  is of the order of, or even larger than 10. The large difference between the two frequencies indicates that the upstream acoustic waves with a frequency  $f_r$  cannot be phase locked with the high frequency initial instability waves  $f_{in}$ .

The mechanism describing the drop in the passage frequency of large eddies in a two-dimensional free shear layer was first reported by Winant and Browand (1974). Pairing between vortex structures reduces the passage frequency by a factor of two and takes place over about one wavelength. It takes at least 3 to 4 pairings then, to reduce the frequency by a factor of 10. Petersen (1978) further reported that the passage frequency in a free jet decreases linearly with downstream distance from the nozzle. This is not true in the impinging jet since the frequency of the pressure signals of Fig. (5-10) dropped sharply over a short distance from the nozzle. Therefore, conventional pairing cannot be adopted to explain the sharp drop from the instability frequency to the resonance

**THIS  
PAGE  
IS  
MISSING  
IN  
ORIGINAL  
DOCUMENT**

one. A new mechanism is needed to explain the situation near the nozzle.

Ho and Huang (1978) observed multiple vortices merging into a single structure when a low frequency driving force is applied to a plane shear layer. Fig. (5-13) shows one of their dye pictures. The flow is from left to right with the higher velocity flow at the bottom. The low-frequency forcing displaces the vortices from their original locations and leads to the formation of an array of vortices in a wavy shear layer. Vortices located in a portion of the shear layer which is convex as seen from the low speed side are unstable and interact together to form a large vortex.

We adopt the term "collective interaction" to describe the phenomenon of multiple merging of coherent structures. The characteristics associated with this phenomenon are a sharp drop in passage frequency and a relatively large shear layer growth. Collective interaction can then be used to explain the frequency drop near the nozzle exit in the impinging jet.

The schematic drawing in Fig. (5-14) can assist in explaining the collective interaction in a high speed impinging jet. Since the jet is asymmetric, only the upper

half will be discussed. The shear layer emerging from the nozzle is pulsating due to periodic forcing from the upstream propagating wave. The shear layer goes through cycles of divergence ( $t = 0, T_r, \dots$ ), and convergence ( $t = T_r/2, 3T_r/2, \dots$ ). At  $t = 0$  the small vortices are unstable with respect to each other, and tend to coalesce into a large vortical structure under the combined effect of their induced field and the mean shear. At  $t = T_r/2$ , these merging vortices accelerate in the curved shear layer and are subject to the stabilizing effect of stretching. The result, as shown at  $t = 3T_r/2$ , is a sharp drop in passage frequency from the instability frequency  $f_{in}$  to the resonance frequency  $f_r$ .

Looking back at Fig. (5-10b) the behavior of the pressure signals can now be explained in the following way: the high frequency signal superimposed on the low frequency one represent the instability vortices convected in a pulsating shear layer. A short distance downstream ( $x/d = 1.31$ ) the high frequency vortices diminish due to the collective interaction. Lau et al. (1972) have related the positive peak of the pressure signal to the passage of the valley between two structures, and the negative peak to the passage of the bulge of the structure. At  $x/d = 1.31$  in Fig. (5-10b), the amplitude of the high frequency waves on the positive parts of the low frequency

---

waves are higher than those on the negative peaks. These characteristics further confirm the collective interaction mechanism, because the convex part of the shear layer towards the low speed side (i.e. the bulge) is less stable. Therefore, the high frequency waves on the bulge decay faster than those on the valley, and the low frequency negative peaks appear smoother than the positive peaks in the figure.

The results of this section indicate that the upstream acoustic wave does not force the initial shear layer instability near the nozzle exit. The forcing acoustic waves merely drive the thin shear layer in phase. Then, and only then, does the wavy shear layer act on the high frequency initial instability waves and collect them into large coherent structures at the resonance frequency.

In conclusion, the feedback loop between the nozzle and the plate is presented in the flow diagram of Fig. (5-15). The large scale coherent structures are convected downstream and impinge on the plate. Waves are generated and propagate upstream with the speed of sound. These waves drive the shear layer near the nozzle. The instability waves undergo collective interaction, while the wavy shear layer rolls into new larger coherent eddies at the resonance frequency.

## 5.4 THE RESPONSE OF THE SHEAR LAYER TO ACOUSTIC EXCITATION

### FROM OUTSIDE OR INSIDE THE JET

The feedback mechanism described in the previous section has evolved from an analysis of measurements taken outside the jet. This does not rule out the possibility of a feedback between the nozzle and the plate from inside the jet column. Wagner (1971) and Neuworth (1973) adopted a model for the resonance based on waves travelling in the jet core, supported by visualizations of standing waves in the jet column. The present investigation does not rule out a feedback within the jet. In fact, a phase lock of  $\pi$  between the acoustic waves propagating inside the jet and outside the jet would be most powerful in driving the shear layer near the nozzle. Unfortunately, measurements inside a high subsonic speed jet are difficult and unreliable. Hussain and Zaman (1977) have shown that the probe itself can trigger an upstream instability mode when inserted in a free shear layer. Neuworth (1973) argued that feedback could even occur due to a small perturbing body as long as it has a stagnation surface within the flow.

In this section a theoretical approach is used to determine the relative importance of acoustic feedback in-

side the jet. The effectiveness of acoustic waves in triggering the shear layer instability near the nozzle from outside the jet (case-A) is compared to that from inside the jet core (case-B). The two cases (A and B) are shown schematically in Fig. (5-16).

For simplicity, consider plane acoustic waves propagating in a two-dimensional flow field on both sides of a zero thickness shear layer. A zero thickness shear layer is justified since the acoustic wavelength is much larger than the anticipated shear layer thickness. Quantitative correction factors due to finite shear layer thickness and cylindrical flow field are reported by Amiet (1977). These corrections, however, do not alter the physical picture of the present analysis.

The approach is based on the theoretical work of Ribner (1957). The induced cross flow velocity at the interface  $V_t$  due to the incident acoustic waves pressure  $p_i$ , is a measure of the forcing of shear layer instability. For the same incident acoustic wave pressure, the ratio of cross flow velocities in the two cases is

$$\frac{V_{tA}}{V_{tB}} = \frac{|T_A|}{|T_B|} \frac{\sin \theta_{LA}}{\sin \theta_{LB}}, \quad (5-5)$$

where

$$\sin \theta_{tA} = \frac{\sin \theta_i}{1 - M \sin \theta_i} ,$$

and

$$\sin \theta_{tB} = \frac{\sin \theta_i}{1 + M \sin \theta_i} .$$

$|\vec{T}|$  and  $\theta_t$  are the transmitted acoustic wave amplitude and angle to the interface. The amplitude  $|\vec{T}|$  takes the form

$$|\vec{T}|_{y=0} = \frac{2 \sin 2\theta_i}{\sin 2\theta_i + \sin 2\theta_t} .$$

The ratio  $v_{tA}/v_{tB}$  is plotted for a range of incidence angles  $0^\circ < \theta_i < 90^\circ$  in Fig. (5-16). This is the range of concern here since it represents only upstream acoustic propagating waves. At normal incidence ( $\theta_i = 90^\circ$ )  $v_{tA}/v_{tB}$  is unity. As  $\theta_i$  decreases, the ratio increases sharply to infinity when  $\theta_i$  is equal to a critical angle  $\theta_c$ . Below  $\theta_c$ , a complete sound reflection occurs in case-B and the shear layer acts as a sound hard boundary. For a typical resonant case of  $M = .9$ , the critical angle is as high as  $63^\circ$ . Thus, for a considerable range of incidence angle, the shear layer is far more vulnerable to upstream acoustic waves from outside the jet, especially at high Mach

---

number.

The above simple results suggest that the present measurements outside the jet are indeed sufficient to provide a complete picture of the feedback mechanism.

## CHAPTER 6

### FAR FIELD NOISE OF THE IMPINGING JET

The far field noise of the impinging jet for both resonant and nonresonant cases is investigated in this chapter. Powell (1960) suggested that the rigid surface plays a passive role in the noise radiation. The noise is generated by the flow and is being reflected by the plate. A mirror image of the flow could replace the plate in generating far field noise. Therefore, in his model, the flow and the plate have equal shares in the noise radiation. Preisser (1979) measured the noise spectra of the impinging jet. The spectral peaks at  $(St) = .3$ , were higher in magnitude than those in the spectra of a free jet. He suggested that the presence of the plate had enhanced the noise generated by the large scale structures. Most of the noise is reported to be generated in the stagnation region near the plate. However, Preisser could not determine whether the noise was generated in the jet and reflected by the plate or whether it was generated due to

the impinging of the jet on the plate. Pan (1975) proposed a theoretical method based on correlation techniques to separate the turbulent flow contributions to the far field noise from those due to surface pressure fluctuations. He expressed the need for near field measurements as well as surface pressure measurements to determine the exact role of the plate in the generation of noise.

The present far field measurements are coupled with near field and surface pressure measurements to determine the mechanism of noise generation and its radiation path. The far field measurements are taken from a microphone at  $\Theta = 89^\circ$  i.e., approximately in a plane perpendicular to the jet axis at the nozzle exit. Shielding of the plate prevented reliable measurements at smaller angles, while that of the nozzle assembly prevented large angle measurements.

Fig.(6-1) shows the coordinate system that will be used.  $\xi$  is used here as a composite coordinate that extends from the nozzle along the jet axis to the stagnation point on the plate, and then radially on the plate. This is approximately the path of induced disturbances in the near field and on the plate of an impinging vortical ring [Ref. 33]. Hence,  $\xi$  satisfies the following relations:

$$\begin{aligned}\xi &= x && \text{in the near field,} \\ \xi &= x_0 + (r_0 - r_s) && \text{on the plate.}\end{aligned}$$

In the figure  $z$  is the distance between any point in the near field, or on the plate, and the far field microphone.

#### 6.1 THE ROLE OF LARGE SCALE STRUCTURES IN NOISE GENERATION

The overall far field sound pressure level  $p'^2$ , measured in decibels, are shown in Fig. (6-2) as a function of the plate location  $x_0/d$  for  $M = .9$ . The value of  $p'^2$  fluctuates around 135dB and then falls off to 110dB for  $x_0/d > 6.5$ . The variations of  $p'^2$  with jet Mach number  $M$  are shown in Fig. (6-3) for  $x_0/d = 4.5$ .  $p'^2$  increases proportionally to  $M^8$  as in a free jet. The sound pressure level for a free jet at  $M=0.8$  is included and is seen to approximately equal that of the impinging jet. This is in agreement with measurements by Preisser (1979), indicating that at directions perpendicular to the jet axis the noise levels are almost the same for both the free and the impinging jets. However, at large angles, Preisser's measurements do show higher noise levels for the case of an impinging jet indicating that the presence of the plate is felt more in the far field at large angles.

The mechanism of noise radiation is investigated here using the correlation functions between far field, near field, and surface pressure measurements. Fig. (6-4)

shows the correlations between the far field microphone and three near field microphones. Also, the correlation between the far field microphone and a pressure transducer on the plate at  $r_0/d = 1.0$  is presented. The time delay in the figure starts from an offset delay  $\tau_d = 5.625$  msec. in order to present only the dominant features of the correlation functions. A negative optimum peak appears in the correlations with the near field microphones, while a positive one appears in the correlation with the transducer on the plate. The time delay  $\tau^{(i)}$  of the peaks of the correlations with the near field satisfies the inequality

$$\tau_{j,FF}^{(i)} > \lambda_j / a_0 \quad j = I, II, III. \quad (6-2)$$

The above inequality indicates that the time delay between any point in the near field and the far field is longer than the time it takes for direct acoustic radiation between the two. Therefore, the possibility of an acoustic path from the near field directly to the far field is excluded.

For different jet Mach numbers and plate locations  $x_0/d$ , the following relations were always true:

$$\left. \begin{aligned} \tau_{I,FF}^{(i)} &= (\tau_{I,II}^{(i)} + \tau_{II,III}^{(i)} + \tau_{III,2}^{(i)}) + \tau_{2,FF} \\ \tau_{II,FF}^{(i)} &= (\tau_{II,III}^{(i)} + \tau_{III,2}^{(i)}) + \tau_{2,FF} \\ \tau_{III,FF}^{(i)} &= (\tau_{III,2}^{(i)}) + \tau_{2,FF} \end{aligned} \right\} (6-3)$$

$$\tau_{2,FF} = \lambda_2 / a_0. \quad (6-4)$$

The terms between brackets are the optimum time delays of peak (1) in the correlations of Fig. (4-16) corresponding to the downstream convection of large scale structures. Eqn. (6-3), therefore, indicates that the time delay between any point in the near field and the far field is equal to the summation of near field time delays up to point 2 on the plate, plus the time delay between point 2 and the far field. Moreover Eqn. (6-4) shows that the time delay between point 2 (in the region where large scale structures impinge on the plate) and the far field corresponds to direct acoustic radiation.

According to Eqns. (6-3) the role of the plate as a reflector of sound generated by the flow as indicated by Powell's (1960) model is incorrect. The time delay terms in brackets in Eqn. (6-3) should correspond to a convection velocity that is equal to the speed of sound in order for Powell's model to be correct. However, these time delays correspond to  $.62 U$ , far below the speed of sound  $a_0$  (e.g., at  $M = .8$ ,  $.62U \approx .5a_0$ ).

The results of the experimental data as indicated in Eqns. (6-3) and (6-4) explain the noise generation and its radiation path. The large scale structures interacting with the plate play an important role in the genera-

tion of noise. The noise does not radiate directly from the downstream convected large coherent structures, but rather as these structures impinge on the plate. That is why the surface and far field measurements of Preisser (1979) indicated a strong apparent noise-producing region within one jet diameter of the stagnation point on the plate.

Petersen (unpublished) cross correlated signals from microphones in the near and far fields of a free jet. The time delays of the correlation peaks indicated that pressure fluctuations propagate down the jet column and radiate sound from a compact acoustic source region near the end of the potential core. However, the propagation speed of the pressure fluctuations in the near field was high (0.88U). Since Michalke's (1971) theory indicates that for small amplitude disturbances long waves travel faster than short waves, Petersen suggested the possibility that hydrodynamic disturbances relevant to the noise production may be fast moving long waves. Except for this questionable high convection velocity, it is interesting to note that his model for the noise radiated from a free jet is in a sense similar to ours. The noise seems to radiate from near the end of the potential core where pairing between large structures usually takes place and somehow resembles, the impingement of large structures on the

plate in our case.

The peak (1) in the correlation functions between the near and far field microphones is shown in the figure to be negative, while it is positive in the correlation between the far field and the surface signals. With reference to Fig. (6-4), the following explanation of this phenomenon is offered. Consider a frame of reference moving downstream with the large scale structures. A large eddy at I, for example, would be stationary with a flow convected over it with velocity  $C_1$  (from right to left). The flow accelerates as it moves over the top of the eddy, while its pressure drops according to Bernoulli equation. A microphone at I would then record a negative pressure disturbance. This is supported by the near field measurements of Lau, et al (1972), who showed that the negative pressure disturbance corresponds to the passage of a "bulge" in the shear layer. When this eddy impinges downstream on the plate, a positive pressure disturbance is recorded at 2 and radiated to the far field. The microphone in the far field measures the positive disturbance and, accordingly, a positive peak appears in the correlation with the plate  $R_{2,FF}$ . On the other hand, the same positive disturbance at FF has been measured earlier as a negative one at I, resulting in a negative peak in  $R_{I,FF}$ .

A second peak appears in the figure and is denoted by (ii). In the correlations between FF and other more distant downstream locations (II and III), peaks (i) and (ii) move towards each other and ultimately come into coincidence in the correlation with the plate  $R_{2,FF}$ . The time delay of the second peak  $\tau^{(ii)}$  was found to satisfy the following relation

$$\tau_{j,FF}^{(i)} - \tau_{j,FF}^{(ii)} = -\tau_{j,2}^{(2)} \quad j = I, II; III \text{ and } 2 .$$

..... (6-2)

The right hand side of Eqn. (6-5) is the time delay of peak (2) in Fig. (4-16), which corresponds to the upstream acoustic propagation. Peak (ii) in the correlation functions of Fig. (6-4) can, therefore, be explained as follows: as the large scale structures impinge on the plate, acoustic waves are not only radiated to the far field FF, but also to I on account of the near field upstream waves. While a peak (i) in  $R_{I,FF}$  is due to the path from I to 2 to FF, peak (ii) corresponds to the same path, minus the upstream propagation from 2 to I. So as I moves downstream (to II and III), the difference between the time delays of the two peaks decreases due to the shorter upstream propagation distance. When I reaches the plate, the two peaks merge into one. It should be mentioned here that peak (ii) does not represent direct radia-

tion from the large scale structures to the far field. The radiation mechanism corresponding to the measured  $\tau^{(i)}$  and  $\tau^{(ii)}$  will be further confirmed later by comparison with a model based on Eqns. (6-3), (6-4) and (6-5).

#### 6.1.1 Major Noise-Production Region on the Plate

The correlation functions between the far field microphone and the pressure transducers on the plate are plotted in Fig. (6-5). Correlations with points in the developed wall jet region are too weak and, therefore, are not presented. The plots are presented for time delays larger than 5.781 msec., since no significant correlation levels are observed before that. The level of the correlation peak decreases, and the width slightly increases with distance from the stagnation point on the plate. The increase in width is indicative of the stretching of large vortices during and after impingement. Based on the distance to the far field microphone, and the speed of sound  $a_0$ , the time delays of these peaks do not correspond to direct acoustic radiation except for point 2. Furthermore, the optimum time delay at any point on the plate satisfies the relation

$$\tau = \frac{z_s}{a_0} + \frac{r_{02} - r_0}{c} \quad (\text{on the plate}) \quad (6-6)$$

where  $C$  is the eddy convection velocity along the plate, presented earlier in Fig. (3-26). As seen from Eqn. (6-6), the noise radiates from the impinging region around  $r_0/d = .$  on the plate (represented by point 2). At points outside that region, the time delay differs by an amount corresponding to the convection of large eddies from point 2 to that point.

The large correlation coefficient in  $R_{0,FF}(\tau)$  of Fig. (6-5) is not due only to high surface pressure fluctuations at  $r_0/d = 0$ , since the same was observed for small  $x_0/d$ , where surface pressure fluctuations at the stagnation point were low. In order to explain the high level peak in  $R_{0,FF}(\tau)$ , one should take into consideration that large cross-correlation coefficients not only imply phase-related signals, but also overlapping spectral contents. These results further support our earlier observation [see Fig. (3-21)] that the induced signal at  $r_0=0$  depicts the gross features of the impinging vortical structures. Therefore, it is not surprising that this particular point is strongly correlated with the far field. We conclude from Fig. (6.5) and Eqn. (6-6) that the inner impinging region is the major noise source on the plate, in agreement with Preisser (1979).

### 6.1.2 A Model for the Noise Generated by Large Coherent Impinging Structures

The behavior of the correlations of the far field microphone with both the near field microphones and surface pressure transducers can be explained by the sketch of Fig. (6-6). The noise is mainly generated by the impingement of the large scale structures. The impinging region on the plate is represented by the apparent sound source "S". "S" has been identified for different plate locations in Chapter 5, and was found in most cases to lie near  $r_0/d = 1$ . After impingement, the large eddies convect along the plate, while a wave propagates upstream in the near field.

Eqns. (6-3), (6-4) and (6-6) can be reduced to the nondimensional equation

$$\frac{\tau^{(ii)} a_0}{\lambda_s} = 1 + \frac{\xi_s - \xi}{\lambda_s} \frac{1}{MK_v}, \quad (6-7)$$

where the composite coordinate of Eqn. (6-1) is used. Implicit in Eqn. (6-7) is the assumption of equal convection speeds in the near field and along the plate. This is justified since the question is to be examined using

surface measurements near the impinging region on the plate where the eddy convection velocity has the average value  $0.62U$  [see Fig. (3-26)].

The unit coefficient appearing as the first term in the right hand side of Eqn. (6-7) represents the direct acoustic radiation from "S". The second term is due to the convection of large eddies to or from "S".

The time delay of the second peak  $\tau^{(ii)}$  [Fig. (6-4)] can be derived from Eqn. (6-5) and put in the nondimensional form

$$\frac{\tau^{(ii)} a_0}{\lambda_s} = 1 - \frac{x_0 - x}{\lambda_s} \cos. \Theta_a \quad (\text{near field only}). (6-8)$$

The second term on the right hand side is due to the near field upstream wave propagating at an angle  $\Theta_a$  to the jet axis.

Eqns. (6-7) and (6-8) are compared with the measured data in Fig. (6-7). The cases of  $x_0/d = 5.5$  and  $7$  at  $M = .8$  are shown. A value of  $\Theta_a = 27^\circ$  is used for both cases as given by Fig. (4-12). The apparent sound source is at  $r_0/d = 1.0$  on the plate. Measured data points at

$(\frac{f_a - f}{2n}) = .015, 0, -.0055 \text{ and } -.012$  correspond to correlation functions with points on the plate. It is evident that the measured data are in excellent agreement with Eqns. (6-7) and (6-8).

The results discussed so far indicate that the noise is generated by the impingement of large scale structures on the plate. Accordingly, the power spectrum of the far field signal is expected to peak at a low frequency band that corresponds to the passage frequency of these structures. The far field signals were digitized at a very high sampling rate to retain any possible high frequency content. A presentation of a "surprising behavior" of the power spectra is given in the next section.

## 6.2 HIGH-FREQUENCY FAR FIELD NOISE RADIATION

Fig.(6-8) shows two normalized power spectra  $G(f)$  for  $x_0/d = 4.5$ . The spectra were evaluated from data that were digitized at a fast sampling rate of 4.7 microsec. The non-resonant case at  $M=.4$  is plotted in Fig.(6-8a). The spectrum has a peak at  $f=2000$  Hz corresponding to  $St=.33$ . This value falls within the frequency range of the large scale structures, a fact which supports the noise radiation mechanism discussed earlier. However, a considerable amount of energy is contained at high fre-

quencies, as indicated by the second peak around 25 KHz. A sharp spectral peak also appears at  $f=17.7$  KHz this being exactly the instability frequency measured at the nozzle lip (Sec. 5.3).

A similar behaviour is shown in Fig.(6-8b) for  $M=.9$ . The high frequency peak is now much smaller than the low frequency peak. This is not unexpected since in this resonant case, most of the energy is concentrated at the resonance frequency [  $(St)_r=.35$  ], a point which will be discussed later. Note that a spectral peak also appears at the resonance frequency's first harmonic ( $2f_r$ ).

It was shown earlier that the frequency of the waves in the shear layer drops sharply over a short distance from the nozzle due to the collective interaction. As a result, large structures convect downstream and impinge on the plate, radiating sound to the far field. The following questions may then be raised: From which location does the high frequency noise in the measured spectra originate ? How does it radiate ? It seems reasonable to look for high frequency sound radiators close to the nozzle exit, and to expect a different sound path from the one due to the low-frequency large-scale structures discussed in the previous section. Correlations between the far field microphone and near field microphones placed

---

along the outer edge of the shear layer and near the nozzle exit were used to investigate the high frequency noise radiation.

An example of the correlation with a near field microphone at  $x/d=.92$  for the case of  $M=.4$  and  $x_0/d=4.5$  is plotted in part (a) of Fig(6-9). A broad negative peak similar to peak (i) in the correlation functions of Fig.(6-4) is shown. The time delay of this peak satisfies Eqn.(6-7), thereby indicating that it is associated with the noise generated by the impingement of large scale structures on the plate. Peak (ii) does not appear, however, because of the weak feedback from the plate for such a low jet speed. A peak denoted by (iii) emerges at an earlier time delay. The narrow width of this peak indicates a correlation between high frequency events.

To ensure that the above correlation peak corresponds to the radiated high frequency noise, the pressure signals were passed through a digital high-pass filter. The low frequency cutoff frequency of the filter was chosen to be the 8 KHz frequency of the valley between the two spectral peaks in Fig.(6-8). The correlation between the filtered signals is shown in part (b) of Fig.(6-9). Although the broad peak(i) disappeared, peak(iii) due to the high frequency components of the signals is retained.

Peak (iii) could not be identified in correlations with farther downstream microphones in the near field. This indicates that high frequency noise is generated mainly near the nozzle exit, before collective interaction takes place. The region of high frequency fluctuations in the shear layer gets smaller with strong feedback at high jet speeds [ Fig.(5-11) ]. Hence a relatively small high frequency spectral peak is observed at  $M=.9$  in comparison to the case  $M=.4$  of Fig. (6-8).

The noise radiation path can be determined from the time delay of peak (iii). This is plotted in Fig. (6-10) in the nondimensional form  $\lambda/a_0 \tau^{(iii)}$  where  $\lambda$  is the distance between the near field and the far field microphones. Cases  $M = .3, .4,$  and  $.5$  are shown. The data collapse onto a straight line at  $\lambda/a_0 \tau^{(iii)} = 1.0$ , indicating direct high frequency acoustic radiation to the far field.

Note that at  $M = .5$ , only radiation from I (next to the nozzle exit) is detected and shown in Fig. (6-8) This corresponds to the fact that high frequency radiation is restricted to shorter distances from the nozzle exit when the jet speed is increased. At higher subsonic jet speeds resonance dominated the correlations. When the prewhitening technique was used, a peak always appeared at a time

delay corresponding to direct noise radiation. However, the level of this peak was low and within the correlation levels of the noise in the signals. As expected, this is due to the low energy content of the high frequency spectral peak as shown in Fig. (6-8b) for  $M = .9$ . Consequently, data points at high Mach numbers were not plotted in Fig. (6-10).

A literature survey did not reveal any previous evidence for the presence of two peaks in the far field spectra for either a free jet or an impinging jet. Preisser's (1979) impinging jet has a thick initial shear layer due to the use of a long nozzle. Since the frequency of the instability waves scales with the shear layer thickness at the nozzle exit, high frequency noise radiators are expected to be substantially reduced in his jet. Accordingly, no high frequency peaks are observed in the far field spectra. On the other hand, the spectra measured in the far field of a free jet by Lush (1970) and Ahuja & Bushell (1973) exhibit a broad peak. The frequency of the peak increases with angle to the jet axis, at which the far field measurements are taken. The overall spectra are fairly broad due to the random character of the whole turbulent flow. It is felt that with the presence of the plate, the flow is more organized as seen from the far field. High frequency radiators are restricted to a short

distance near the nozzle by the collective interaction, while downstream, orderly structures dominate and radiate low frequency noise when they impinge on the plate.

Tam (1971) observed from shadowgraph pictures that strong directional acoustic waves are emitted from the shear layer close to the exit of a supersonic free jet. Furthermore, he stated that "in a rather puzzling manner these waves seem to exist only in a limited region of space downstream of the nozzle". Tam developed a theory about the generation mechanism of these waves, based on the instability of the shear layer close to the nozzle. These observations and the corresponding theory are in good agreement with the two concepts presented in our study, namely, the high frequency radiation by the instability waves near the nozzle exit and the collective interaction phenomenon.

In conclusion, Fig. (6-11) may help in explaining the mechanism of far field noise radiation for an impinging jet. Based on measurements at approximately  $90^\circ$  to the jet axis, the far field noise measured is a superposition of low frequency and high frequency components. The low frequency noise is radiated from the plate by the impinging large coherent structures. The high frequency noise radiates directly from the shear layer near the nozzle exit.

---

CHAPTER 7  
CONCLUDING REMARKS

The present experimental investigation has successfully introduced several important concepts concerning both the feedback mechanism of a resonant impinging jet and the far field noise generated by jet impingement in general.

7.1 THE FEEDBACK MECHANISM

The feedback loop between the nozzle and the plate consists of two branches: a downstream travelling wave with a speed  $.62U$  due to the convected large coherent structures, and an upstream wave propagating with the speed of sound of the quiescent medium in a direction inclined at an angle  $\theta_a$  to the jet axis.

A phase lock necessary for self-sustained oscillations is established between the two waves at the nozzle exit. Pressure measurements [Figs. (5-1) and (5-2)] have

indicated that the two waves are in-phase at the nozzle exit plane during resonance. The phase lock led to a clear understanding of the resonance frequency stages, events which are also observed in cavity and edge tones. The number of resonant periods along the entire feedback loop is an integer  $N$  and is preserved during each stage [Fig. (5-5)]. The quantum frequency jump between stages takes place through a quantum unit change in  $N$ .

It was felt at the beginning that the upstream acoustic waves would force the initial shear layer instability near the nozzle. Instead, measurements near the nozzle exit have substantiated the idea that the acoustic forcing resulted in pulsation of the thin shear layer. This pulsation forced a coherent merging of small vortices at the initial instability frequency into large vortices at the resonance frequency. The phenomenon is named "collective interaction", and its presence is further supported by similar observations in forced two-dimensional free shear layers by Ho and Huang (1978).

A simple mathematical model was presented to explain the characteristic behavior of measured correlation functions in a field with two counter-propagating waves. The model provided evidence that the upstream wave is generated by the incidence of the downstream travelling vortices

on the plate.

The analysis of the resonance phenomenon in the present study was based on near field measurements which were taken outside the jet column. The resulting picture includes forcing of the shear layer by the acoustic waves from the ambient side. The model of Neuworth (1973) is based on acoustic feedback from within the jet core, but unfortunately no reliable measurement could be made inside a high speed jet. However, the mathematical analysis in Sec. 5.4 showed that the thin shear layer is more susceptible to upstream acoustic forcing from outside the jet than from inside.

## 7.2 THE MECHANISM OF NOISE GENERATION

The far field noise for a wide range of impinging jet speeds was investigated. Measurements were taken at  $90^\circ$  to the jet axis at the nozzle exit plane. Surprisingly, the far field spectra not only showed a low frequency peak but also a high frequency one [Fig. (6-8)]. Cross-correlations between the far field and the near field suggested that the noise corresponding to the two peaks are generated by two different mechanisms, and propagate along two different paths. The low frequency noise is mainly generated by the impingement of large scale

structures on the plate near  $r_0/d=1$ . The high frequency noise radiates directly from the vicinity of the nozzle exit. This noise is produced by the high frequency instability waves in the thin shear layer near the nozzle.

It is felt that the success in localizing the above regions of high and low frequency noise radiation is due to (i) the collective interaction which confines high frequency noise radiators to a region near the nozzle exit and (ii) the presence of the plate which leads to feedback and vorticity stretching, thereby enhancing large scale eddies. The impingement of these eddies on the plate generates low frequency noise that is radiated to the far field.

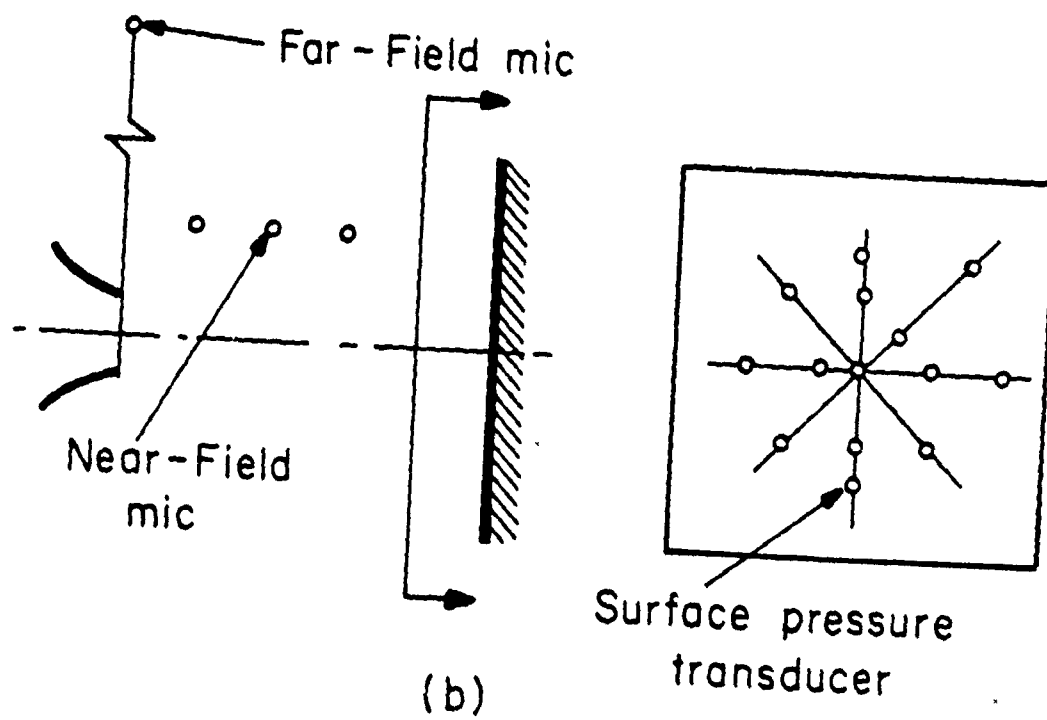
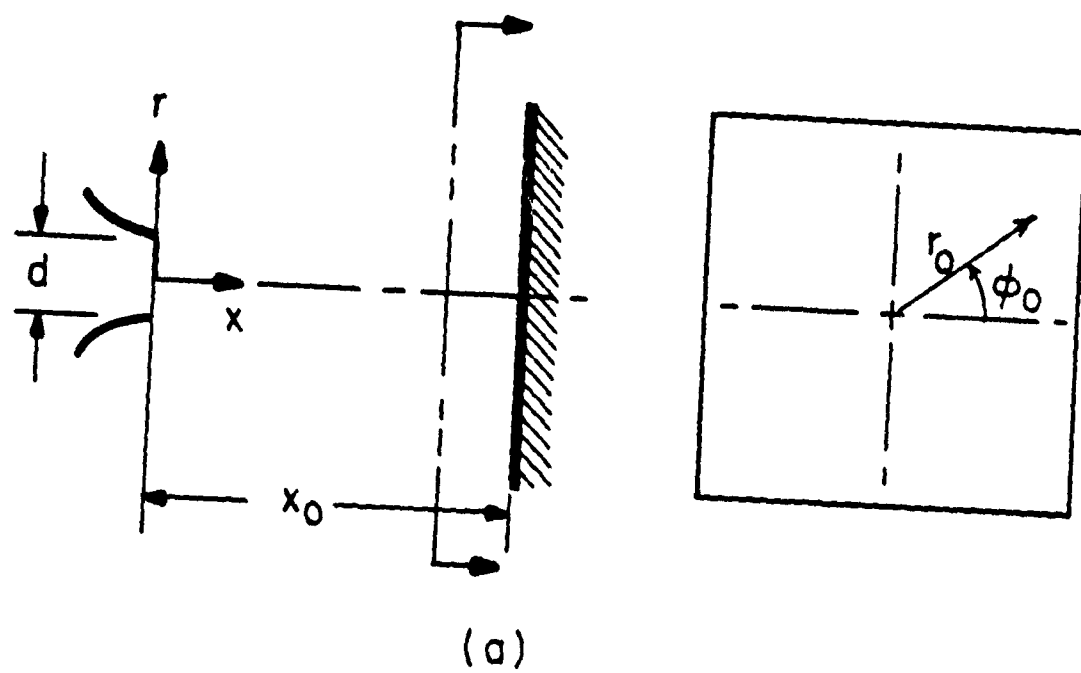


Fig. (1-1) (a) Coordinate System, (b) Schematic Diagram of Pressure Transducers.

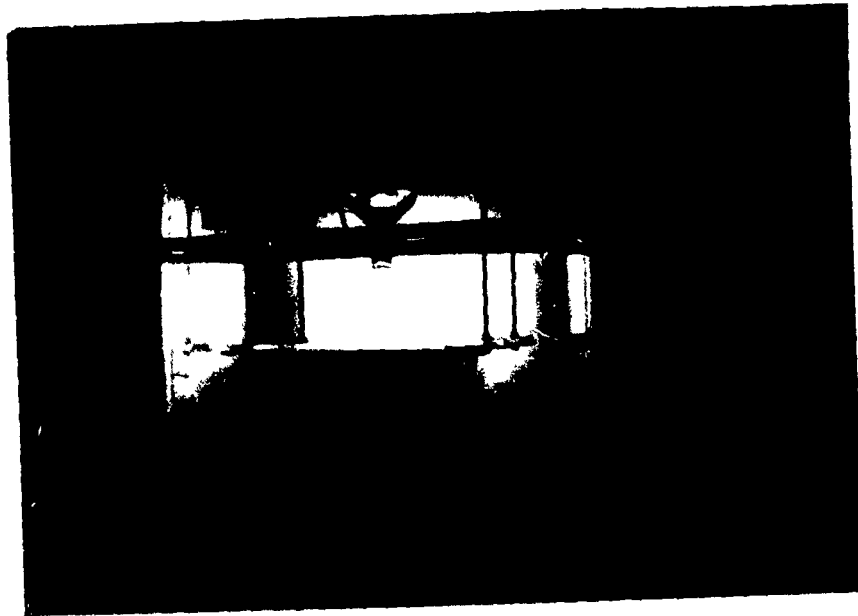


Fig. (2-1a) Photograph of the Impinging Water Jet Facility

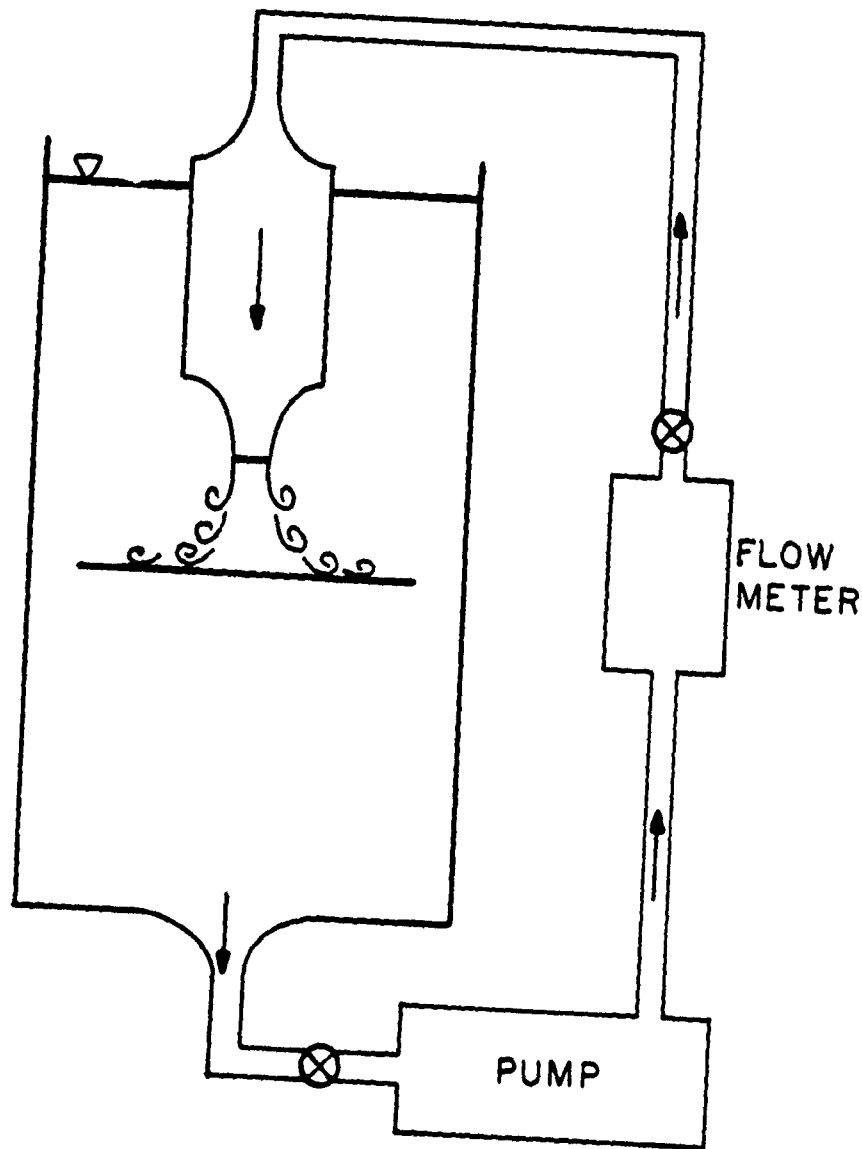


Fig. (2-1b) Schematic of the Impinging Water Jet Facility

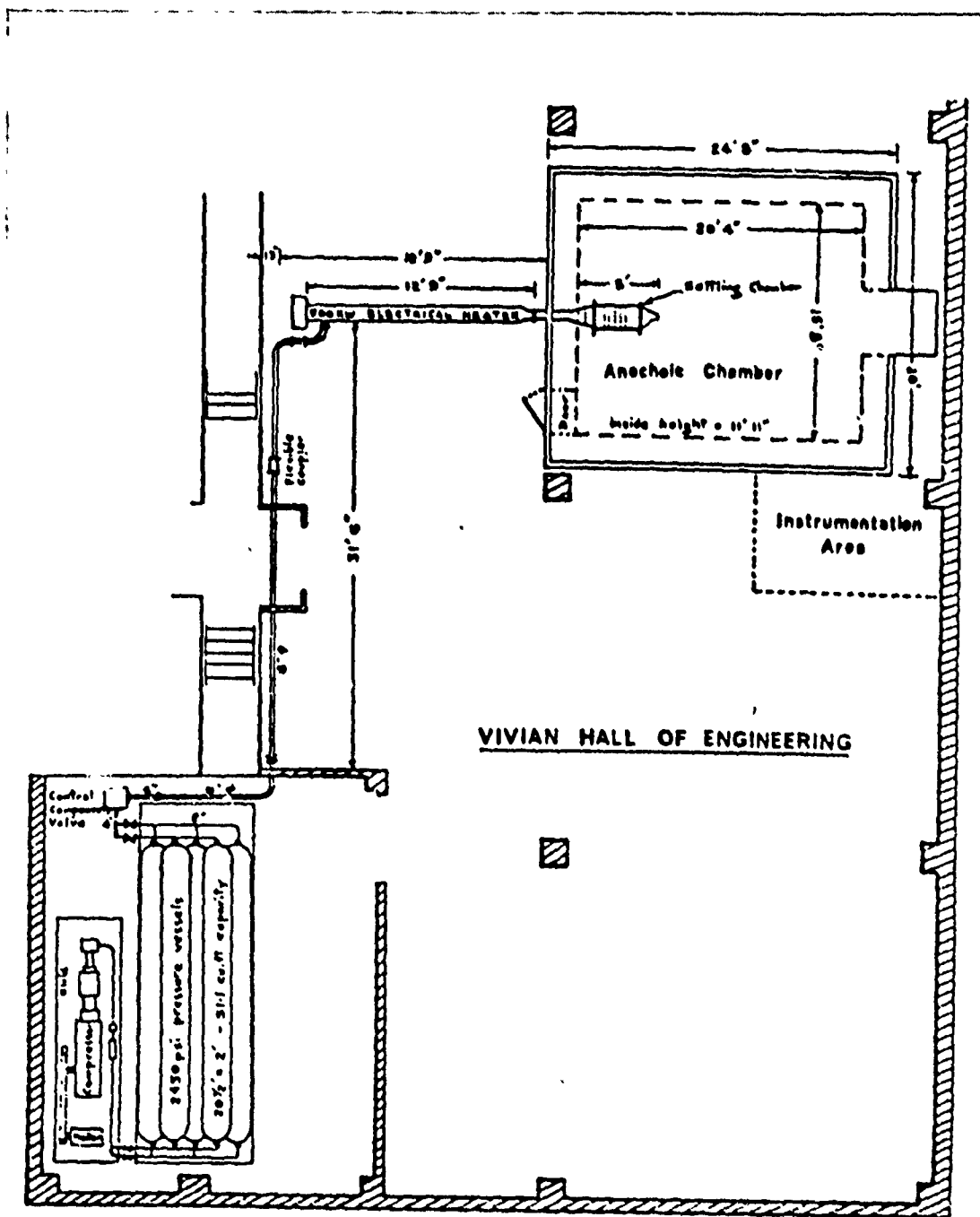


Fig. (2-2) Jet Noise Research Facilities at USC



Fig. (2-3) Photograph of the Flat Plate Inside the Anechoic Chamber

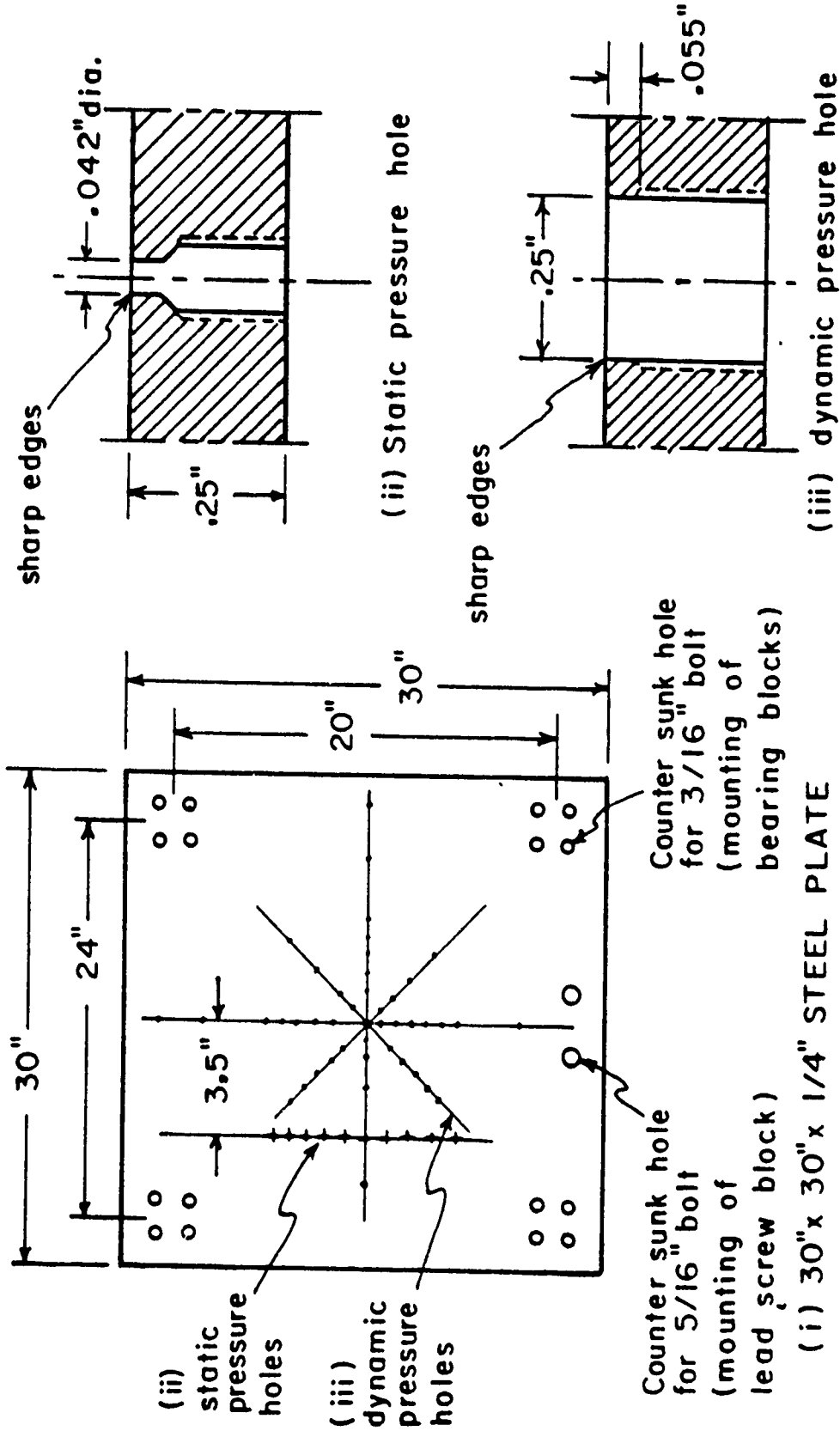


Fig. (2-4) Dynamic and Static Pressure Holes in the Flat Plate

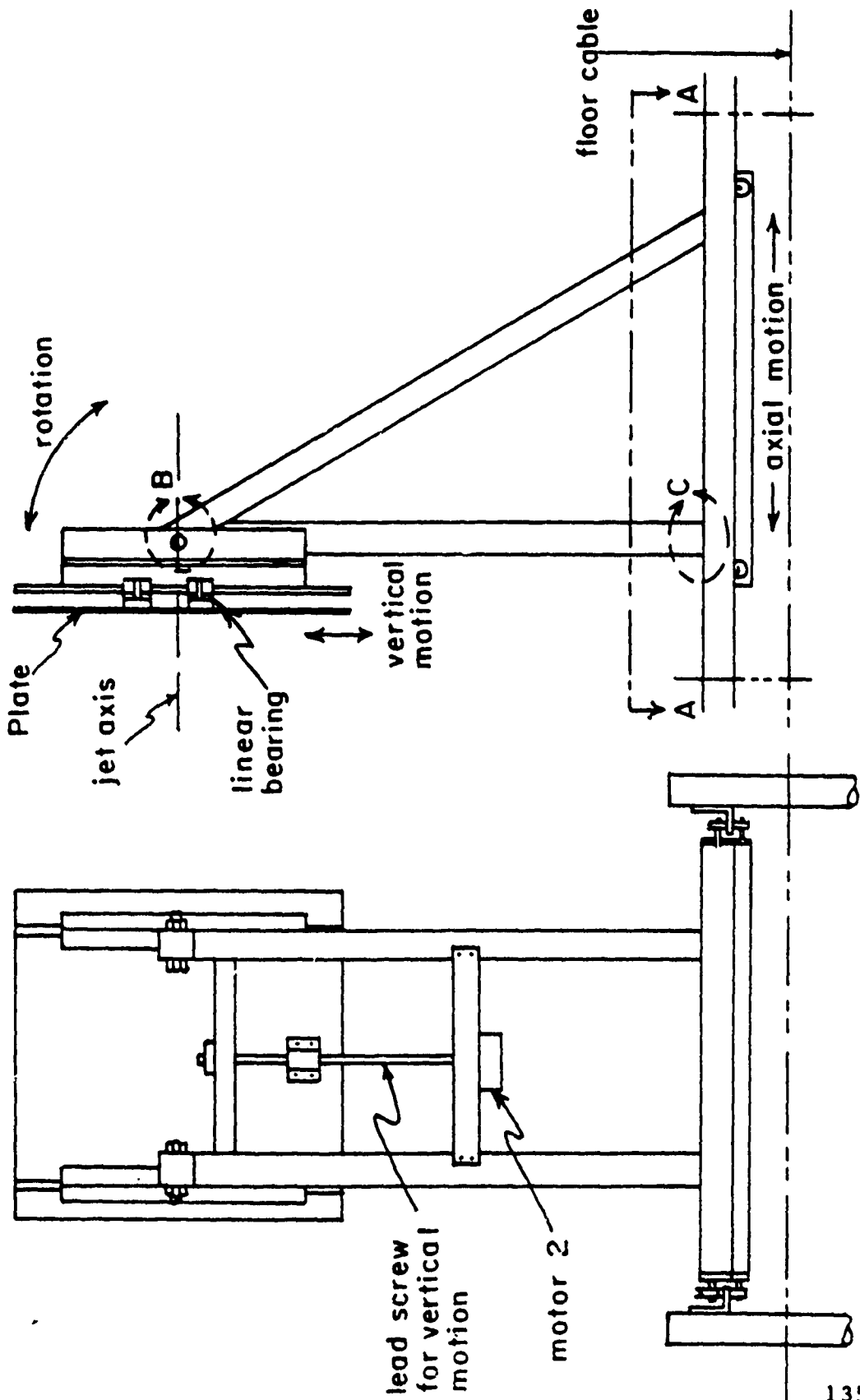
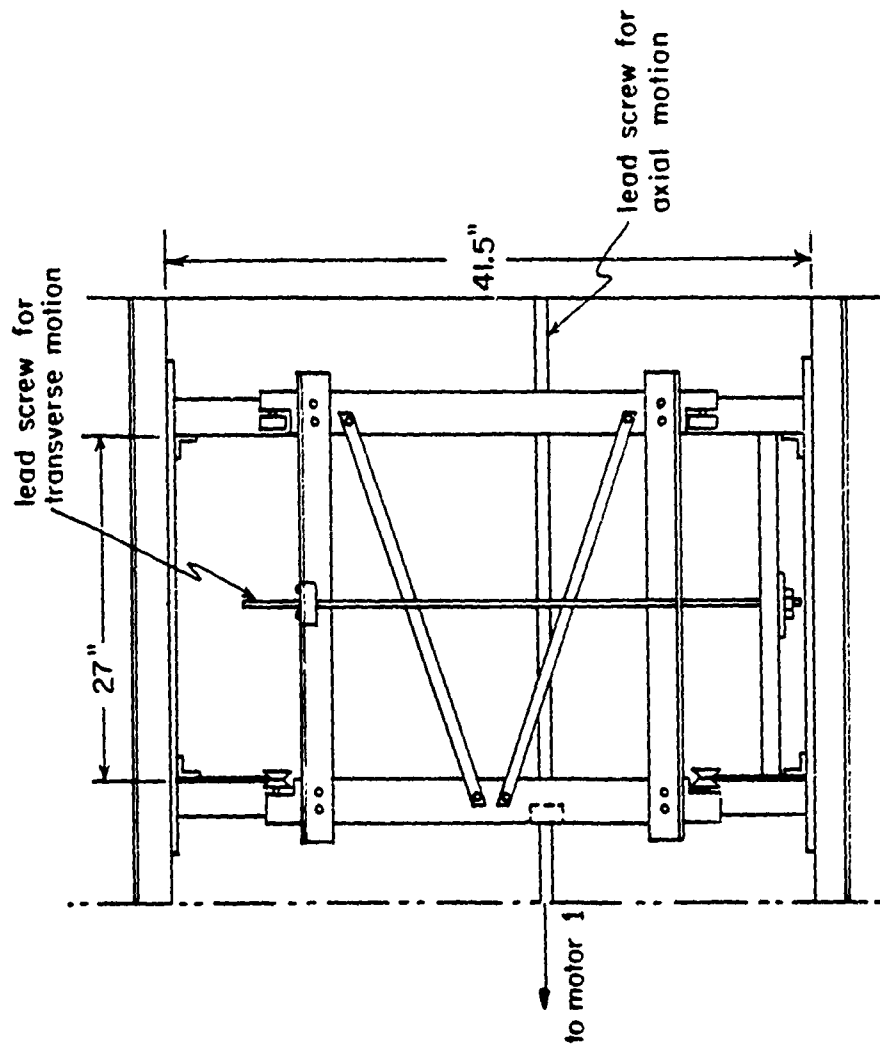


Fig. (2-5) Flat Plate Traverse Mechanism



(A-A)

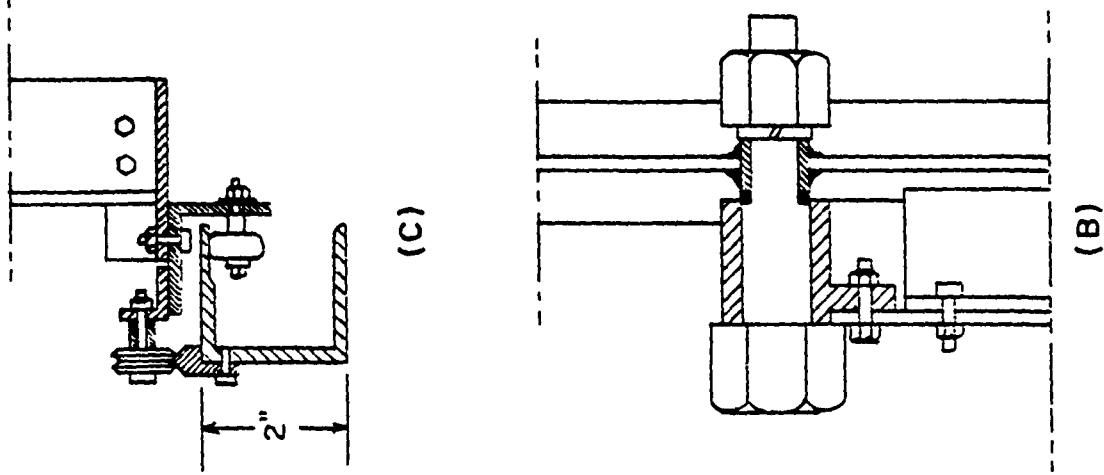


Fig. (2-5) Concluded

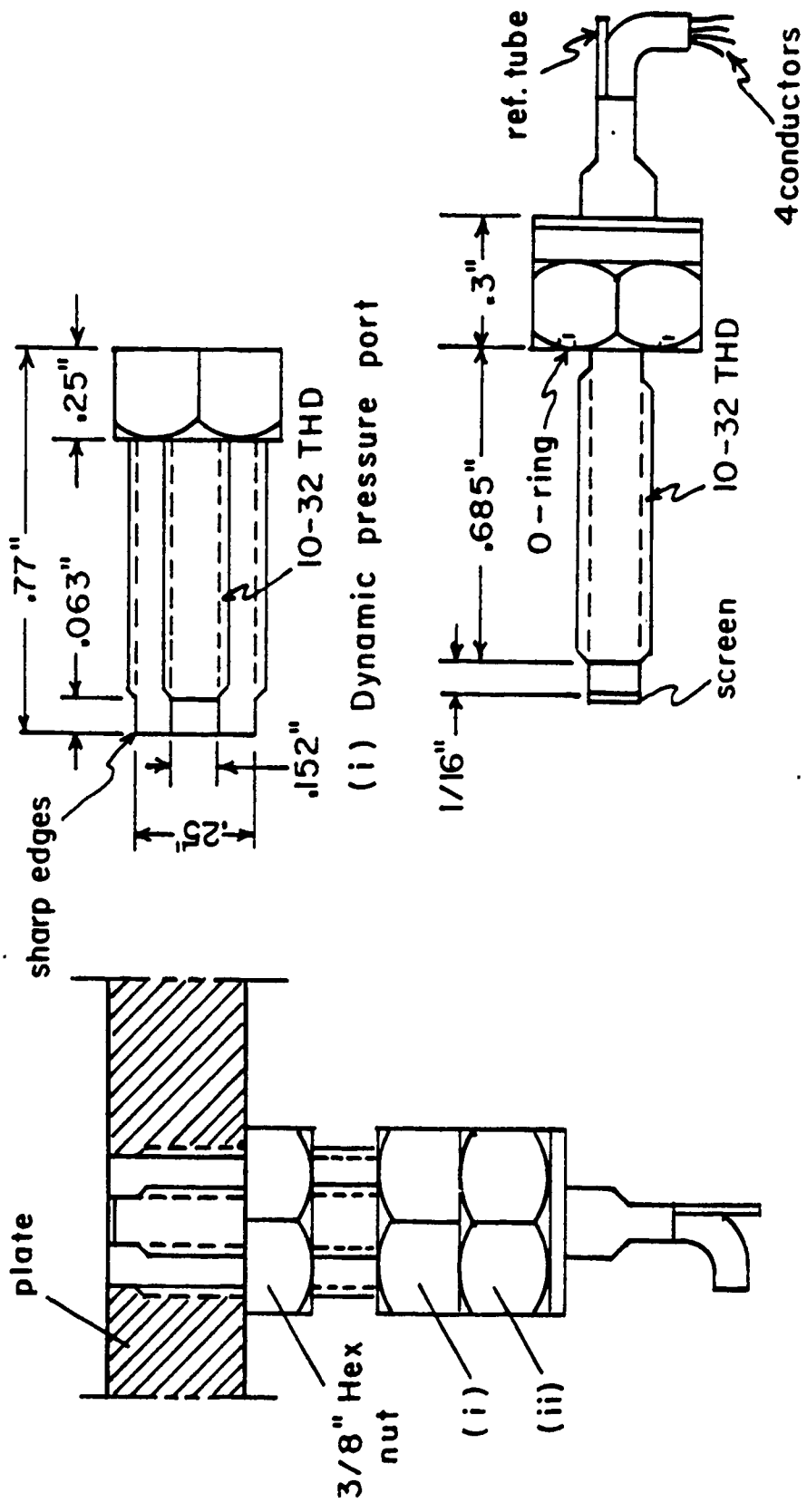
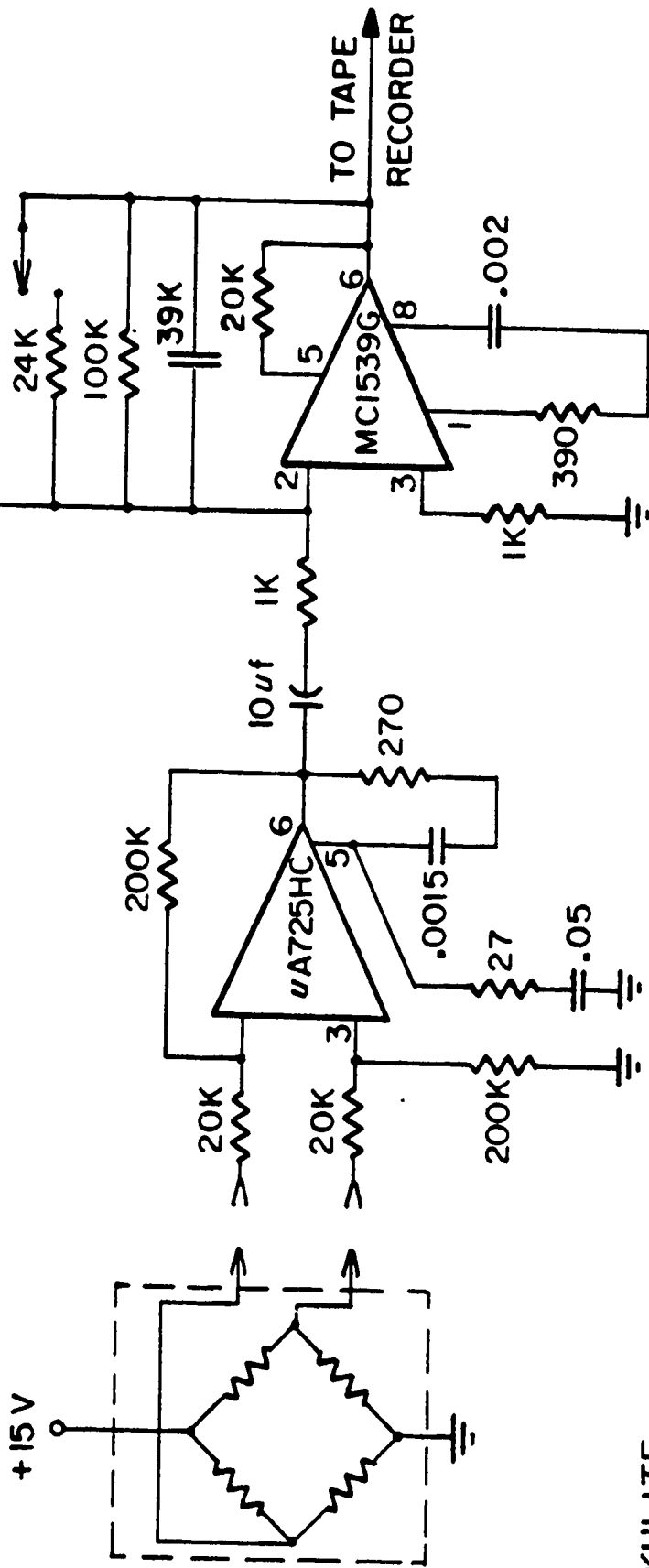


Fig. (2-6) Kulite Pressure Transducer Assembly



KULITE  
TRANSDUCER

KULITE AMPLIFIER

Fig. (2-7) Kulite Transducer Amplifier Circuit

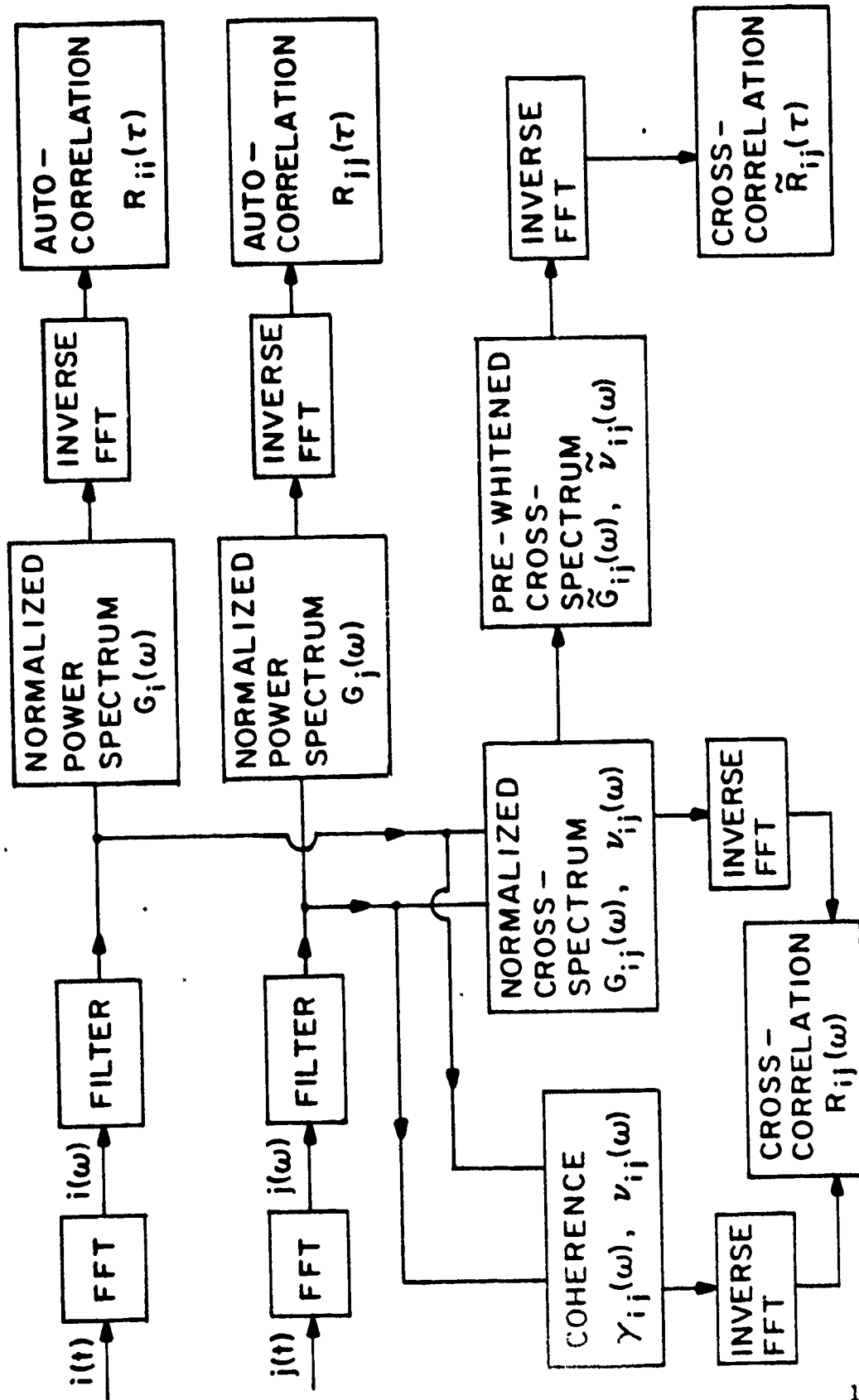


Fig. (2-8) Block Diagram of Digital Data Processing

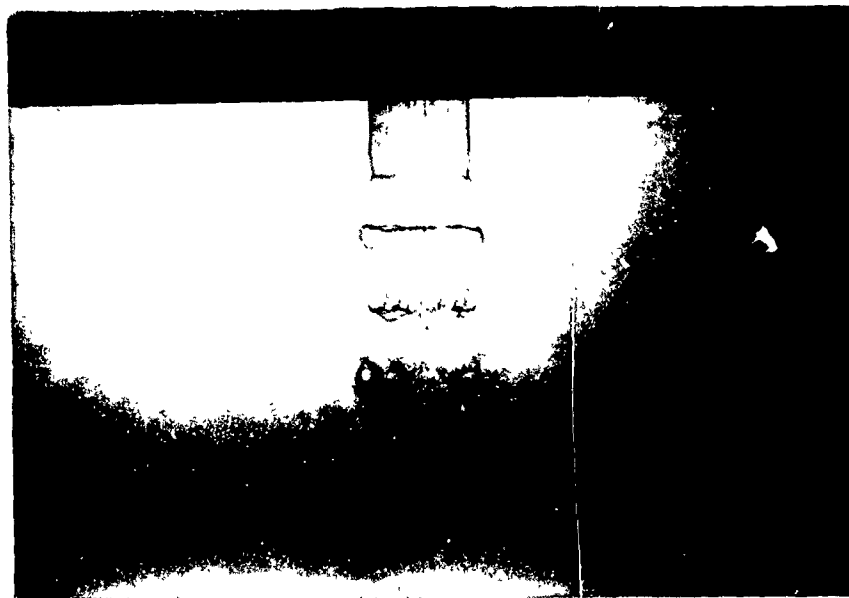


Fig. (3-1) Axisymmetric Vortical Rings in the Impinging Water Jet, Pattern 1: Small Spacing Between Rings, ( $Re=5000$ ,  $x_0/d=4$ )

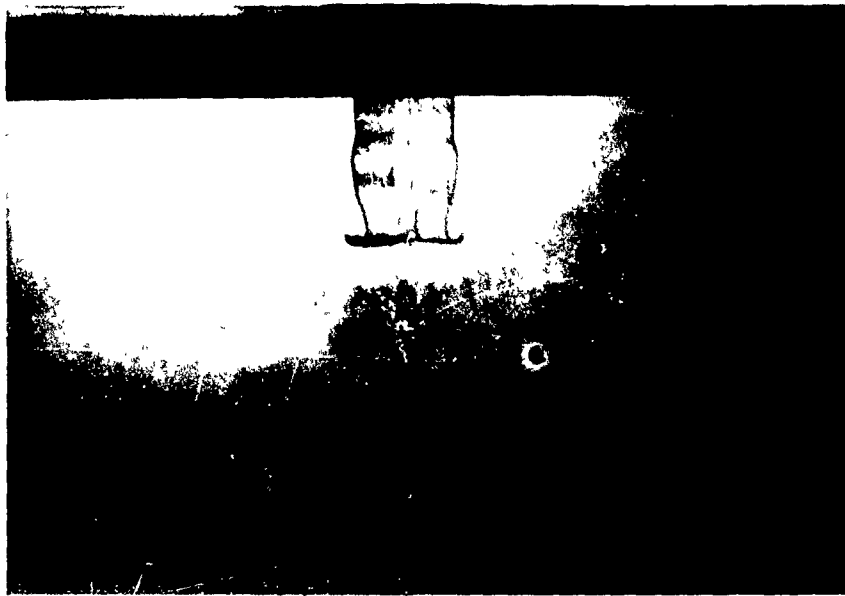


Fig. (3-2) Pattern 2: Large Spacing Between Rings, same conditions as in Fig. (3-1)

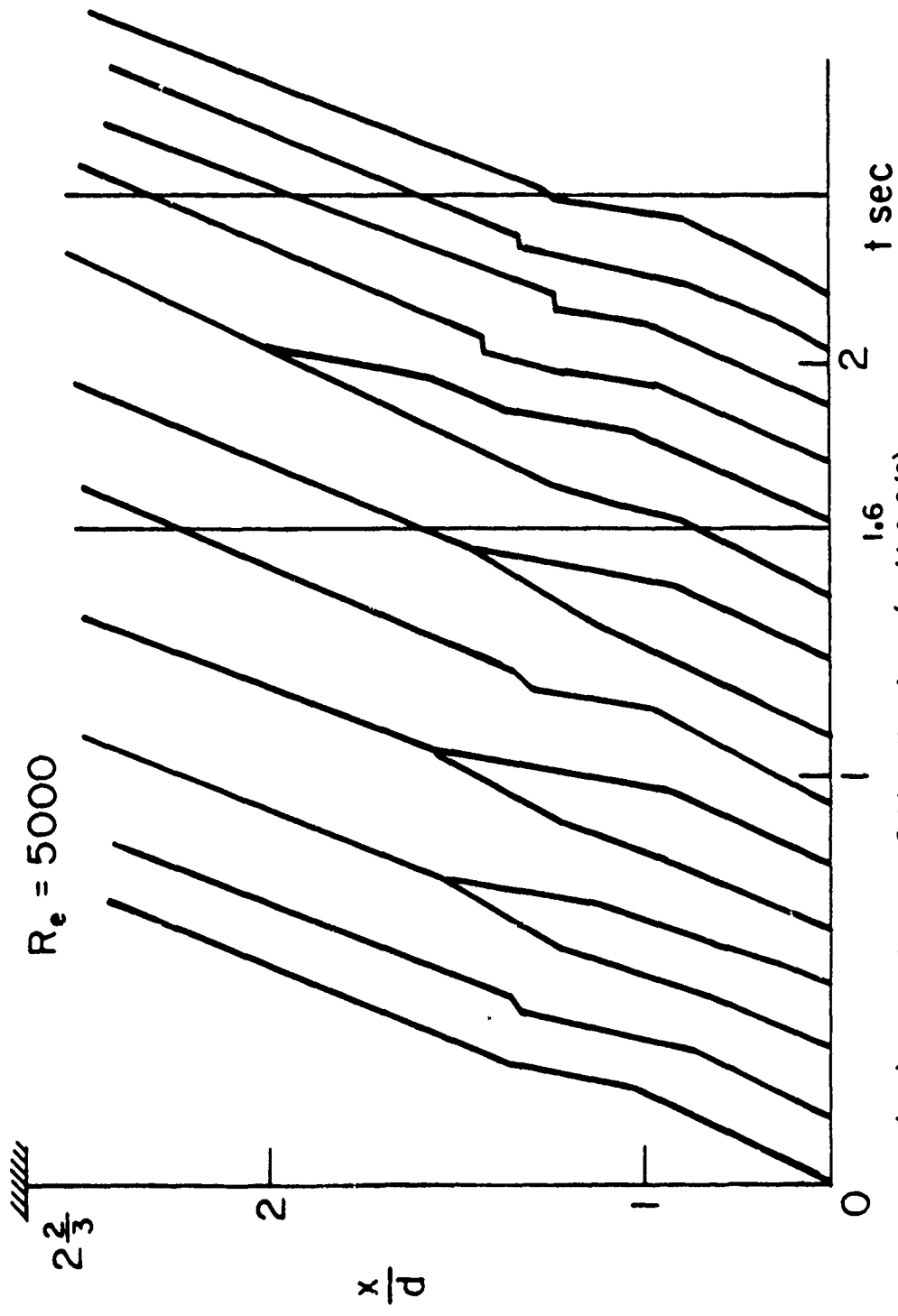


Fig. (3-3) x-t Diagram of Ring Vortices ( $x_0/d=2\frac{2}{3}$ )



Fig. (3-4) Vortex Pairing, same conditions as in Fig. (3-1)



Fig. (3-5) Hydrogen Bubble Visualization  
( $Re=5000$ ,  $x_0=4$  in.,  $d=1.5$  in.)

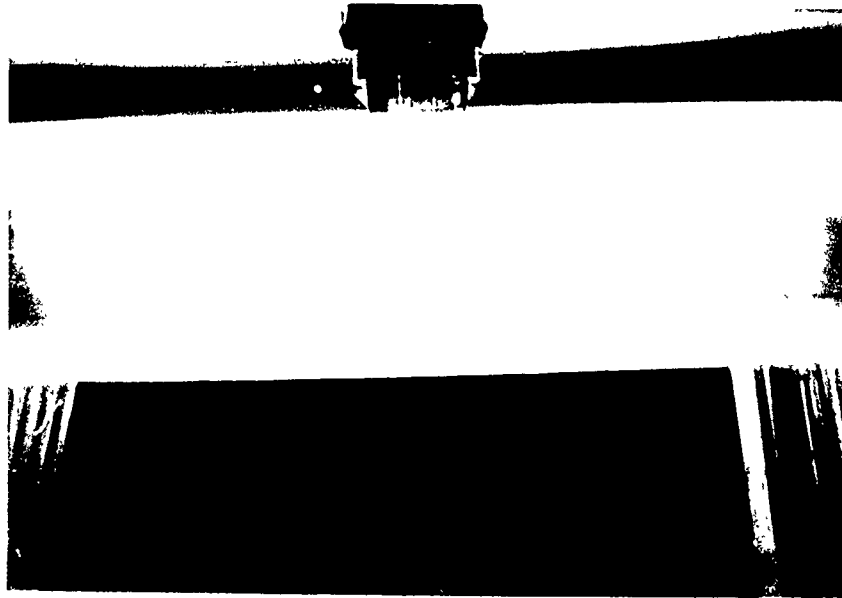


Fig. (3-6) Stretching of Ring Vortices on the Plate.  
( $Re=5000$ ,  $x_0/d=2$ )

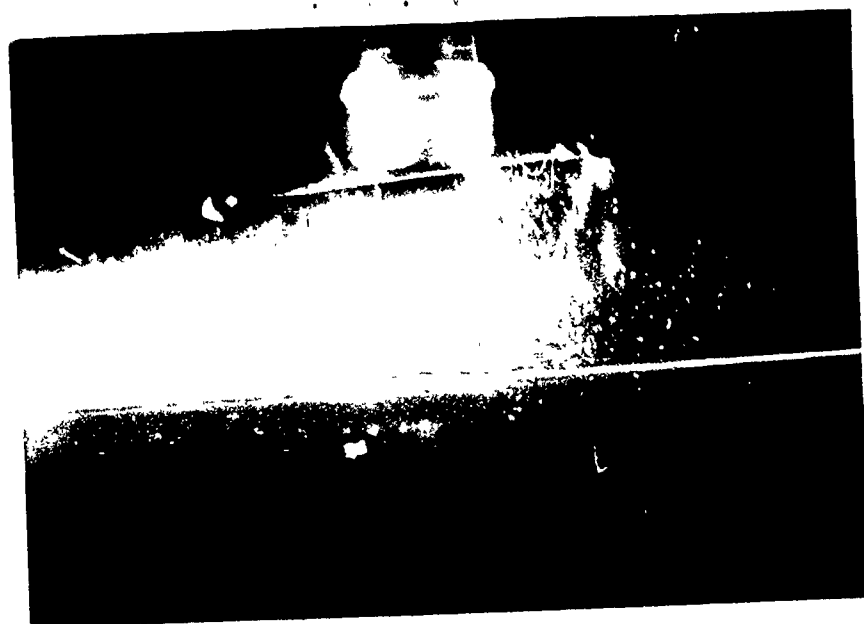


Fig. (3-7) Curvature of Bubble Lines Indicating Velocity Profiles  
During Impingement, ( $Re=5000$ ,  $x_0/d=2$ )



Fig. (3-8) Multiple Exposure of Hydrogen Bubbles Showing Shear Layer Growth and Ambient Entrainment, same conditions as in Fig. (3-7)



Fig. (3-9) Azimuthal Instability of Vortex Ring,  
( $Re=7000$ ,  $x_0/d=4$ )

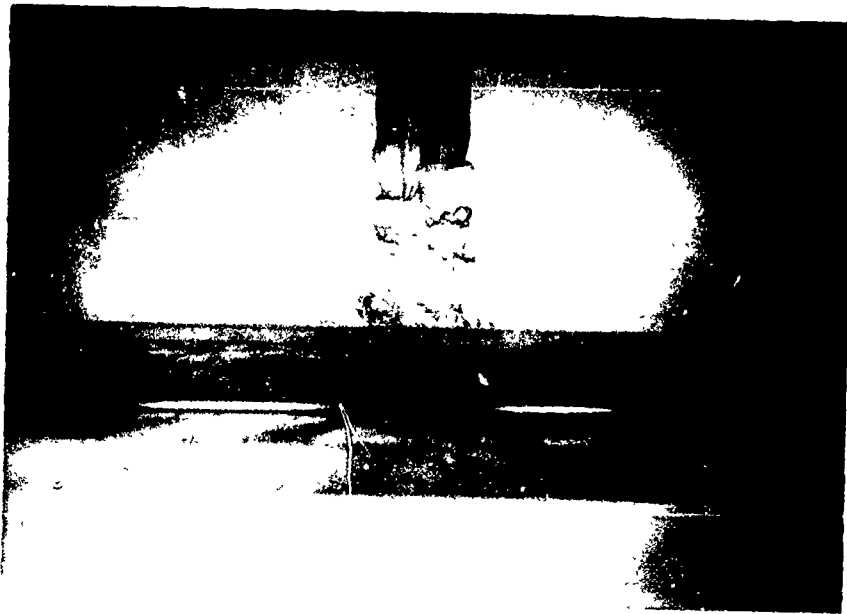
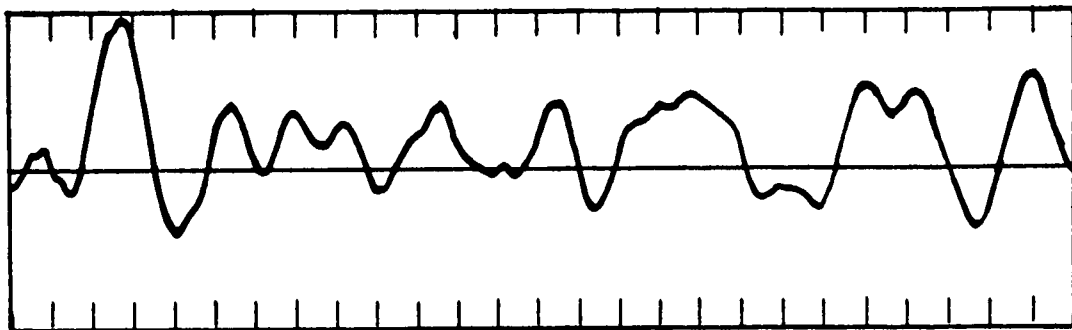


Fig. (3-10) Higher Instability Mode: A Spiral Mode,  
( $Re=8000$ ,  $x_0/d=3$ )

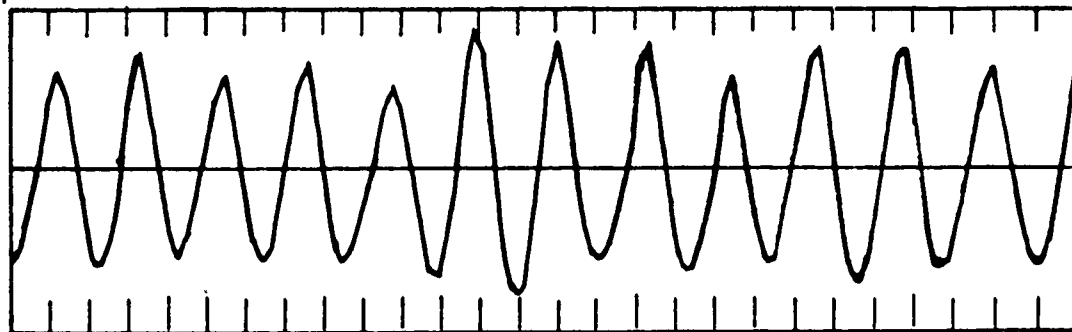
$p(t)$



→ | ← 0.1 msec

(i)  $M = .5$  (non-resonance)

$p(t)$



→ | ← 0.1 msec

(ii)  $M = .9$  (resonance)

Fig. (3-11) Raw Signals of Surface Pressure Fluctuations,  
( $x_0/d=4$ ,  $r_0/d=0$ .)

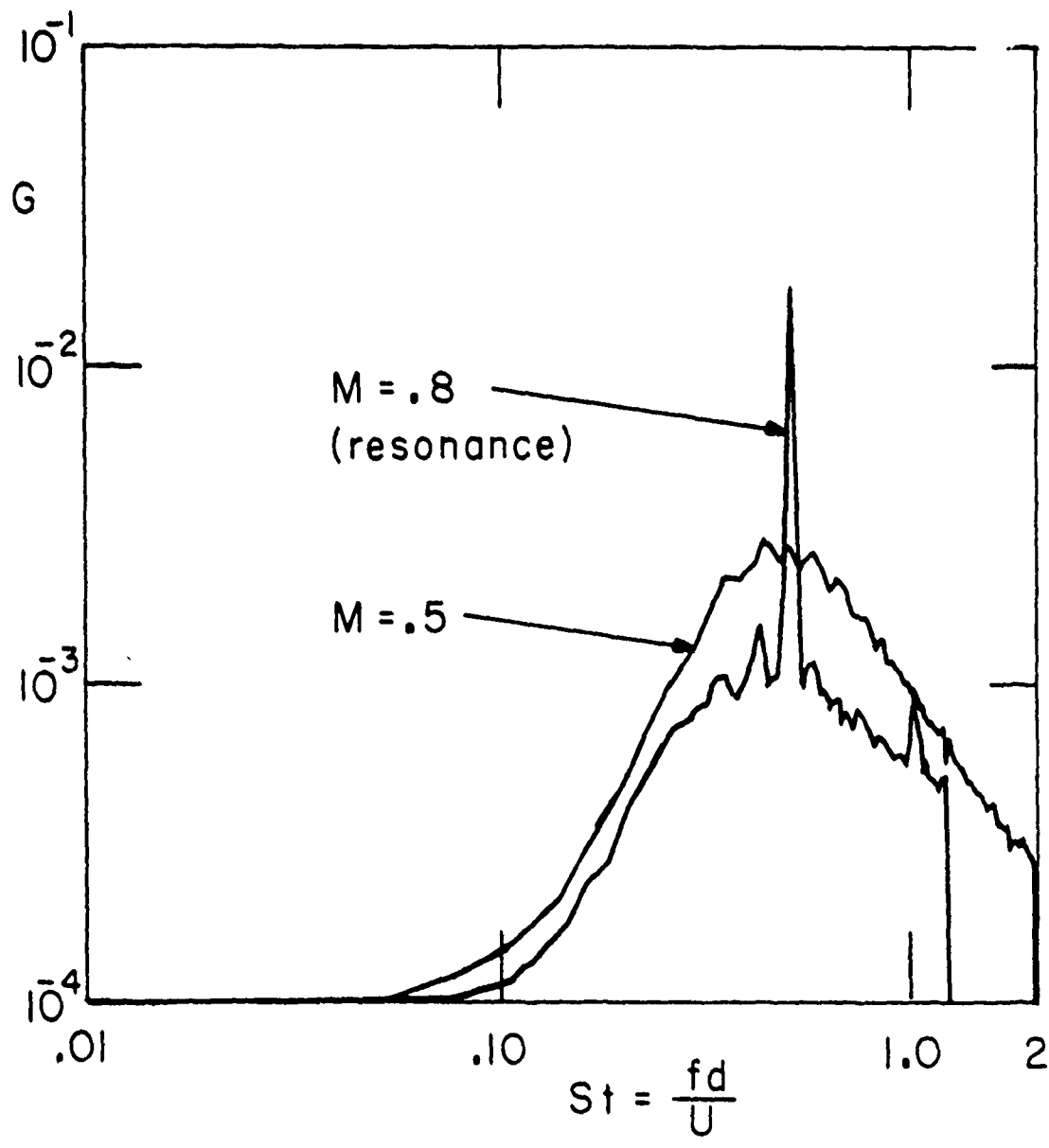


Fig. (3-12) Normalized Power Spectra of Surface Pressure Fluctuations, ( $x_0/d=4$ ,  $r_0/d=1.5$ )

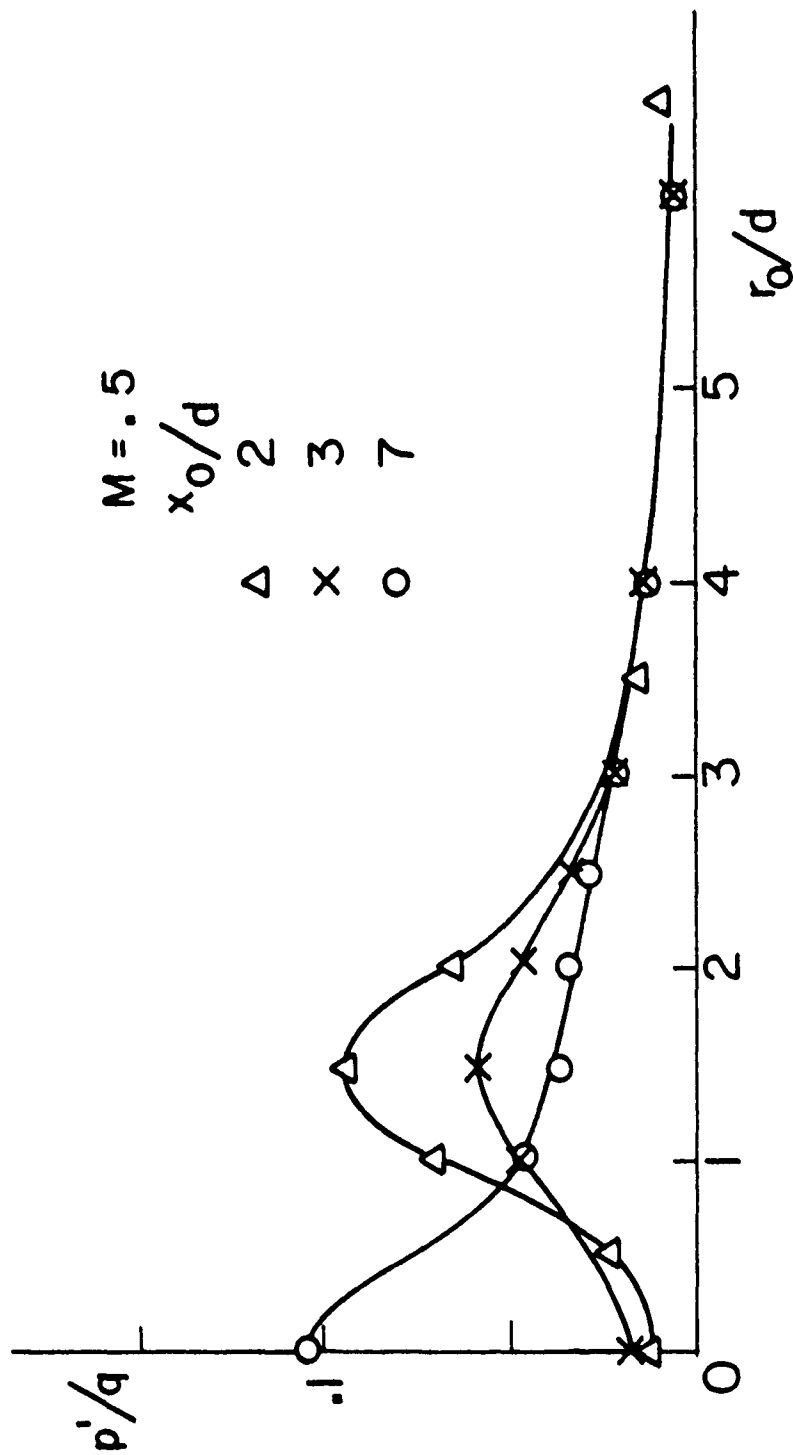


Fig. (3-13a) Radial Variation of rms Surface Pressure Fluctuations

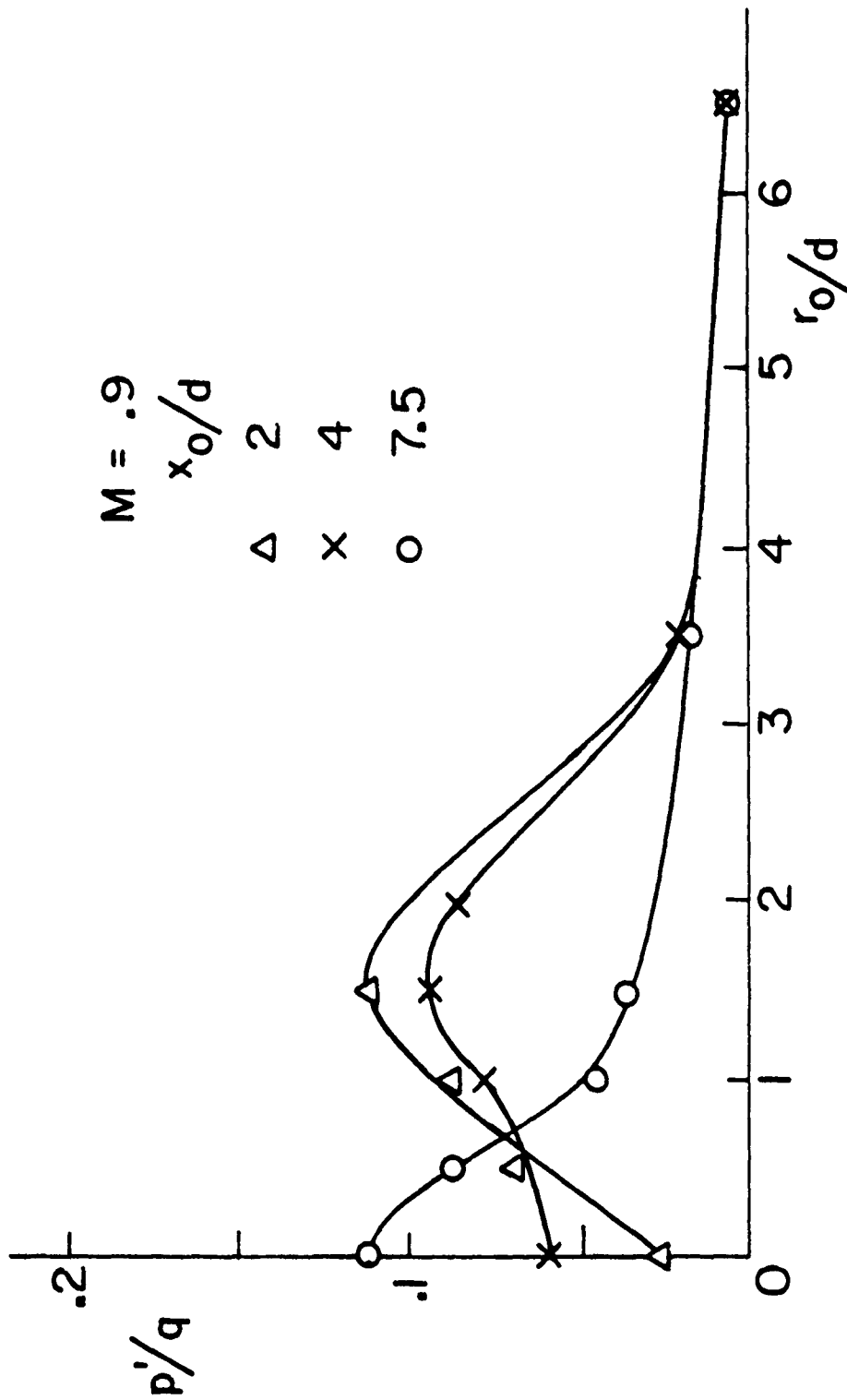


Fig. (3-13b) Radial Variations of rms Surface Pressure Fluctuations

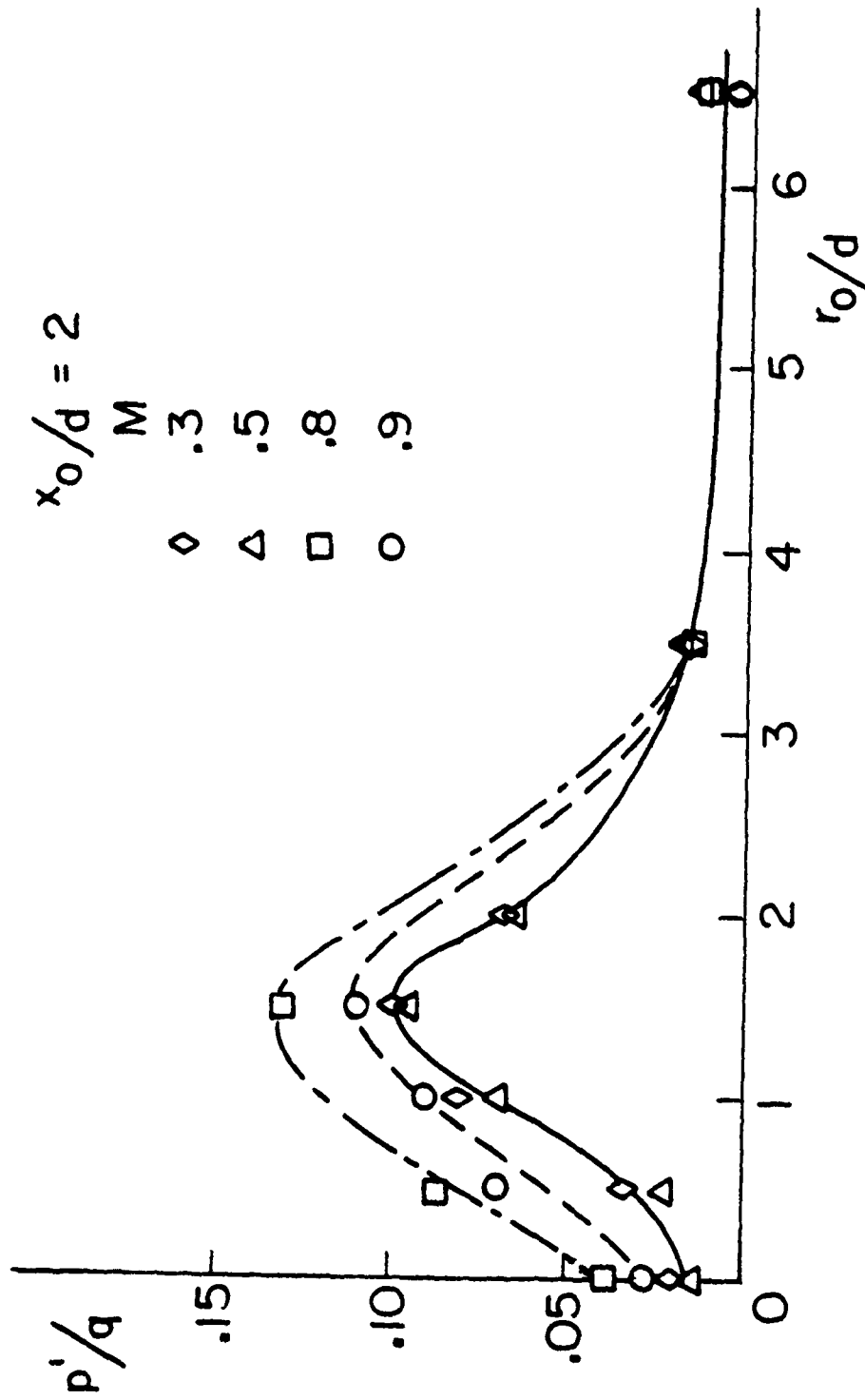


Fig. (3-14) Radial Variation of rms Surface Pressure Fluctuations

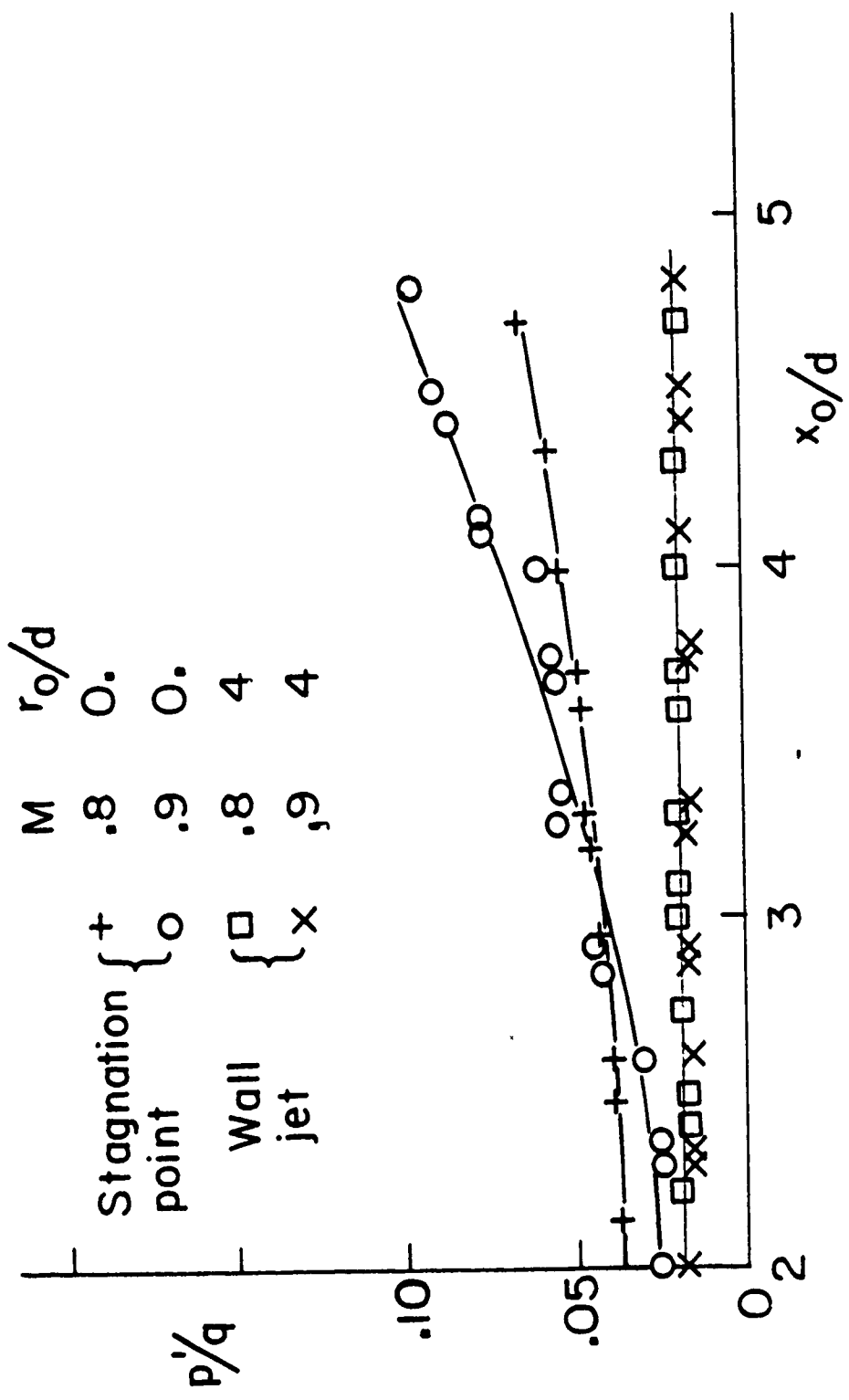
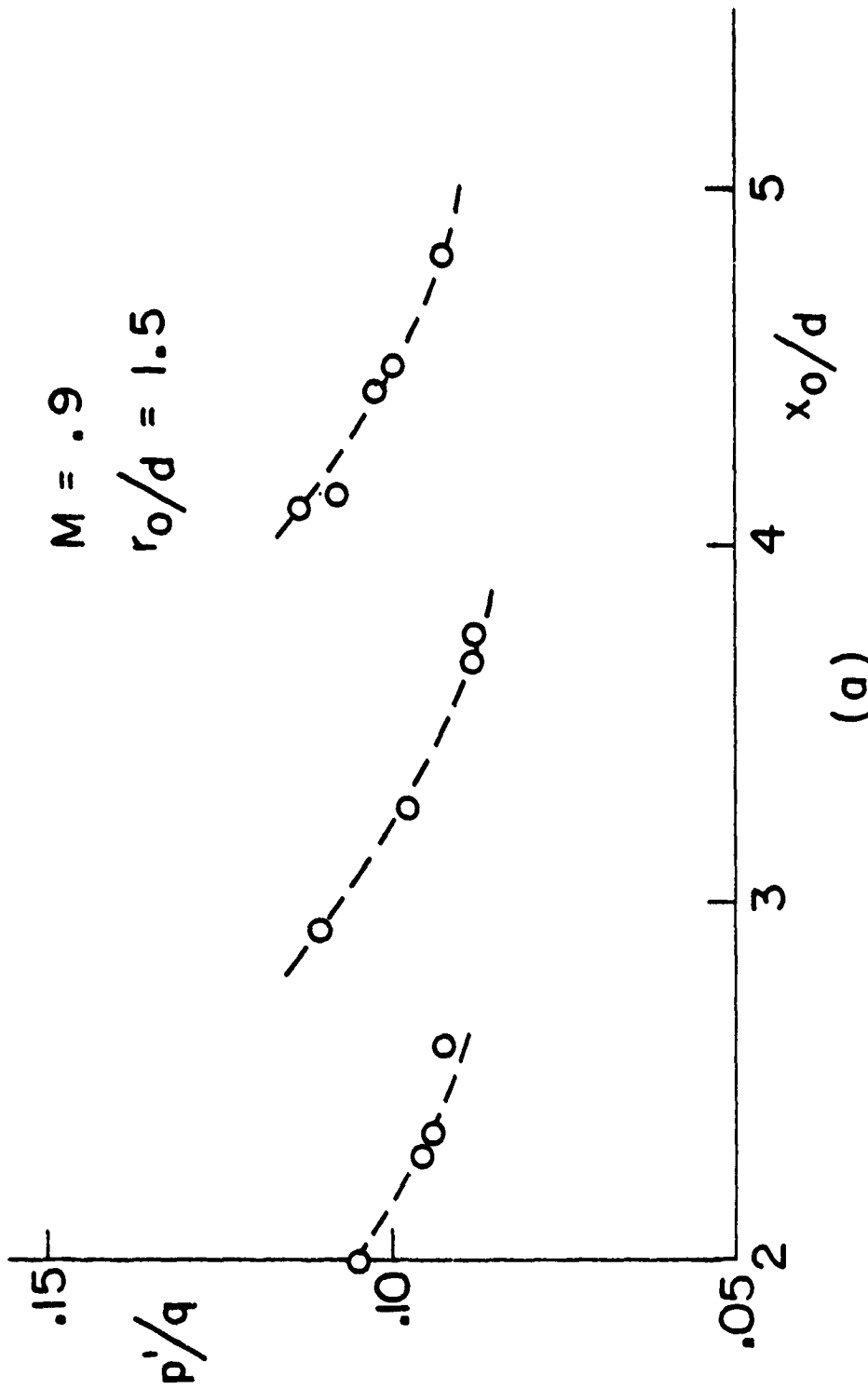
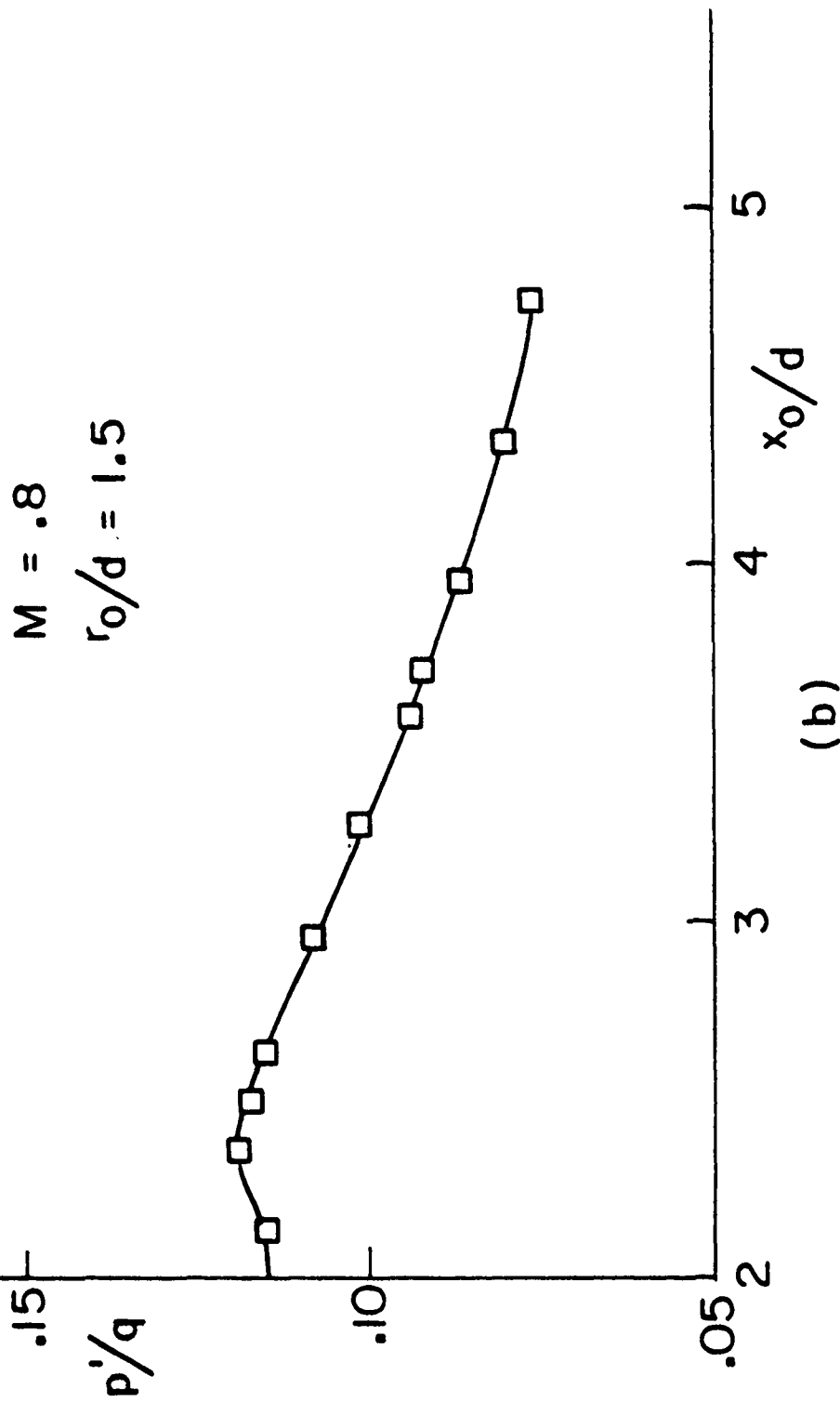


Fig. (3-15) Variation of rms Surface Pressure Fluctuations with Plate Locations



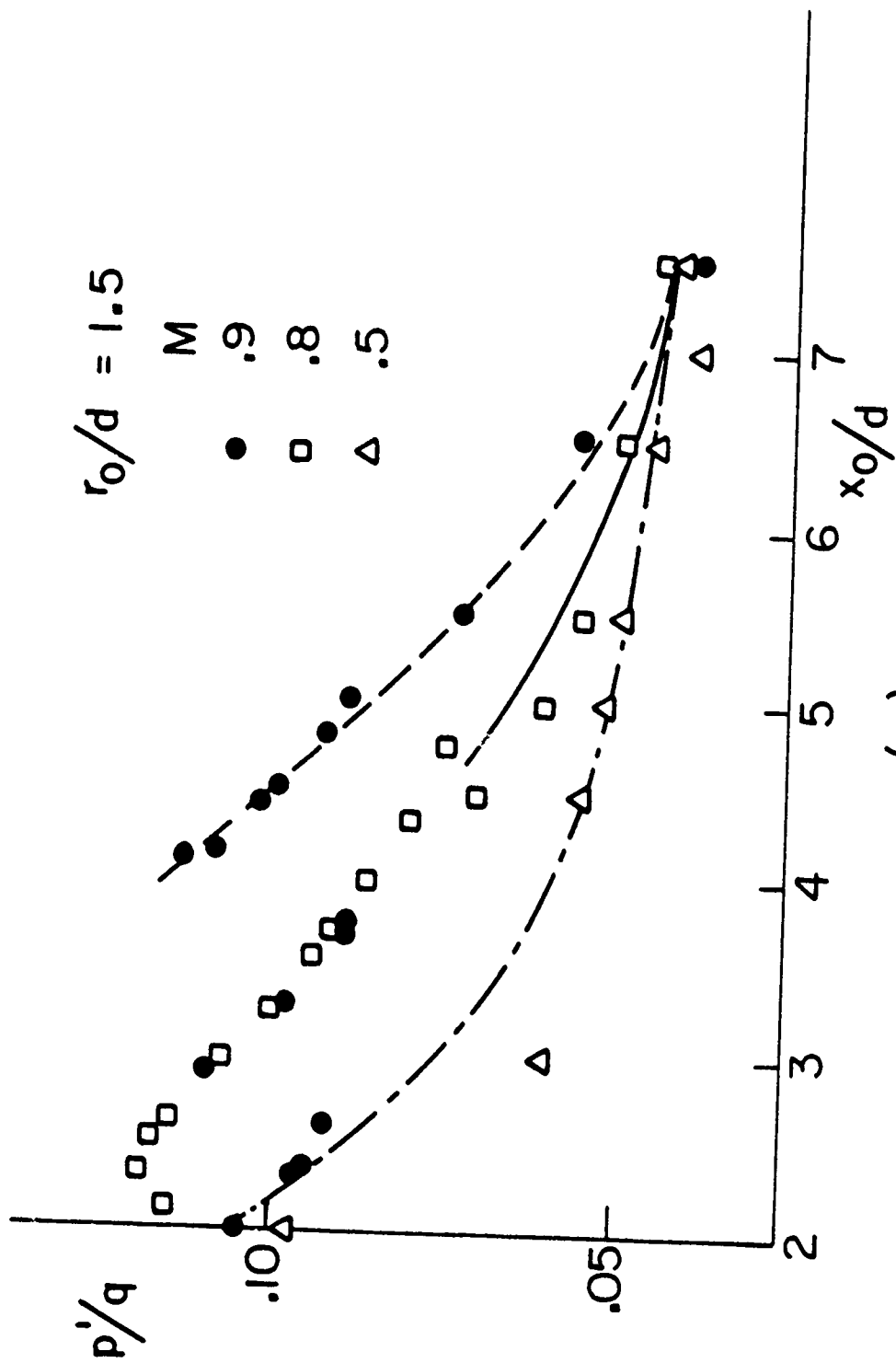
(a)

Fig. (3-16) Variation of rms Surface Pressure Fluctuations with Plate Locations



(b)

Fig. (3-16) Continued



(c)

Fig. (3-16) Concluded

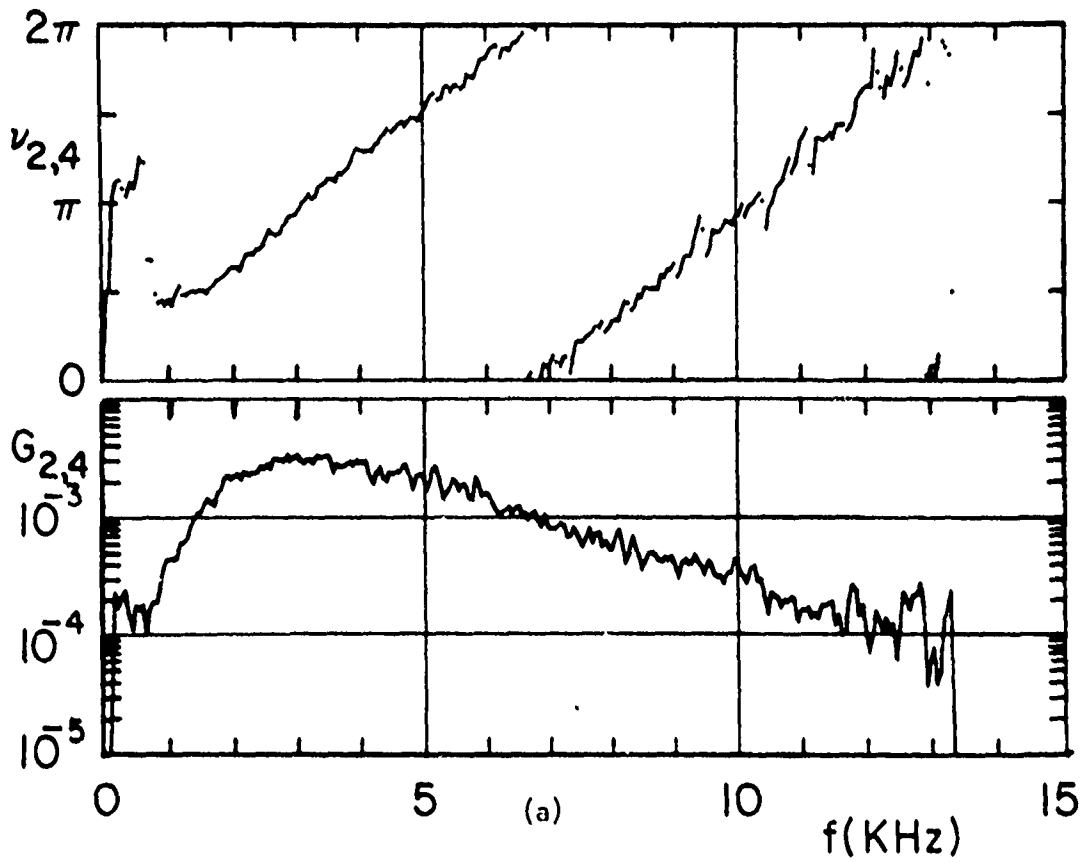


Fig. (3-17) Two-Point Measurements, indices refer to the sketch in Fig. (3-19), ( $M=.8$ ,  $x_0/d=6$ )

- (a) Cross-Spectrum and Phase Angle
- (b) Coherence and Phase Angle
- (c) Coherence and Phase Velocity

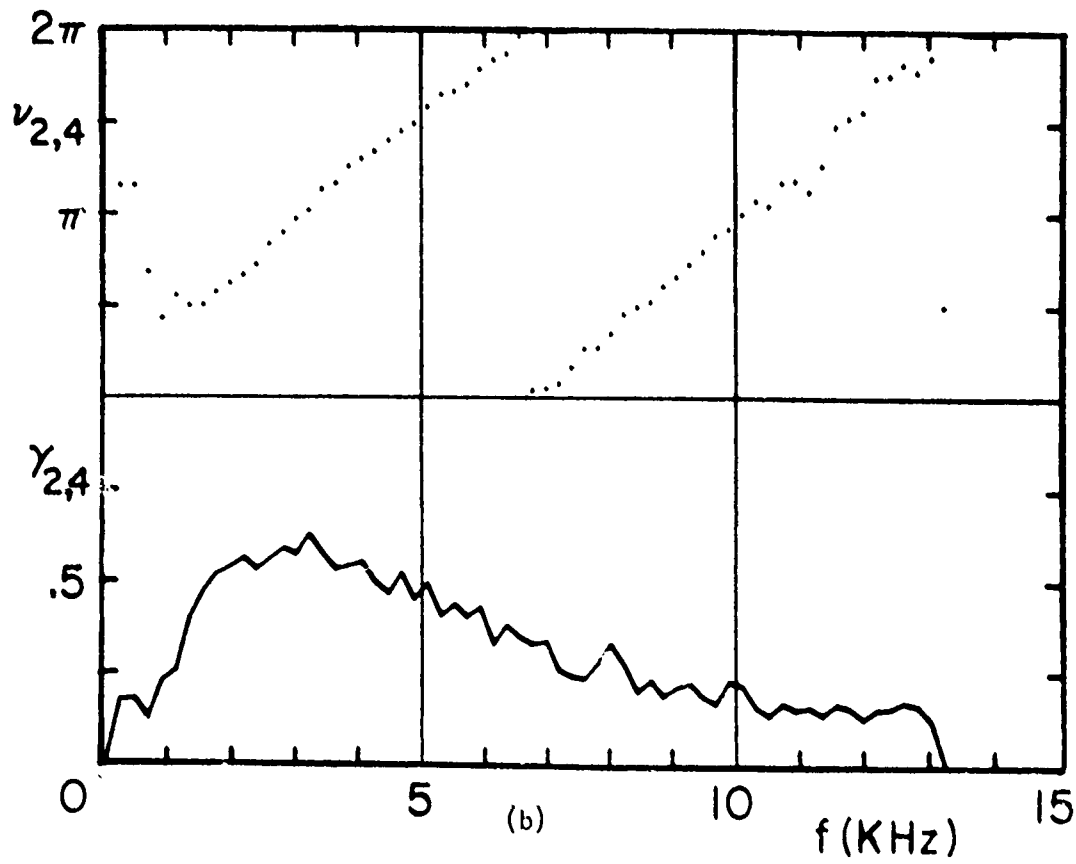


Fig. (3-17) Continued

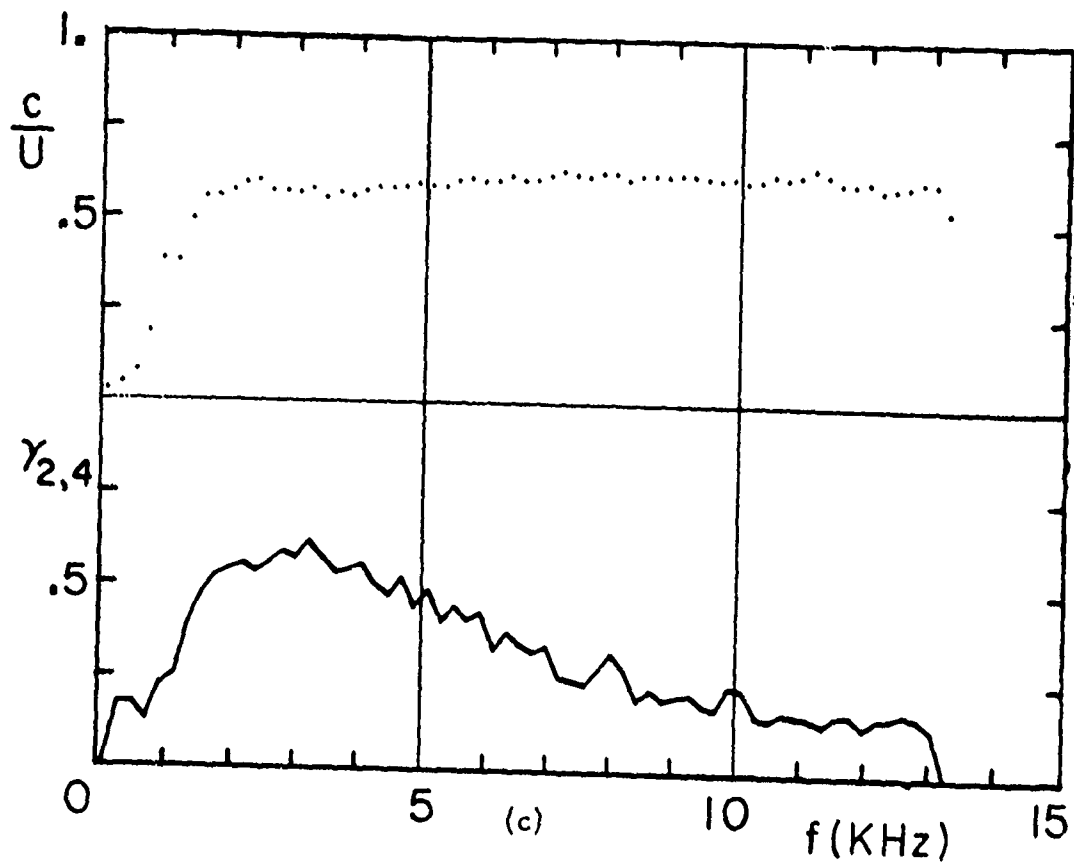


Fig. (3-17) Concluded

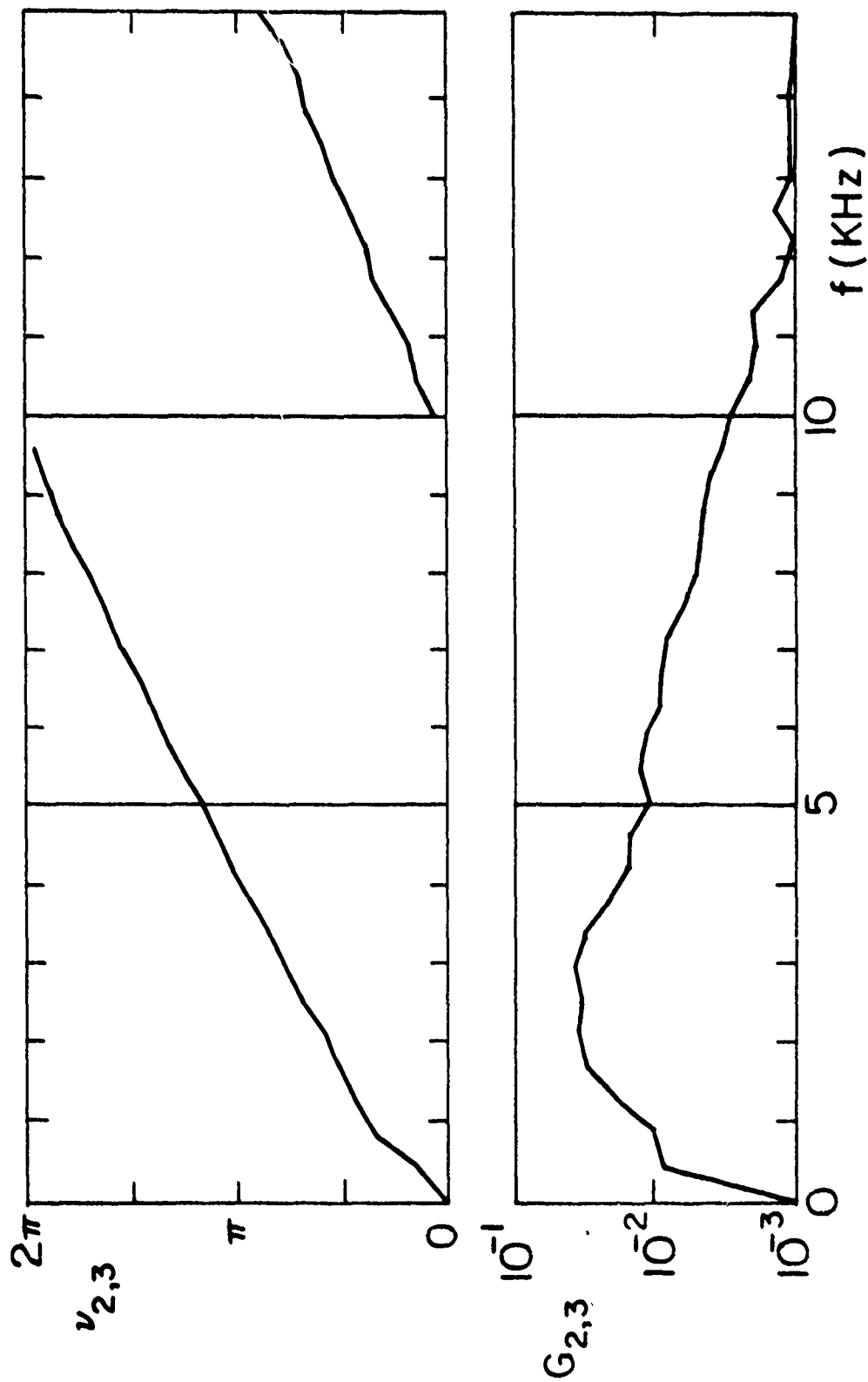


Fig. (3-18) Cross-Spectrum and Phase Angle Functions, indices refer to the sketch in Fig. (3-19), ( $M=0.5$ ,  $x_0/d=4.5$ )

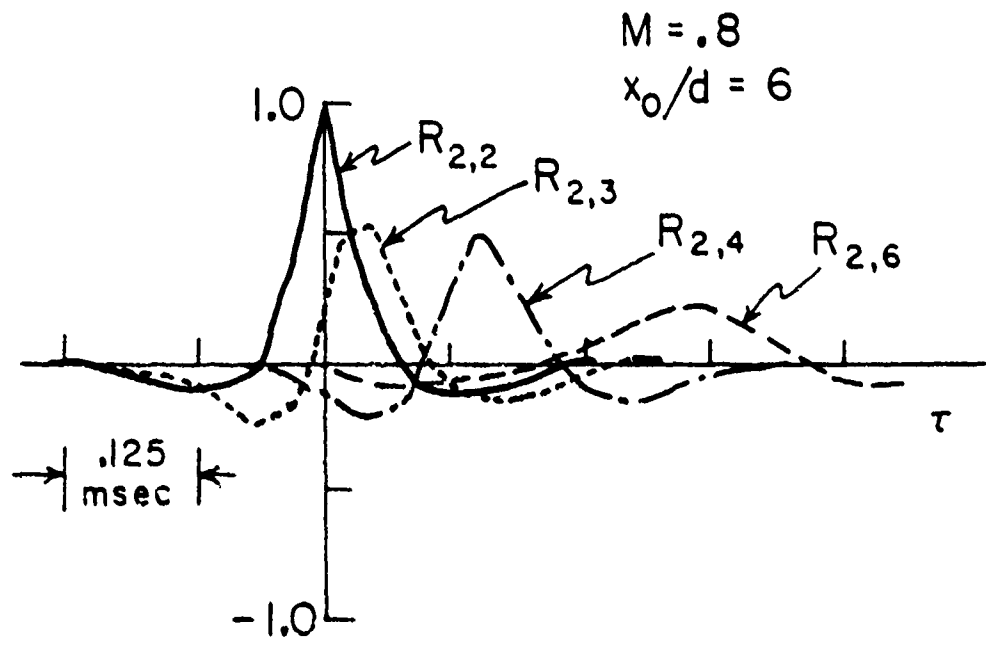
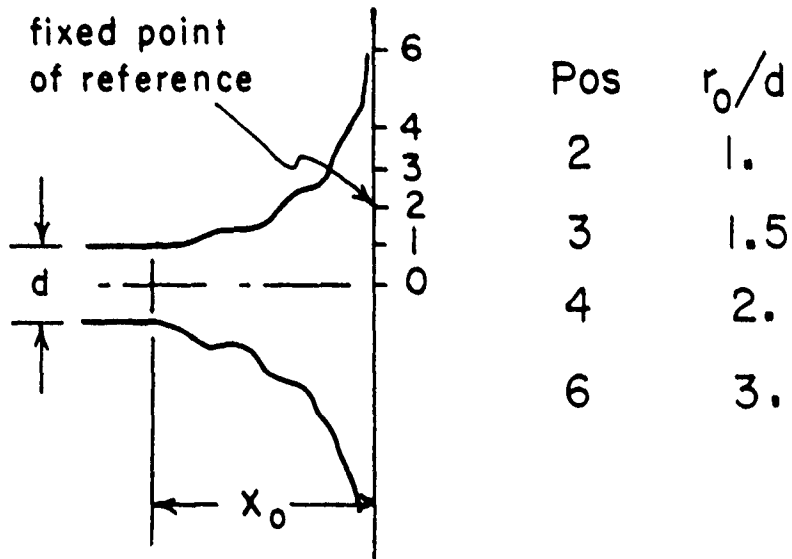


Fig. (3-19) Space-Time Surface Pressure Correlations

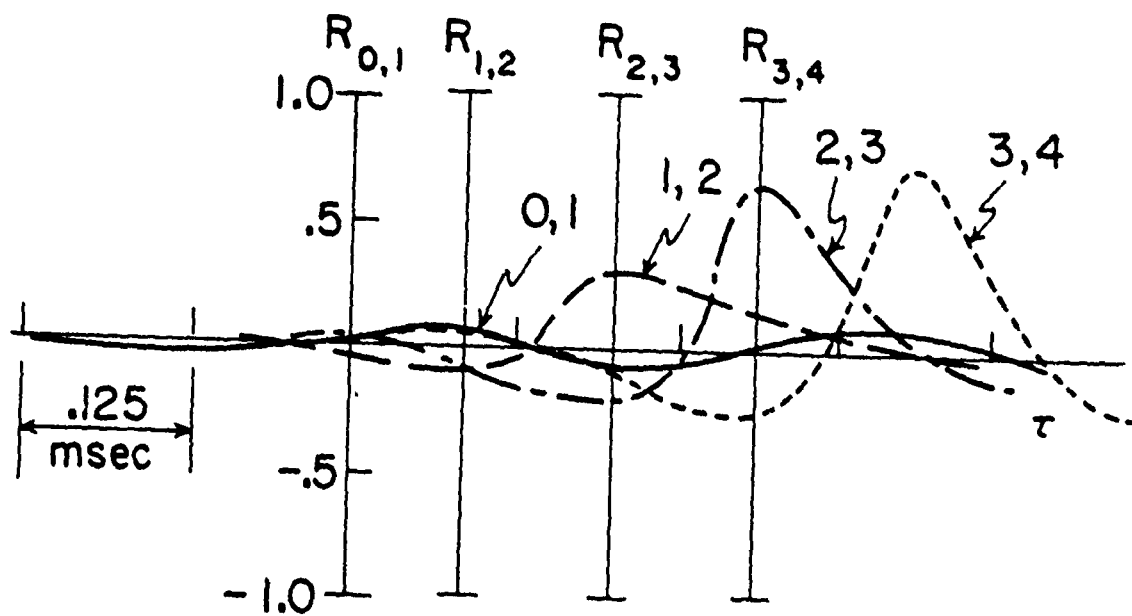
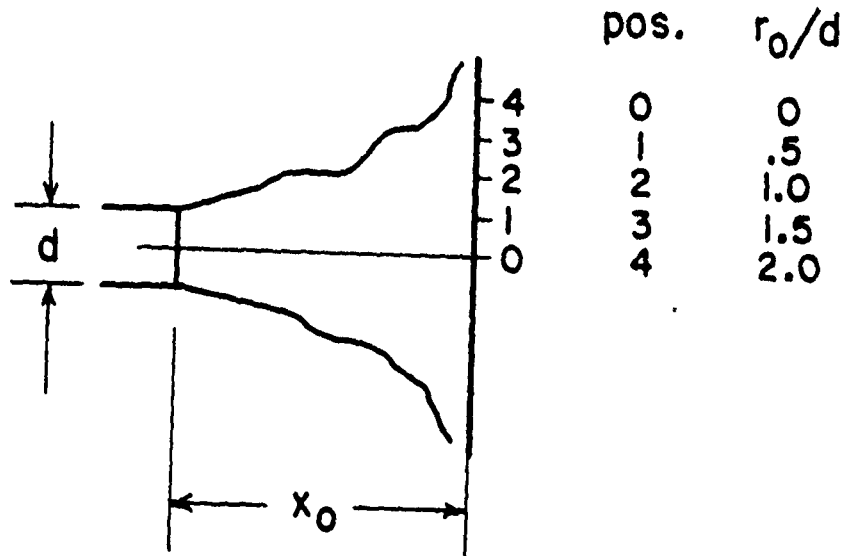


Fig. (3-20) Surface Pressure Correlations-Constant Separation  
 Distance  $\xi_0/d=.5$ , ( $M=.5$ ,  $x_0/d=4.5$ )

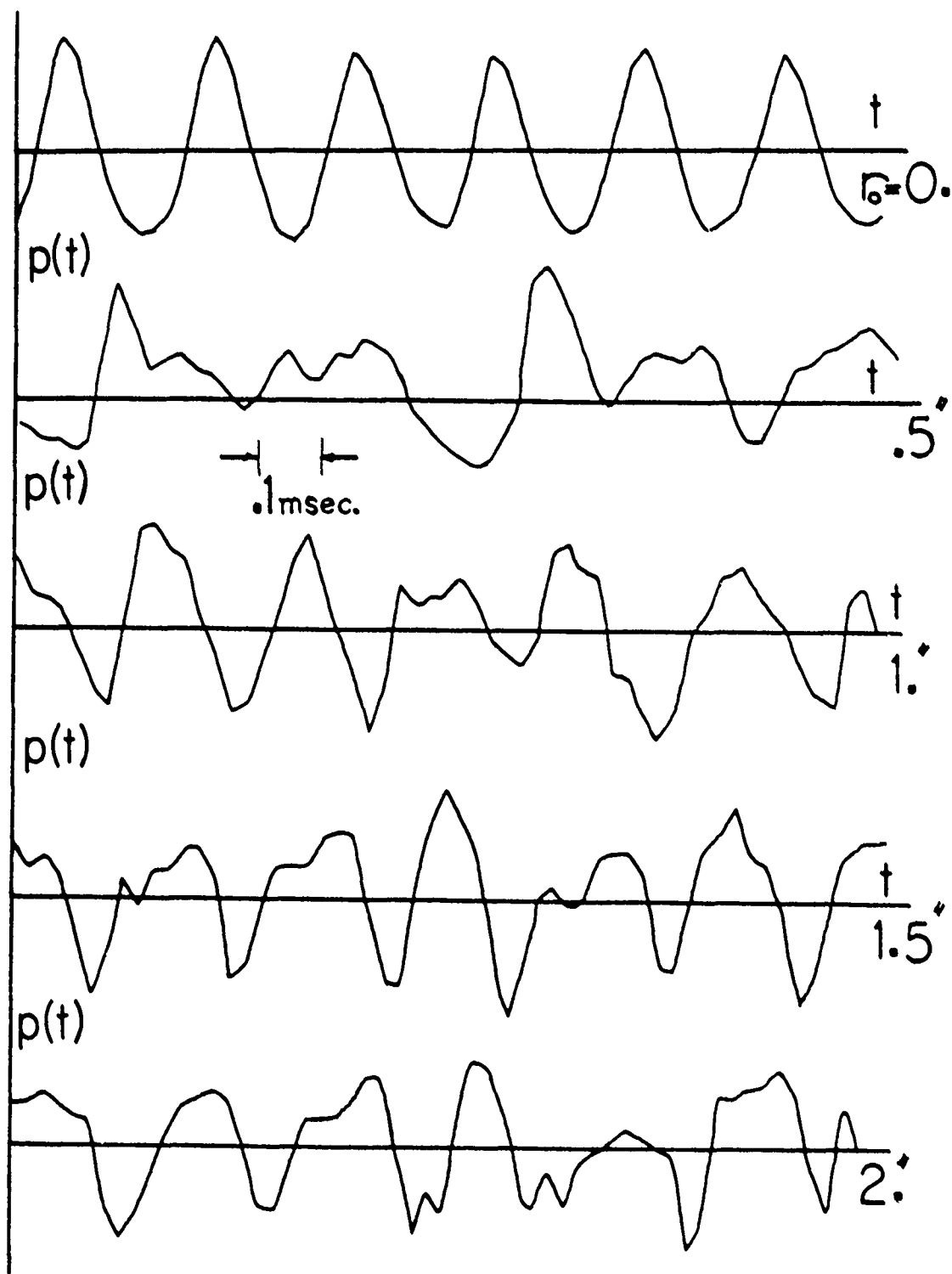


Fig. (3-21) Surface Pressure Raw Signals  $p(t)$ -arbitrary units,  
 ( $M=0.9$ ,  $x_0/d=4.5$ ,  $d=1.0$  in.)

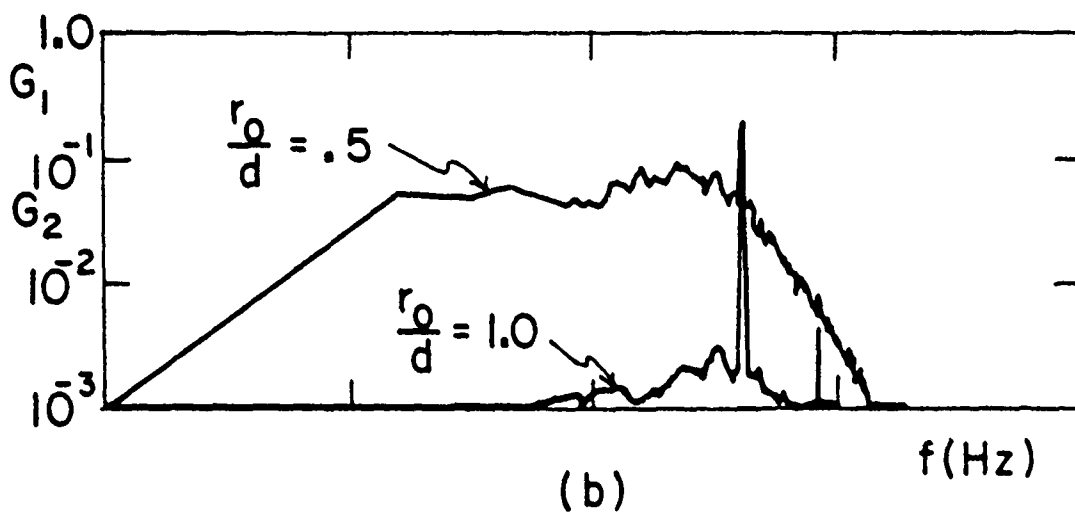
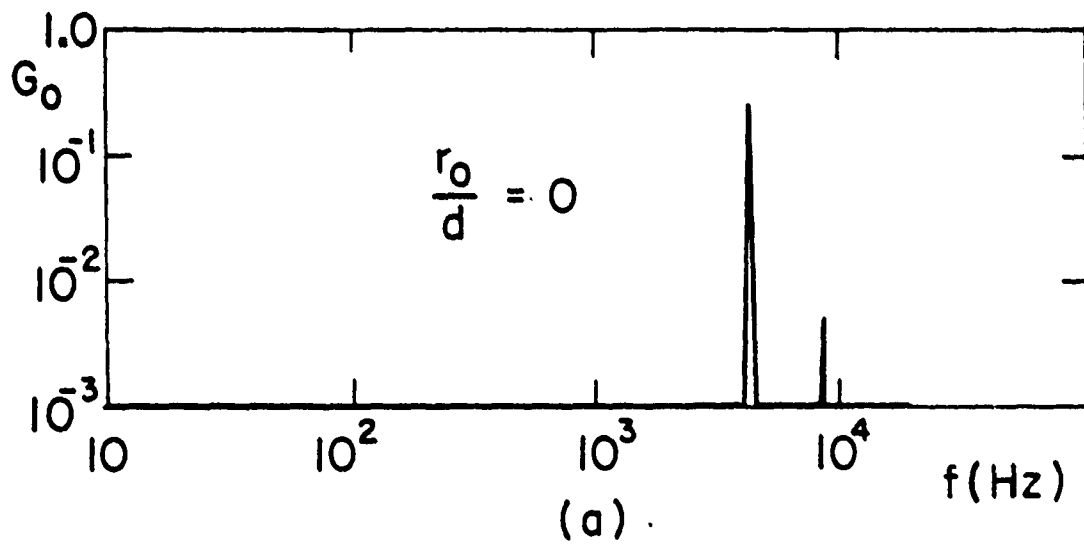
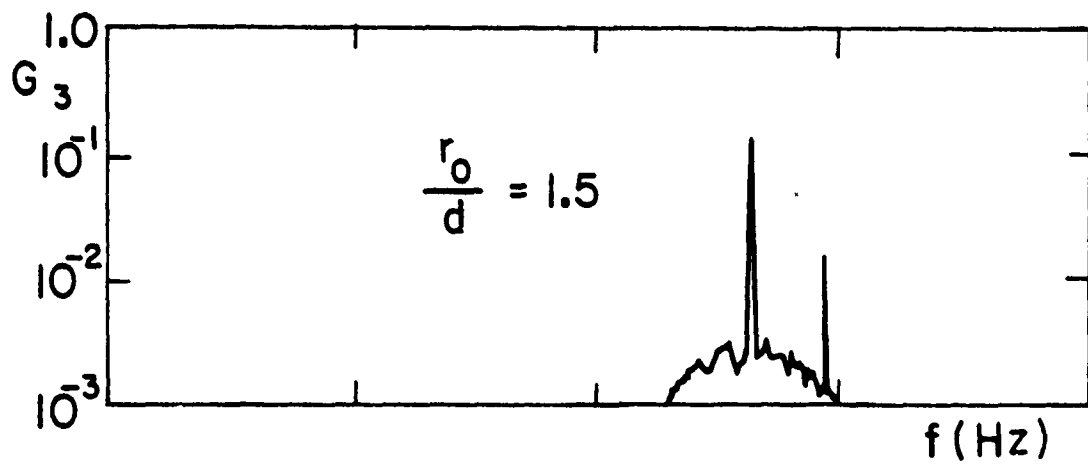
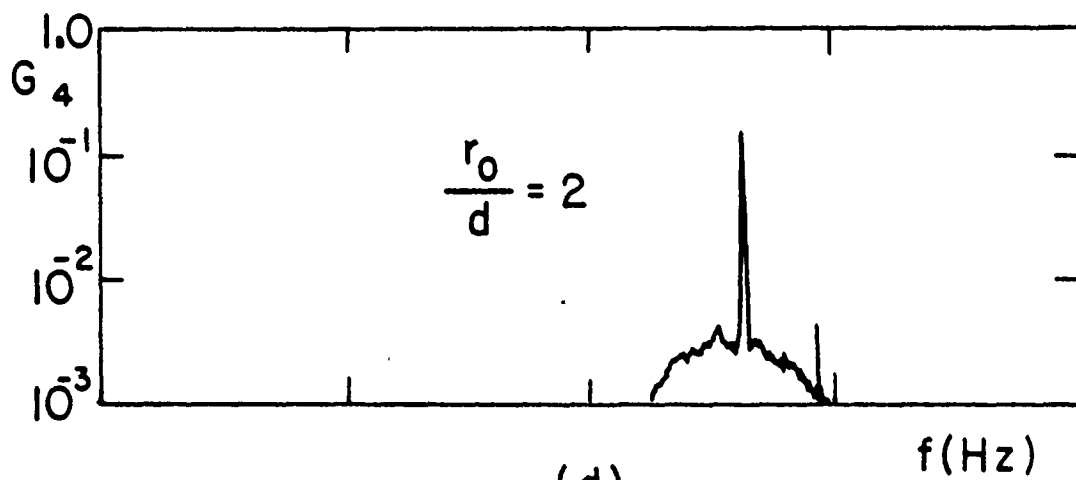


Fig. (3-22) Normalized Surface Pressure Power Spectra,  
 ( $M=0.9$ ,  $x_0/d=4.5$ )



(c)



(d)

Fig. (3-22) Concluded

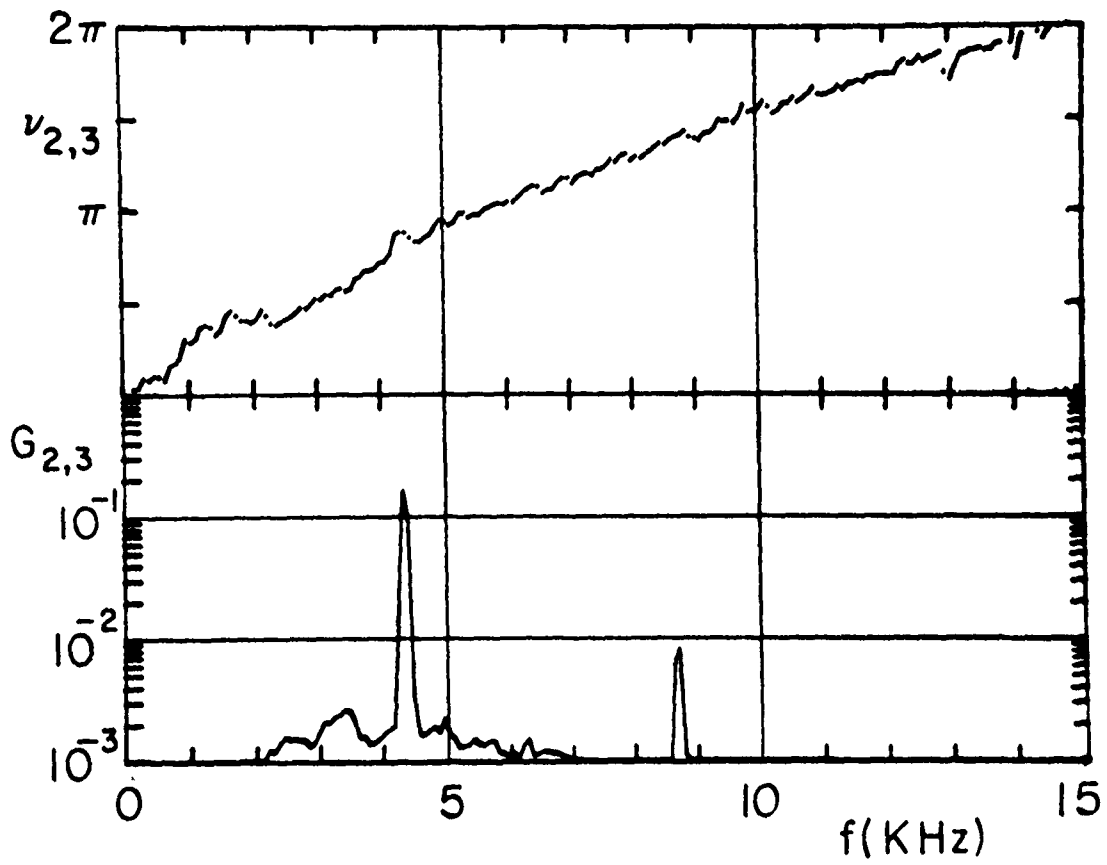


Fig. (3-23a) Cross-Spectrum and Phase Angle, indices refer to the sketch in Fig. (3-19), ( $M=.9$ ,  $x_0/d=4.5$ )

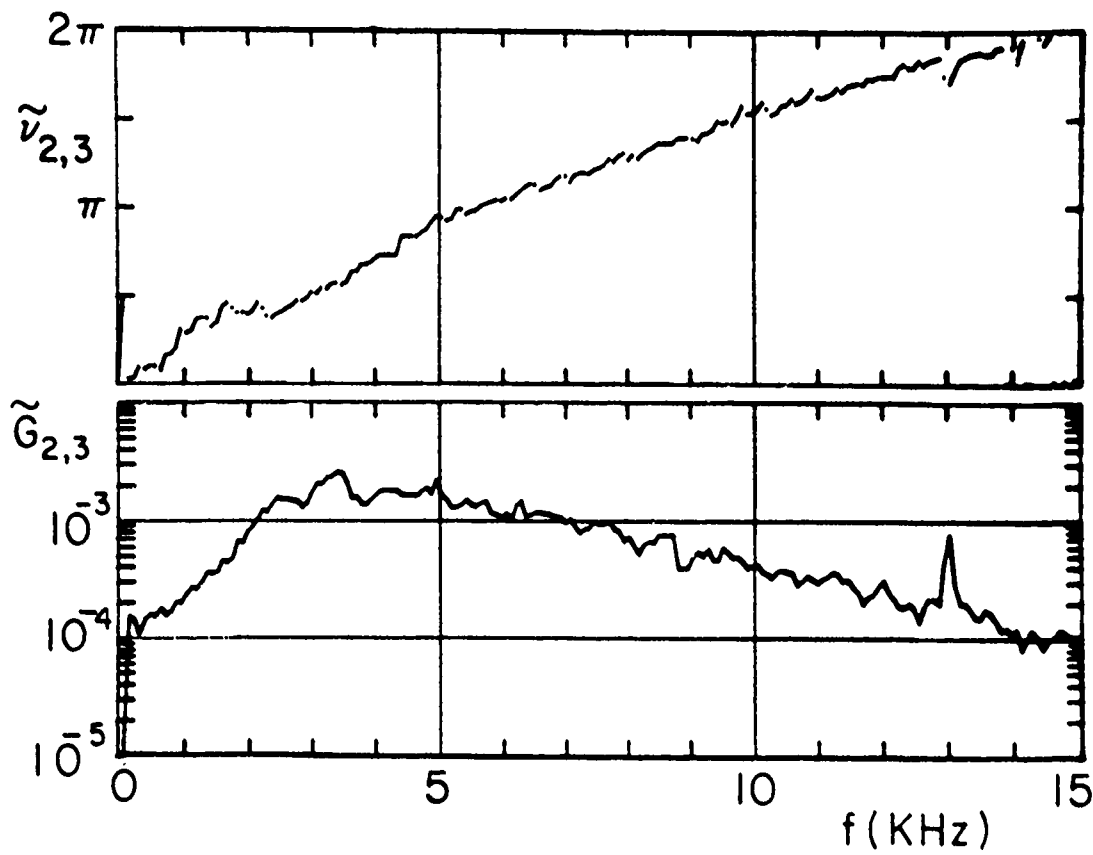
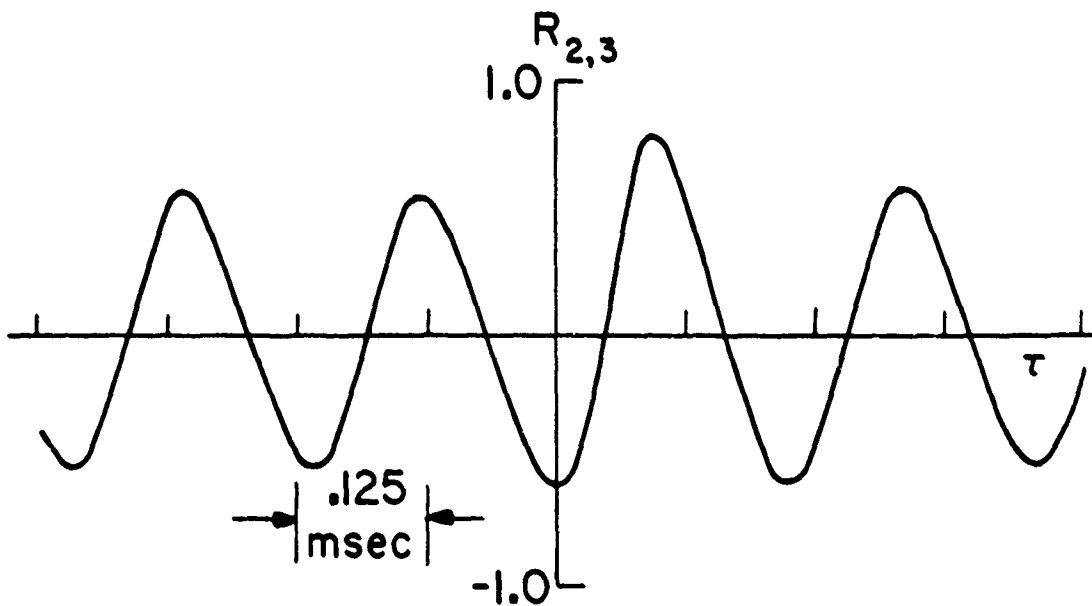
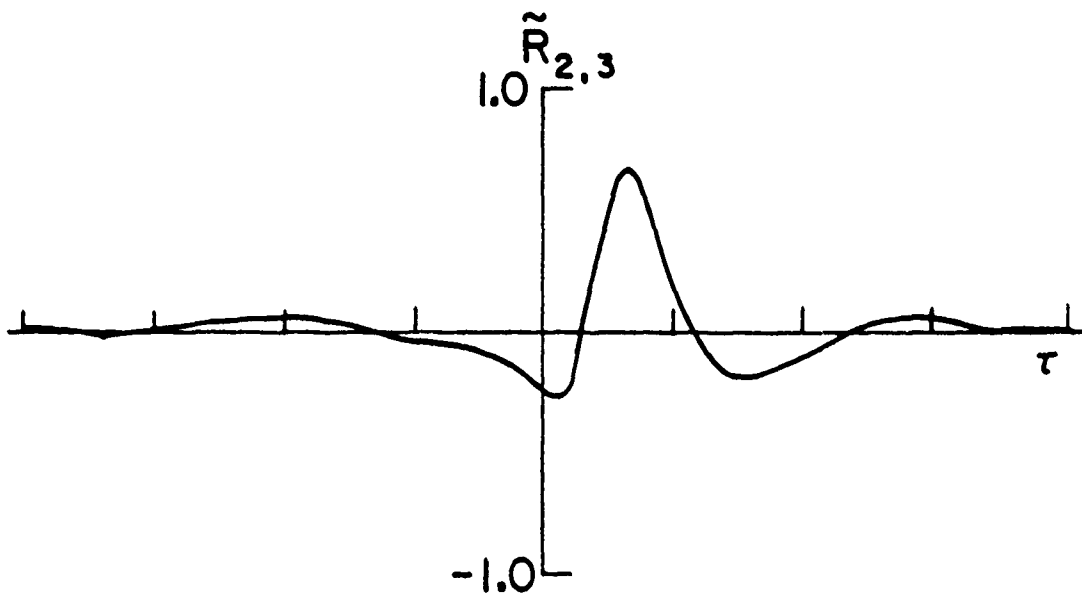


Fig. (3-23b) Prewhitened Cross-Spectrum and Phase Angle, same conditions as in Fig. (3-23a)



(a) before prewhitening



(b) after prewhitening

Fig. (3-24) Surface Pressure Cross-Correlation, same conditions as in Fig. (3-23a)

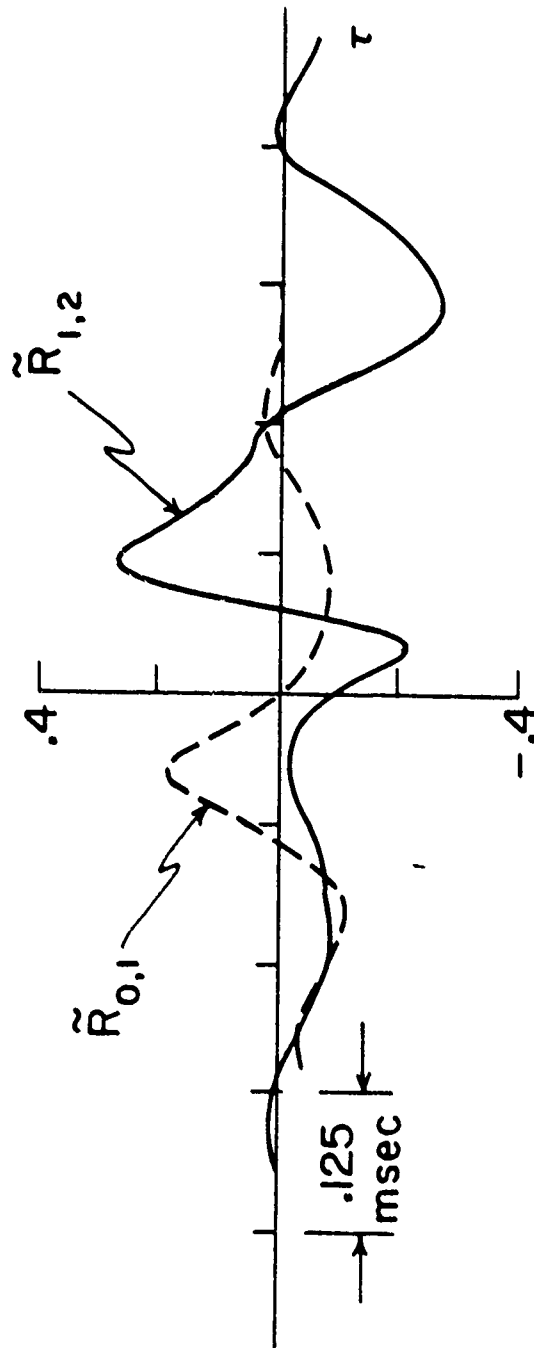


Fig. (3-25a) Space-Time Prewhitened Correlations at the Stagnation Region, indices refer to the sketch in Fig. (3-19), ( $M=.9$ ,  $x_0/d=4.5$ )

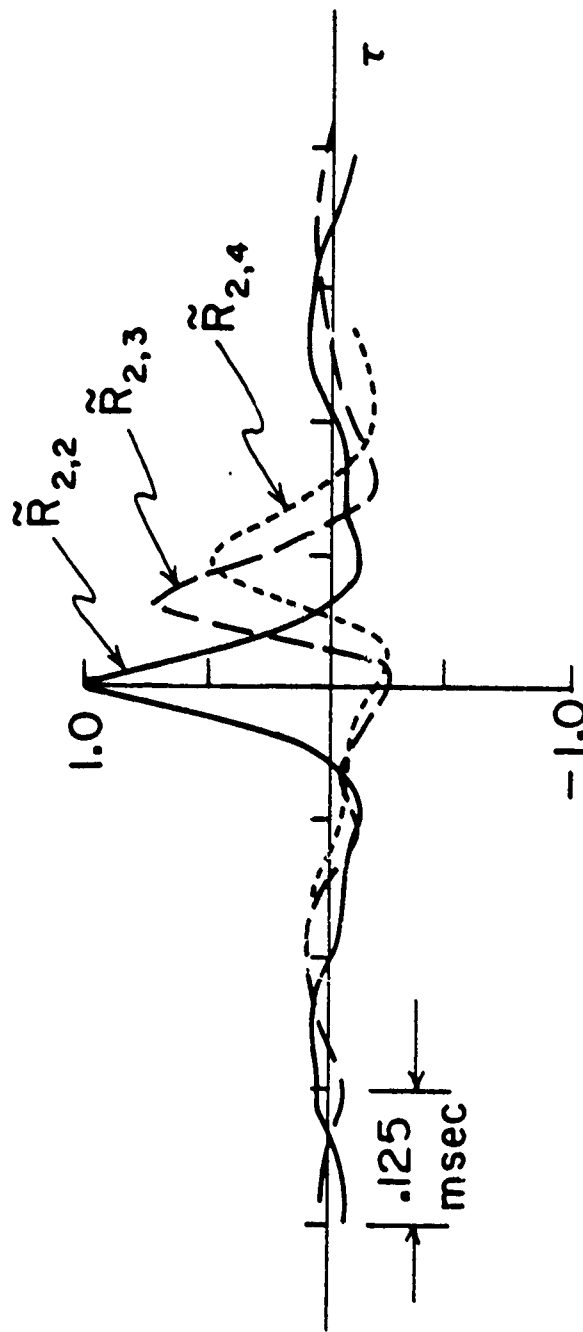


Fig. (3-25b) Space-Time Prewhitened Correlations, same conditions as in Fig. (3-25a)

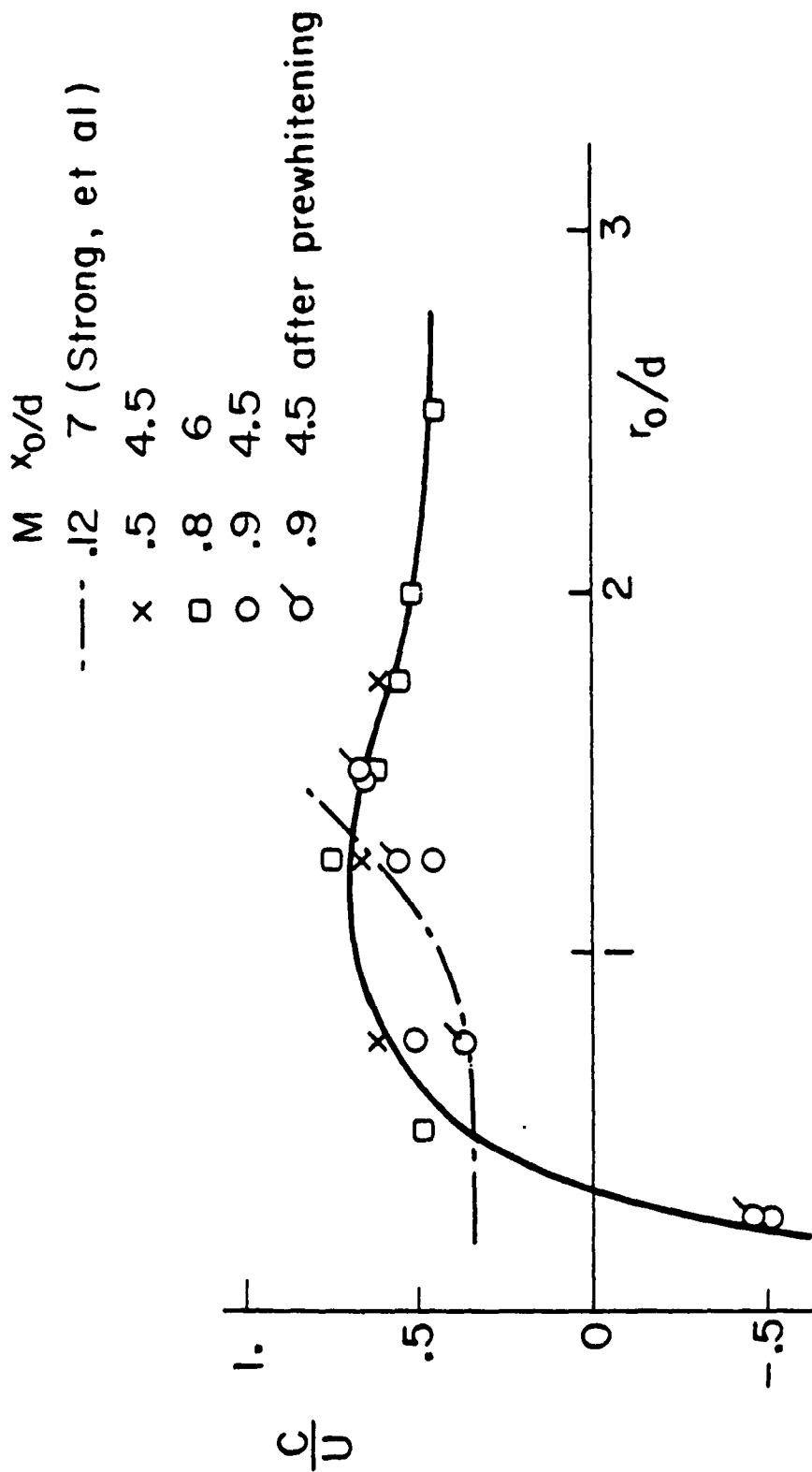
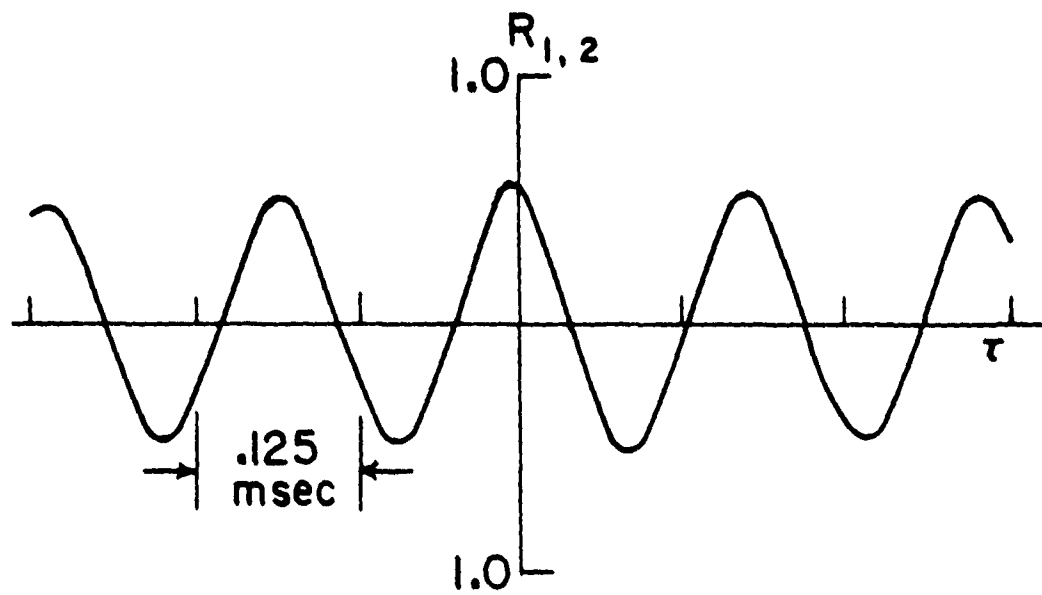
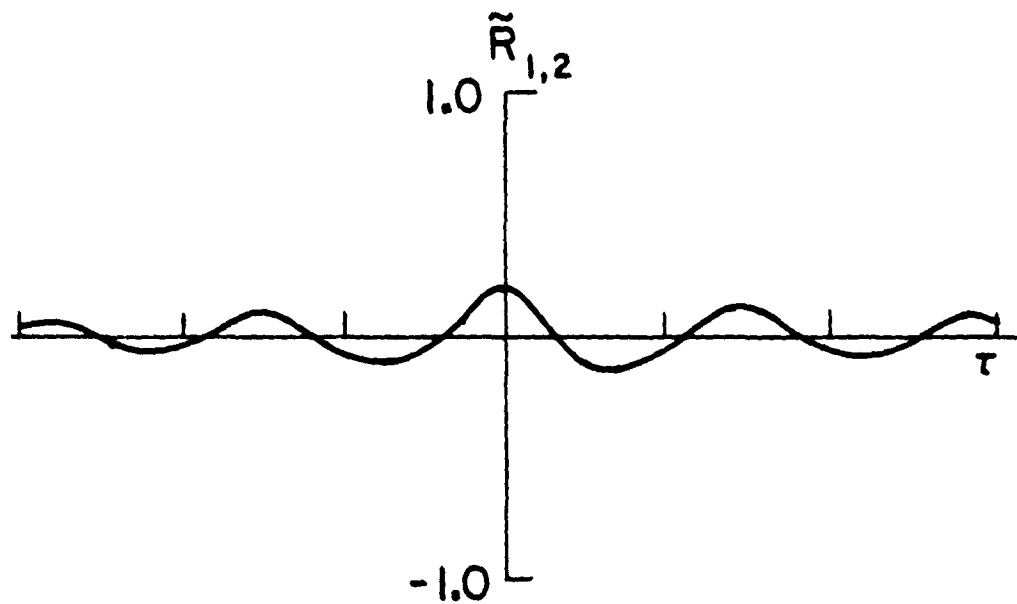


Fig. (3-26) Eddy Convection Velocity on the Plate



(a) before prewhitening



(b) after prewhitening

Fig. (3-27) Correlations between Surface Transducers at Different Azimuthal Angles,  $\theta_{01}=0^\circ$  and  $\theta_{02}=270^\circ$ , ( $M=.8$ ,  $x_0/d=4$ ,  $r_{01}=r_{02}=1.5d$ )

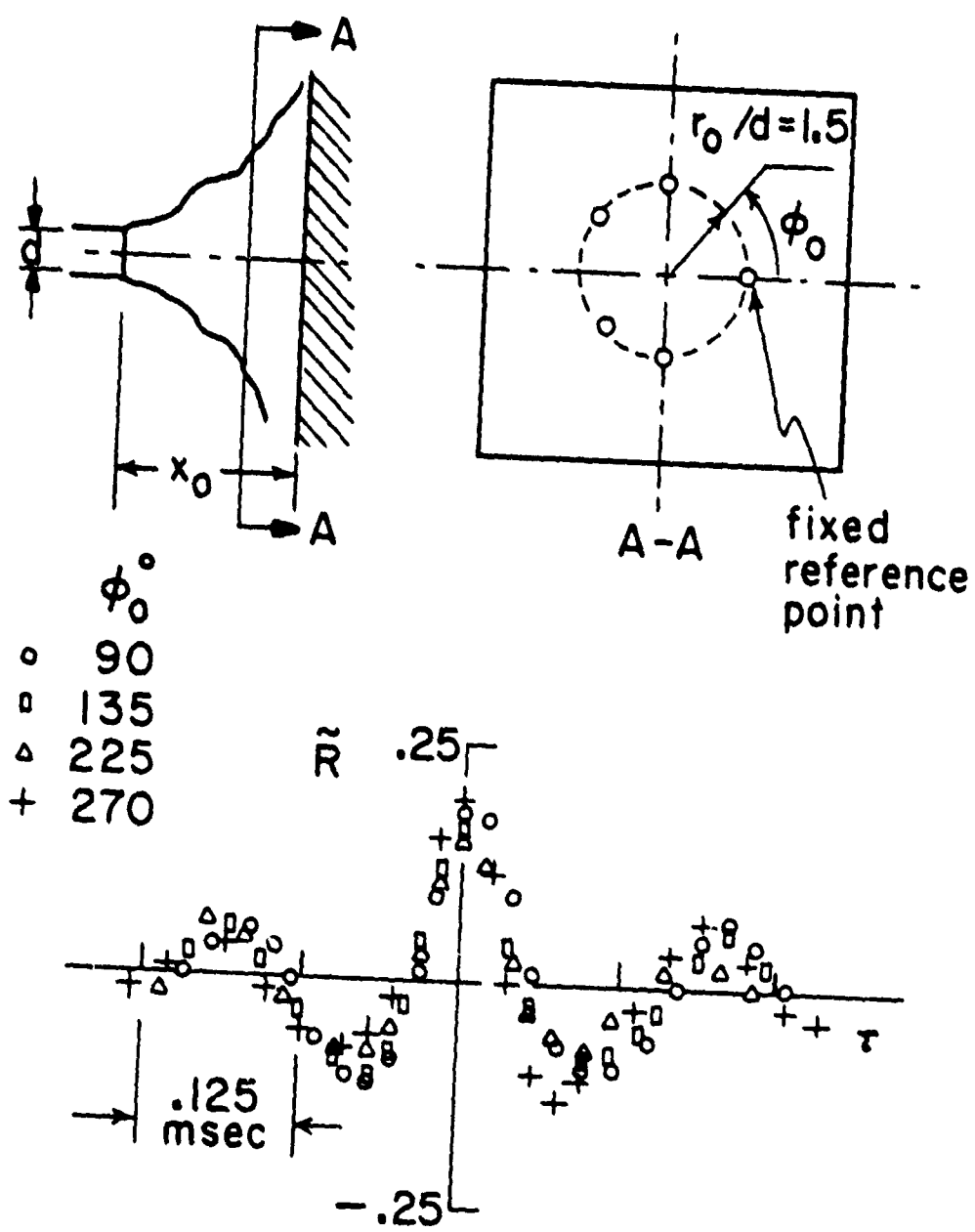


Fig. (3-28) Prewhitened Azimuthal Correlations, same conditions as in Fig. (3-27)

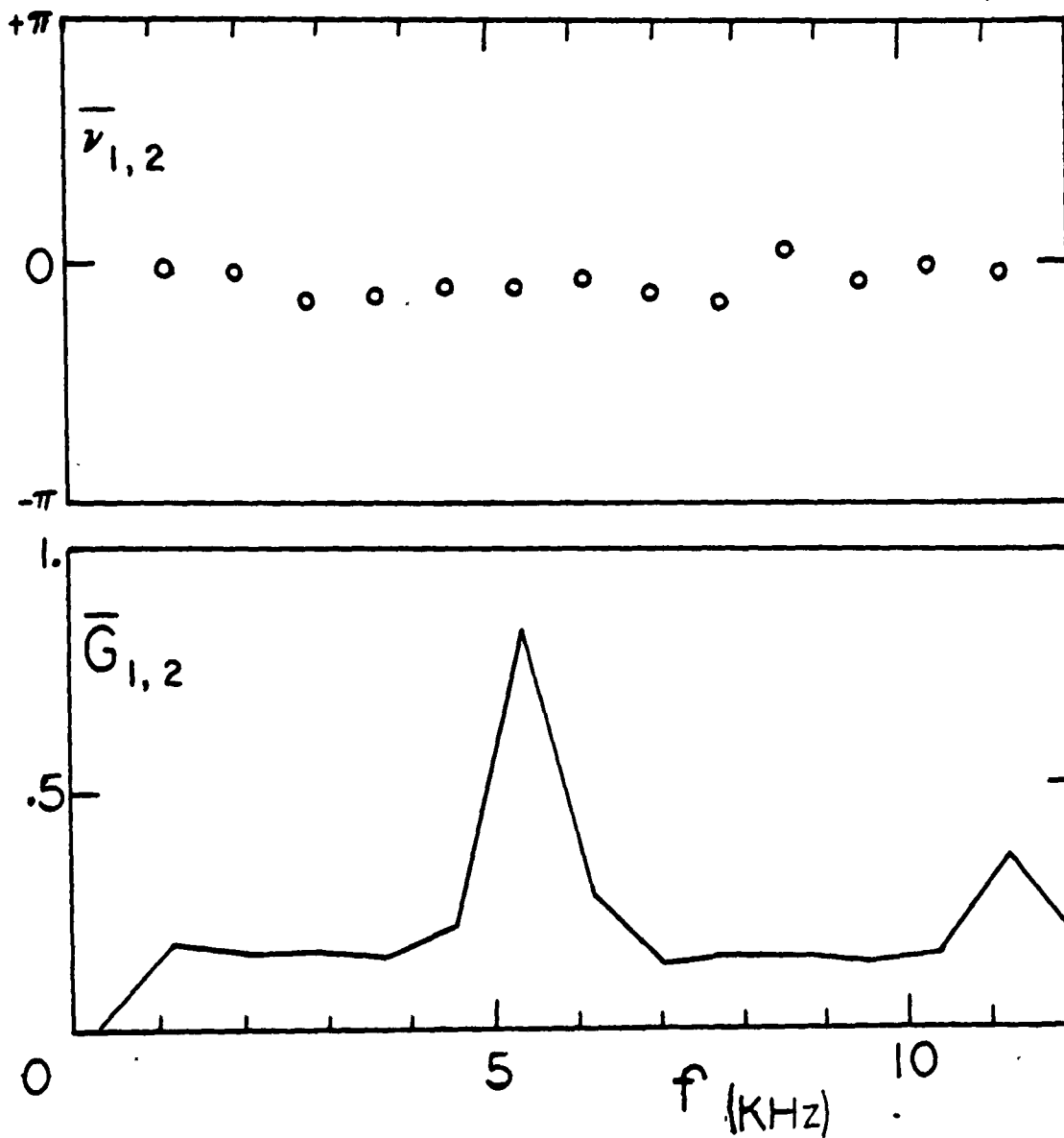


Fig. (3-29) Azimuthal Cross Spectrum (Smooth Estimate) and Phase Angle, same conditions as in Fig. (3-27)

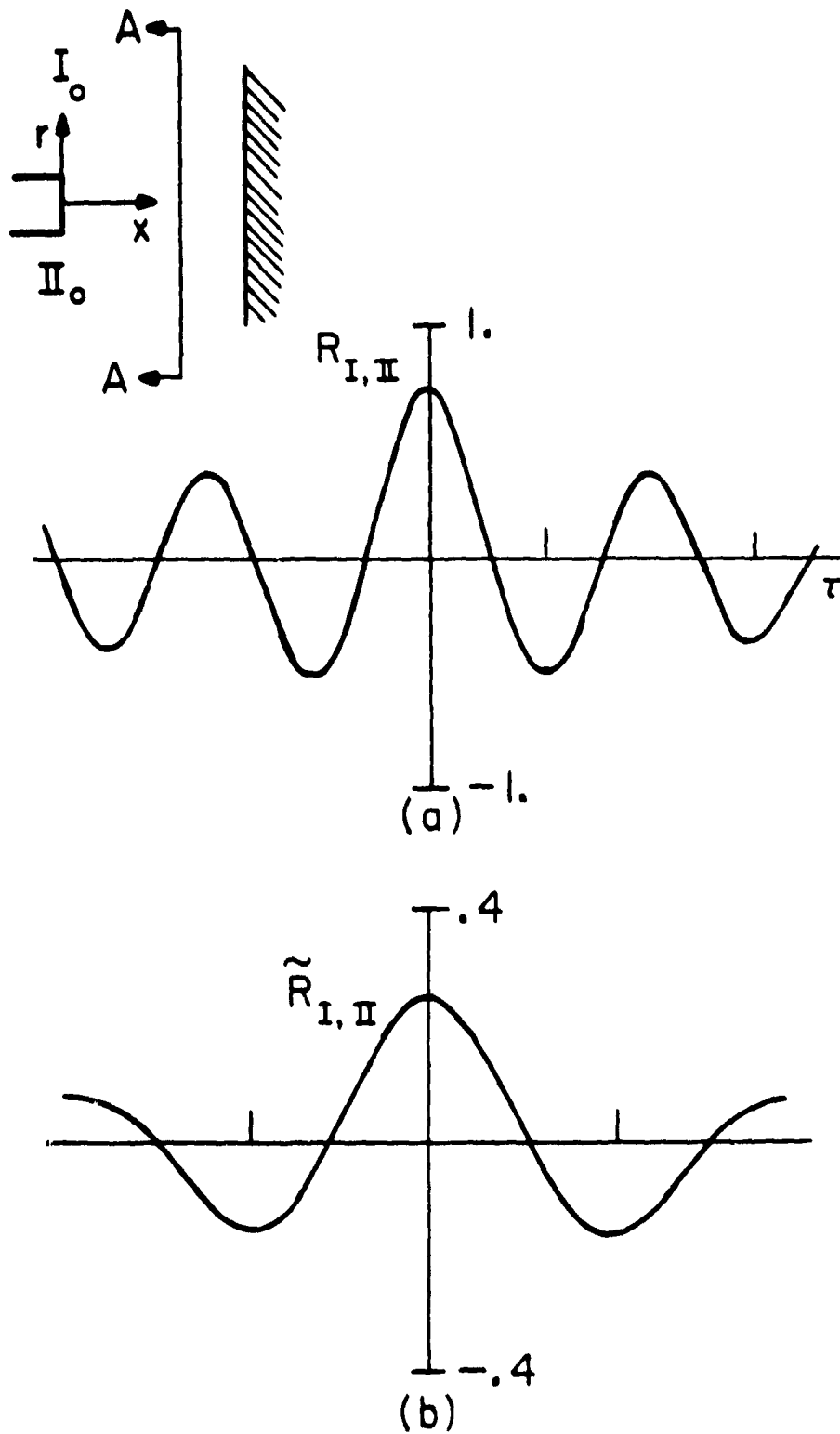


Fig. (3-30) Azimuthal Correlations at the Nozzle Exit Plane, (a) before and (b) after Prewhitening,  $\theta=135^\circ$ ,  $r_I=r_{II}=1.5d$ , ( $M=.8$ ,  $x_0/d=4$ )

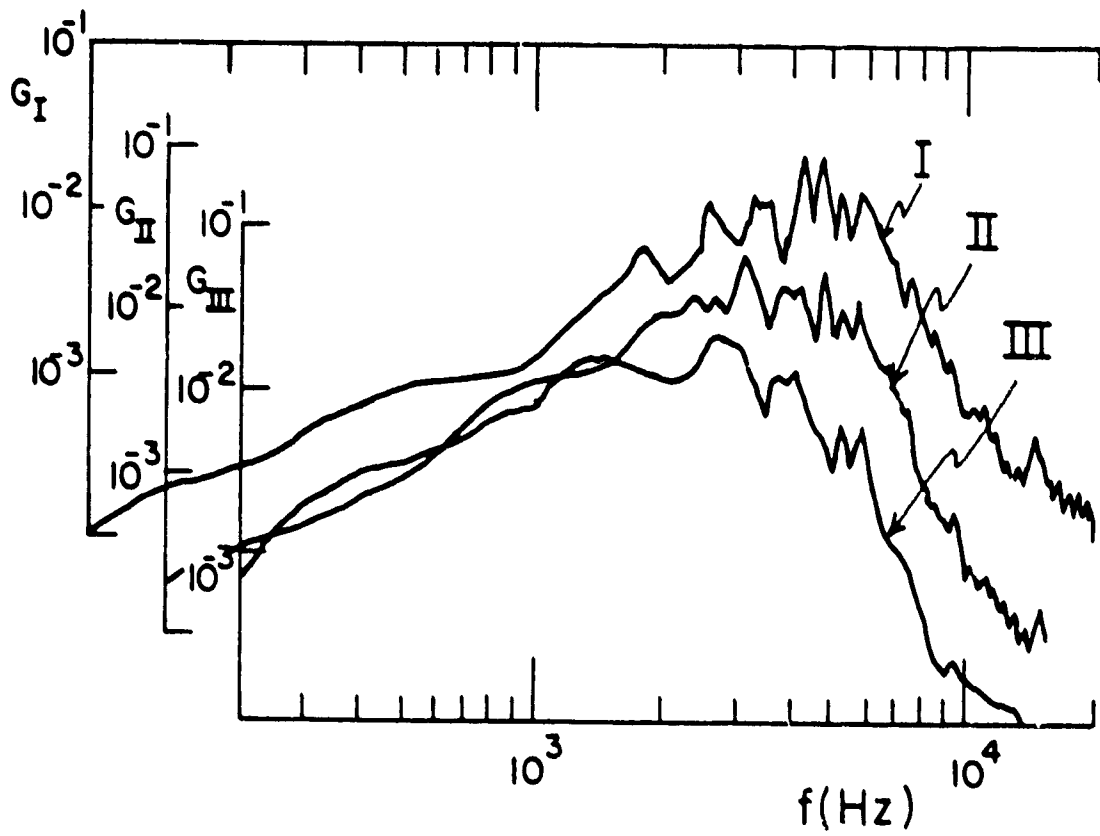
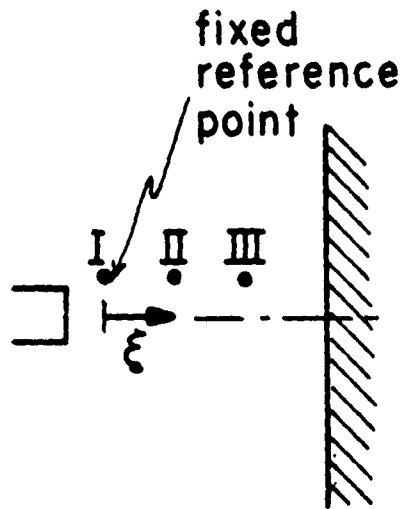


Fig. (4-1) Near Field Normalized Power Spectra, indices refer to the sketch in Fig. (4-2), ( $M=.8$ ,  $x_0/d=7$ )



	$x/d$	$r/d$
I	1.09	1.13
II	1.97	1.13
III	3.25	1.31

$$M = .8$$

$$x_0/d = 7$$

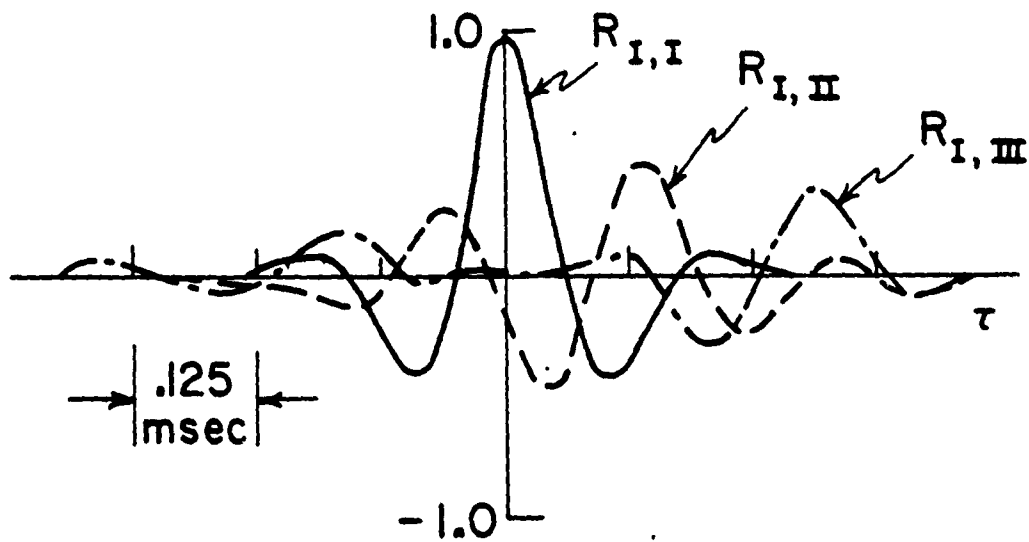


Fig. (4-2) Correlations of Near-Field Pressure Signals

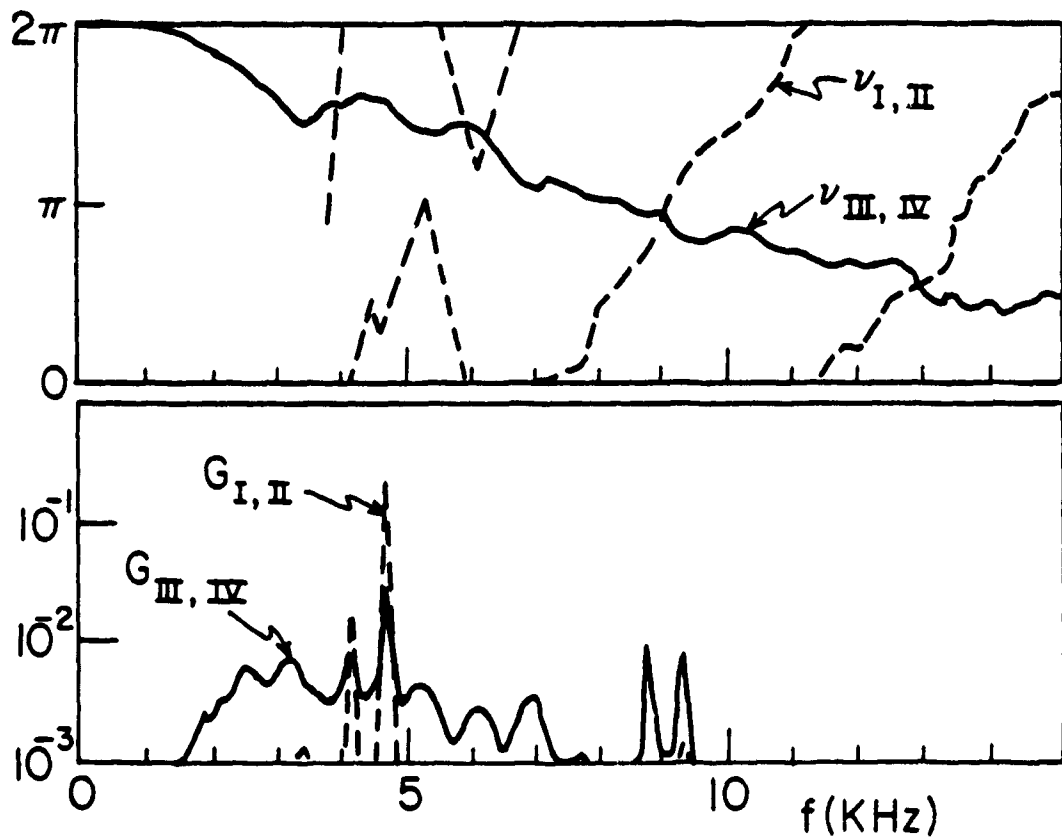
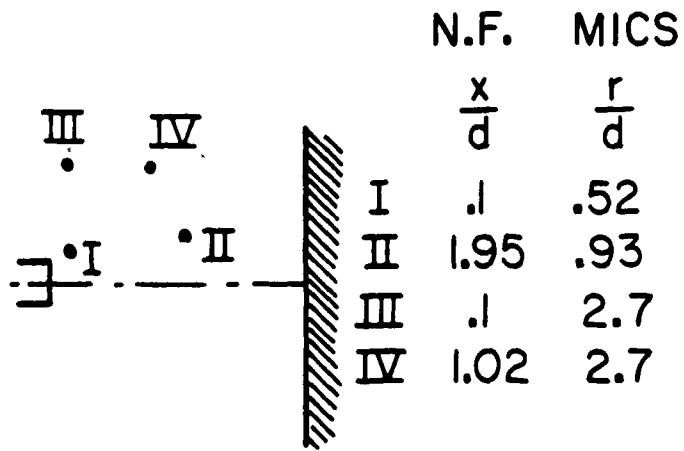


Fig. (4-3) Near Field Cross-Spectra and Phase Angle Functions,  
 ( $M=.9, x_0/d=5$ )

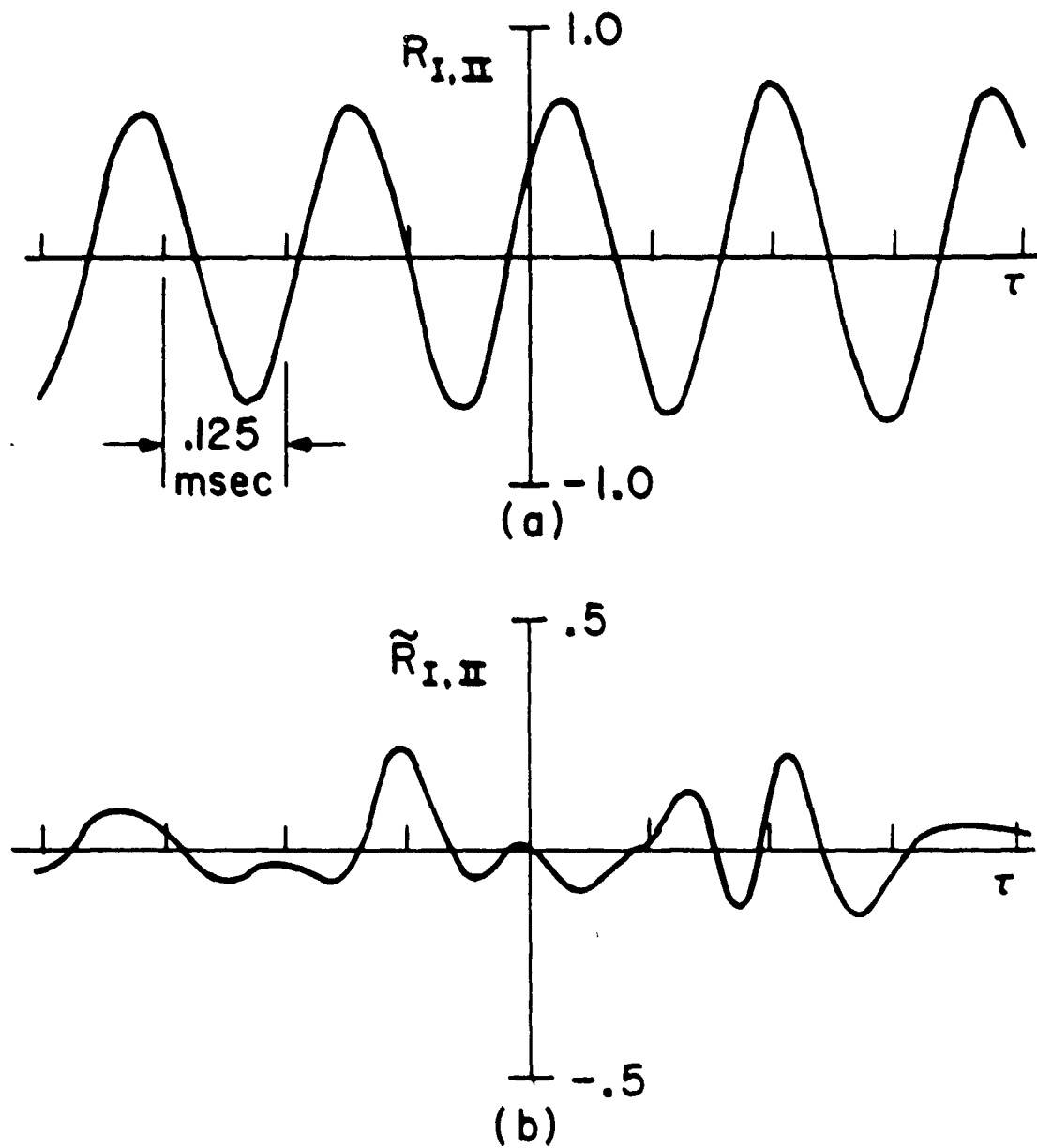


Fig. (4-4) Cross - Correlation of Near Field Pressure Signals,  
 (a) before and (b) after Prewhitening, same conditions  
 as in Fig. (4-3)

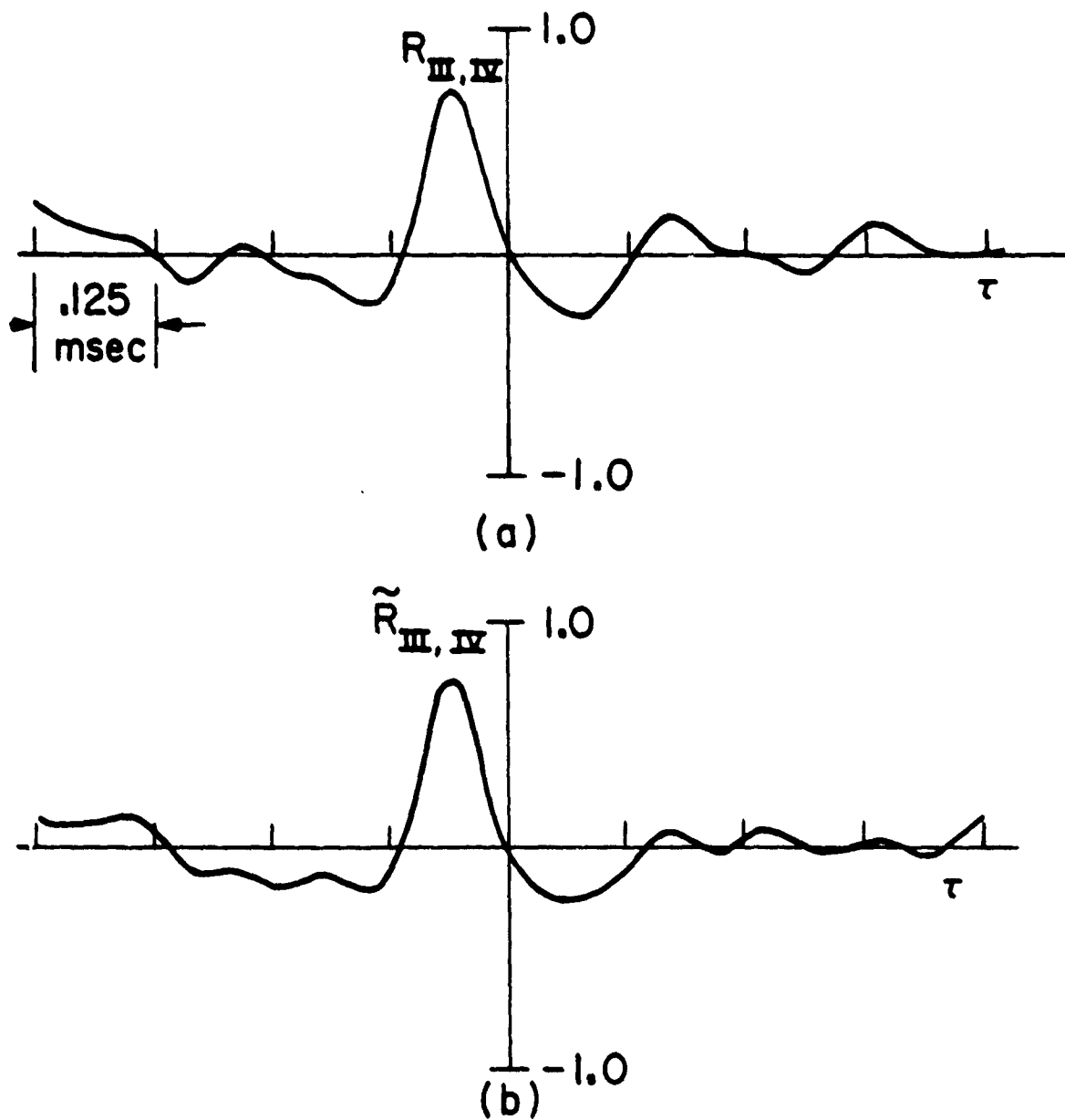


Fig. (4-5) Cross-Correlation of Near Field Pressure Signals,  
 (a) before and (b) after Prewhitening, same conditions  
 as in Fig. (4-3)

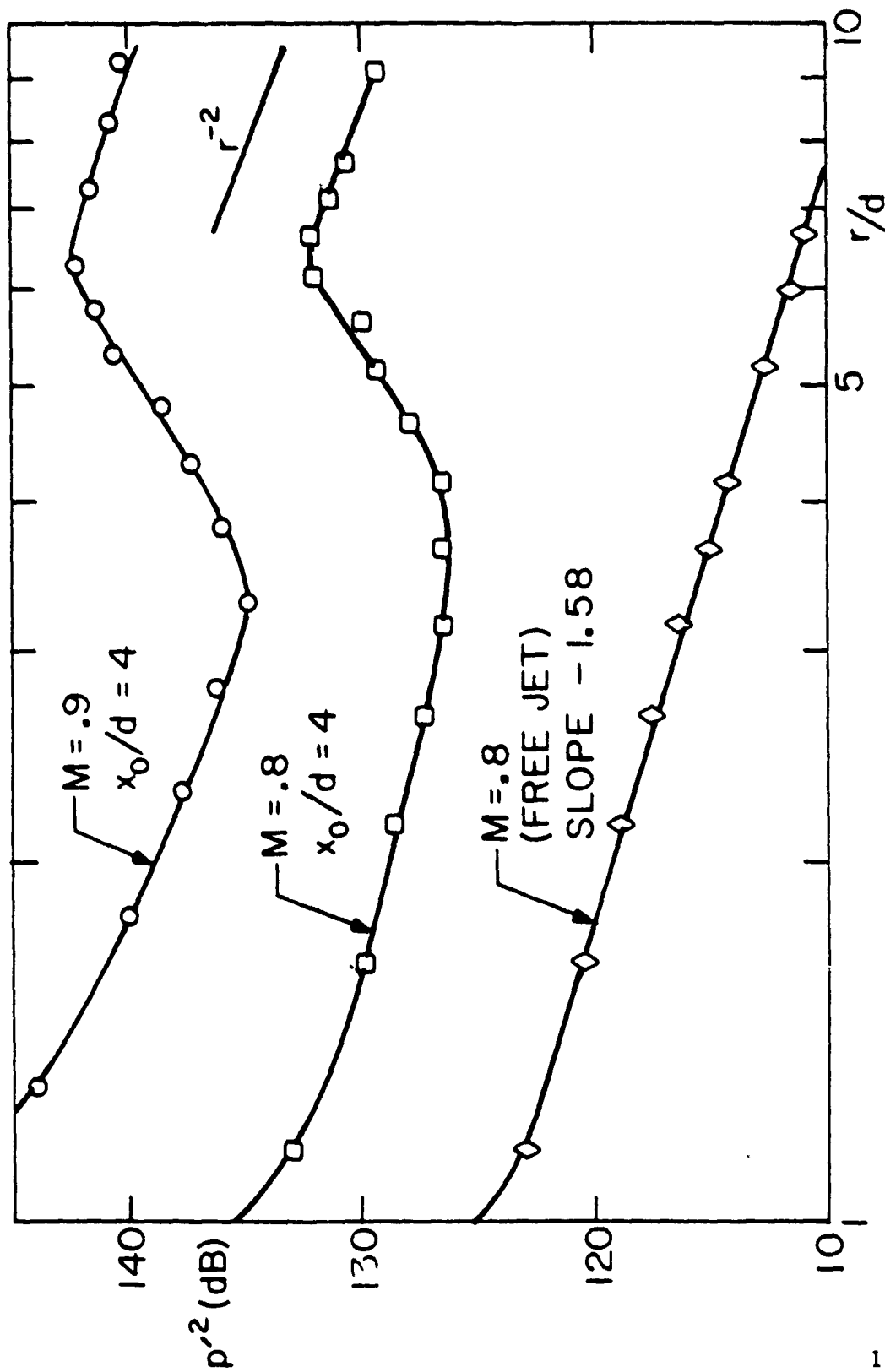


Fig. (4-6) Radial Variation of rms Pressure Fluctuations in Decibels, at the Nozzle Exit Plane

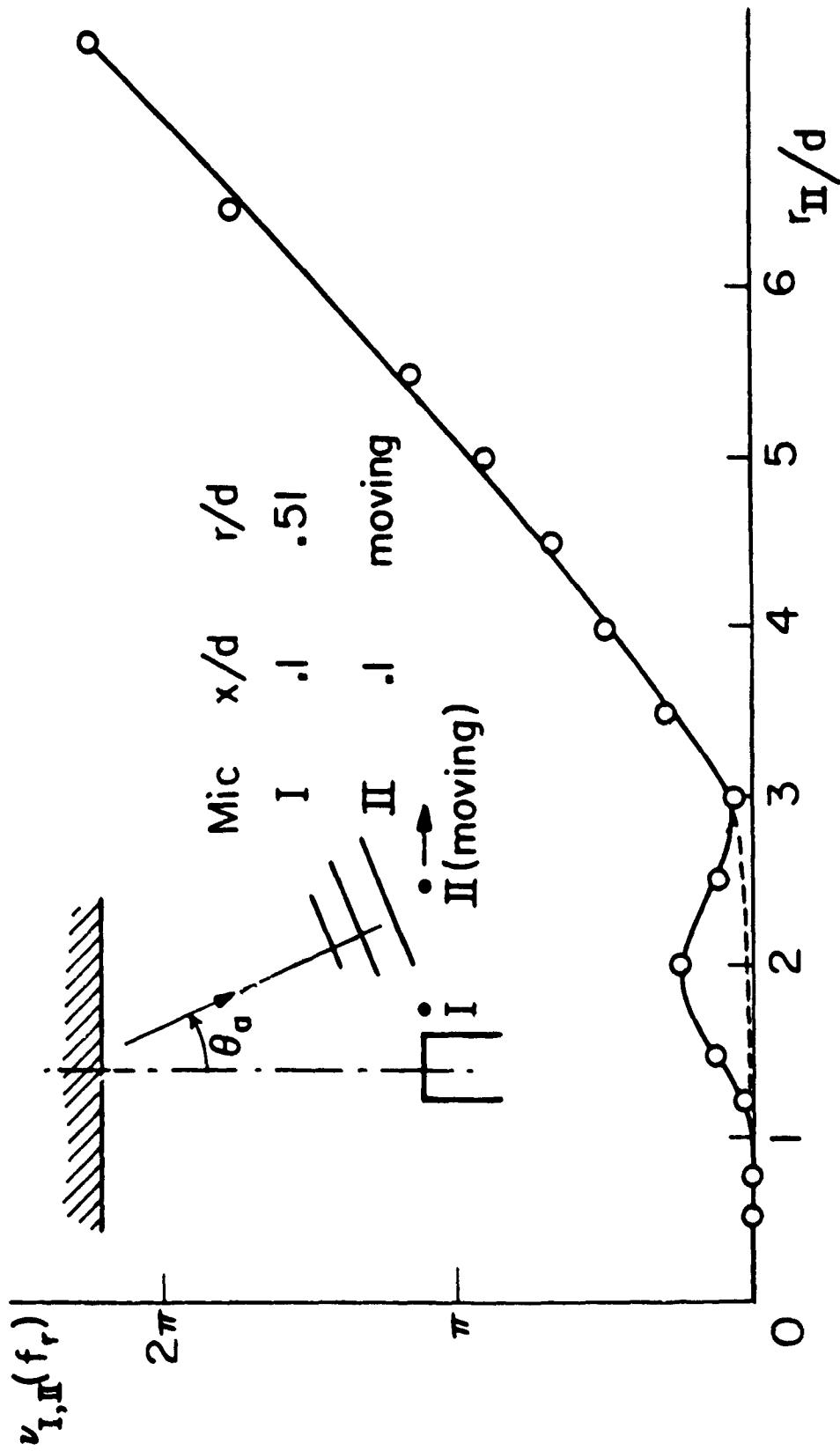
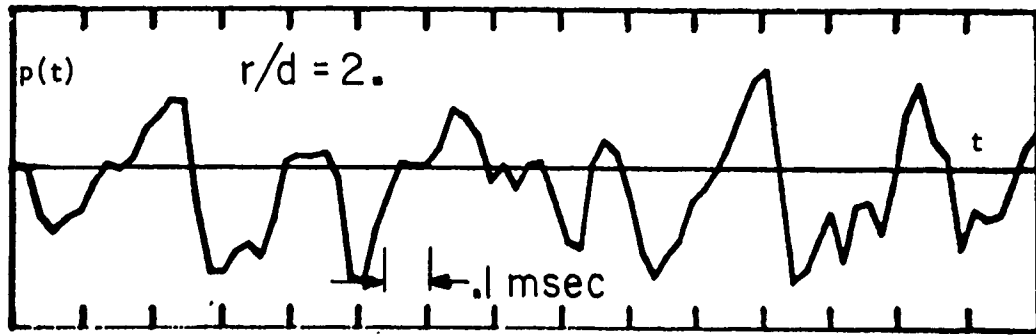
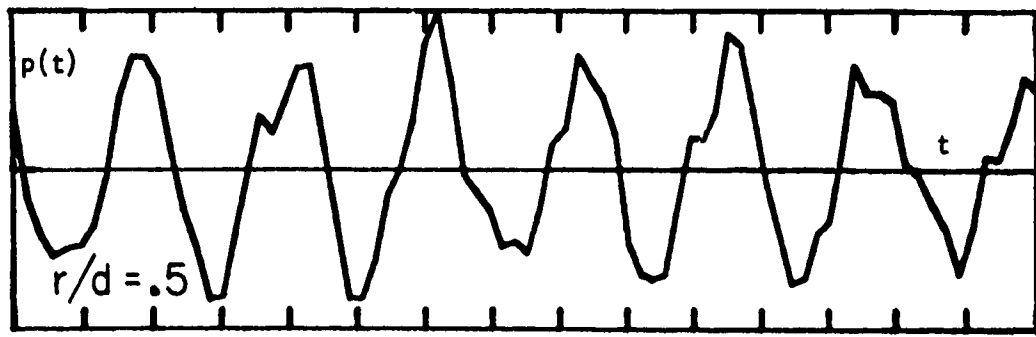
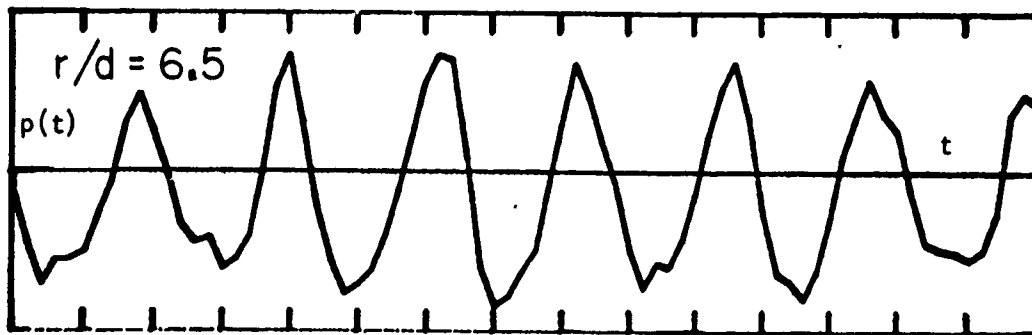


Fig. (4-7) Variation of the Phase Angle at the Resonance Frequency at the Nozzle Exit Plane, ( $M=0.9$ ,  $x_0/d=5$ )



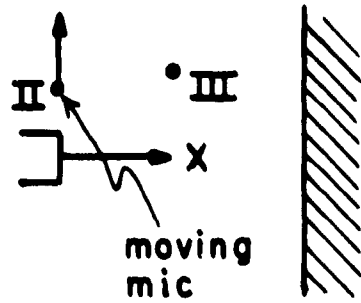
(a)

Fig. (4-8) Raw Pressure Signals at the Nozzle Exit Plane, same conditions as in Fig. (4-7)



(b)

Fig. (4-8) Concluded



$\frac{x_{III}}{d}$	$\frac{r_{III}}{d}$
1.02	2.7 (for $\frac{r_{II}}{d} = 2.5$ )
1.82	3.0 (for $\frac{r_{II}}{d} = 4$ & 6.5)

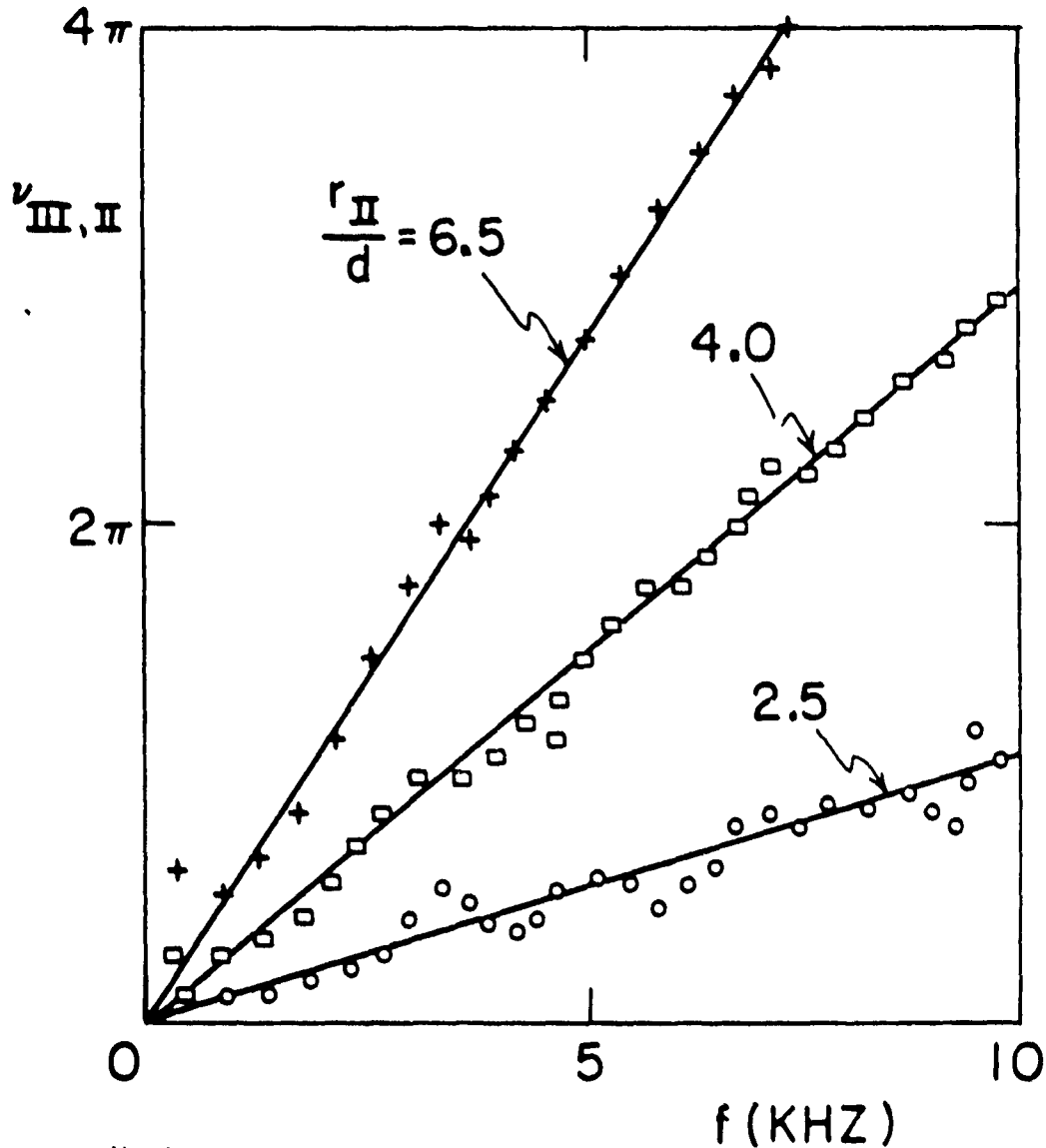


Fig. (4-9) Phase Angle Functions of Near Field Signals near the Nozzle, same conditions as in Fig. (4-7)

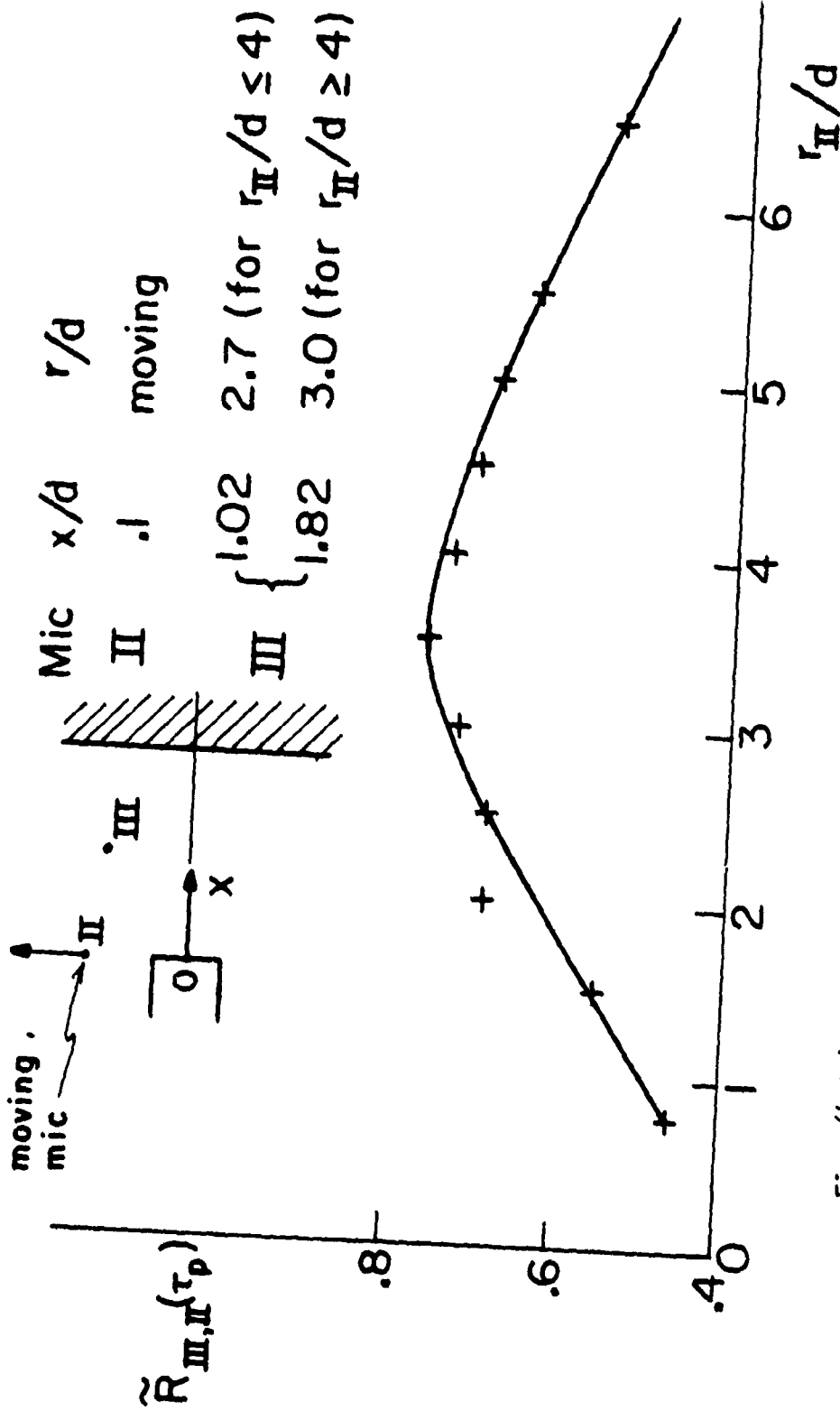


Fig. (4-10) Prewhitened Optimum Cross-Correlation Coefficients, same conditions as in Fig. (4-7)

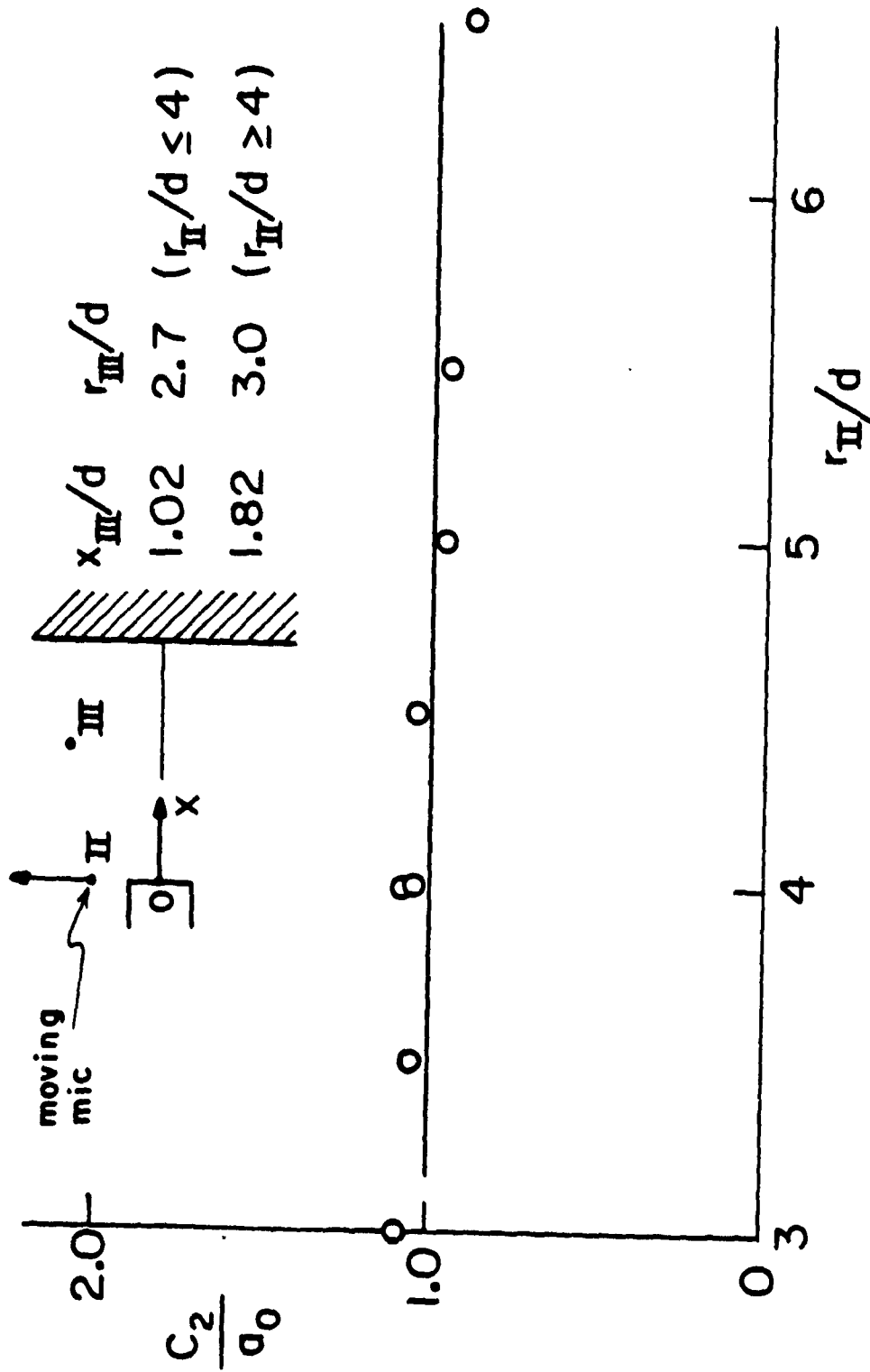


Fig. (4-11) Comparison between Measured Upstream Wave Velocity in  $\theta_a$ -Direction ( $c_2$ ), and Plane Acoustic Waves from Eqn. (4-2), ( $M=0.9$ ,  $x_0/d=5$ ,  $\theta_a=35^\circ$ )

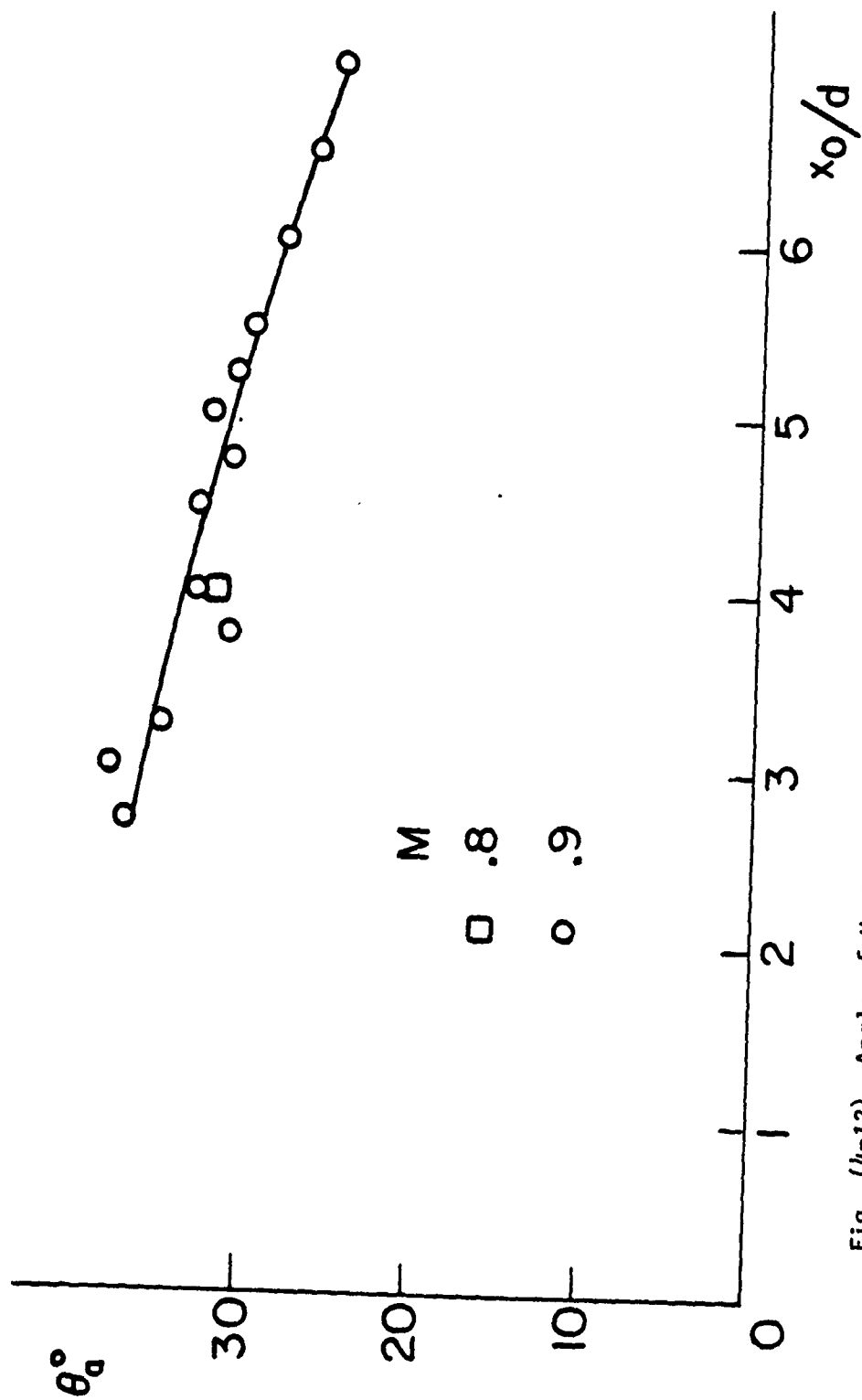


Fig. (4-12) Angle of Upstream Acoustic Propagation to the Jet Axis, for Different Plate Locations



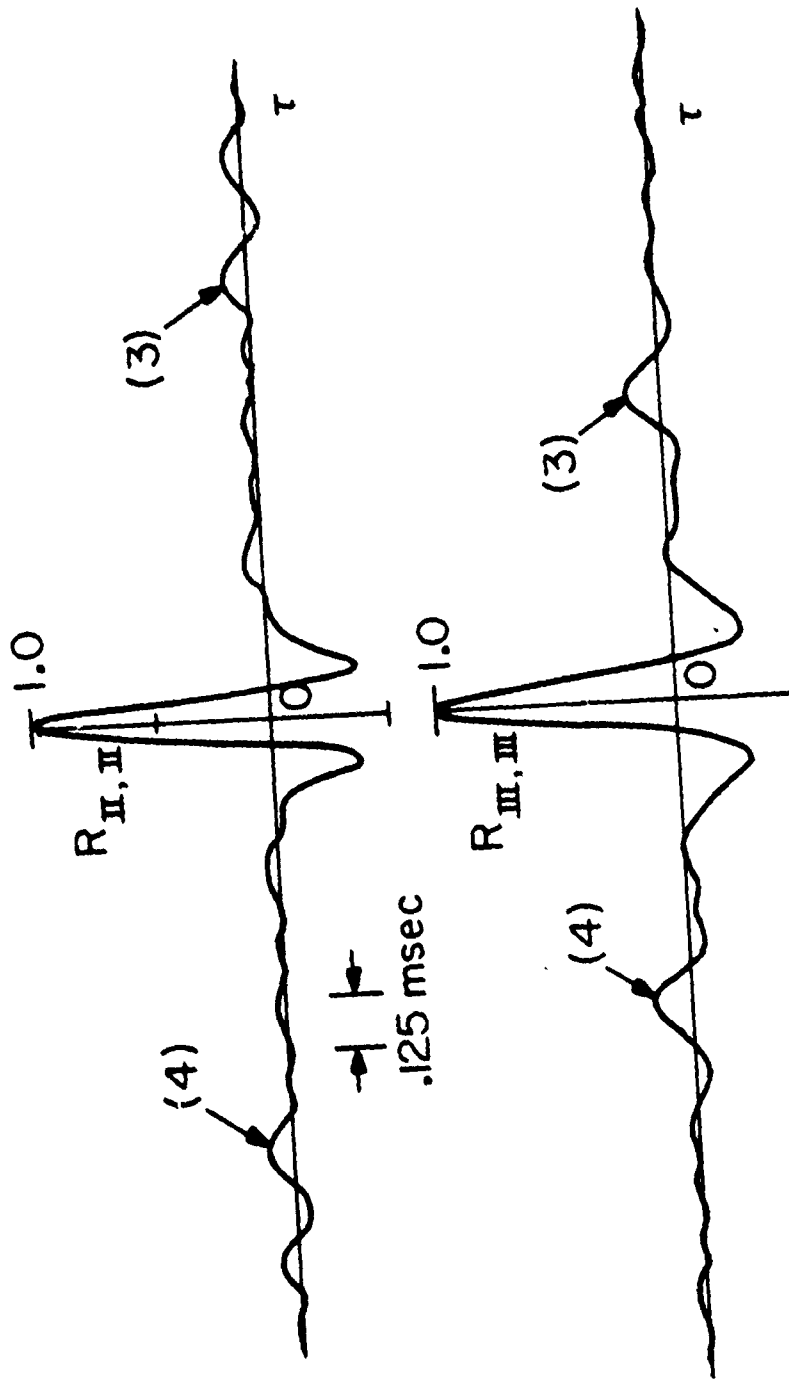


Fig. (4-14) Autocorrelations of Near Field Pressure Signals, indices refer to the sketch in Fig. (4-2), ( $M=.8$ ,  $x_0/d=7$ )

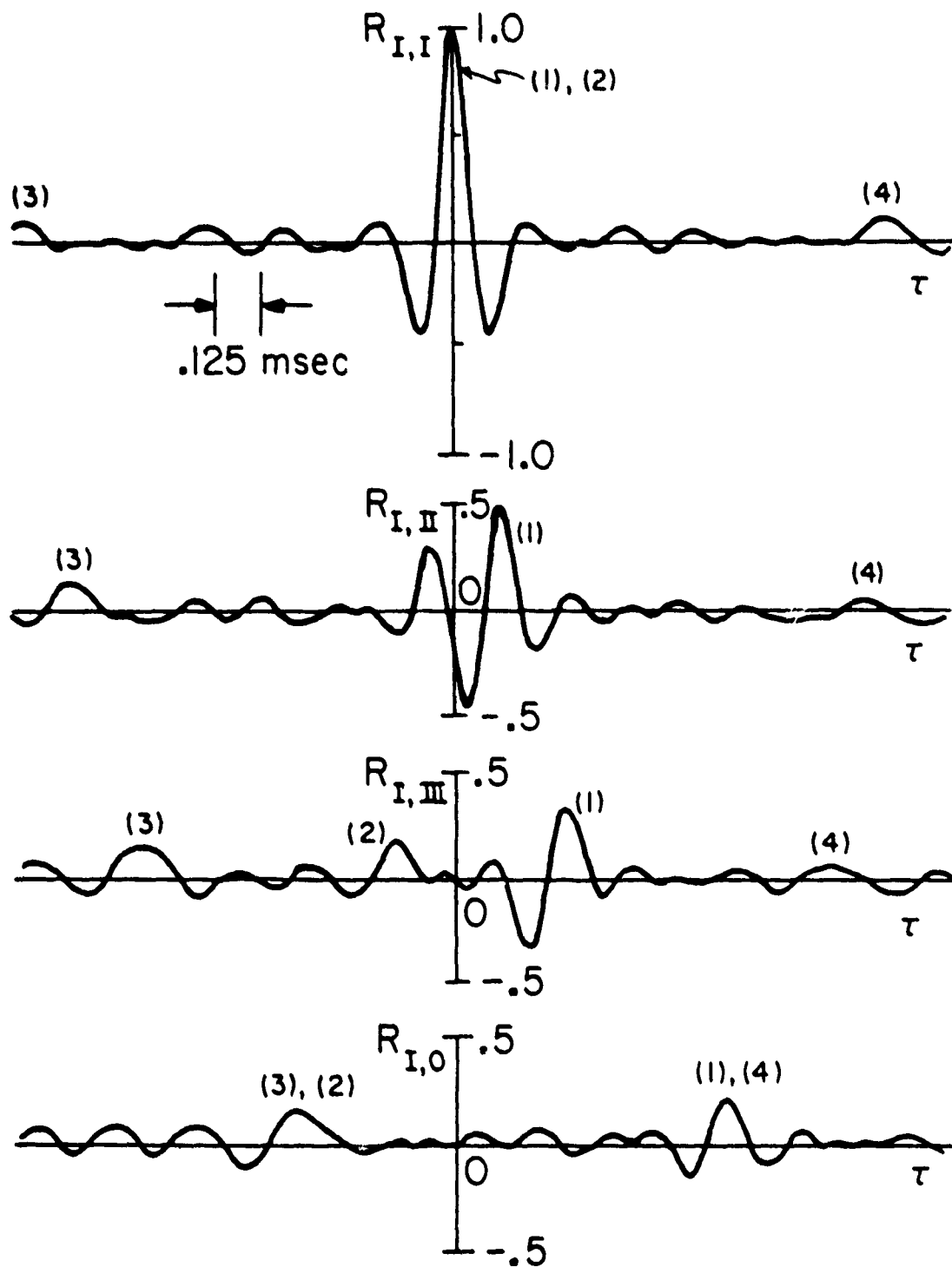


Fig. (4-15) Correlations of Near Field Pressure Signals, same conditions as in Fig. (4-14)

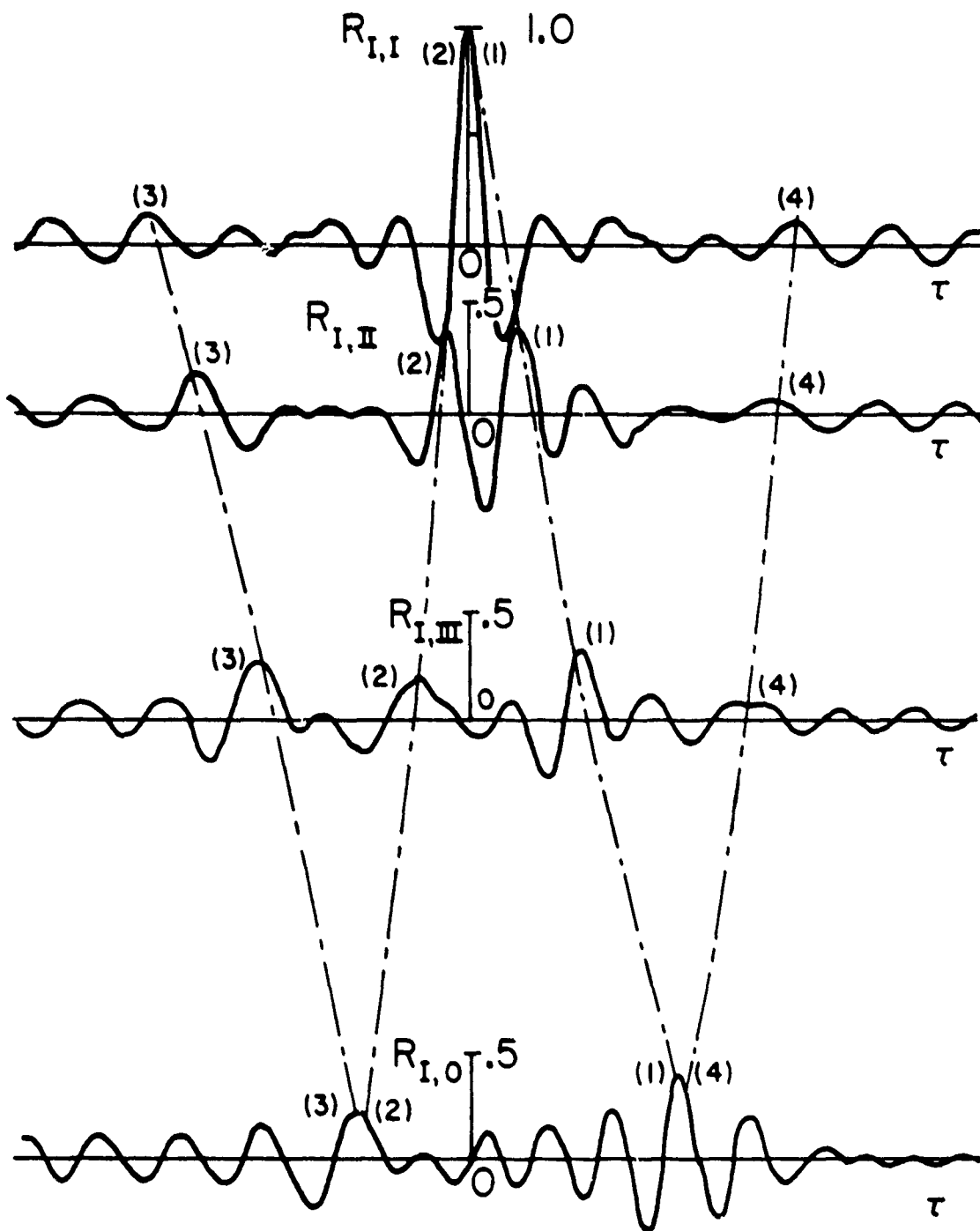


Fig. (4-16) Correlations of Near Field Pressure Signals, indices refer to the sketch in Fig. (4-2), ( $M=.8$ ,  $x_0/d=5.5$ )

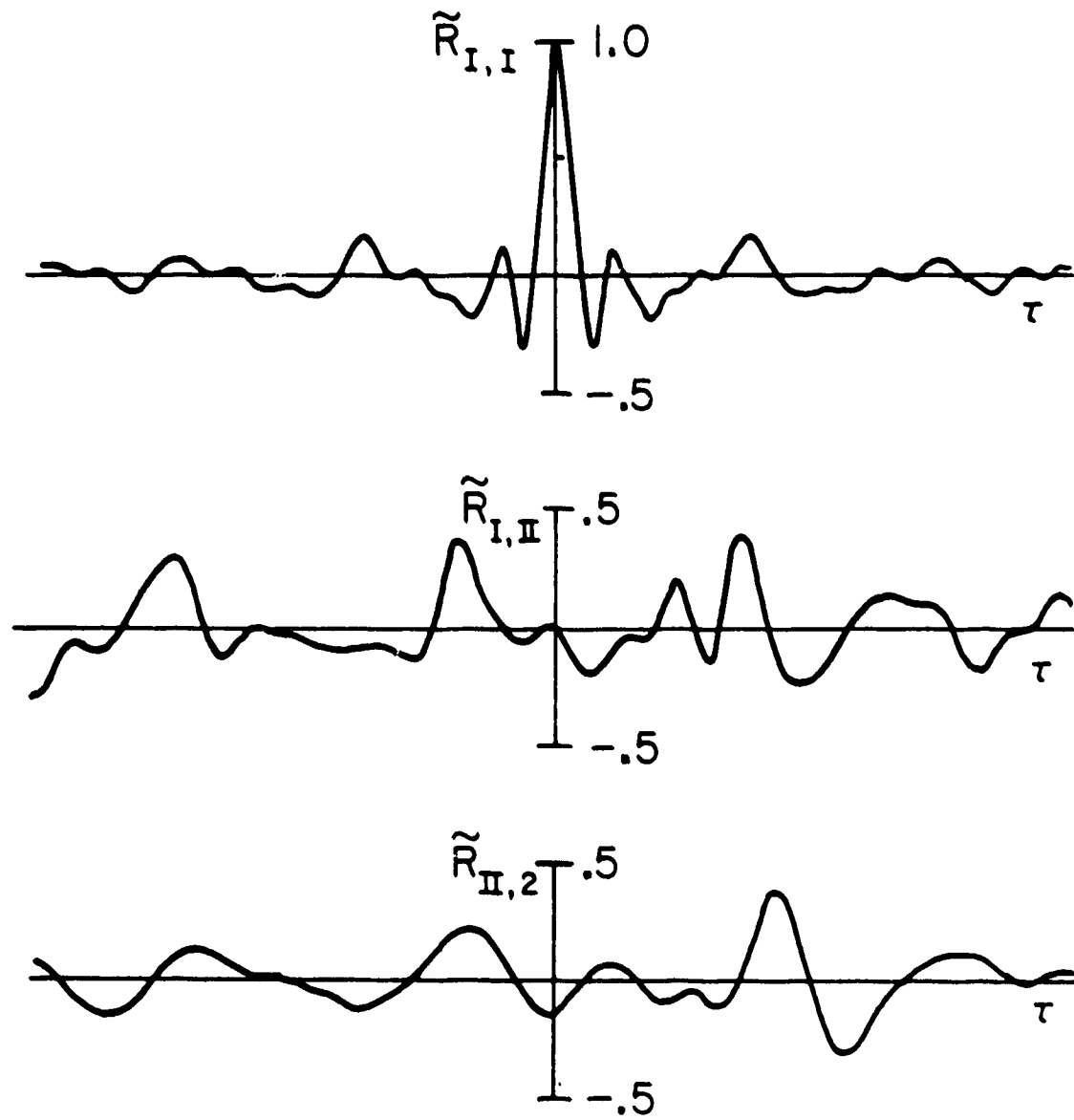


Fig. (4-17) Prewhitened Correlations of a Resonance Case, indices refer to the sketch in Fig. (4-2) ( $M=.9, x_0/d=4$ )

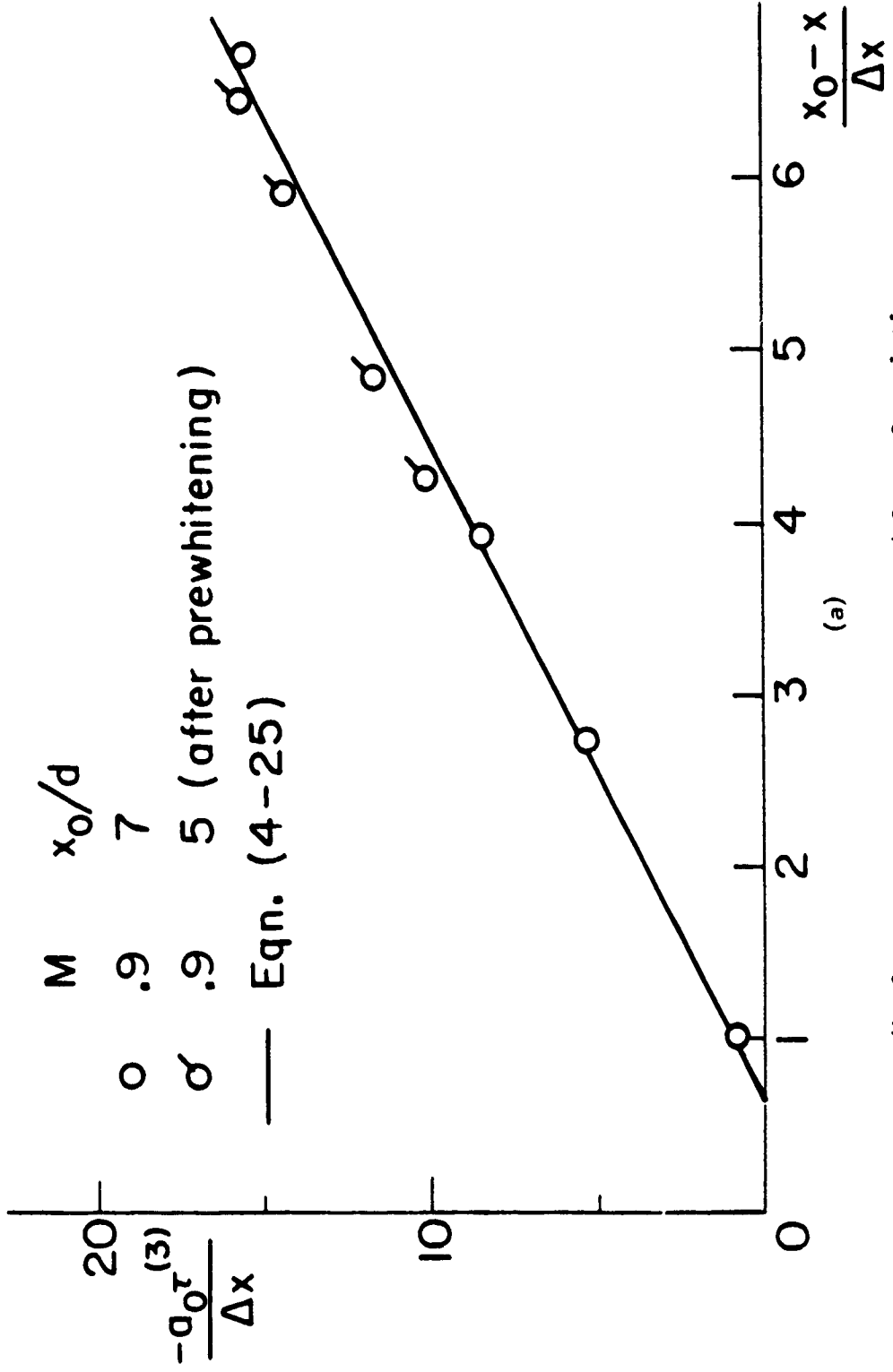


Fig. (4-18) Comparison between Measured Cross-Correlations  $\tau^{(3)}$  and the Model

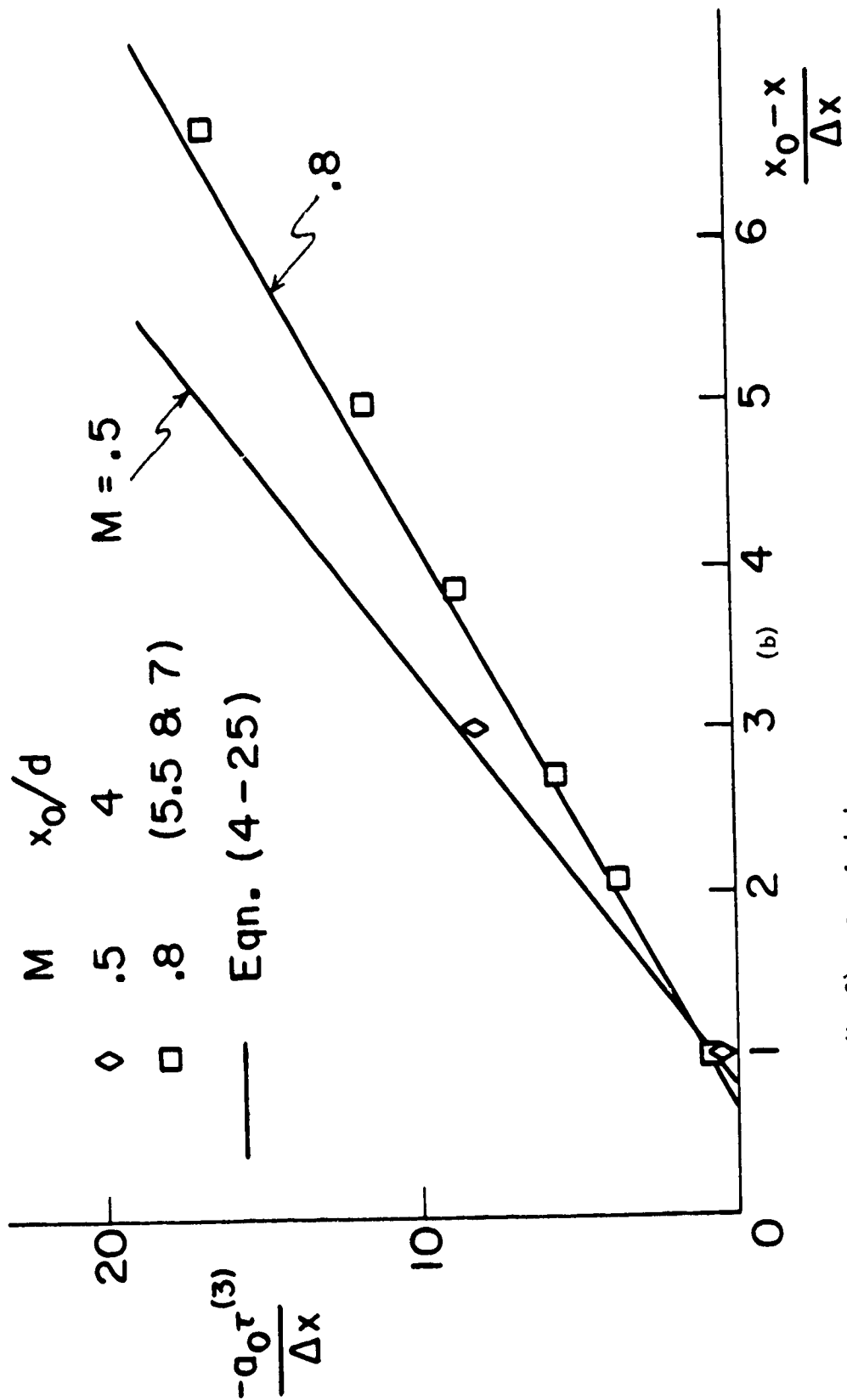


Fig. (4-18) Concluded

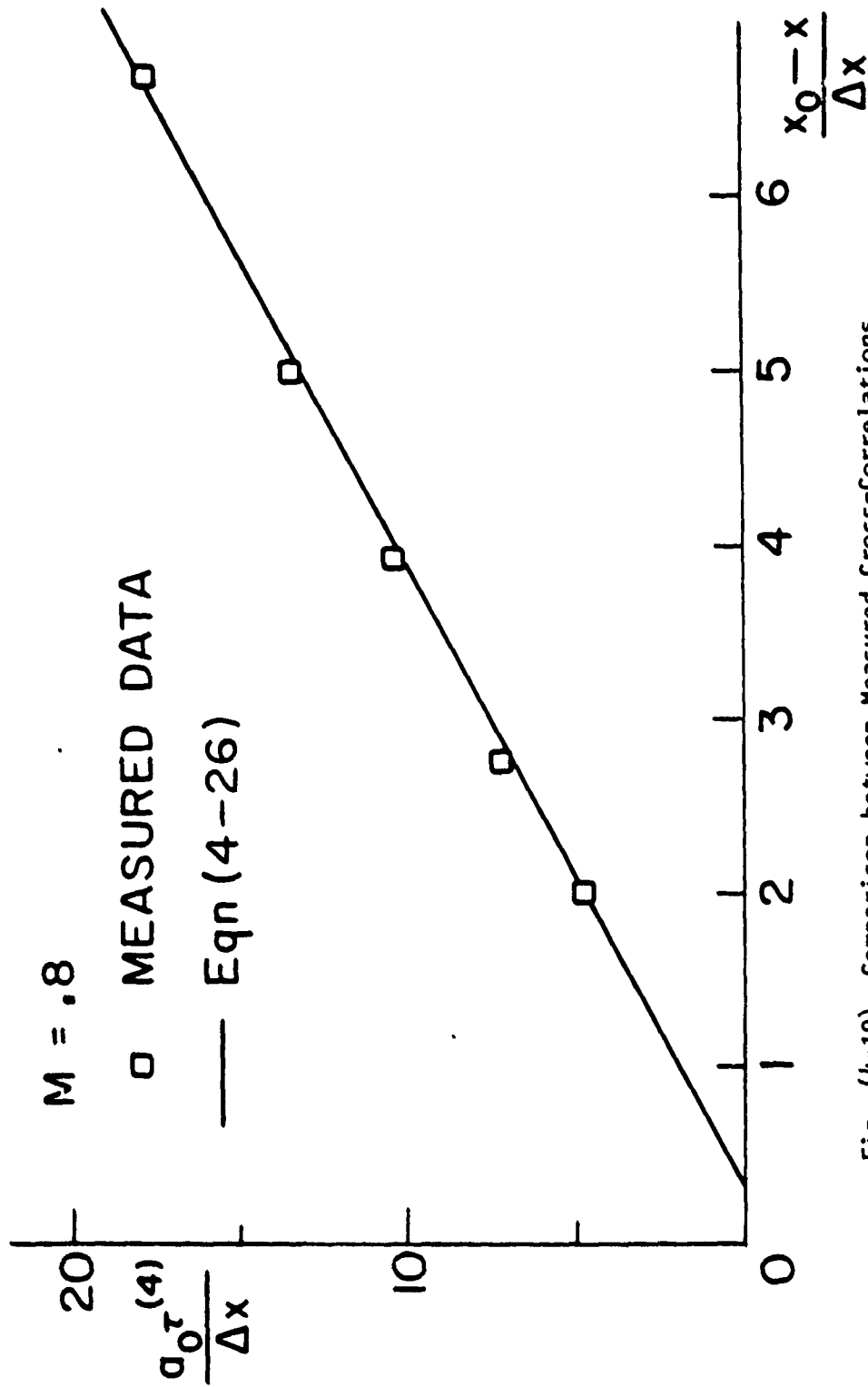


Fig. (4-19) Comparison between Measured Cross-Correlations  $\tau^{(4)}$  and the Model, ( $x_0/d=5.5$  and 7)

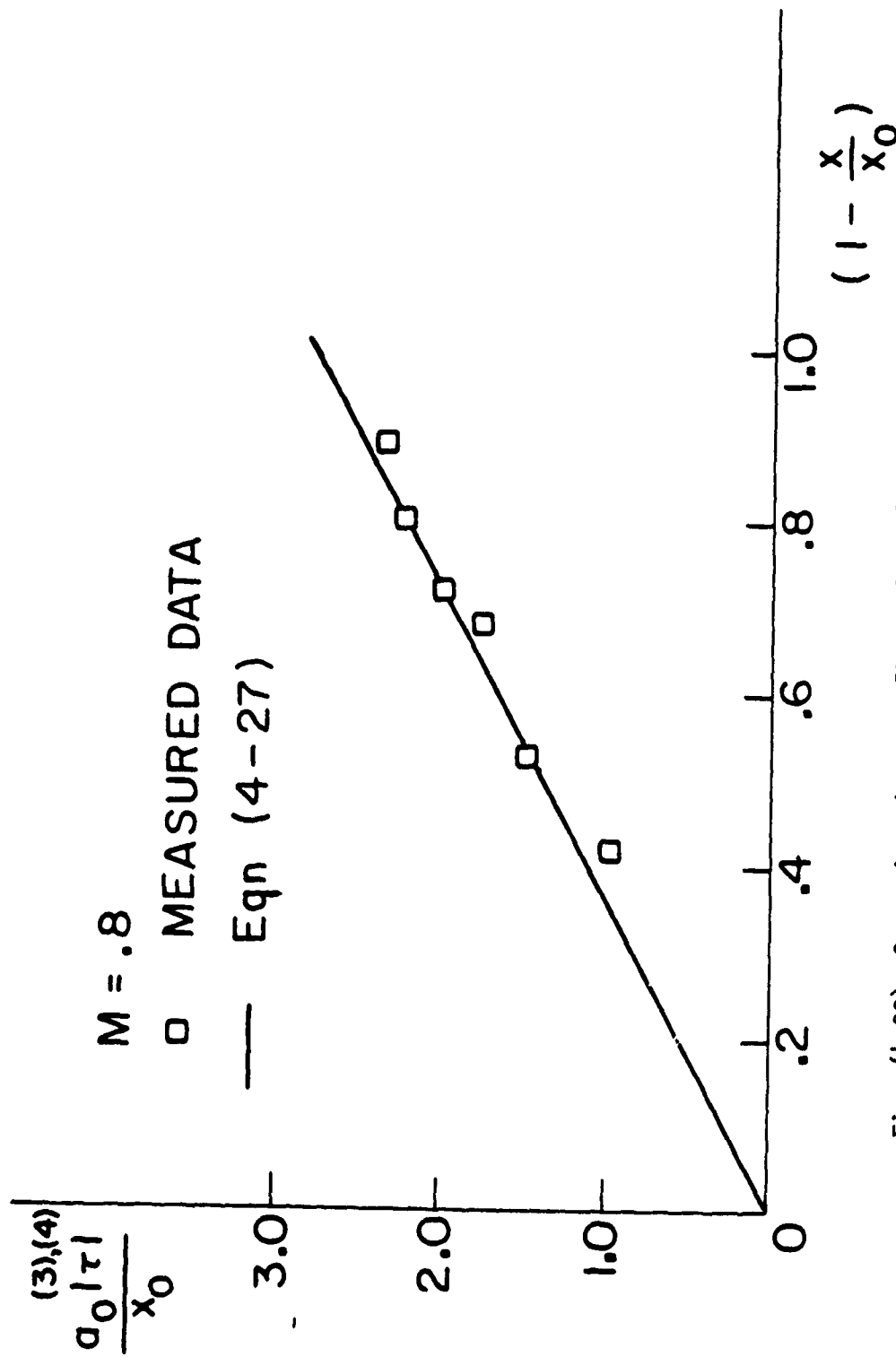


Fig. (4-20) Comparison between Time Delay of the Second Peak in the Measured Autocorrelations and the Model

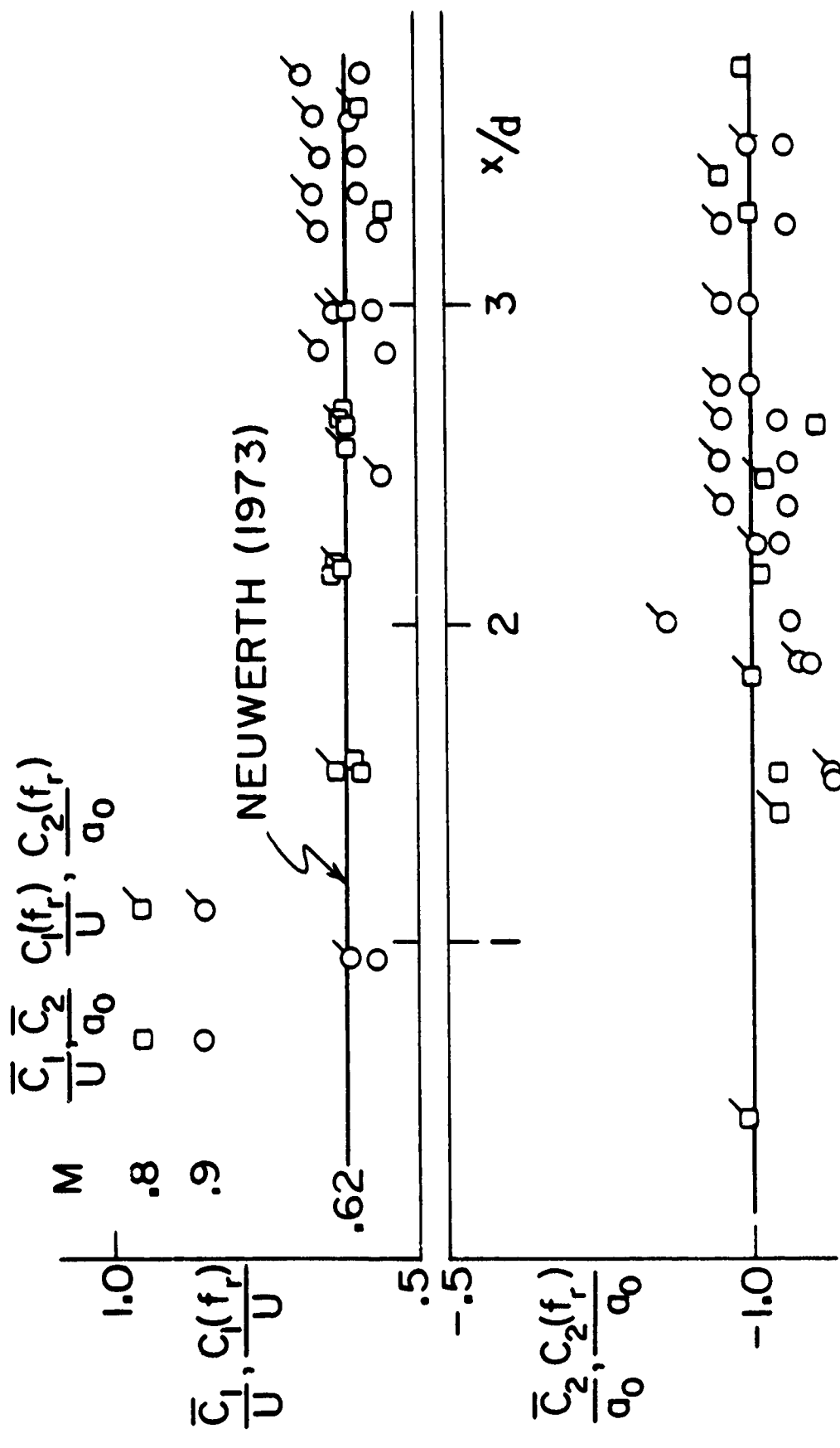


Fig. (4-21) Downstream and Upstream Wave Propagation Velocities Broadband Velocity ( $\bar{C}_1, \bar{C}_2$ ) and Phase Velocity at the Resonance Frequency  $C_1(f_r), C_2(f_r)$

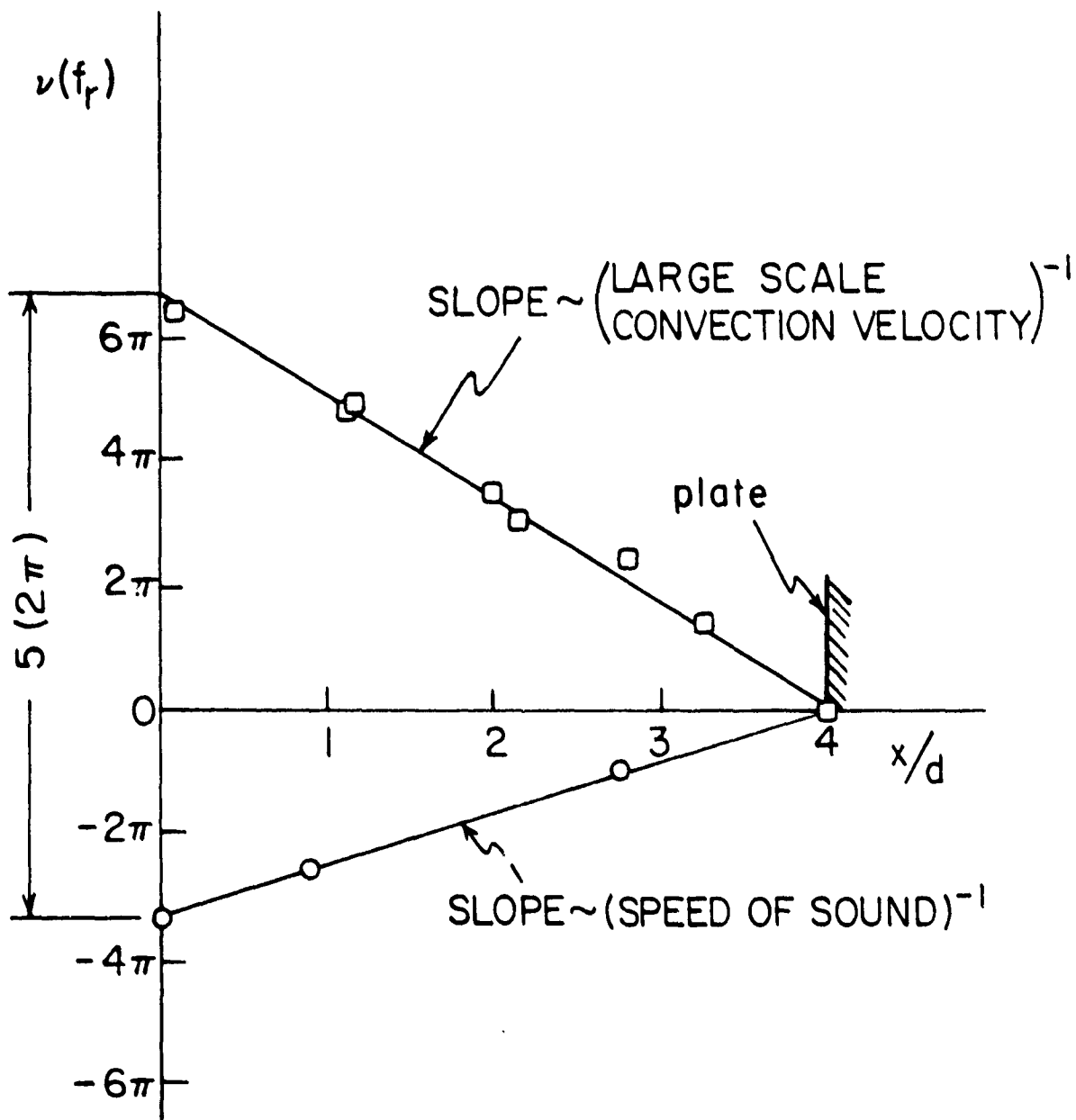


Fig. (5-1) Phase Angle Variations of the Two Waves at the Resonance Frequency ( $M=.8, x_0/d=4$ )

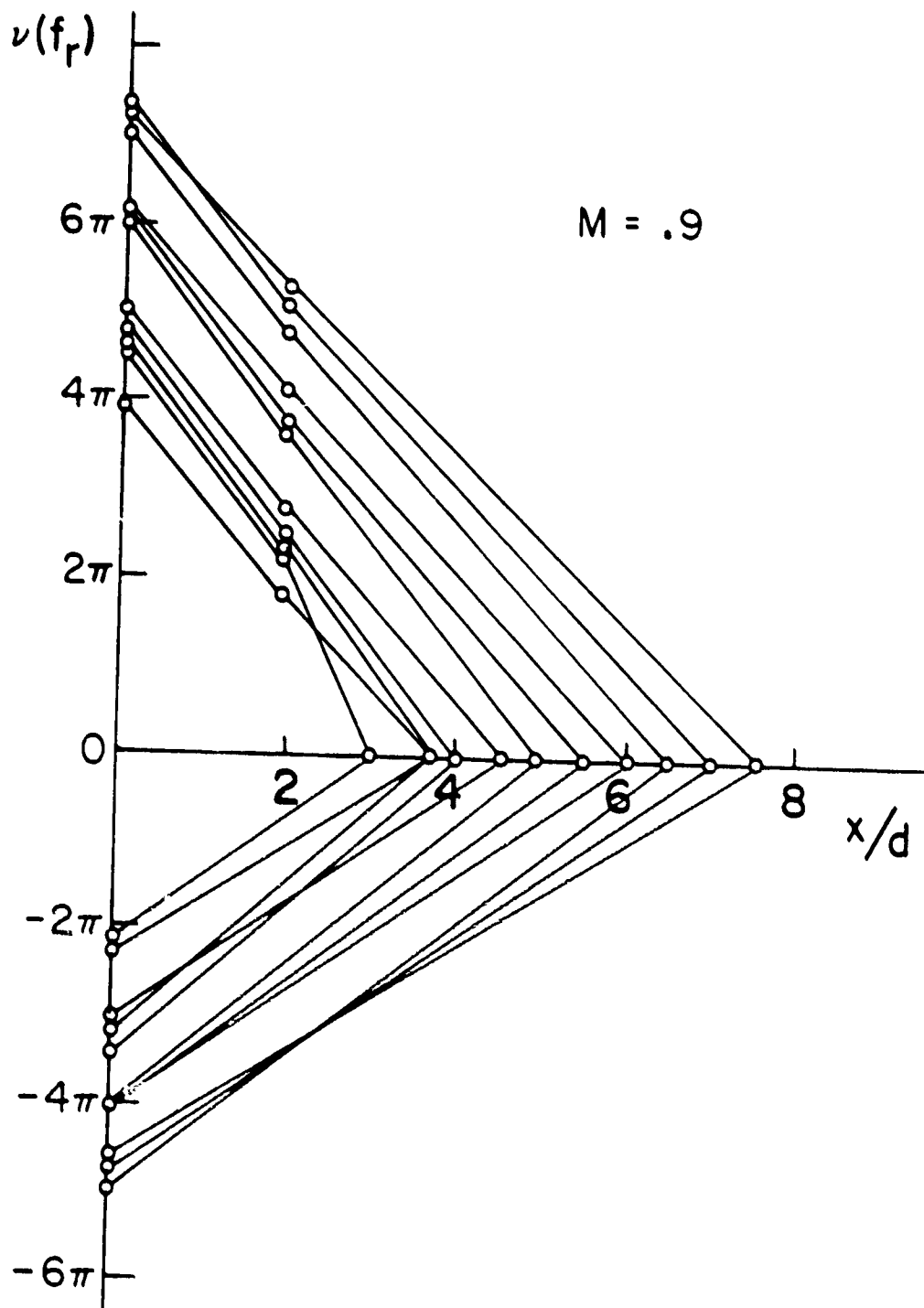


Fig. (5-2) Phase Angle Variations for Different Plate Locations

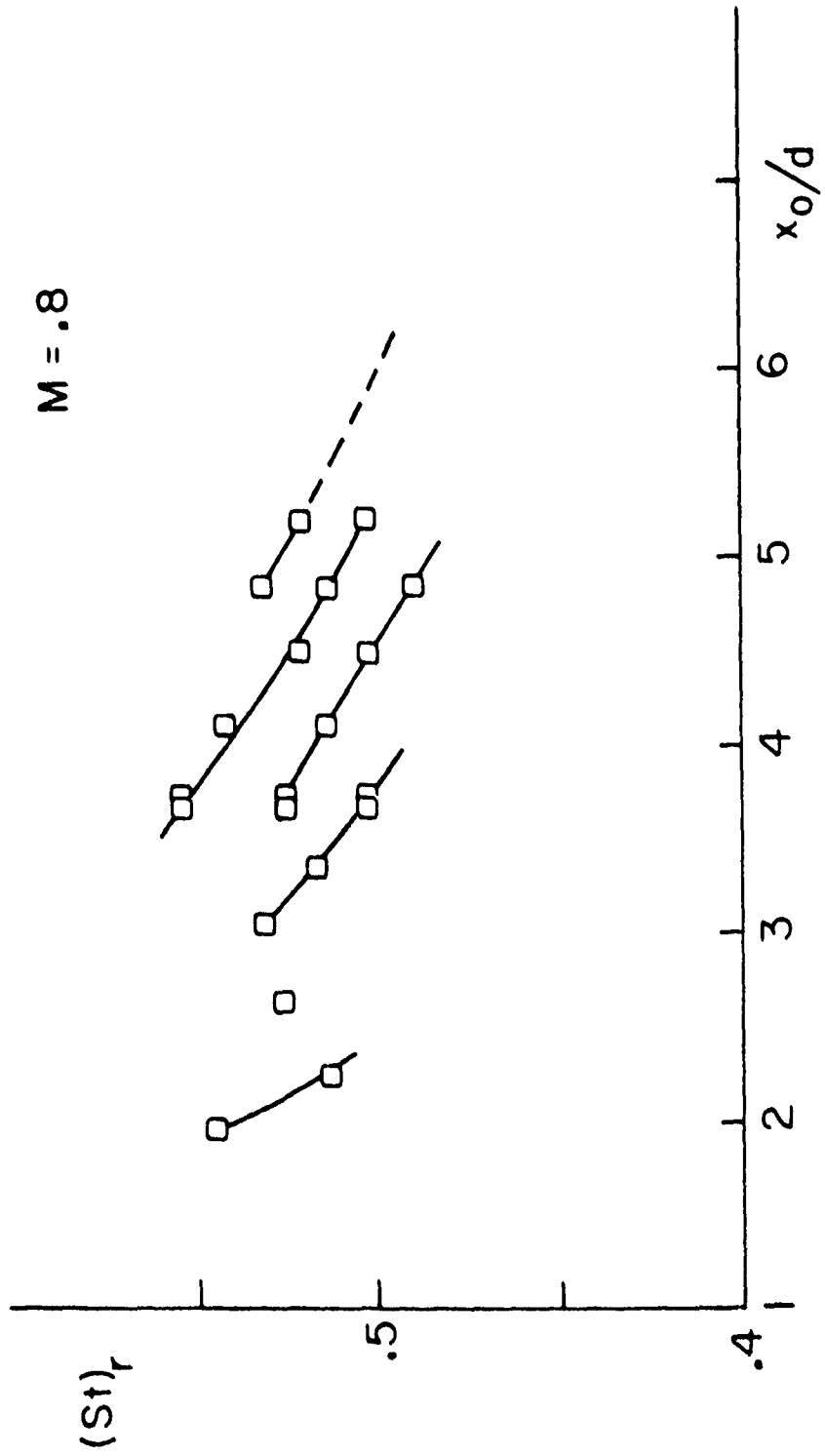


Fig. (5-3) Variation of Resonance Strouhal Number  $(St)_r = \frac{f_r d}{U}$ , with Plate Location

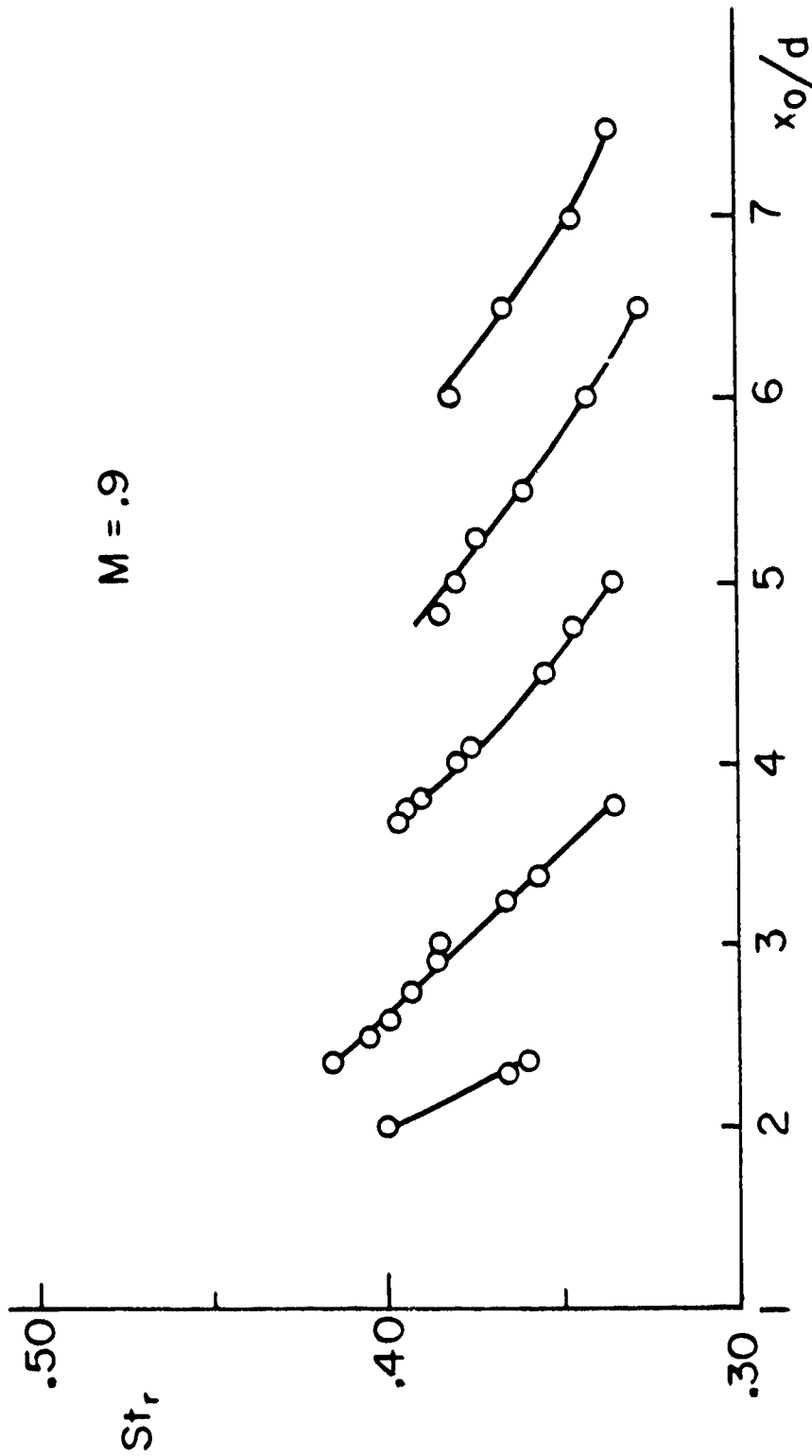


Fig. (5-4) Variation of Resonance Strouhal Number  $St_r = \frac{f_r d}{U}$ , with Plate Location

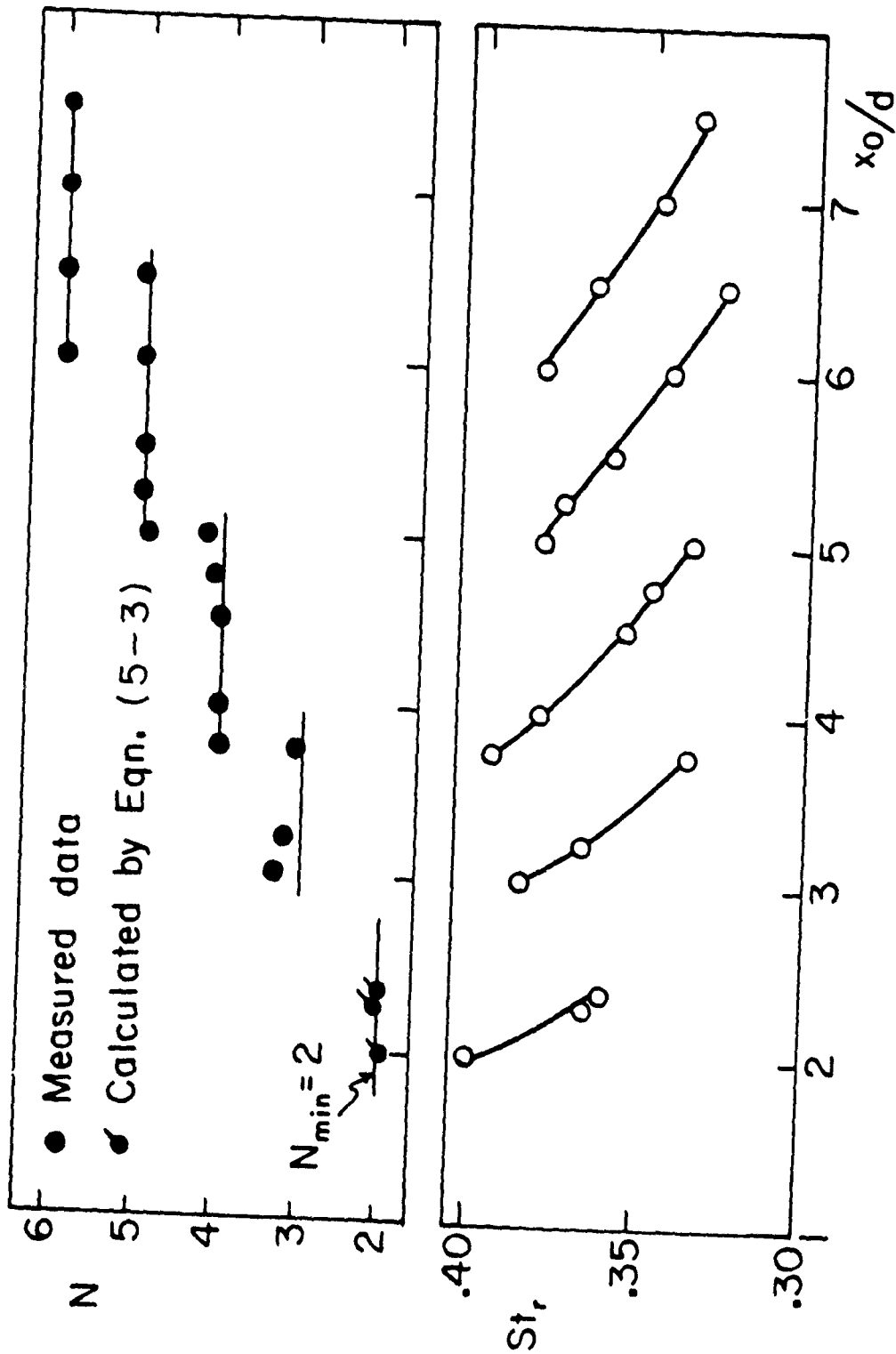
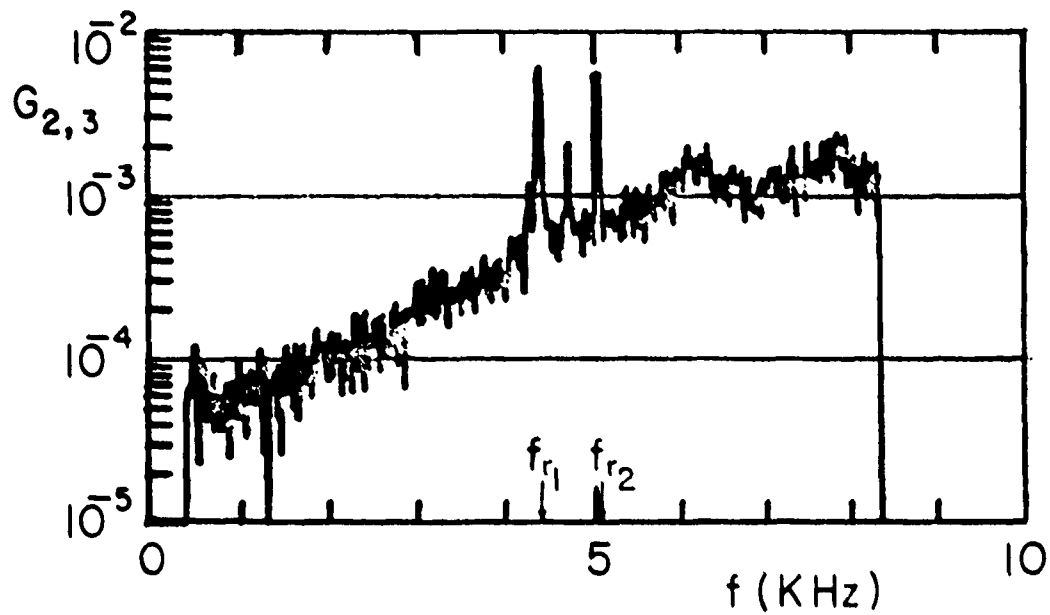
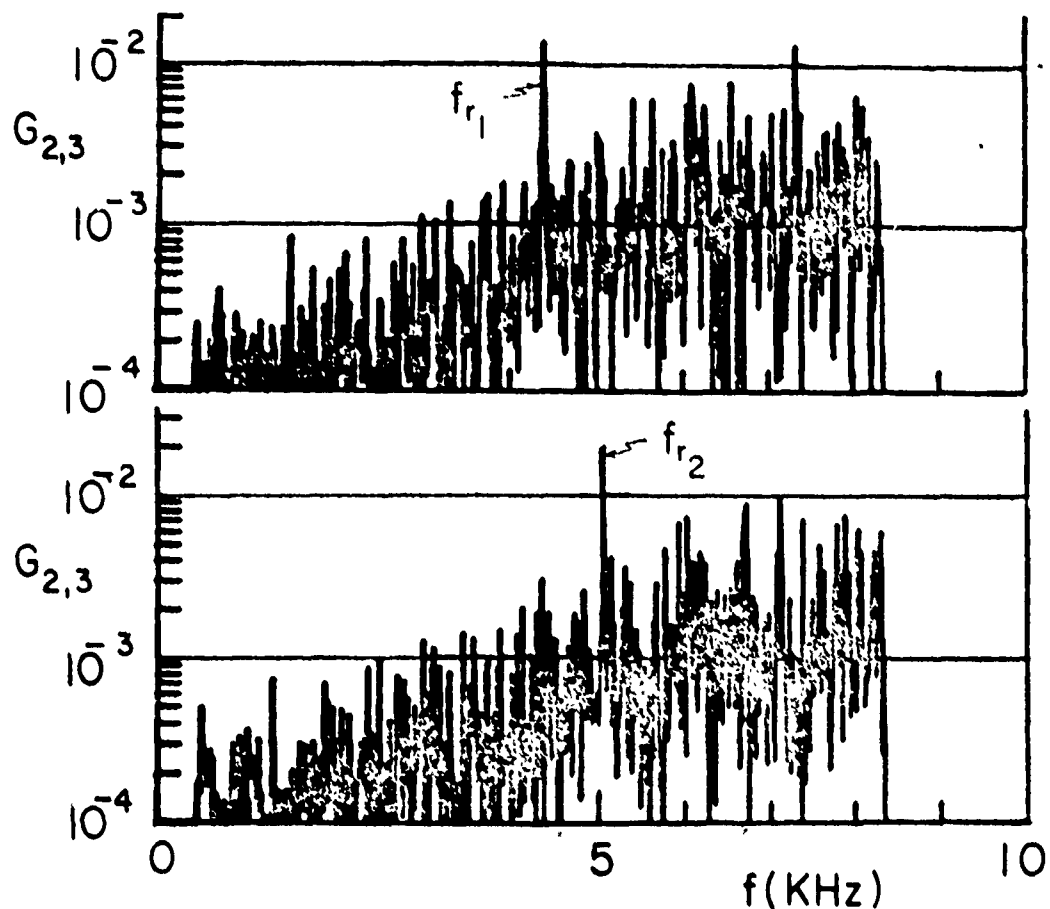


Fig. (5-5) Resonance Frequency Stages,  $N = \frac{x_0}{\lambda_1} + \frac{x_0}{\lambda_{2x}}$ , ( $M = .9$ )



(a) Long time average (2.4 sec) cross-spectrum



(b) Two short time average (.061 sec) cross-spectrum

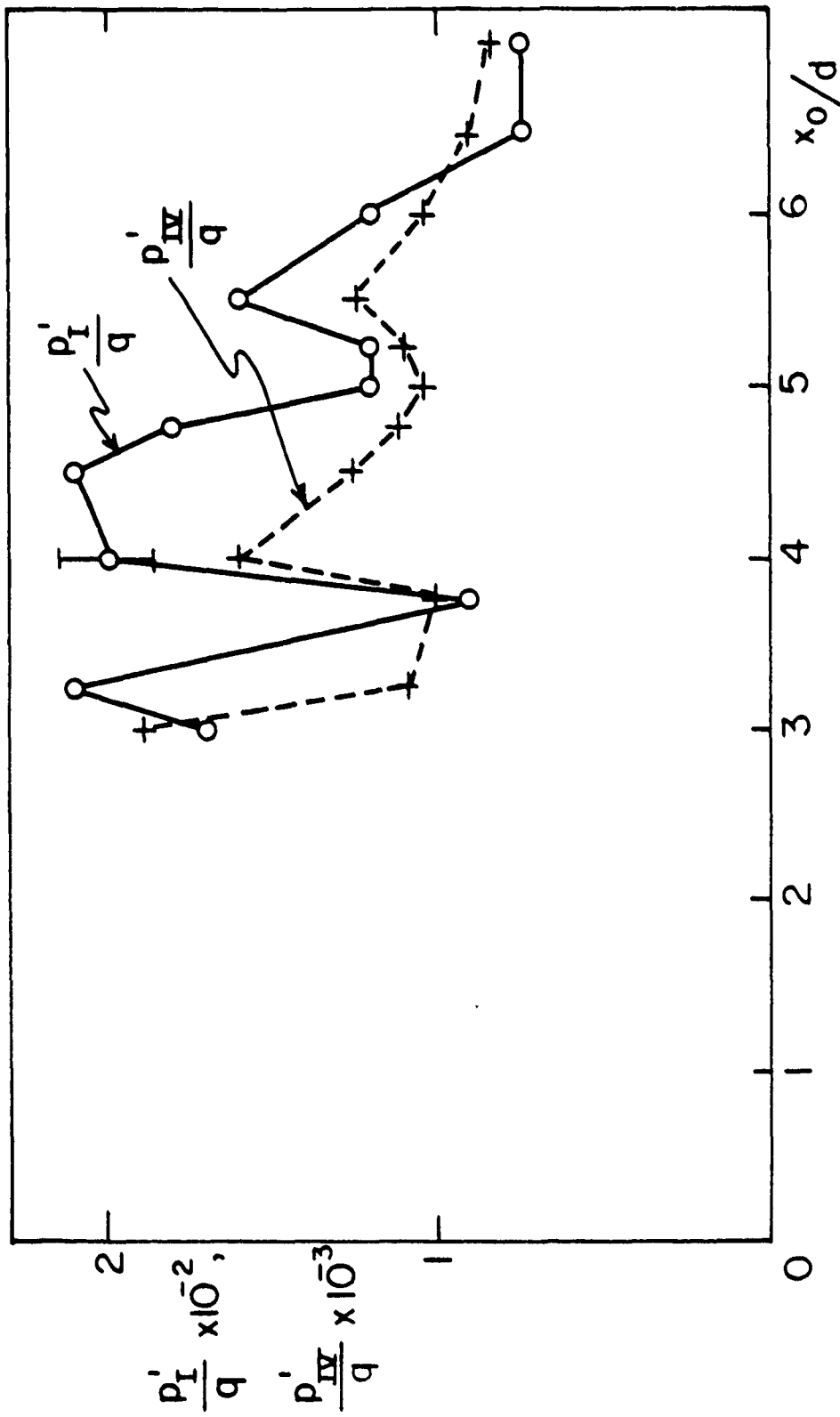


Fig. (5-7) Variation of rms Near Field Pressure Fluctuations at the Nozzle Exit Plane with Plate Location, ( $M=0.9$ ,  $\frac{x}{d} = 0.51$ ,  $\frac{r_{IV}}{d} = 2.7$ )

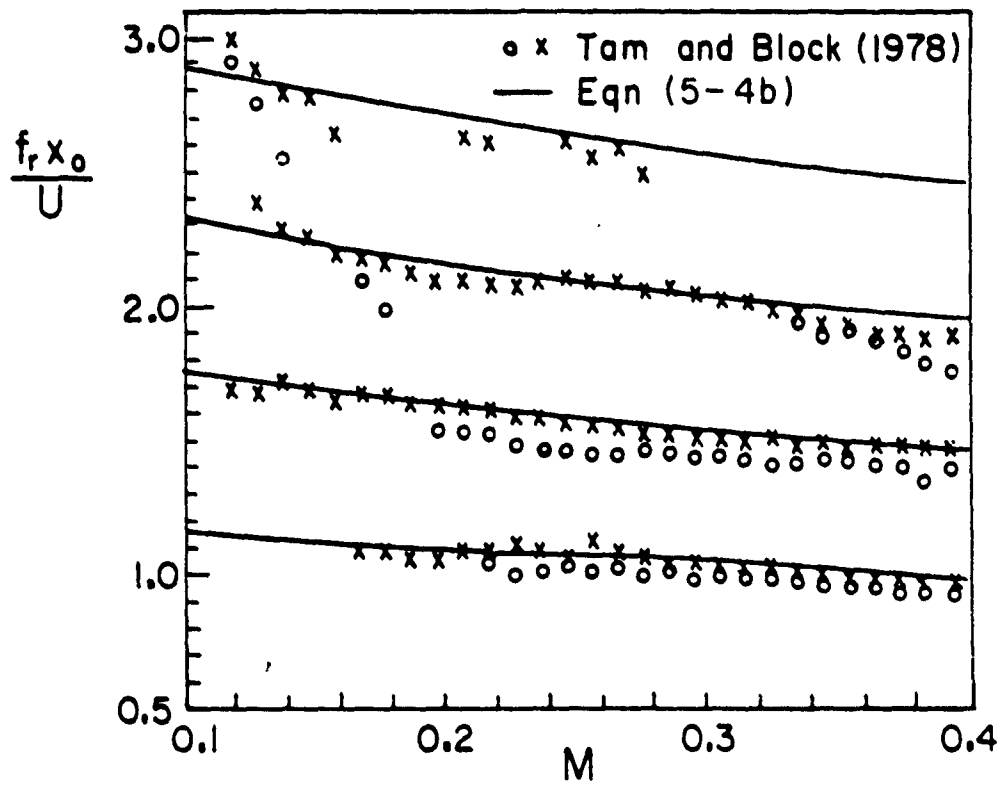


Fig. (5-8) Comparison between Measured Cavity Tones and Eqn. (5-4b)

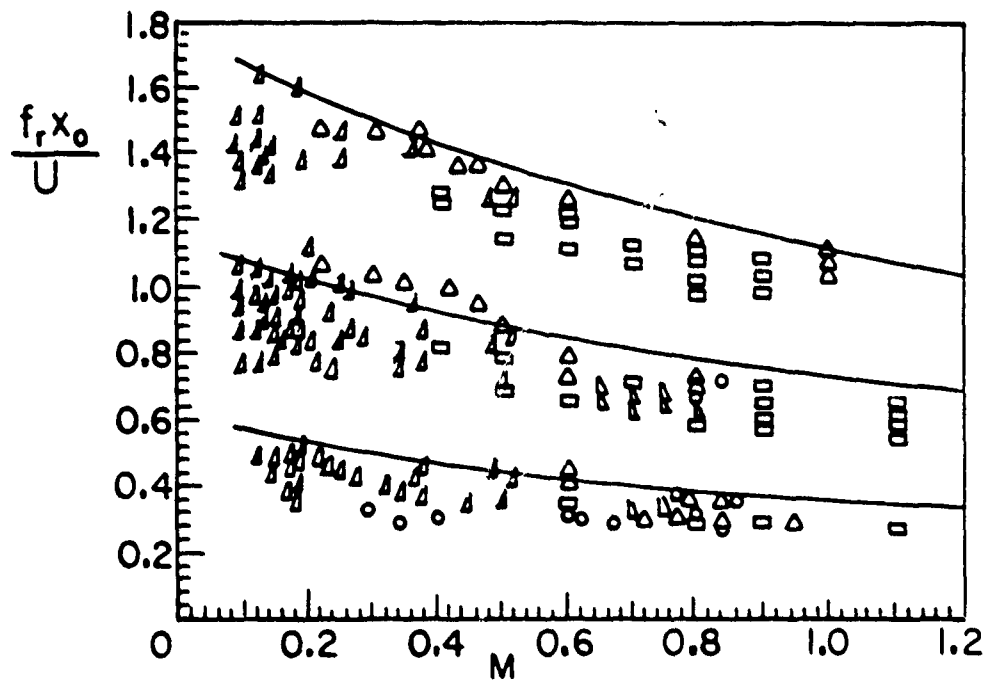
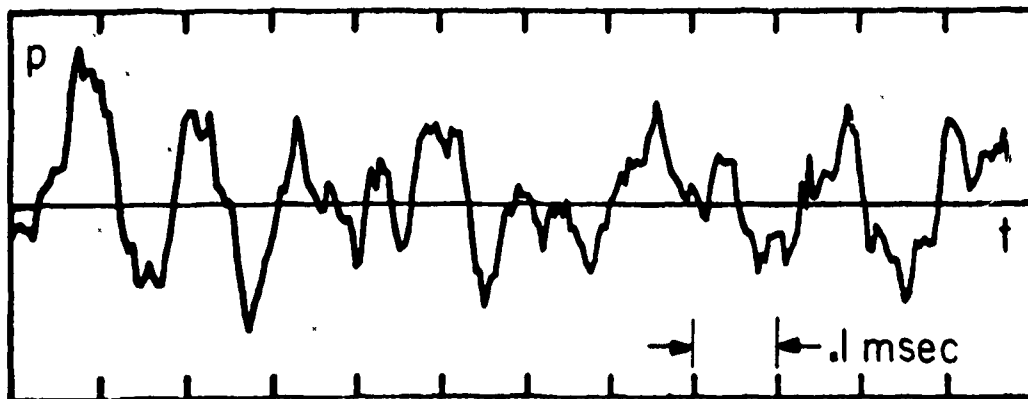
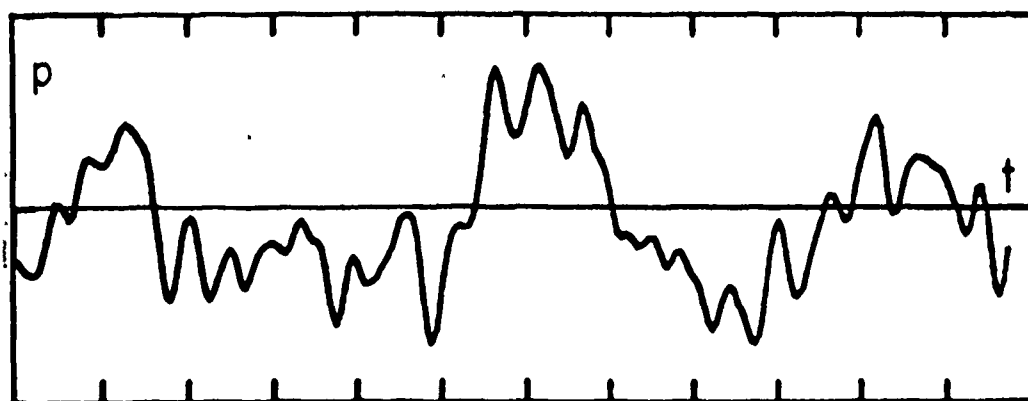


Fig. (5-9) Comparison between Cavity Tones for Different Cavity Dimensions as Measured by many Investigators (taken from Tam and Block (1978) , and Eqn. (5-4b)

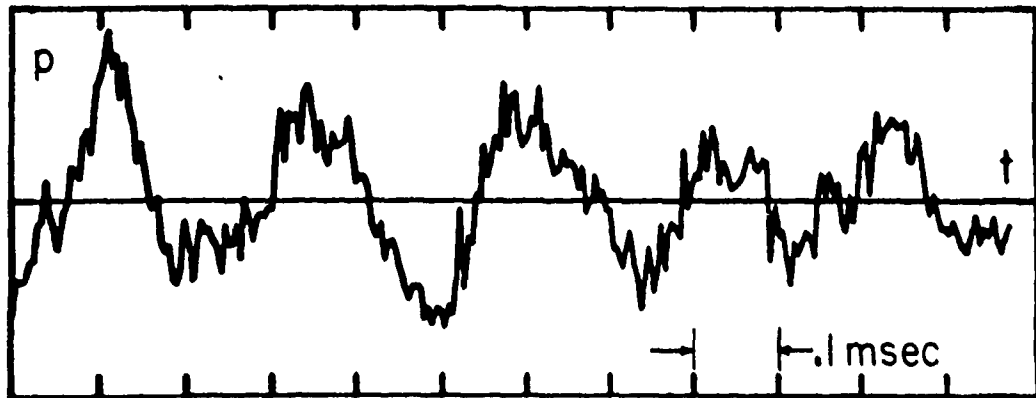


(i)  $x/d = .13$ ,  $r/d = .5$

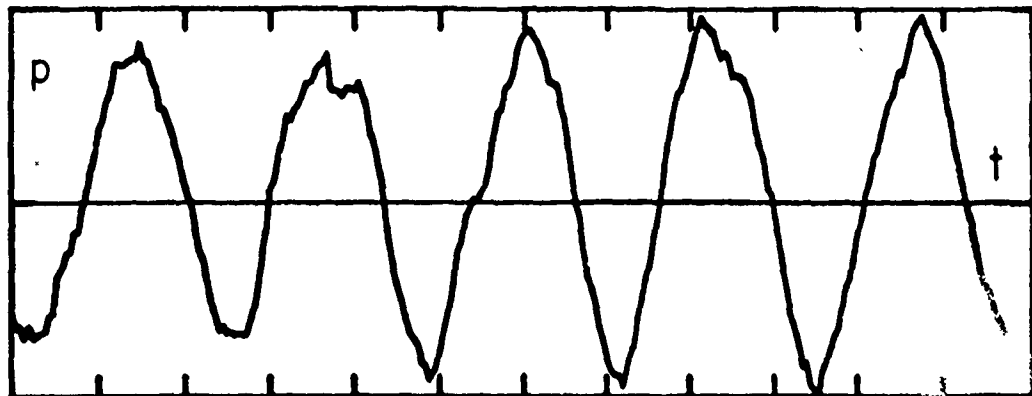


(ii)  $x/d = .92$ ,  $r/d = 1.125$

Fig. (5-10a) Raw Near Field Pressure Signals of a Non-Resonance Case, ( $M = .4$ ,  $x_0/d = 4.5$ )

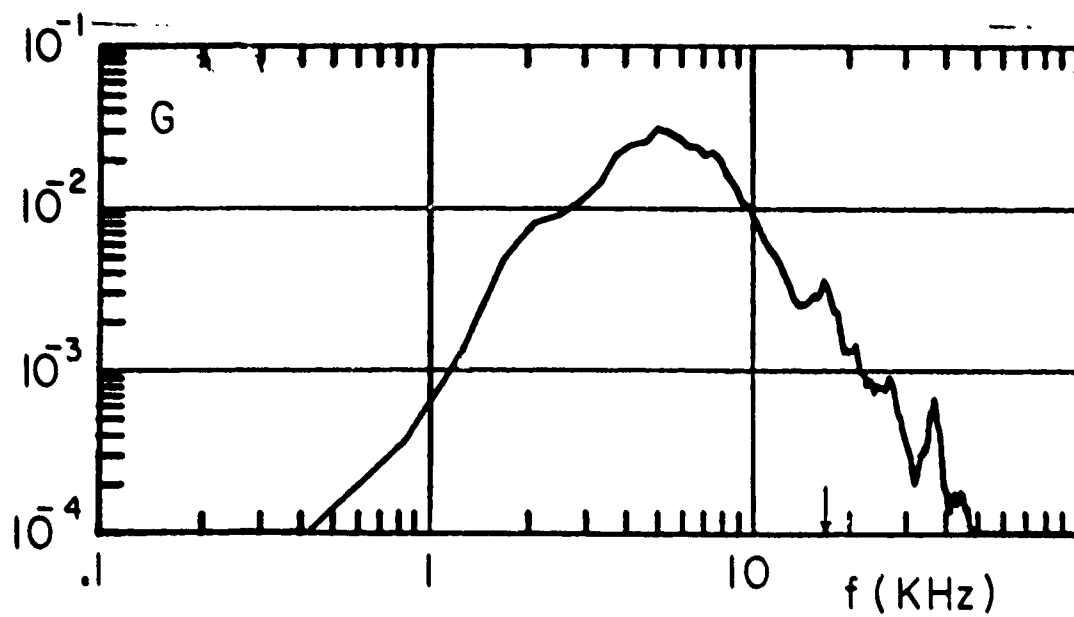


(i)  $x/d = .13$ ,  $r/d = .5$

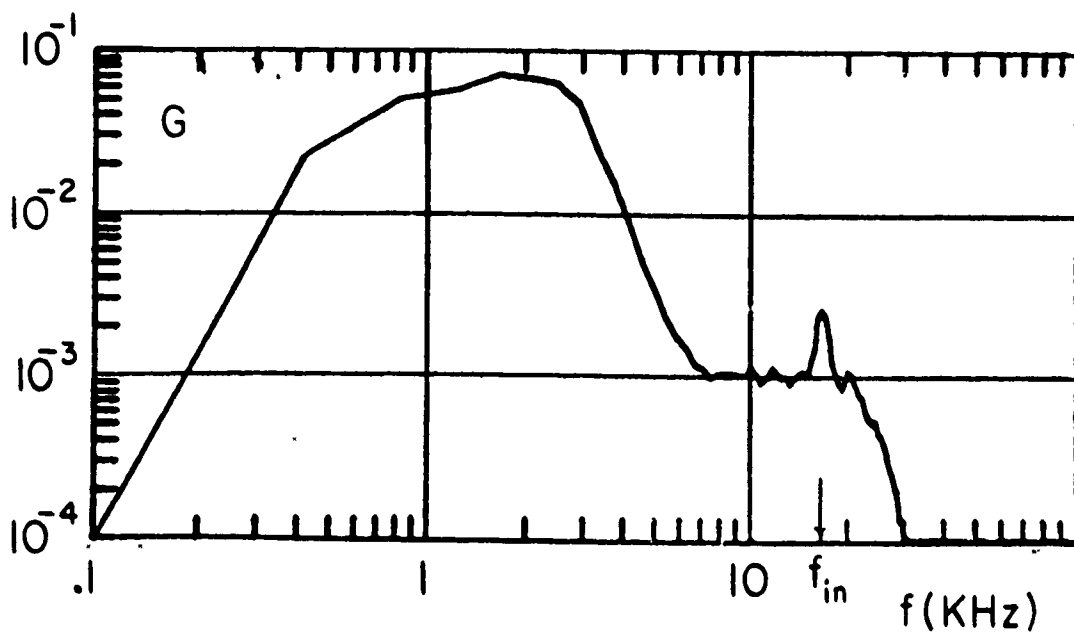


(ii)  $x/d = 1.31$ ,  $r/d = 1$

Fig. (5-10b) Raw Near Field Pressure Signals of a Resonance Case,  
 $(M=.9, x_0/d=4.5)$

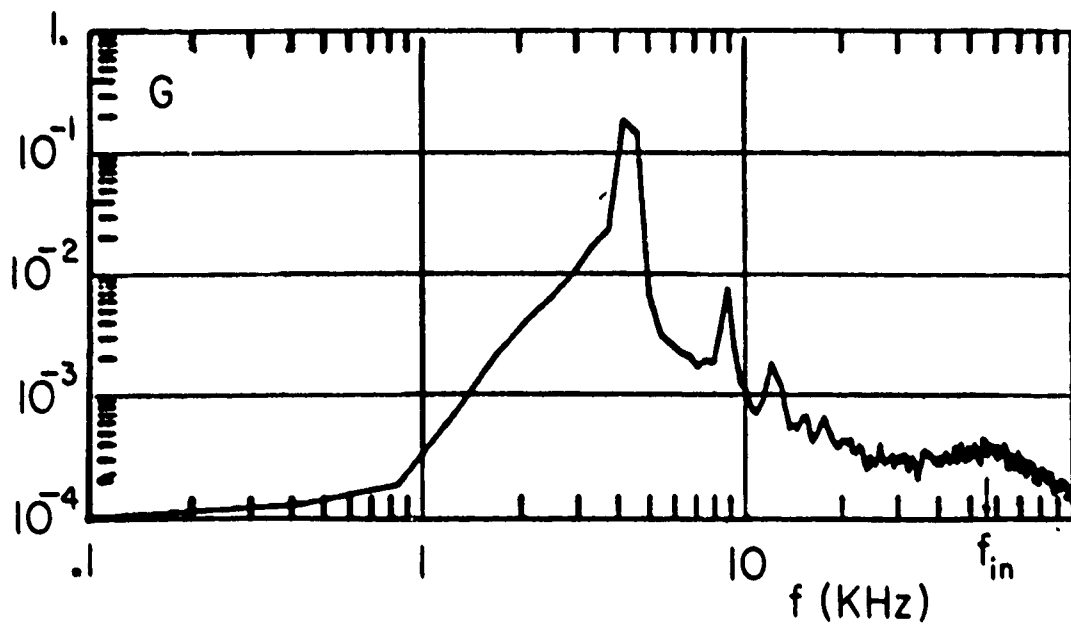


(i)  $x/d = .13$ ,  $r/d = .5$

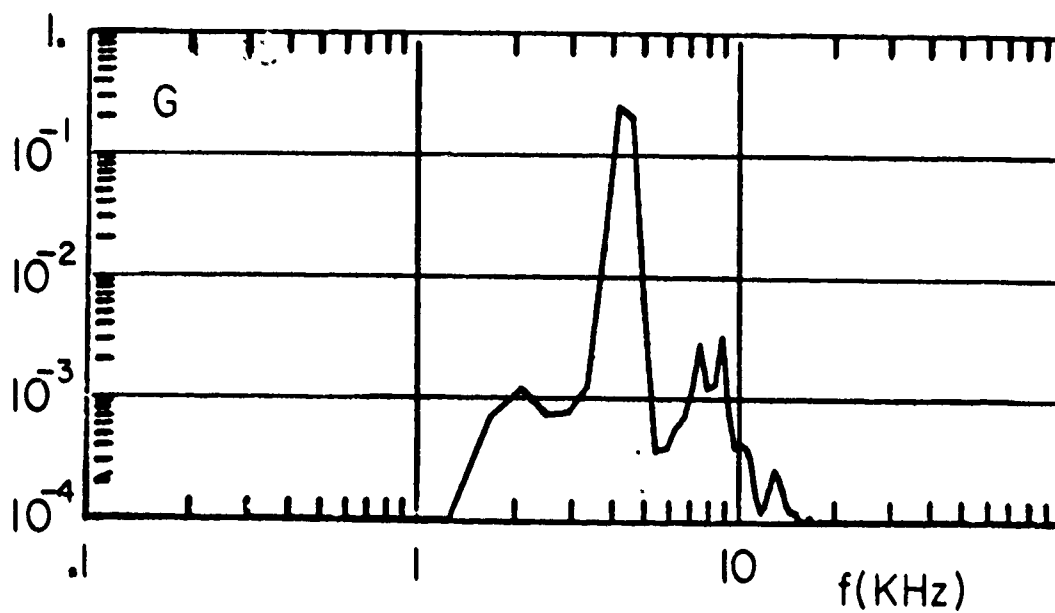


(ii)  $x/d = .92$ ,  $r/d = 1.125$

Fig. (5-11a) Near Field Power Spectra, same conditions as in Fig. (5-10a)



(i)  $x/d = .13$ ,  $r/d = .5$



(ii)  $x/d = 1.31$ ,  $r/d = 1$ .

Fig. (5-11b) Near Field Power Spectra, same conditions as in Fig. (5-10b)

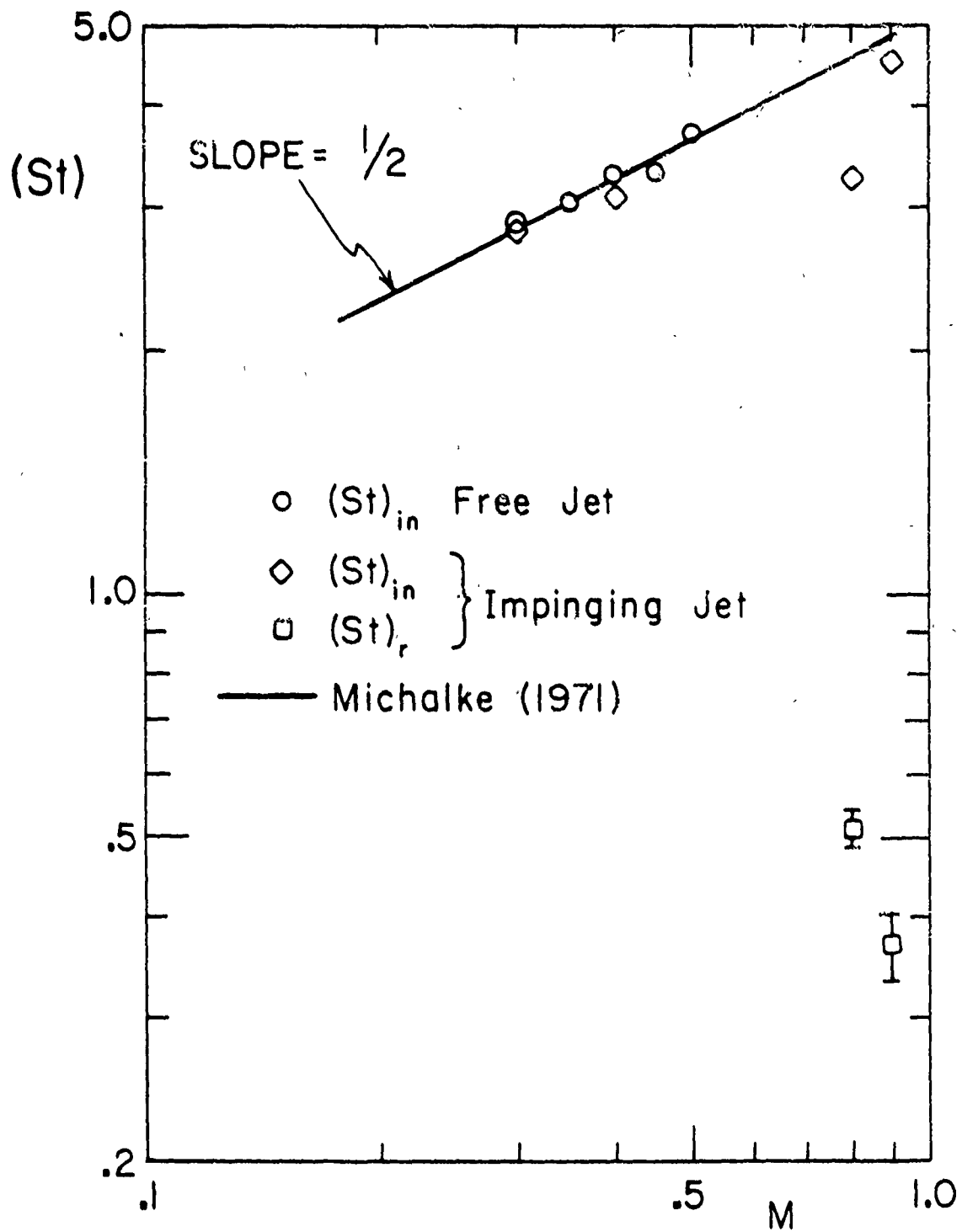


Fig. (5-12) Instability and Resonance Strouhal Numbers for Free and Impinging Jets

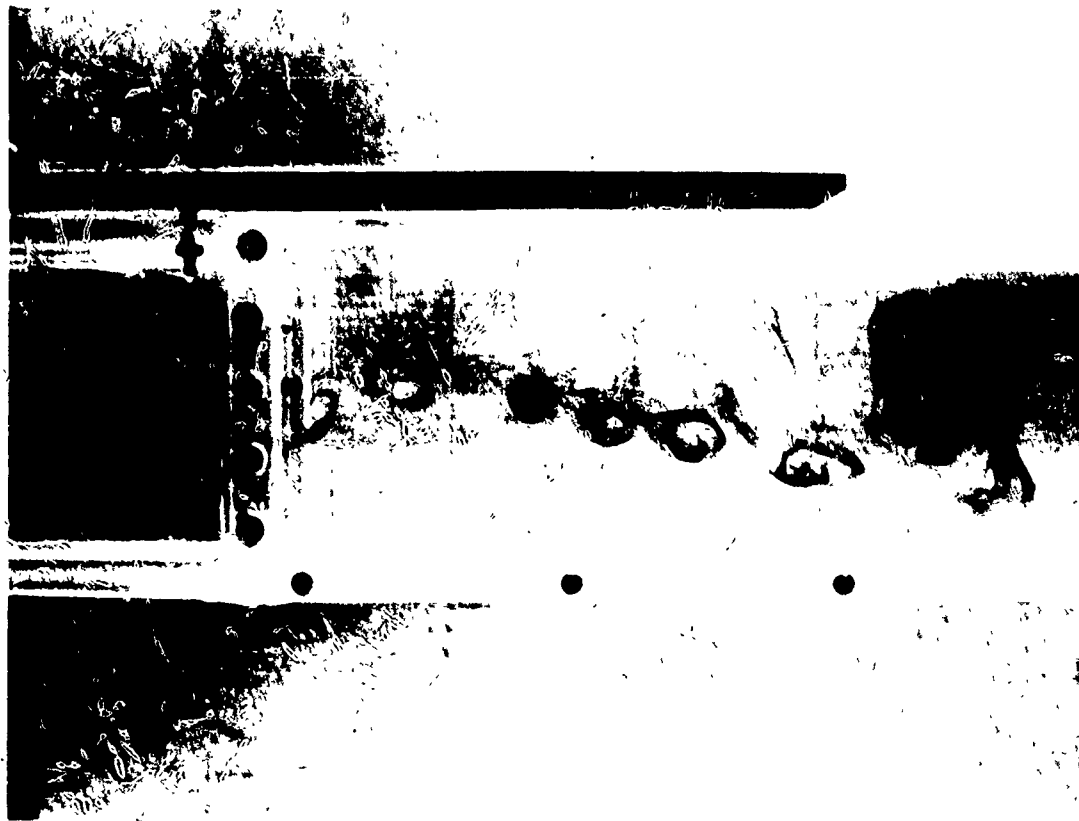


Fig. (5-13) Collective Interaction in a Two-Dimensional Free Shear Layer, Flow from Left to Right, Forcing Frequency  $\ll$  Natural Initial Instability Frequency, Courtesy of Ho and Huang (1978)

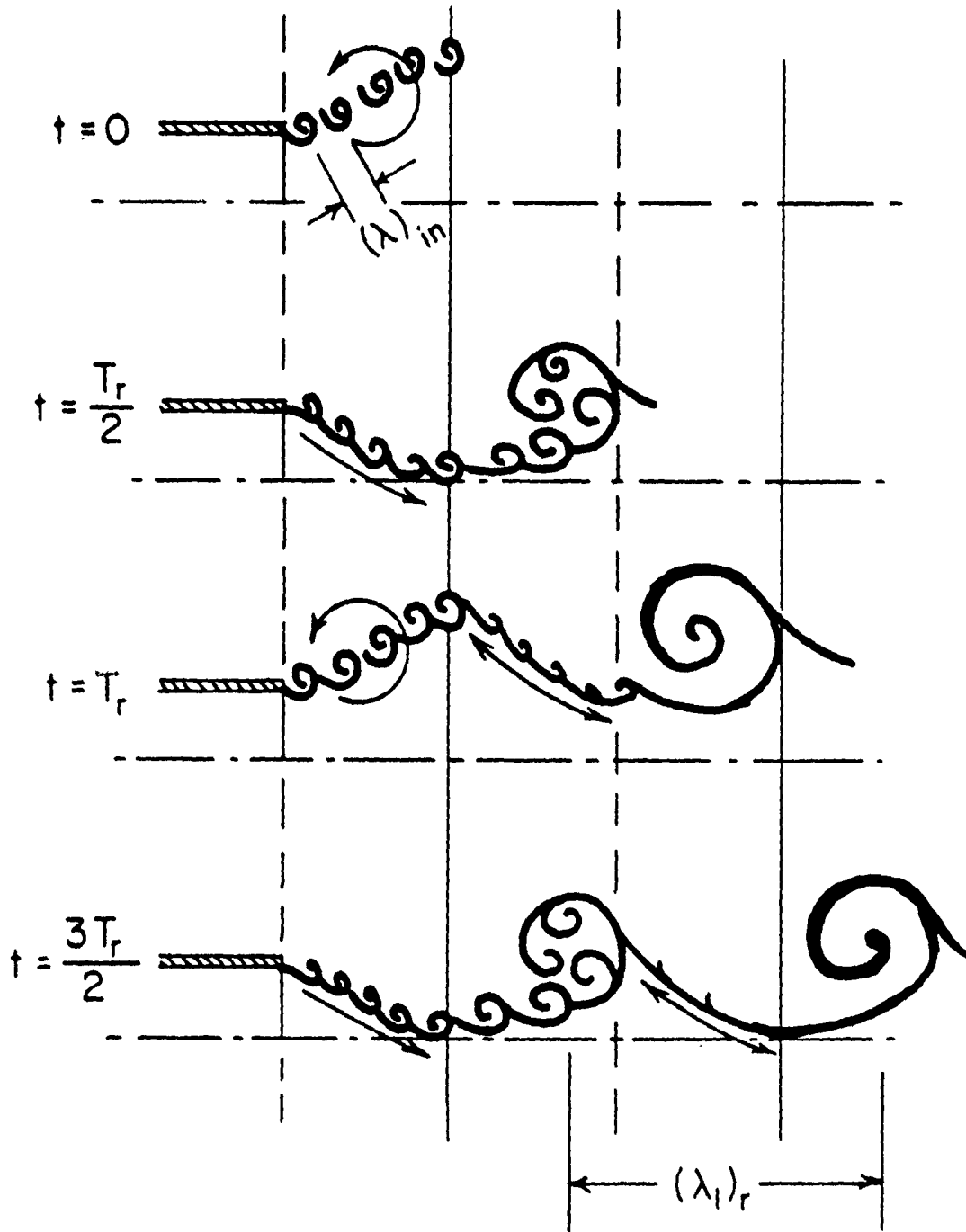


Fig. (5-14) Collective Interaction

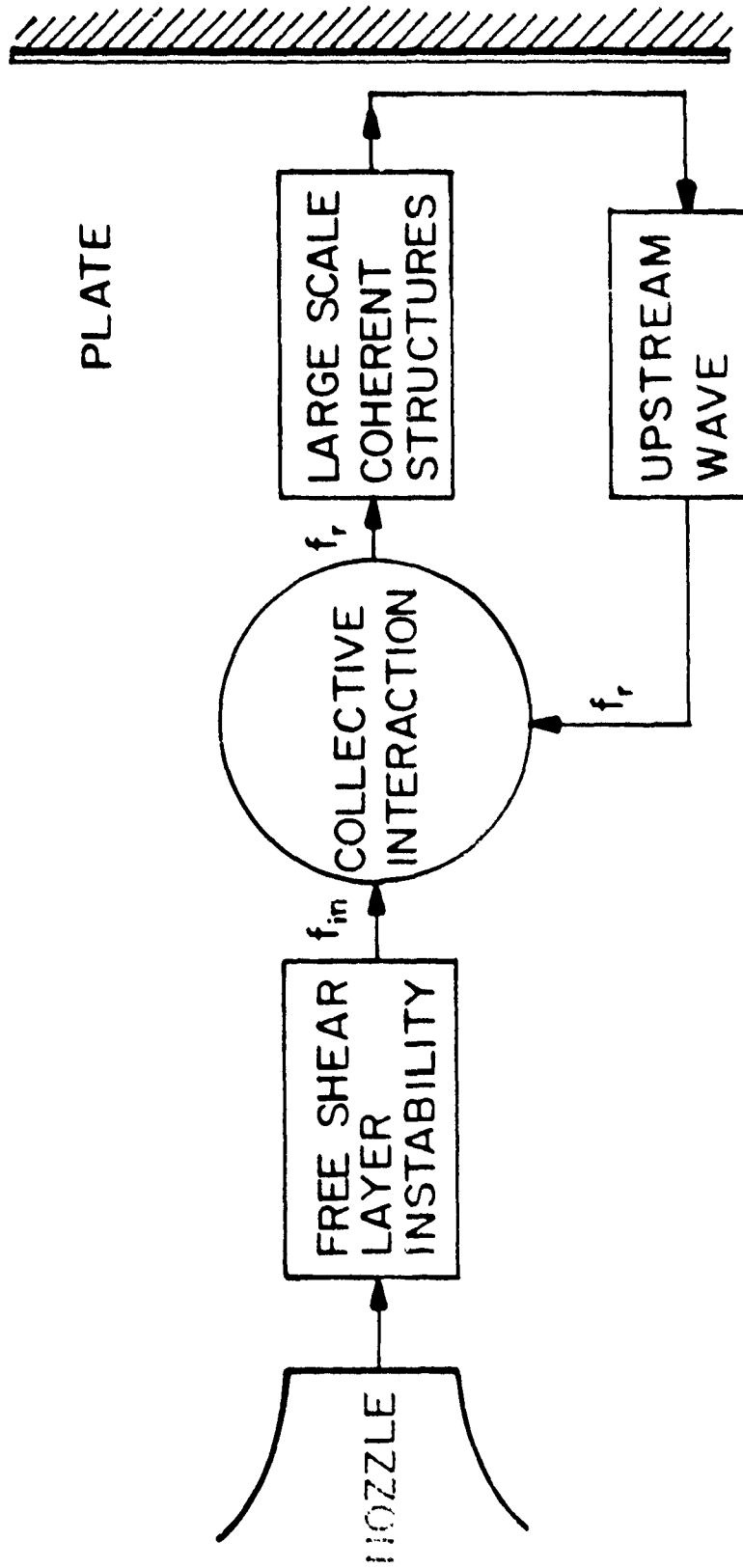


Fig. (5-15) Flow Diagram Explaining the Feedback Loop of an Impinging Jet

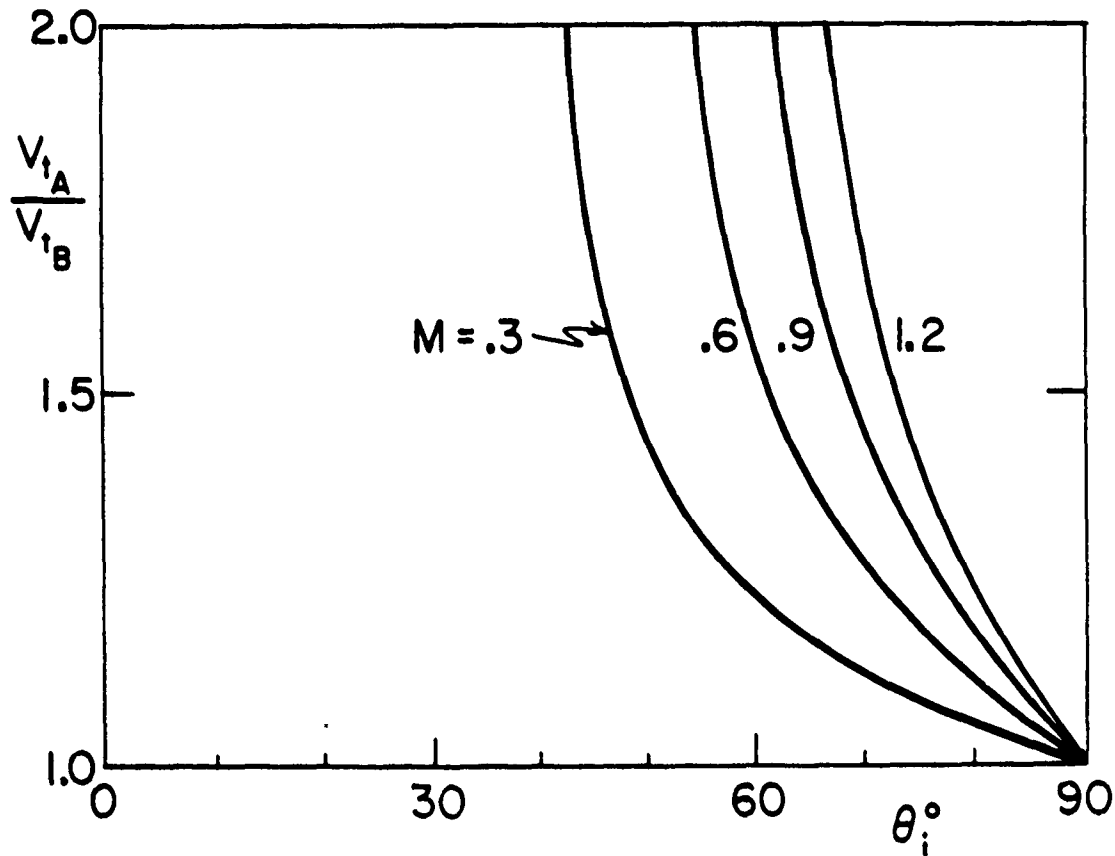
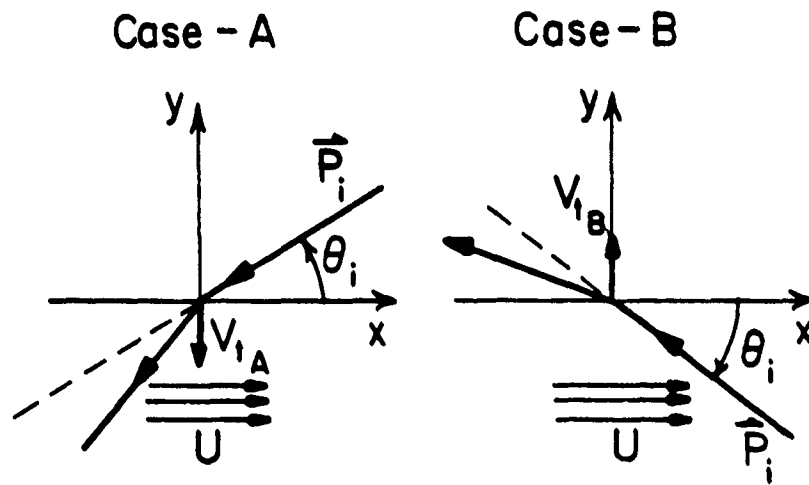


Fig. (5-16) Ratio of Cross-Flow Velocity at the Shear Layer for Case-A and Case-B, versus Upstream Acoustic Incidence Angle

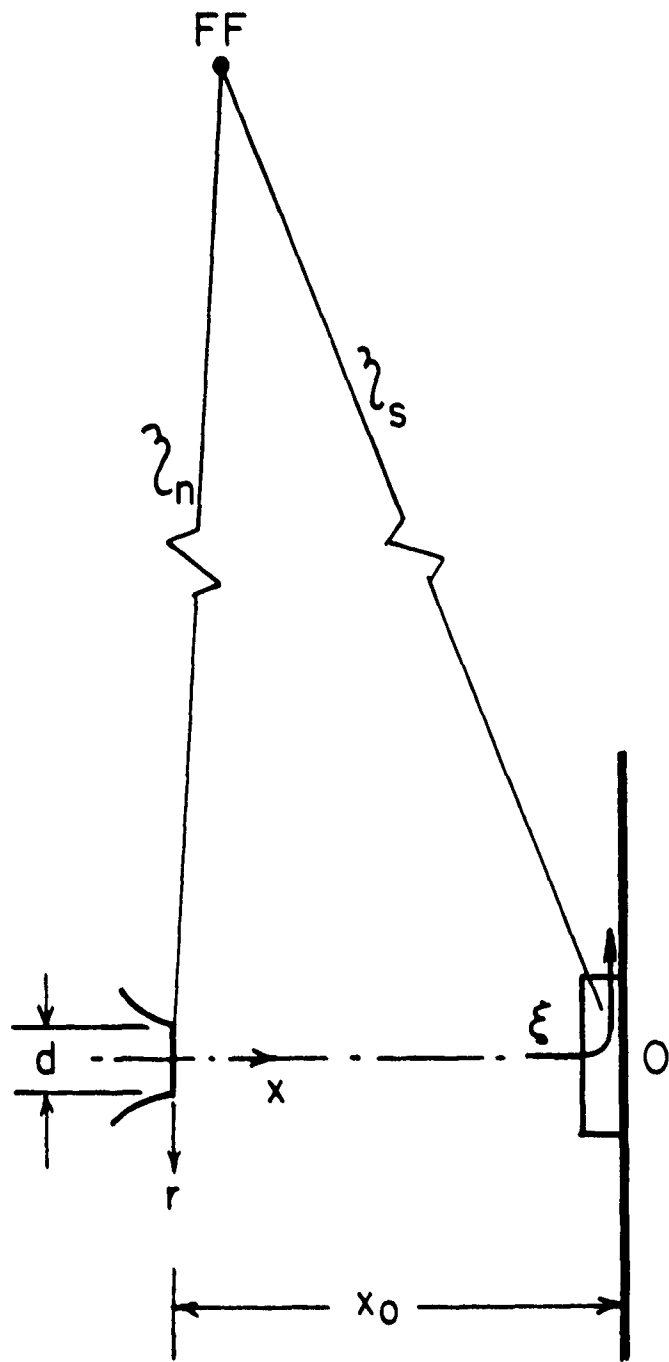


Fig. (6-1) Coordinate System for Far Field Noise Analysis

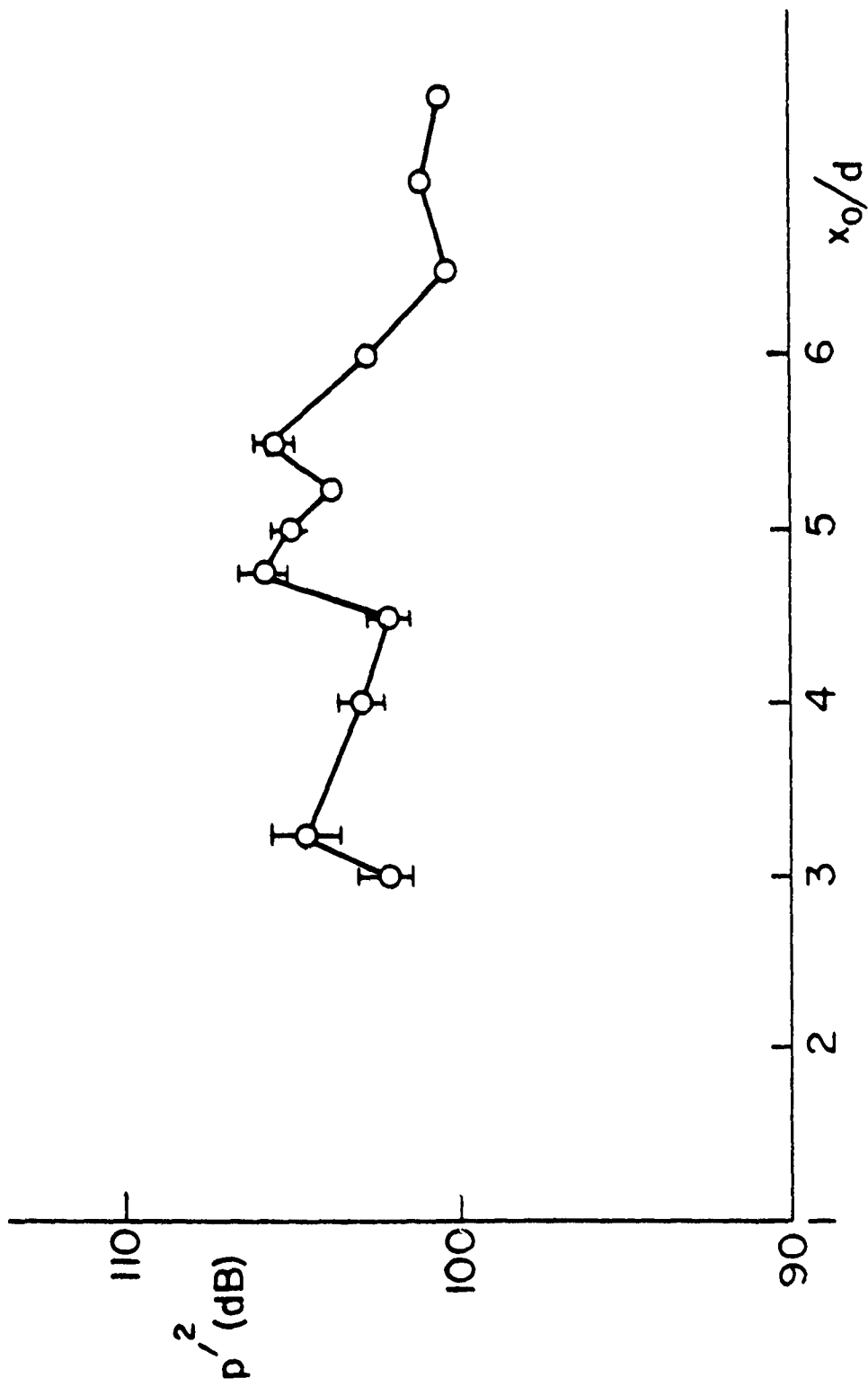


Fig. (6-2) Overall Sound Pressure Level Variation with Plate Locations, ( $M=0.9$ ,  $\theta=89^\circ$ )

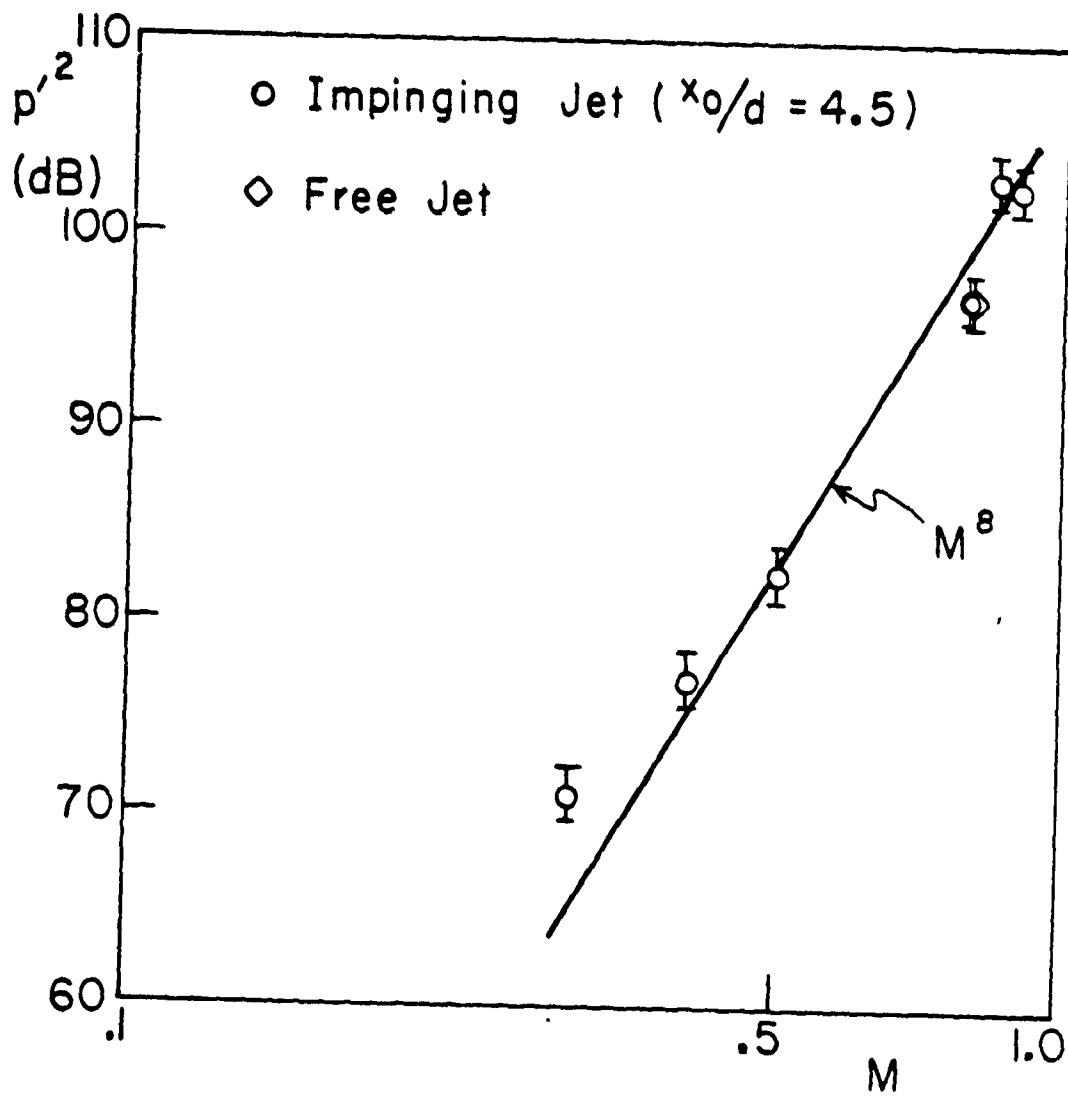


Fig. (6-3) Variations of Sound Pressure Level with Mach Number,  $\theta=89^\circ$

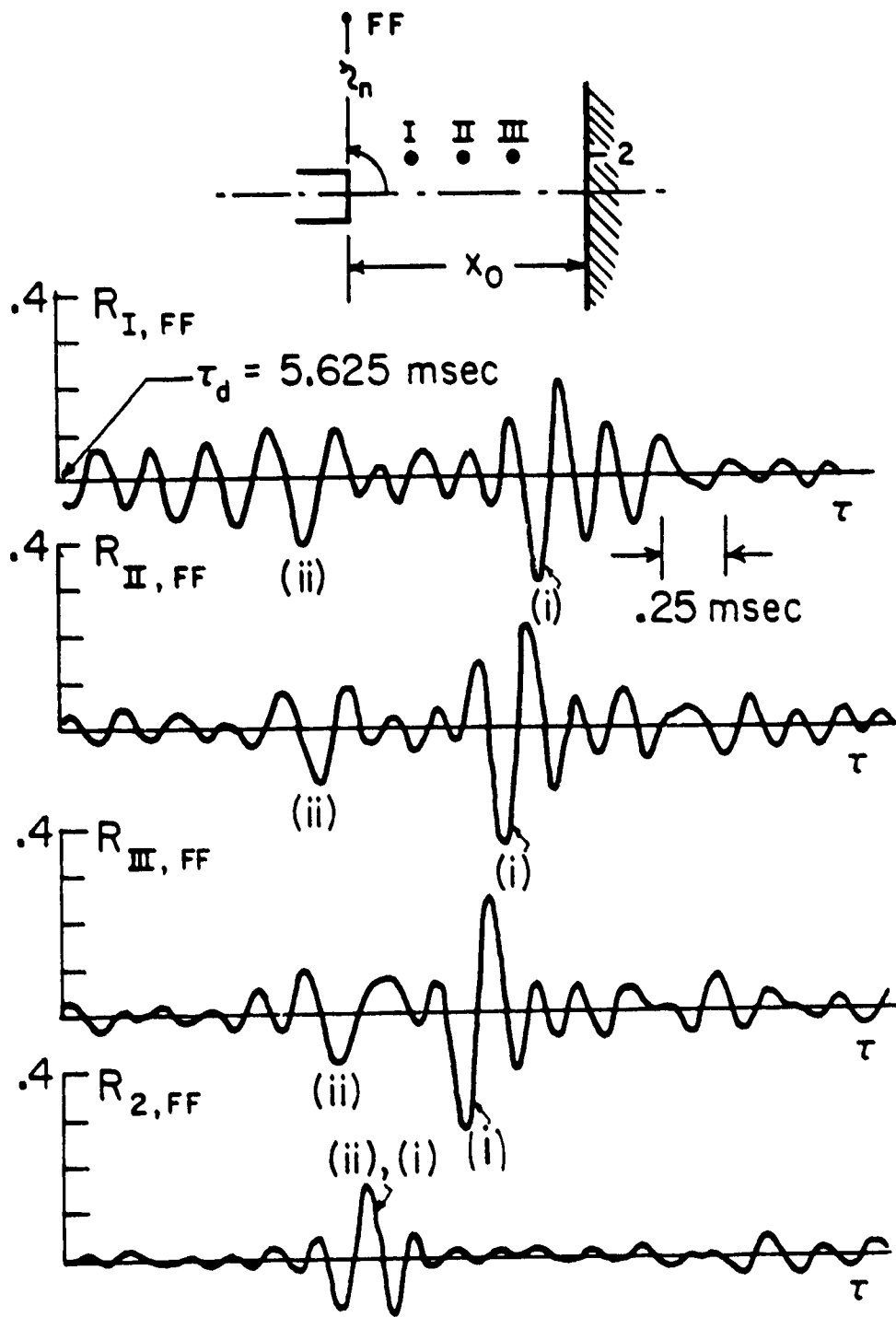


Fig. (6-4) Cross-Correlations with Far Field Microphone, point 2 is at  $r_0/d=1$ , indices refer to the sketch in Fig. (4-2) ( $M=.8$ ,  $x_0/d=5.5$ ,  $z_n/d=90$ )

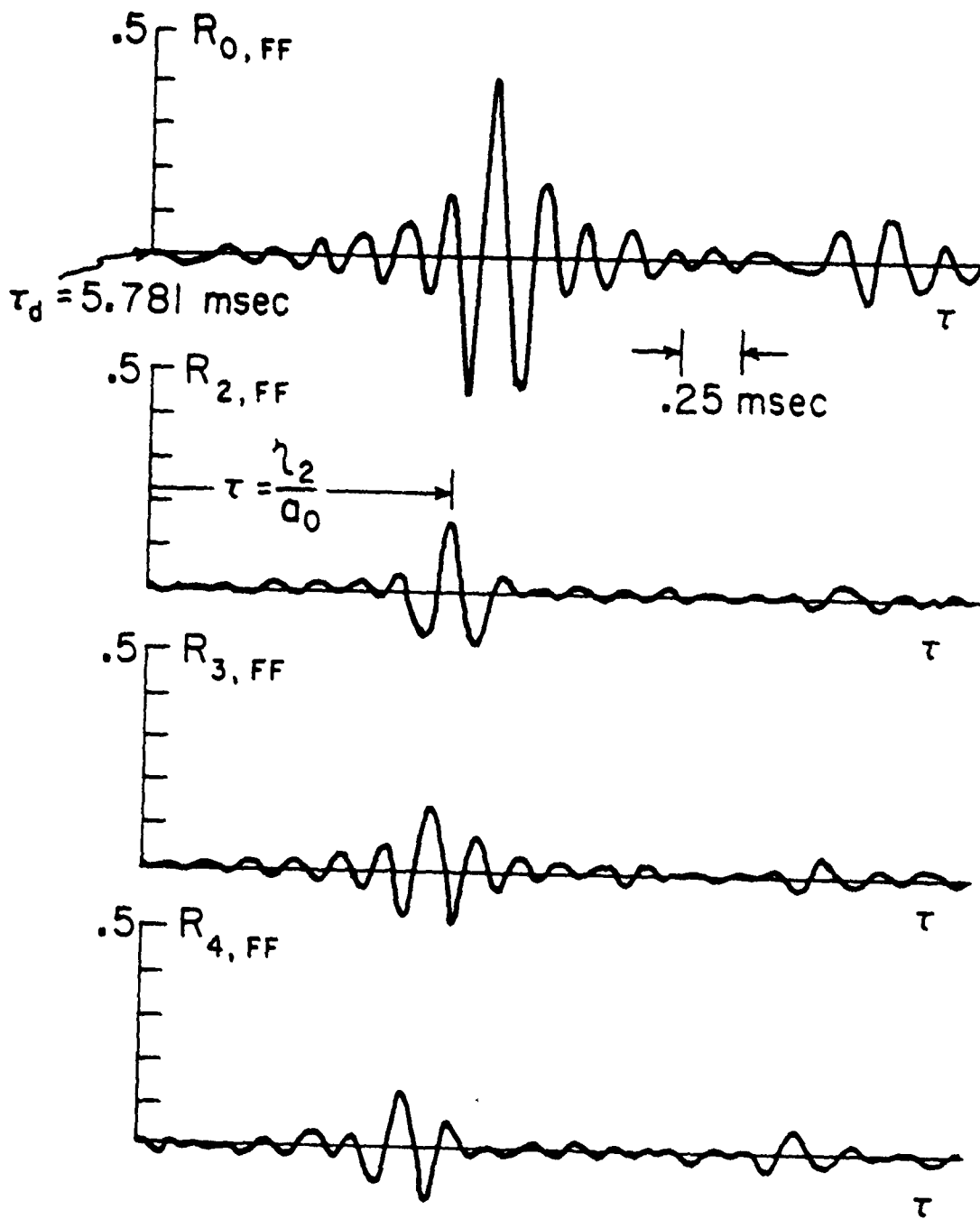


Fig. (6-5) Cross-Correlations between Surface and Far Field Signals, indices refer to the sketch in Fig. (3-19), same conditions as in Fig. (6-4)

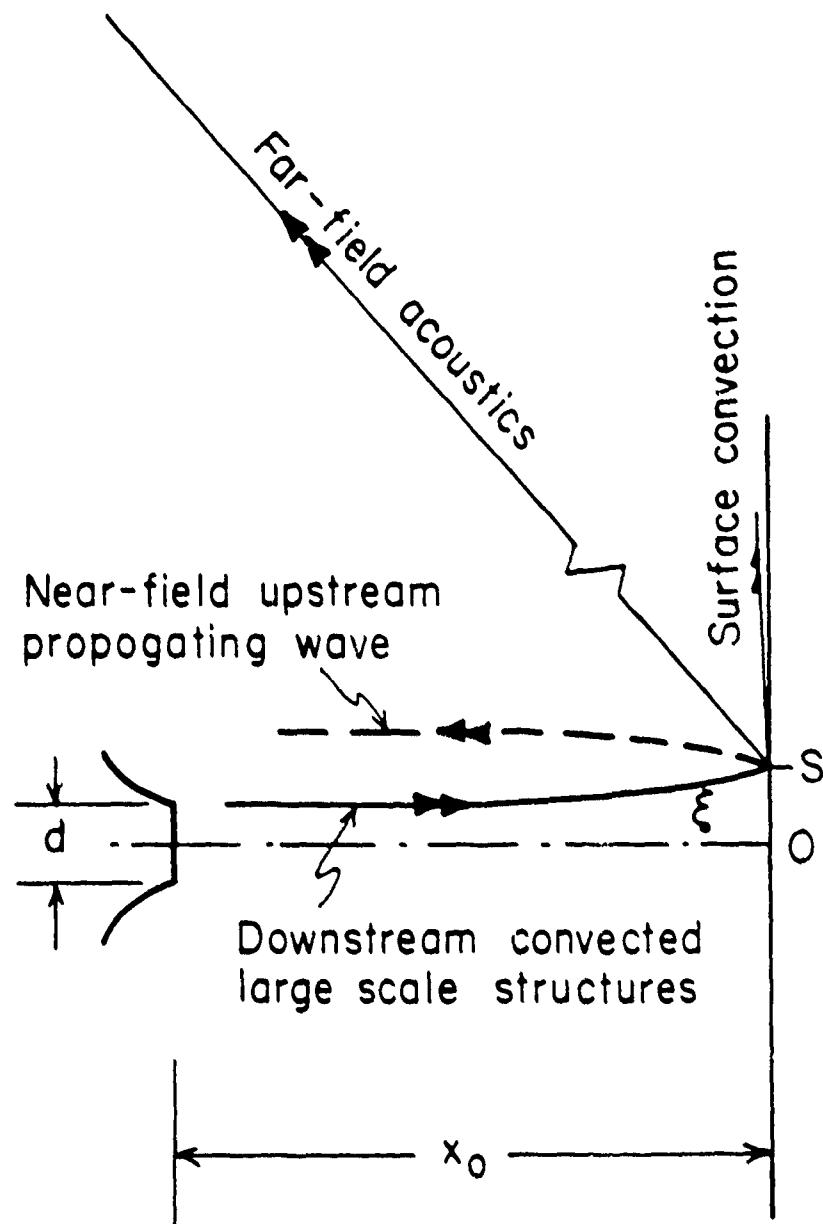
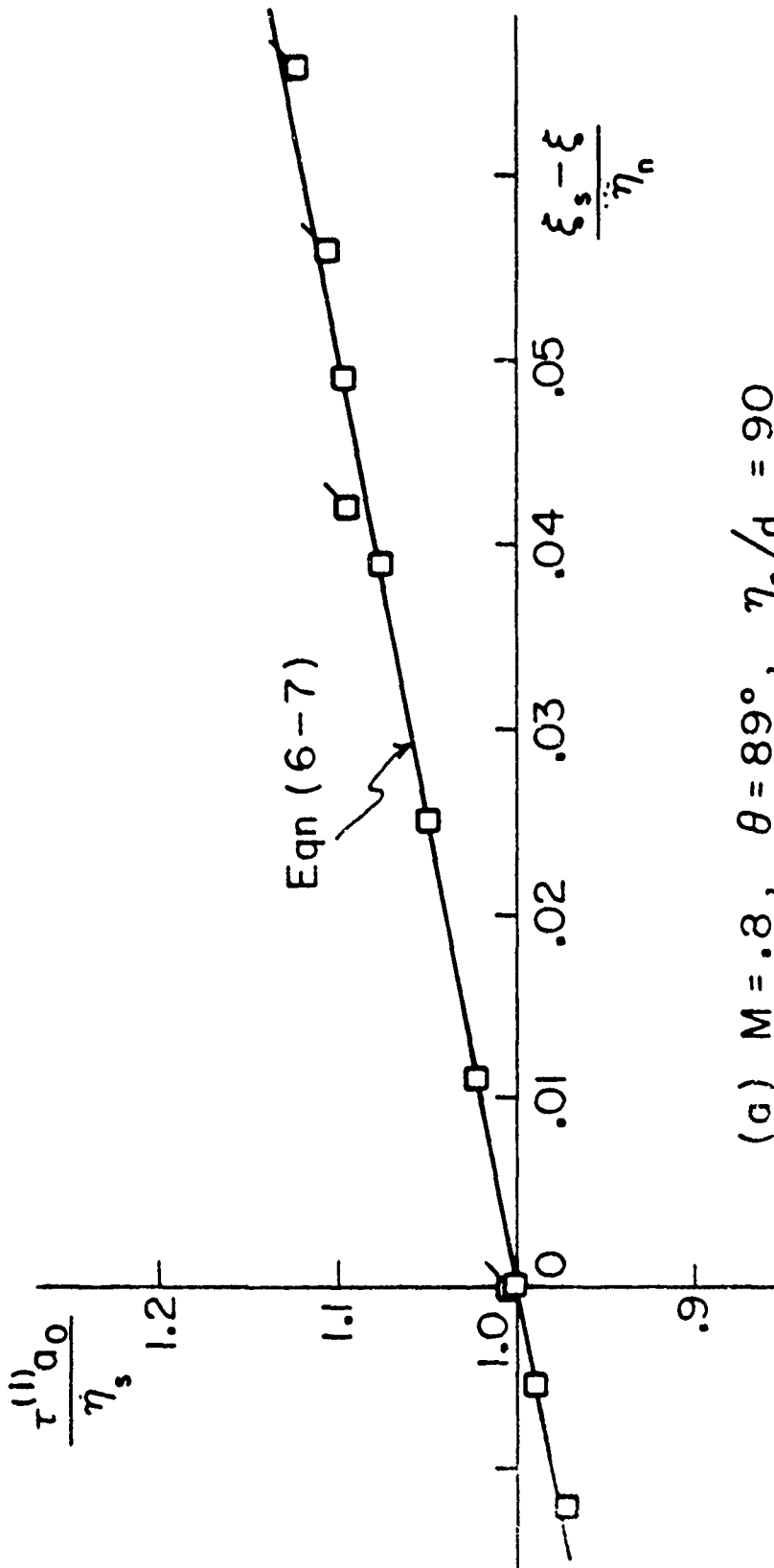


Fig. (6-6) Schematic of a Model for Far Field Noise Radiation due to the Impinging Large Scale Structures



(a)  $M = .8$ ,  $\theta = 89^\circ$ ,  $\eta_n/d = 90$   
 $\square$   $x_0/d = 5.5$ ,  $\alpha x_0/d = 7$   
 $\eta_s/d = 92.6$ ,  $\eta_s/d = 93$

Fig. (6-7) Comparison between the Optimum Time Delays of the Correlation with the Far Field and the Model

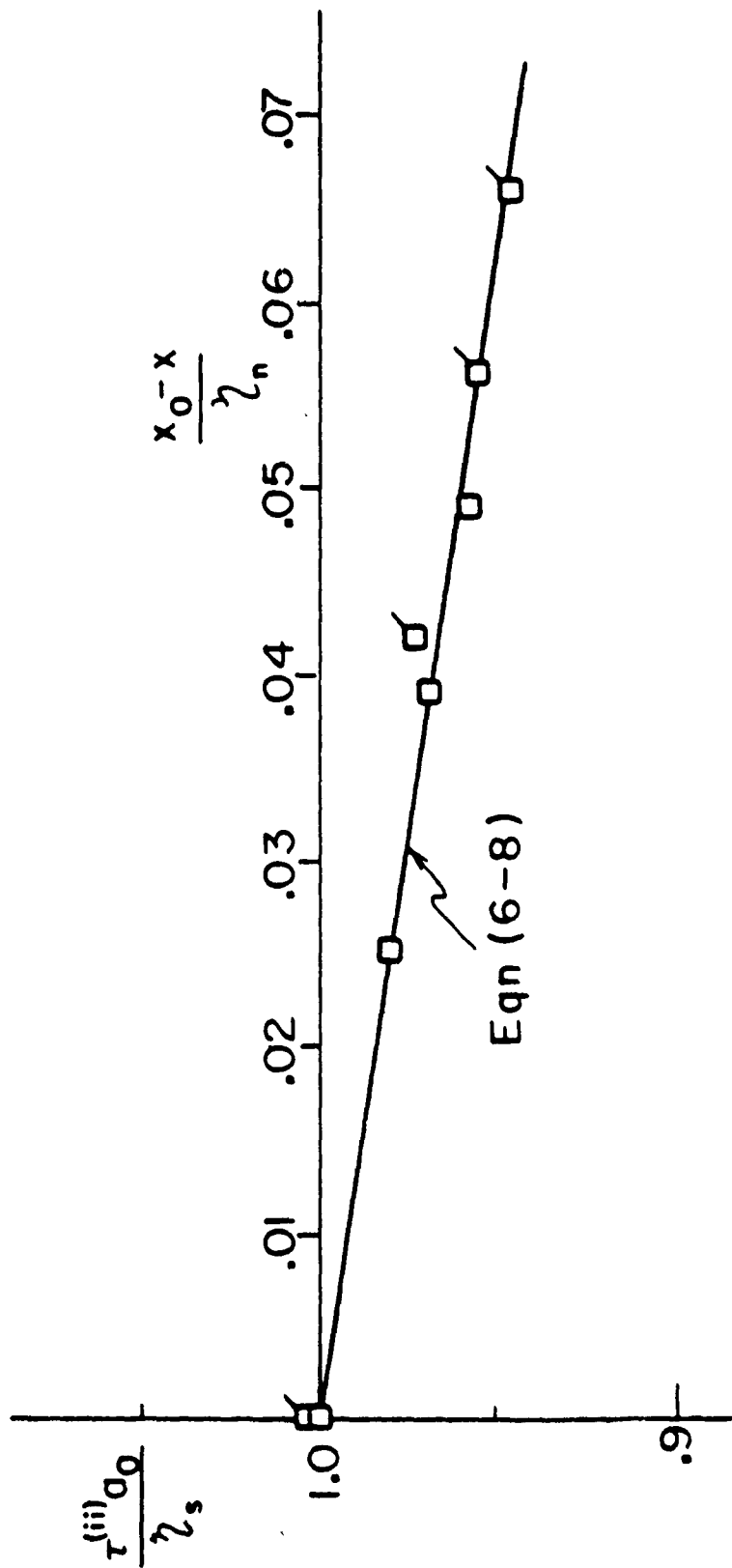


Fig. (6-7) Concluded

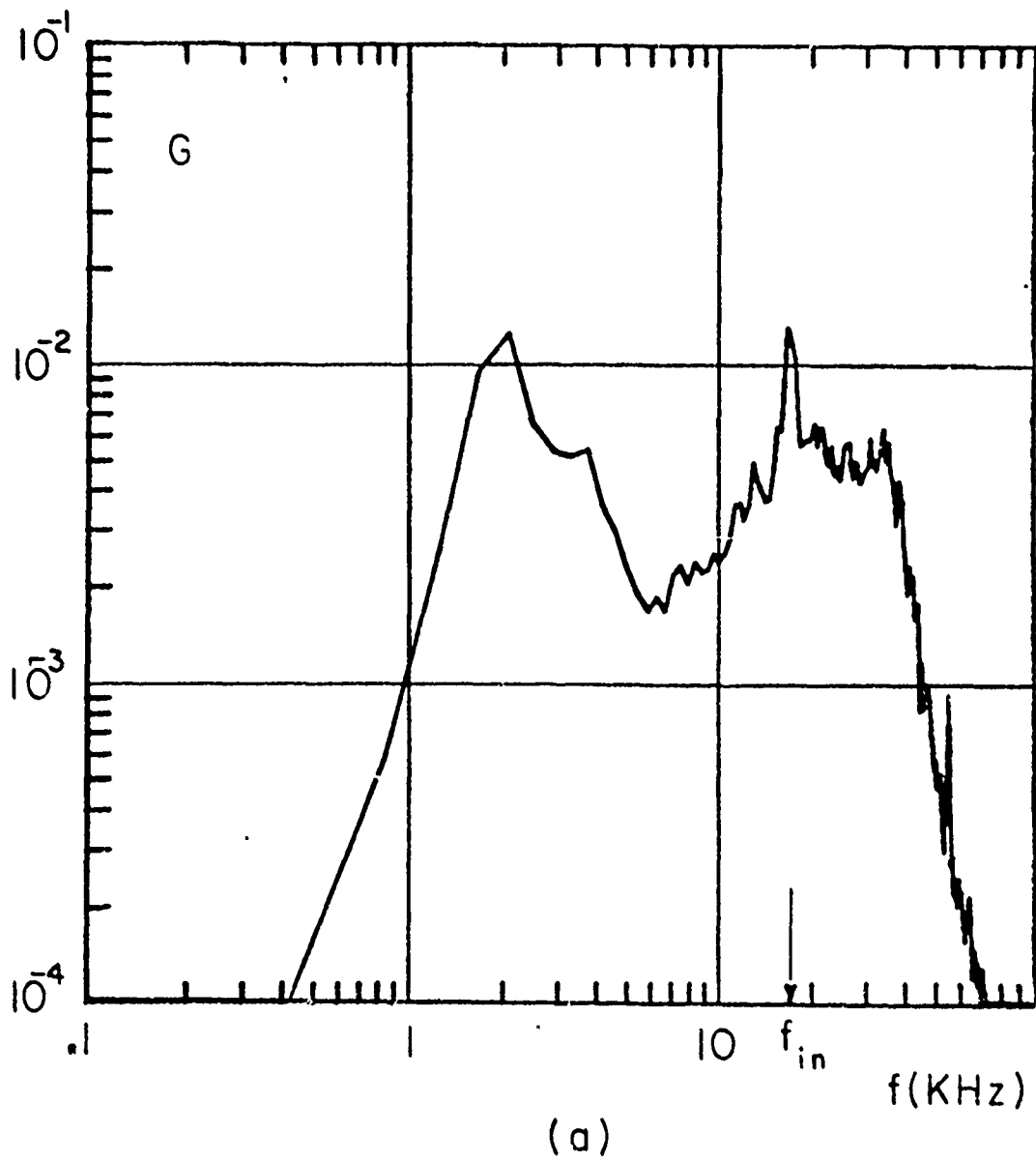
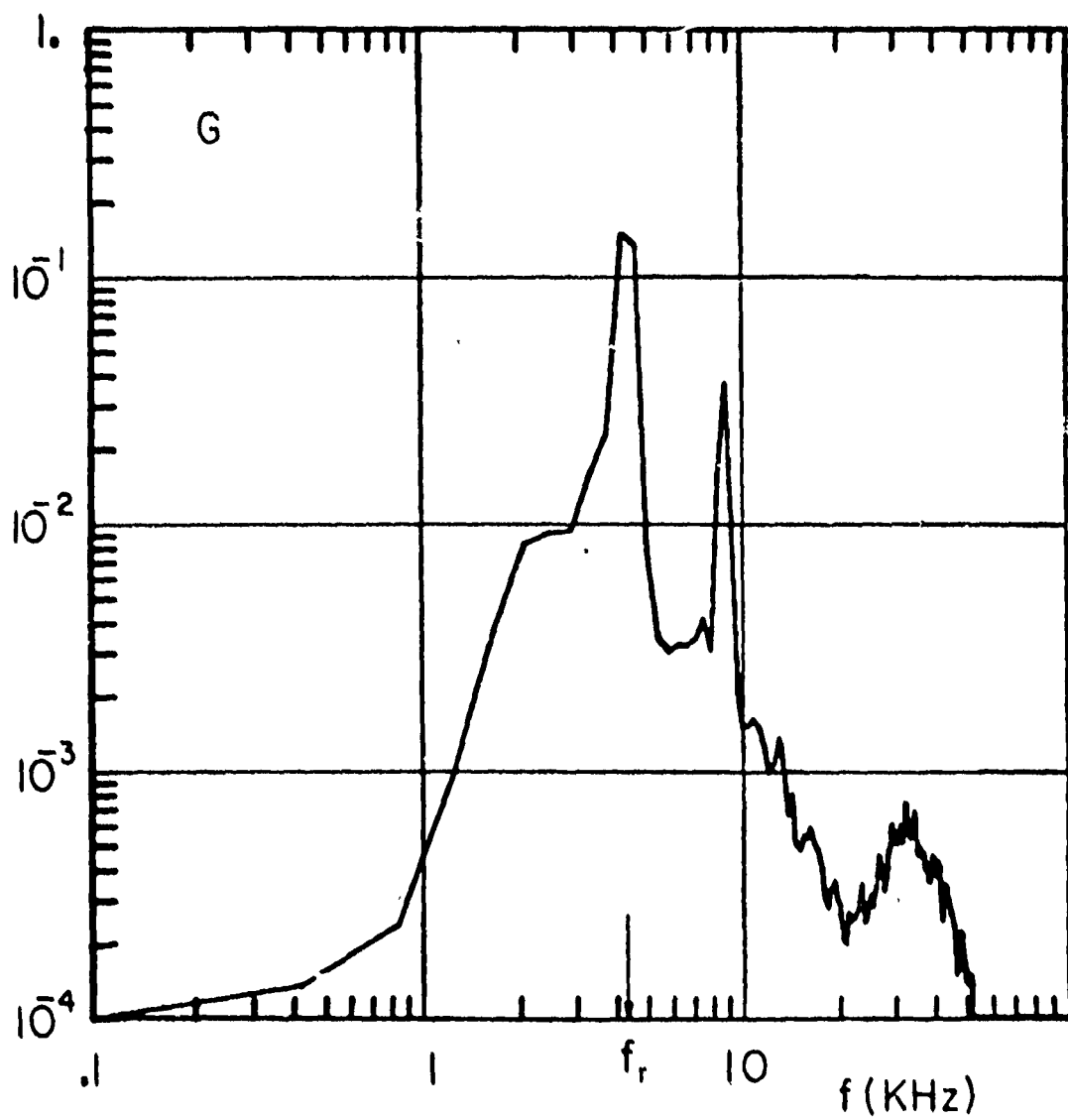
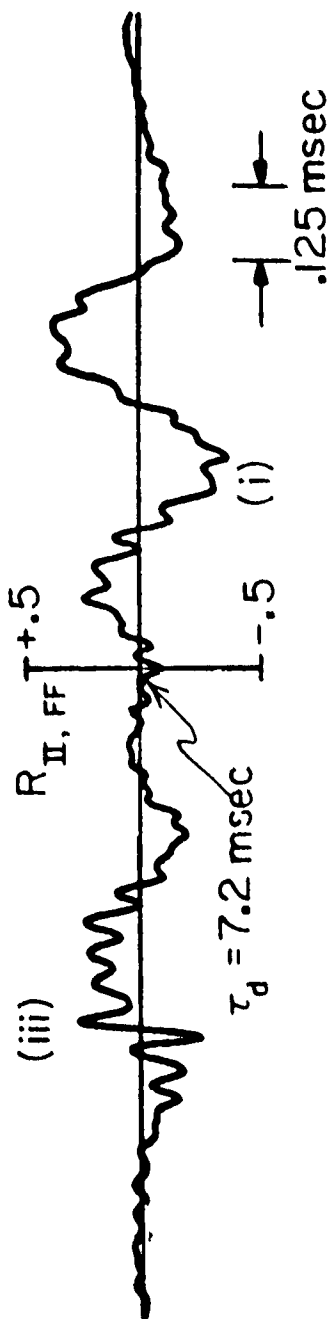


Fig. (6-8) Far Field Power Spectra,  $x_0/d=4.5$ , (a)  $M=.4$ , (b)  $M=.9$

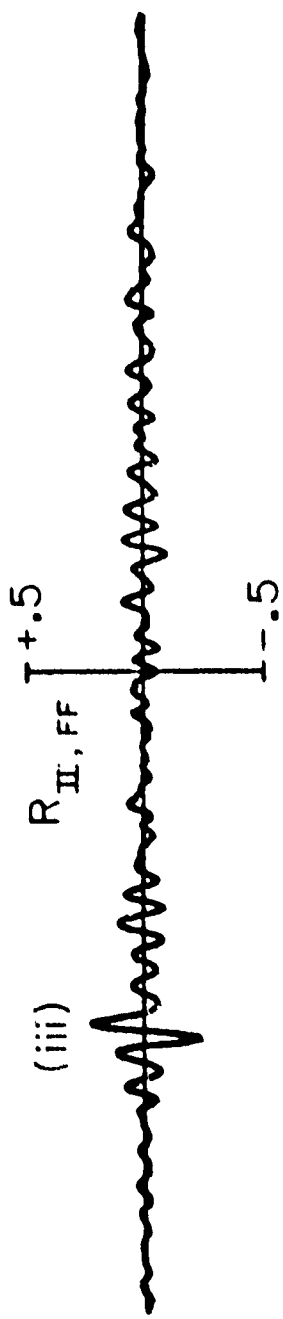


(b)

Fig. (6-8) Concluded



(a) Before



(b) After high-pass filter [cutoff frequency = 8 (KHz)]

Fig. (6-9) Cross-correlation between Far Field and Near Field (Close to the Nozzle Exit) Signals, indices refer to locations shown in Fig. (6-10) ( $M=.4, x_0/d=4.5$ )

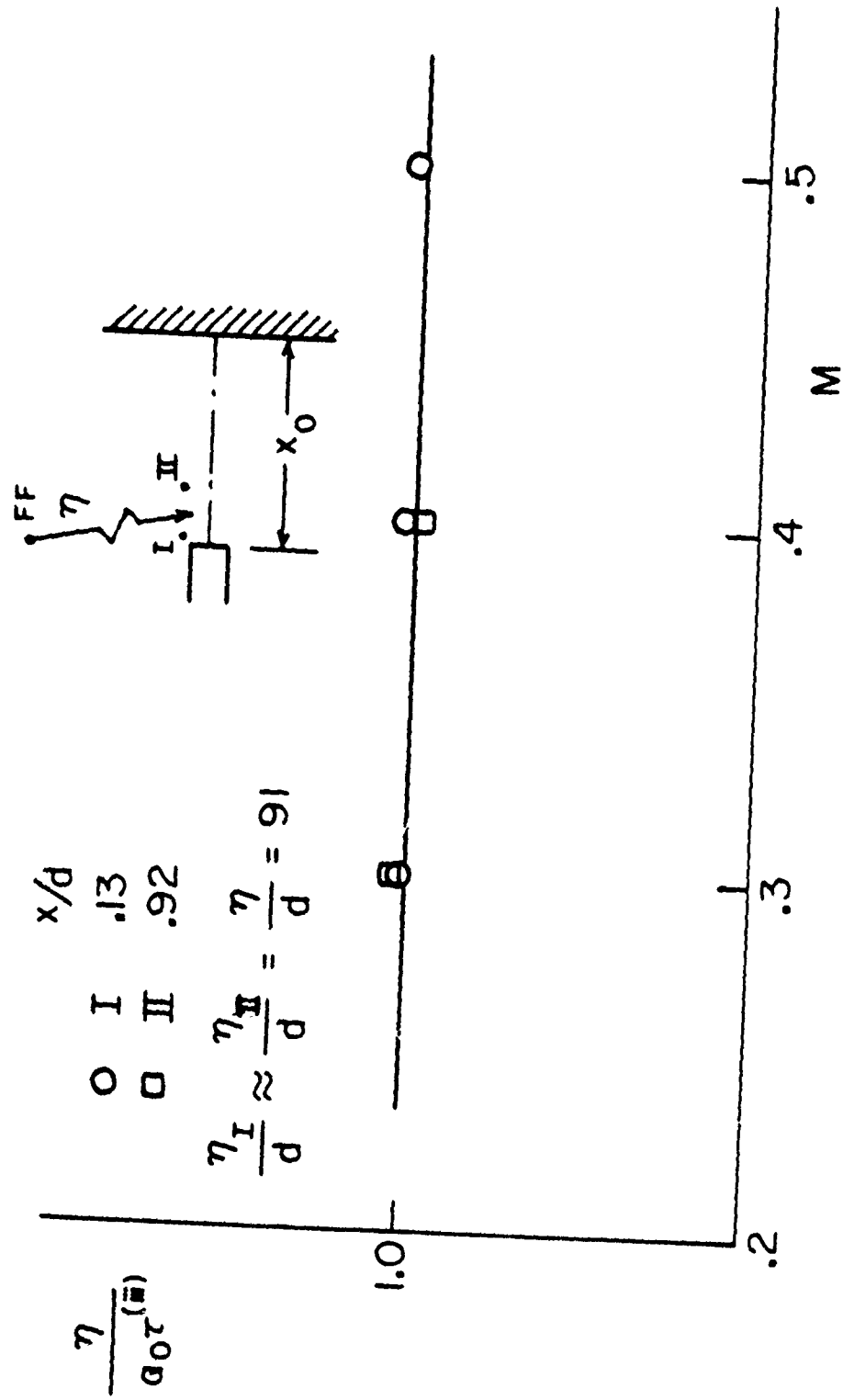


Fig. (6-10) High Frequency Far Field Noise Radiation Path, from  $\tau_{(iii)}$  e.g. Peak (iii) in Fig. (6-9) ,  $x_0/d=4.5$

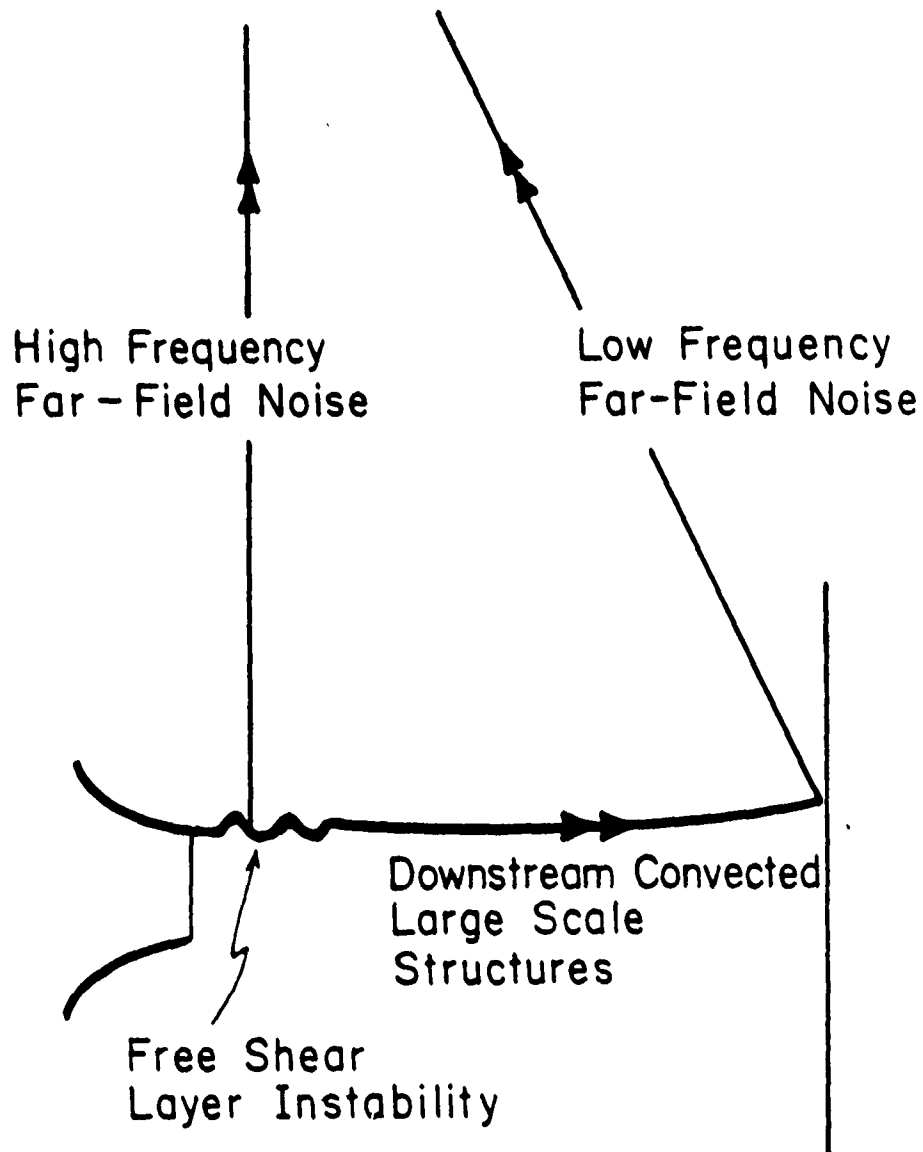


Fig. (6-11) Summary of Noise Generation Mechanisms in an Impinging Jet.

## REFERENCES

1. Donalson, C. and Snedeker, R.S., "A Study of Free Jet Impingement. Part 1. Mean Properties of Free and Impinging Jets," J. Fluid Mech., Vol. 45, Part 2, pp. 281-319 (1971).
2. Donalson, C., Snedeker, R.S. and Margolis, D.P., "A Study of Free Jet Impingement. Part 2. Free Jet Turbulent Structure and Impingement Heat Transfer," J. Fluid Mech., Vol. 45, Part 3, pp. 477-512 (1971).
3. Preisser, J.S. and Block, P.J.W., "An Experiment Study of the Aeroacoustics of a Subsonic Jet Impinging Normal to a Large Rigid Surface," AIAA Paper No. 76-520 (1976).
4. Giralt, F., Chia, C. and Trass, O., "Characterization of the Impingement Region in an Axisymmetric Turbulent Jet," Ind. Eng. Chem., Fundm., 16, 27 (1977).
5. Gutmark, E., Wolfshtein, M. and Wagnanski, I., "The Plane Turbulent Impinging Jet," TECHNION, Haifa, Israel, TAE Report No. 226 (1976).
6. Strong, D.R., Siddon, T.E. and Chu, W.T., "Pressure Fluctuations on a Flat Plate With Oblique Jet Impingement," NASA CR-839 (1967).
7. Westley, R., Wooley, J.H. and Brosseau, P., "Surface Pressure Fluctuations From Jet Impingement on an Inclined Flat Plate," AGARD Symposium on Acoustic Fatigue, Sept. 1972.
8. Wagner, F.R., "The Sound and Flow Field of an Axially Symmetric Free Jet Upon Impact on a Wall," Zeit. fur Flugwiss 19, 30-44 (1971); NASA TT F-13942 (1971).
9. Neuworth, G., Dr.-Ing. Thesis Tech. Hochsch. Aschen, West Germany, (1973).
10. Rockwell, D. and Naudascher, E., "Self-Sustained Oscillations of Impinging Free Shear Layer," Ann. Rev. Fluid Mech., 11:67-94 (1979).
11. Powell, A., "On the Edgetone," J. Acoust. Soc. Am. 33, pp.395-409 (1961).
12. Powell, A., "Vortex Action in Edgetones," J. Acoust. Soc. Am. 34, pp. 163-166 (1961).
13. Rossiter, J.E., "Wind-Tunnel Experiments on the Flow over Rectangular Cavities at Subsonic and Transonic Speeds," Aero. Res. Council. R & M., No. 3438 (1964).

14. Tam, C. and Block, P.J.W., "On the Tones and Pressure Oscillations Induced by Flow over Rectangular Cavities," J. Fluid Mech., Vol. 89, pp. 373-399 (1978).
15. Sarohia, V., "Experimental Investigation of Oscillations in Flows over Shallow Cavities," AIAA Paper No. 76-182 (1976).
16. Rockwell, D. and Knisely, C., "The Organized Nature of Flow Impingement upon a Corner,"
17. Brown, G. and Roshko, A., "The Effect of Density Differences on the Turbulent Mixing Layer," AGARD CP 93, pp. 23.1-23.12 (1971).
18. Laufer, J., "New Trends in Experimental Turbulence Research," Ann. Rev. Fluid Mech., 7:307-326 (1975).
19. Lau, J.C., Fisher, M.J. and Fuchs, H.V., "The Intrinsic Structure of Turbulent Jets," J. Sound and Vibration, 22, pp. 379-406 (1972).
20. Petersen, R.A., "Influence of Wave Dispersion on Vortex Pairing in a Jet," J. Fluid Mech., Vol. 89, pp. 469-495 (1978).
21. Michalke, A., "Instabilität eines Kompressiblen runden Freistrahls unter Berücksichtigung des Einflusses der Strahlgrenzschichtdicke," Z. Flugwiss, 19, pp. 319-328 (1972).
22. Crow, S.C. and Champagne, F.H., "Orderly Structure in Jet Turbulence," J. Fluid Mech., Vol. 48, pp. 547-591 (1971).
23. Winant, C.D. and Browand, F.K., "Vortex Pairing: the Mechanism of Turbulent Mixing Layer Growth at Moderate Reynolds Number," J. Fluid Mech., Vol. 63, pp. 237-255 (1974).
24. Browand, F.K. and Laufer, J., "The Role of Large Scale Structures in the Initial Development of Circular Jets," Proc. Fourth Biennial Symp. on Turbulence in Liquids, Univ. of Missouri-Rolla, Sept. 22-24, 1975.
25. Fuchs, H.V. and Michalke, A., "Introduction to Aerodynamic Noise Theory," Progress in Aerospace Sciences, Vol. 14, Ed. by Kuchemann, Pergamon, New York, pp. 227-297 (1973).
26. Powell, A., "Aerodynamic Noise and the Plane Boundary," J. Acous. Soc. Am., Vol. 32, pp. 982-990 (1960).
27. Preisser, J.S., "Fluctuating Surface Pressure and Acoustic Radiation for Subsonic Normal Jet Impingement," NASA Tech. Paper 1361 (1979).

28. Pan, Y.S., "Cross-Correlation Methods for Studying Near- and Far Field Noise Characteristics of Flow-Surface Interactions," J. Acoust. Soc. Am., Vol. 58 (1975).
29. Chu, W.T., Kaplan, R.E. and Laufer, J., "Description and Performance Characteristics of the USC Aerodynamic Noise Research Facility," USCAE 123, 1975.
30. Bendat, J.S. and Piersol, A.G., "Random Data: Analysis and Measurement Procedures," Wiley-Interscience (1971).
31. Williams, K.C. and Purdy, K.R., "A Prewhitening Technique for Recording Acoustic Turbulent Flow Data," Rev. Sc. Instr., Vol. 41, No. 12, pp. 1897-1899 (1970).
32. Ho, C.M. and Nosseir, N.S., "The Hydrodynamic Feedback of an Impinging Water Jet," Bulletin Am. Phys. Soc., Sec. 11, 22, pp. 1280 (1977).
33. Ho, C.M. and Kovaszny, L.S.G., "Unsteady Pressure Field of an Impinging Turbulent Vortex Ring," 27th Annual Meeting, Am. Phys. Soc., Division of Fluid Dynamics, 1974.
34. Widnall, S.E. and Sullivan, J.P., "On the Stability of Vortex Rings," Proc. Roy. Soc. A 332, pp. 335-353 (1973).
35. Maxworthy, T., "Some Experimental Studies of Vortex Rings," J. Fluid Mech., Vol. 81, pp. 465-495 (1977).
36. Widnall, S.E., Bliss, D.B. and Tsai, C.Y., "The Stability of Short Waves on a Vortex Ring," J. Fluid Mech., Vol. 66, pp. 35-47 (1974).
37. Ho, C.M. and Kovaszny, L.S.G., "Acoustical Shadowgraph," Phys. of Fluids, Vol. 19, No. 8, 1976.
38. Wills, J.A.B., "On Convection Velocities in Turbulent Shear Flows," J. Fluid Mech., Vol. 20, pp. 417-432 (1964).
39. Lin, C.C., "On Taylor's Hypothesis and the Acceleration Terms in the Navier-Stokes Equations," Q. Appl. Math. 10, 295 (1952).
40. Fuchs, H.V. and Michel, U., "Experimental Evidence of Turbulent Source Coherence Effecting Jet Noise," AIAA, Paper No. (1977).
41. Chu, W.T., "Certification of the USC Jet Noise Facility," USCAE 131, 1975.

42. Bechert, D. and Michel, U., "The Control of a Thin Shear Layer With and Without a Semi-Infinite Plate by a Pulsating Flow Field," *ACUSTICA*, Vol. 33, No. 5 (1977).
43. Karamcheti, K., Bauer, A.B., Shields, W.L., Stegen, G.R. and Woolley, J.P., "Some Features of an Edge-Tone Flow Field," NASA Spec. Publ. 207, pp. 275-304 (1969).
44. Block, P.J.W., "Noise Response of Cavities of Varying Dimensions," NASA-Tech. Note-D-8351, 1976.
45. Ho, C.M. and Huang, L.S., "Subharmonics and Vortex Merging in an Unsteady Shear Layer," *Bulletin Am. Phys. Soc.*, Sec. 11, 23, p. 1007 (1978).
46. Hussain, A.K. and Zaman, K.B., "The Free Shear Layer Tone Phenomenon and Probe Interference," *Proc. Symp. on Turbulence*, TU, Berlin, Aug. 1-5, ed. H. Fiedler (1977). Also *J. Fluid Mech.*, (in press).
47. Amiet, R.K., "Refraction of Sound by a Shear Layer," AIAA Paper No. 77-54, 1977.
48. Ribner, H.S., "Reflection, Transmission, and Amplification of Sound by a Moving Medium," *J. Acoust. Soc. of Am.*, Vol. 29, No. 4 (1957).
49. Lush, P.A., "Measurements of Subsonic Jet Noise and Comparison With Theory," *J. Fluid Mech.*, Vol. 46, pp. 477-500 (1971).
50. Ahuja, K.K. and Bushell, K.W., "An Experimental Study of Subsonic Jet Noise and Comparison with Theory," *J. Sound and Vib.*, 30 (3), 317-341 (1973).
51. Tam, C.K.W., "Directional Acoustic Radiation from a Supersonic Jet Generated by Shear Layer Instability," *J. Fluid Mech.*, Vol. 46, pp. 757-768 (1971).

APPENDIX A  
STANDING WAVE PATTERN

The pressure  $p$  in Eqn.(4-5) can be written, without loss of generality, in the form

$$p = a e^{i[\omega_r t - k_1(x-x_0)]} + b e^{i[\omega_r t + \bar{k}_2 \cdot (\bar{r} - \bar{r}_s)]} \quad (A-1)$$

The boundary condition at the plate (4-9) is satisfied in Eqn.(A-1). This equation can also be written

$$p = a e^{i[\omega_r t - k_1(x-x_0)]} + b e^{i[\omega_r t + k_{2x}(x-x_0) + k_{2r}(r-r_s)]} \quad (A-2)$$

where  $\bar{k}_2$  is expressed in terms of its components  $k_{2x}$  and  $k_{2r}$  in the  $x$  and  $r$  directions, and the amplitudes  $a$  and  $b$  are functions of position. It is assumed that the amplitudes satisfy the inequalities

$$a > b \quad (r/d < 1.0)$$

$$a < b \quad (r/d > 1.0)$$

Using the identity

$$e^{i\theta_1} + e^{i\theta_2} = 2 \cos. \frac{\theta_1 - \theta_2}{2} e^{i\left(\frac{\theta_1 + \theta_2}{2}\right)}$$

Eqn.(A-2) takes the following forms:

$r/d < 1.0$ :

$$p = 2bK' e^{i\epsilon} e^{i\omega_r t} + (a-b) e^{i[\omega_r t - K_1(x-x_0)]} \quad (A-3a)$$

$r/d > 1.0$ :

$$p = 2aK' e^{i\epsilon} e^{i\omega_r t} + (b-a) e^{i[\omega_r t + K_2 \cdot (\bar{J} - \bar{J}_s)]} \quad (A-3b)$$

where,

$$K' = \cos. \left[ \frac{K_1 + K_{2x}}{2} (x - x_0) + \frac{K_{2r}}{2} (r_s - r) \right],$$

and

$$\epsilon = \left[ \frac{K_1 + K_{2x}}{2} (x - x_0) - \frac{K_{2r}}{2} (r_s - r) \right]. \quad (A-4)$$

The first term in Eqns.(A-3) is a standing wave, while the second term represents a downstream propagating wave in Eqn.(A-3a) and an upstream propagating wave in

Eqn.(A-3b). There are nodes and antinodes, but because of the second propagating term the nodes are not zero points. The factor  $\exp i\epsilon$  disperses the maximum amplitudes of various antinode oscillations so they no longer occur at the same time [Neuwirth (1973)].

Since observations indicate that resonance occurs at high Mach number and small plate to nozzle distances,  $\epsilon$  can be shown to be small. At high M the convection speed of large scale structures is close to the speed of sound. Therefore, at the resonance frequency the two wave numbers  $k_1$  and  $k_2$  are of the same order of magnitude, i.e.,  $(k_1 - k_2)_x$  is small. Also,  $(x_0 - x)$  is small at resonance and  $(r_s - r)$  is generally small as long as  $r$  is in the near field.

Using the expansion

$$\exp i\epsilon = 1 + i\epsilon - \epsilon^2/2 + \dots$$

Eqns.(A-3) simplify to

$r/d < 1.0$ :

$$p = 2bk' e^{i\omega_r t} + (a-b) e^{i[\omega_r t - k_1(x-x_0)]} + o(\epsilon)$$

$r/d > 1.0$ :

$$p = 2ak' e^{i\omega_r t} + (b-a) e^{i[\omega_r t + \vec{k}_2 \cdot (\vec{r} - \vec{r}_s)]} + o(\epsilon)$$

which are the forms used in Eqn. (4-28).